SANDIA REPORT

SAND2015-0803
Revision of SAND2009-2282
Unlimited Release
Printed Original Report: March 2009; this revision: January 30, 2015

KAYENTA: Theory and User's Guide

R.M. Brannon, T.J. Fuller, O.E. Strack, A.F. Fossum, and J.J. Sanchez

Prepared by
Sandia National Laboratories
Albuquerque, New Mexico 87185 and Livermore, California 94550

Sandia National Laboratories is a multi-program laboratory managed and operated by Sandia Corporation, a wholly owned subsidiary of Lockheed Martin Corporation, for the U.S. Department of Energy's National Nuclear Security Administration under contract DE-AC04-94AL85000.

Approved for public release; further dissemination unlimited.

Sandia National Laboratories

Issued by Sandia National Laboratories, operated for the United States Department of Energy by Sandia Corporation.

NOTICE: This report was prepared as an account of work sponsored by an agency of the United States Government. Neither the United States Government, nor any agency thereof, nor any of their employees, nor any of their contractors, subcontractors, or their employees, make any warranty, express or implied, or assume any legal liability or responsibility for the accuracy, completeness, or usefulness of any information, apparatus, product, or process disclosed, or represent that its use would not infringe privately owned rights. Reference herein to any specific commercial product, process, or service by trade name, trademark, manufacturer, or otherwise, does not necessarily constitute or imply its endorsement, recommendation, or favoring by the United States Government, any agency thereof, or any of their contractors or subcontractors. The views and opinions expressed herein do not necessarily state or reflect those of the United States Government, any agency thereof, or any of their contractors.

Printed in the United States of America. This report has been reproduced directly from the best available copy.

Available to DOE and DOE contractors from
U.S. Department of Energy
Office of Scientific and Technical Information
P.O. Box 62
Oak Ridge, TN 37831

Telephone: (865) 576-8401
Facsimile: (865) 576-5728
E-Mail: reports@adonis.osti.gov
Online ordering: http://www.osti.gov/bridge

Available to the public from
U.S. Department of Commerce
National Technical Information Service
5285 Port Royal Rd
Springfield, VA 22161

Telephone: (800) 553-6847
Facsimile: (703) 605-6900
E-Mail: orders@ntis.fedworld.gov
Online ordering: http://www.ntis.gov/help/ordermethods.asp?loc=7-4-0#online

SAND2015-0803
Revision of SAND2009-2282
Unlimited Release
Printed Original Report: March 2009; this revision:
January 30, 2015

KAYENTA: Theory and User's Guide

Rebecca Brannon
University of Utah Mechanical Engineering
2134 MEB, 50 S. Central Campus Drive
Salt Lake City, UT 84112-9208
Rebecca.Brannon@utah.edu

T. J. Fuller
Orbital ATK Inc.
Magna, UT 84044
Timothy.Fuller@atk.com

O. Erik Strack
Computational Shock and Multiphysics
Sandia National Laboratories
Albuquerque, NM 87185-0378
oestrac@sandia.gov

Arlo F. Fossum
BP America, Inc.
PO BOX 3092
Houston, TX 77079-3092
Arlo.Fossum@bp.com

Jason J. Sanchez
Computational Shock and Multiphysics
Sandia National Laboratories
Albuquerque, NM 87185-0378
jassanc@sandia.gov

Abstract

The physical foundations and domain of applicability of the Kayenta constitutive model are presented along with descriptions of the source code and user instructions. Kayenta, which is an outgrowth of the Sandia GeoModel, includes features and fitting functions appropriate to a broad class of materials including rocks, rock-like engineered materials (such as concretes and ceramics), and metals. Fundamentally, Kayenta is a computational framework for generalized plasticity models. As such, it includes a yield surface, but the term "yield" is generalized to include any form of inelastic material response (including microcrack growth and pore collapse) that can result in non-recovered strain upon removal of loads on a material element. Kayenta supports optional anisotropic elasticity associated with joint sets, as well as optional deformation-induced anisotropy through kinematic hardening (in which the initially isotropic yield surface is permitted to translate in deviatoric stress space to model Bauschinger effects). The governing equations are otherwise isotropic. Because Kayenta is a unification and generalization of simpler models, it can be run using as few as 2 parameters (for linear elasticity) to as many as 40 material and control parameters in the exceptionally rare case when all features are used. For high-strain-rate applications, Kayenta supports rate dependence through an overstress model. Isotropic damage is modeled through loss of stiffness and strength.

Acknowledgements

The authors are grateful for the support received over the years from a number of Sandia project managers and colleagues who have provided financial support and encouraged the development and enhancement of this general geo-material model for use in Sandia computer codes. The initial development of the model began under a project led by Mike Stone under the U.S. Department of Energy (DOE) Advanced Computational Technology Initiative (ACTI) program. Additional development was made under an Engineering Sciences Research Foundation (ESRF) project led by Hal Morgan; a Defense Programs (DP) Penetration project led first by Jim Hickerson and later by Danny Frew; several DOE Accelerated Strategic Computing Initiative (ASCI) Design and Qualification (DQ) Materials & Physics Models (M&PM) projects led by Mike McGlaun and Justine Johannes, a Hard and Deeply Buried Target (HDBT) project led by Paul Yarrington and Shawn Burns; a Model Accreditation Via Experimental Sciences For Nuclear Weapons (MAVEN) laboratory testing project led by Moo Lee, two LDRD projects, one led by Larry Costin and the other by Rich Regueiro; and an Army project under John Rowe and Scott Schoenfeld.

The authors acknowledge individual contributions of Steve Akers, Lupe Arguello, Paul Booker, Kevin Brown, Ted Carney, Mike Chiesa, James Colovos, Jim Cox, Kent Danielson, Mike Forrestal, Craig Foster, Joanne Fredrich, Lew Glenn, Ed Hoffman, Dave Holcomb, John Holland, Joe Jung, Daniel Kletzli, Colby Lavin, Estaban Marin, Yvonne Murray, Bill Oberkampf, Bill Olsson, John Pott, Tom Pucik, Jonathan Rath, Sal Rodriguez, Bill Scherzinger, Paul Senseny, Allen Shirley, Len Schwer, Steve Sobolik, Scot Swan (who was especially active in this effort during his term as a Masters Student), Bob Swift, Tom Voth, Tom Warren, Joel Wirth, and Mike Wong, who have provided code support, user feedback, bug fixes, theoretical discussions, constructive criticism, and editing services.

We are grateful to our family members for their patience and support during the ongoing development of this model.

Rebecca, Tim, Erik, Arlo, and Jason

June 16, 2014

This page intentionally left blank.

Contents

1 Introduction **19**

Kayenta overview 20

Features of Kayenta 20

Limitations of Kayenta 22

2 Notation **27**

Typesetting conventions 27

Vector and Tensor notation 27

3 The Stress Tensor **31**

Stress invariants 33

Derivatives of the stress invariants 34

Special stress states 35

HYDROSTATIC (HYD) 35

TRIAXIAL (TXC and TXE) 35

SIMPLE/PURE SHEAR and PRESSURE-SHEAR LOADING (SHR) 42

Spatial and Reference stress (frame indifference) 43

Lode coordinates 44

Octahedral yield profile visualization 46

Meridional yield profile visualization 46

Closed-form solution for ordered eigenvalues 48

4 Kayenta theory **51**

Elasticity 52
Nonlinear elasticity 53
Assigning values to the elastic constants 53
The elastic limit (yield surface) 54
The cap function, f_c 62
Elastic-plastic coupling 63
Meridional shear limiter function, F_f 64
The complete Kayenta yield function 69
The "J3TYPE" Lode-angle function, Γ 70
Advancing the solution (groundwork discussion) 73
Evolution equations 79
Evolution equation for the porosity-related internal state variable, κ 80
Relationship between $\overline{X}$ and $\overline{\dot{\varepsilon}_v^p}$ (cap curvature model) 81
The P2 parameter and its implication on pore growth 86
Relationship between $\overline{\kappa}$ and $\overline{X}$ (cap curvature model) 87
The κ evolution law 89
Evolution equation for the kinematic hardening backstress tensor 91
Advancing the solution (final step, consistency parameter) 93
Numerical implementation for elastic isotropy 93
Formal equivalence with oblique return algorithms 95
Quasistatic inelastic tangent stiffness tensor 95
Stability issues 96

5 Softening **99**

Strength and Stiffness Degradation in Softening 100
Accumulated-Damage Framework 106

Implemented Fracture Models 107
Spall Pressure and Void Insertion 108
Implementation Requirements for Softening 109

6 Equation of State: Application. 113

Constitutive Models for Thermoplastic Materials 113
Kayenta 113
Johnson-Cook Plasticity 113
Mie-Grüneisen Equation of State 114
Incorporating Thermal Effects in Kayenta: Initial Development 115
Thermal Softening 116
Thermoelastic Limit 117
Evolution Equations 118
Kinematic Hardening Backstress Tensor 118
Plastic Temperature Evolution 118

7 Rate Dependence 119

Viscoplasticity model overview 119
Viscoplasticity model derivation 122
Limiting case 125
Assigning a value to the characteristic material time 128
Thermodynamics considerations 128

8 Kayenta Numerical Solution scheme 131

Role of Kayenta within a finite-element program 131
Spatial stability (mesh dependence/loss of strong ellipticity) 133
Kayenta files, subroutines, memory requirements, and model installation requirements . . 134

Arguments passed to and from Kayenta's driver routine 135
Input 135
Output 136
Plottable Output 136
Kayenta algorithm 138
Rate independent (inviscid) part of the viscoplasticity equations 138
Viscous part of the viscoplasticity equations 139

9 Software "confidence building" activities 141

Preliminary convergence testing 148
Verification: single-element problems (regression suite) 152
Discussion 157
Other single-element tests 157
Verification: Hendren & Ayier pressurized cylinder 158
Elastic free-field wave form (finite-element verification) 159
Softening verification and validation 161
Verification of Accumulated Damage Framework 165
Constant Equivalent-Strain-at-Failure Verification 169
Johnson-Cook verification 169
Xue-Wierzbicki Verification 169
Thermo-Kayenta Verification 180
Isotropic Deformation 180
Isochoric Deformation 183
Taylor Impact 190
Results 190

10 Parameterization (calibration) 195

Nonlinear elasticity 195
Elastic-plastic coupling 195
Triaxial Compression 197
Parameterization: Rate dependence 203

11 Building confidence in the physical theory 205

Post-calibration Triaxial loading 206
Field-scale penetration 206
Free field wave form for spherical shock loading 207

12 Closing Remarks 213

Appendix

A Parameterizing Kayenta 215

B Nomenclature and Data Sets 229

B.1 Model Parameters (User Input) 230
B.1.1 Other input parameters (available only in special builds) 243
B.2 Internal State Variables (Plottable Output) 246
B.2.1 Other plottable parameters (available only in special builds) 252
B.3 Other Symbols (used only in this report) 254
B.4 Datasets 259
B.4.1 Dataset for Salem Limestone 259
B.4.2 Dataset for Sidewinder Tuff 260
B.4.3 Dataset for lab scale intact Climax Granite 261
B.4.4 Dataset for field scale jointed Climax Granite 262
B.4.5 Dataset for 23MPa Concrete 263

B.4.6 Dataset for Conventional Strength Portland Concrete 264
B.4.7 PARTIAL Dataset for Johnson-Cook verification tests 265
B.4.8 Datasets for mimicking classical (simplified) models 266
Von-Mises material 266
Maximum Principal Stress failure 267
Tresca 268
Mohr-Coulomb 268
Pressure-varying strength ratio 273
Sub-input set for *linear* elasticity 273
Sub-input set for "turning off" all rate dependence 275
Sub-input set for disabling kinematic hardening 275
Sub-input set for associativity 275
Sub-input set for disabling cap and crush curve 275
Sub-input set for disabling tensile cut-off limits 276

References **277**

List of Figures

1.1 Kayenta continuous yield surface 19

1.2 Distinction between a yield surface and the limit surface 24

3.1 Typical hydrostatic (pressure vs. volumetric strain) compression data. 36

3.2 Triaxial compression (TXC) and triaxial extension (TXE) 37

3.3 Triaxial and CSD load paths) 39

3.4 Contrast between uniaxial stress and strain for quasistatic loading of von Mises material 41

3.5 Spatial, Material, and unrotated frames 43

3.6 An octahedral yield profile 47

3.7 Distortion of the meridional profile when using non-isomorphic stress measures . . 48

4.1 Backstress and shifted stress 57

4.2 Qualitatively meridional profile shapes 59

4.3 Distinction between two-surface upper-bound models and Kayenta 60

4.4 Basic shapes of the three key functions that characterize the composite shape of the yield surface 61

4.5 Kayenta cap function 62

4.6 Kinematic hardening 66

4.7 Yield surface evolution with both microcracking and porosity 67

4.8 Shear limiter function (unshifted and shifted) 68

4.9 Octahedral yield profiles, plotted at allowable values of the strength ratio 73

4.10 Lode angle function (for various strength ratios) plotted vs. the Lode angle varying from 30° (TXE) to $+30^\circ$ (TXC) 74

4.11 Hardening mechanisms 80

4.12 A conventional porosity crush curve (dashed) and state path (solid) 82

4.13 Gurson theory for porous yield surfaces compared with Kayenta cap function 83

4.14 Relationship between hydrostatic pressure vs. volumetric strain data, Kayenta X-function, and a traditional porosity vs. pressure crush curve 84

4.15 Soft Knee in the onset of pore collapse requires nonzero value 86

4.16 Continuously differentiable Kayenta yield function and some characteristic dimensions 88

4.17 Meridional plane in which the magnitude of the stress deviator plotted against Lode Z (proportional to pressure) 90

4.18 The effect of kinematic hardening on the meridional plane that contains the backstress 92

5.1 Softening regarded as progressive limit surface collapse 99

5.2 Alternative parameterization of the limit curve 100

5.3 Time-based damage evolution 104

5.4 Demonstration that a time-to-failure criterion leads to apparent plastic-strain-to-failure 105

5.5 Incorporation of uncertainty and scale effects in damage 110

5.6 The strength size effect in “directed-Weibull” theory varies with stress space trajectory 110

5.7 Spall with strength variability and scale effects. The left plot shows intact material. The right plot shows material velocity with clear variability 111

5.8 Brazilian simulation with variability and scale effects 112

7.1 Rate dependence 121

7.2 High-rate weighting factor at various initial states 124

7.3 Rate dependence in uniaxial strain loading of a nonhardening pressure-insensitive material 126

7.4 The effect of strain rate in uniaxial strain 127

8.1 Meaning of the “SHEAR” output variable. 137

9.1 Screen shot of the MS Excel interface for Kayenta's material-model driver (MMD) 145

9.2 MMS verification of Mohr-Coulomb idealization 149

9.3 Subcycling test for hydrostatic loading 150

9.4 Rate of convergence 151

9.5 Single Element Verification Results, Unconfined compression 153

9.6 Single Element Verification Results, 20 MPa triaxial compression 154

9.7 Single Element Verification Results, Reduced triaxial extension 155

9.8 Single Element Verification Results, Plane Strain 156

9.9 Other single-element tests 158

9.10 Hendron & Ayier verification problem 160

9.11 Spherical cavity geometry 161

9.12 Finite-element vs. analytical/numerical elastic wave velocity at 470 meters from a velocity spherical cavity source at 204 meters 162

9.13 Reduced mesh dependence and improved accuracy in dynamic indentation (tungsten carbide sphere impacting SiC-N ceramic at 500 m/s 163

9.14 Reduction in sampling error with number of data points 164

9.15 A comparison of triaxiality versus proportionality angle for plane stress states 168

9.16 EQPS at Fracture for 30 Plane stress realizations 170

9.17 3D EQPS 171

9.18 Limitations of MatModLab 172

9.19 EQPS at Fracture for 30 Plane stress realizations for JC 173

9.20 3D EQPS 174

9.21 Limitations of MatModLab for JC 175

9.22 EQPS at Fracture for 30 Plane stress realizations for XW 177

9.23 3D EQPS 178

9.24 Limitations of MatModLab for XW 179

9.25 Prescribed isotropic strain path for Thermo-Kayenta. 181

9.26 Isotropic deformation - comparison of material response 182

9.27 Prescribed isochoric strain path for Thermo-Kayenta 183

9.28 Comparison of features in Thermo-Kayenta for isochoric deformation. 184

9.29 Comparison of the elastic response in Thermo-Kayenta with ALEGRA for isochoric deformation 185

9.30 Comparison of the yield response in Thermo-Kayenta with ALEGRA for isochoric deformation 186

9.31 Comparison of Thermo-Kayenta with ALEGRA for isochoric deformation with yield and thermal effects enabled. 187

9.32 Comparison of Thermo-Kayenta with ALEGRA for isochoric deformation with yield and hardening effects enabled. 188

9.33 Comparison of Thermo-kayenta with ALEGRA for isochoric deformation with yield and rate effects enabled. 189

9.34 Displacement profile for Thermo-Kayenta at the end of the simulation 191

9.35 Comparison of the displacement profile for Thermo-kayenta and Johnson-Cook. . . 192

9.36 Comparison of the temperature contours for Thermo-Kayenta and Johnson-Cook . 193

10.1 Meridional limit curves for some materials already parameterized to Kayenta 196

10.2 Nonlinear elasticity in shear 197

10.3 Nonlinear elasticity in hydrostatic loading 198

10.4 Meridional limit curves for some materials already parameterized to Kayenta 199

10.5 Shear failure limit curve compared with concrete data 200

10.6 Progression of the hardening yield surface under a triaxial compression test, illustrated with correspondence of the meridional plane to the stress-strain diagram . . . 201

10.7 Shear-enhanced dilatation under compression 202

10.8 Kolsky (split Hopkinson) bar apparatus 203

10.9 Suitability of Kayenta's overstress rate-dependence model to match observed data . 204

11.1 Post-calibration Triaxial loading 206

11.2 After Kayenta was fitted to laboratory-scale material property tests, it was used to predict projectile penetration depth using spherical cavity expansion analysis 208

11.3 Radial cracking in dynamic indentation 209

11.4 Statistically variable strength 210

11.5 Spherical cavity geometry 210

11.6 Kayenta + JAS3D finite-element prediction against velocity and displacement at 470 meters from a spherical cavity velocity source at 204 meters 211

A.1 Elastic legs (dashed) and plastic legs (solid) in hydrostatic loading 215

A.2 Ideal hydrostatic parameterization data 217

A.3 Less-preferable hydrostatic parameterization data 218

A.4 Data representative of a triaxial compression parameterization test 219

A.5 A family of TXC tests conducted to failure. 221

A.6 TXC stress-strain plots and extraction of their peak values to construct the meridional limit curve (data are for porcelanite). 222

A.7 The Lode function information originally shown in Fig. 4.10 of the main report, now displayed with a transformed ordinate 225

A.8 A family of TXC tests conducted to failure. 226

A.9 Sketch of axial stress vs. strain 226

A.10 Sketch of axial stress vs. strain 227

B.1 Other yield surface shapes supported by Kayenta 266

B.2 Classical simplified octahedral profiles 267

B.3 A stress at the limit state under Mohr-Coulomb theory 269

B.4 Pressure varying strength ratio (enabled by setting $RK = -1.0$). 274

This page intentionally left blank.

Chapter 1

Introduction

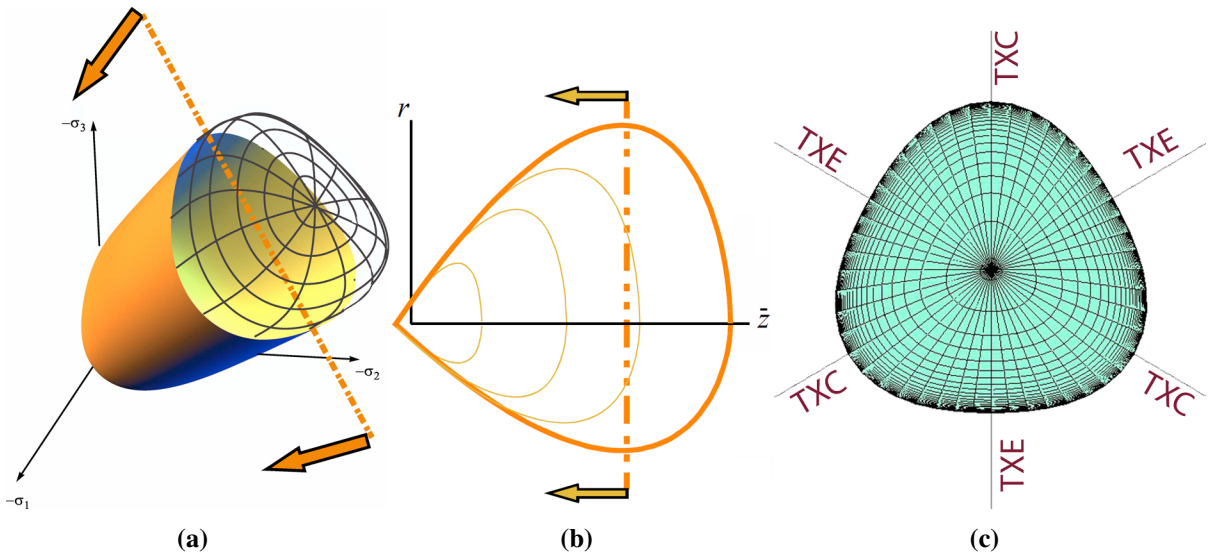

Figure 1.1. Kayenta continuous yield surface. (a) *three-dimensional view* in principal stress space with the high pressure "cap" shown as a wire frame, (b) *the meridional "side" view* (**thick line**) with the cap shown on the more compressive right-hand side of the plot using cylindrical coordinates in which $\bar{z}$ points along the compressive [111] direction, and (c) *the octahedral view*, which corresponds to looking down the hydrostat (onto planes perpendicular to the [111] direction).

Simulating deformation and failure of a variety of materials is at the core of a broad range of applications, including exploration and production activities for the petroleum industry, structural integrity assessment for civil engineering problems, and penetration resistance and debris field predictions for the defense community. Constitutive models are required for metals, natural geological materials (such as limestone, granite, and frozen soil), rock-like engineered materials (such as concrete [94] and ceramics [3]). A common feature is the presence of microscale flaws such as porosity (which permits inelasticity even in purely hydrostatic loading) and networks of

microcracks (leading to low strength in the absence of confining pressure, non-negligible nonlinear elasticity, rate-sensitivity, and differences in material behavior under triaxial extension compared to triaxial compression). Kayenta was originally developed for rock mechanics [34], but it was later generalized to include other features common in metals models (such as classical Drucker-Prager yield with power-law hardening and a high-pressure equation of state).

For computational tractability, and to allow relatively straightforward model parameterization using standard laboratory tests, Kayenta strikes a balance between first-principals micromechanics and phenomenological, homogenized, and semi-empirical modeling strategies. The over-arching goal is to provide a unified general-purpose constitutive model that can be used for a broad range of materials over a wide range of porosities and strain rates. As a unified theory, Kayenta can simultaneously model multiple failure mechanisms, or (by using only a small subset of the available parameters) it can duplicate simpler idealized yield models such as classic von Mises plasticity and Mohr-Coulomb failure. Thus, exercising this model can require as many as ~ 70 parameters for extremely complicated materials to only 2 or 3 parameters for idealized simplistic materials. The model parameters are defined in the nomenclature table (Appendix B). Appendix A gives step-by-step instructions for using experimental data to assign values to Kayenta parameters.

Kayenta overview

Kayenta adopts and extends numerous features from seminal work of Schwer and Murray [81]. For example, a Pelessone function [72] is used to generate a continuously differentiable "cap" yield function for porous media. Relatively new hardening functions are used to accurately predict the competition between dilatation from microcracking and compaction from pore collapse that is observed in standard triaxial testing (where compaction initially prevails, but then smoothly transitions to shear-induced dilatation). For stress paths that result in brittle deformation, failure is associated ultimately with the attainment of a peak stress and work-softening deformation. Tensile or extensile microcrack growth dominates the micromechanical processes that result in macroscopically dilatant (volume increasing) strains even when all principal stresses are compressive. At low pressure, porous brittle materials can fail by shear localization and exhibit strain-softening behavior. At higher pressures, they can undergo strain-hardening deformation associated with macroscopically compactive volumetric strain (i.e., void collapse). Features and limitations of Kayenta are summarized below.

Features of Kayenta

Because it is a unification of simpler models, Kayenta has a large number of material parameters and control parameters (page 230). However, only subsets of these parameters are used in any given simulation. For example, only two parameters (shear and bulk modulus) are needed to reduce Kayenta to linear elasticity. An additional parameter (yield strength) is needed for Kayenta to replicate the idealization of von Mises plasticity. Further parameters are needed to account for non-

linear elasticity, pressure dependence of strength, rate-dependence, porosity, and other advanced features. In other words, the number of parameters increases with the desired sophistication of the constitutive model. Where possible, reasonable default values are used for any material parameters that are unspecified by the user.

Depending on how the model parameters are set, Kayenta is capable of any of the following model features

- Linear and nonlinear, associative or non-associative Drucker-Prager plasticity.
- Linear and nonlinear, associative or non-associative Mohr-Coulomb plasticity.
- Linear or nonlinear, associative or non-associative Willam-Warnke plasticity.
- Von Mises perfect plasticity option as a special case.
- Tresca perfect plasticity option as a special case.
- Sandler-Rubin two-surface cap plasticity (approximated).
- Three-invariant, mixed hardening, continuous surface cap plasticity.
- Three Lode-Angle functions (i.e., non-circular or circular octahedral yield profile).
- The triaxial extension/compression strength ratio can be either a constant or it can be computed internally to vary realistically with pressure.
- Linear or non-linear elasticity.
- Rate-independent or strain-rate-sensitive yield surface.
- Linear or nonlinear peak shear failure threshold marking the onset of softening.
- Linear or nonlinear peak shear failure threshold for fully damaged material.
- Linear or nonlinear kinematic hardening accounting for a Bauschinger effect. The nonlinear option is similar to a power law model in that the amount of hardening decreases with monotonic loading. The linear option is used in verification testing.
- Nonlinear compaction function (pressure-volume) with isotropic hardening.[1]
- Flexibility that permits reducing the model (and the number of required parameters). to classical failure models.
- Pressure- and shear-dependent compaction (similar to p-α models hydrostatic loading, but generalized to include shear effects in general loading).
- Damage to zero strength or to a general damaged-strength state, including formulations for aleatory uncertainty [21, 55, 85] that allow strength to be statistically variable and scale dependent.

[1]Isotropic hardening does not imply a uniform expansion of a yield surface in stress space. Isotropic hardening means that the yield function evolves in such a manner that it continues to depend only on stress invariants. For example, the isotropic hardening associated with pore collapse leads to a "stretching" of the yield surface along the hydrostat in stress space.

- Ubiquitous (homogenized) jointing in which the elastic stiffness is reduced from a network of pre-existing oriented faults. An isotropic option applies to joints of uniformly random orientations. An orthotropic option allows joints aligned with a rectangular grid. A more general anisotropic option allows specification of four joint sets of user-specified orientations (strike and dip).

- Kayenta has been parameterized and tested for tensile loading of titanium alloy and silicon-carbide ceramics in unnotched charpy, brazilian indirect tension, and fragmenting taylor anvil tests [56, 55], though the majority of validation testing has been in compression.

Limitations of Kayenta

- Support for orthotropic or anisotropic jointing is available only as a compile option; the theory and implementation for anisotropic joints is discussed in a separate report [20]. The Kayenta version described in this report treats the material as initially isotropic. Kinematic hardening is the only mechanism for deformation-induced anisotropy.

- The elasticity model is hypoelastic rather than hyperelastic.

- While the hydrostatic crush curve is quite general, only an elliptic cap function is available for modeling shear effects on pore collapse and other mechanisms of plastic volume reduction. Alternative cap models (such as the Gurson function) can be incorporated in future revisions if needed.

- The host code is responsible for satisfying frame indifference (by calling Kayenta using conjugate reference stress and strain rate measures). See page 135.

- Kayenta is designed to be easily installed into a "host code," which refers to a finite element code or any other code that solves the partial differential equations of mass and momentum balance. Kayenta may be installed as a classical local model if it is to be applied in a limited capacity to predict material response up to the onset of softening. However, if Kayenta's damage response functions (loss of strength and stiffness) are to be used to predict post-peak softening, then the host code is responsible for handling the change in type of the governing equations to ensure mesh independence. This additional burden on the host code possibly includes calling Kayenta with appropriately perturbed statistical variations and scale effects in the material parameters [23]. See page 109.

- Compared with simple idealized models (which are well known to give unsatisfactory results in non-trivial structural applications), Kayenta is computationally intensive, though less so than many other models of comparable complexity.

- Kayenta is limited to deformations for which the principal directions of reference stretch do not rotate significantly, though large volume changes are permitted. Arbitrarily large rotations are permitted if the host code manages the reference stress and strain measures properly (see page 43).

- Although Kayenta supports a pore collapse curve having convexity that changes sign, such curves are allowed only under compaction, not pore growth (see page 86).

Kayenta predicts observed material response, without explicitly addressing how the material behaves as it does. Kayenta reflects subscale inelastic phenomena *en ensemble* by phenomenologically matching observed data to interpolation functions. Considerations guiding the structure

of Kayenta's material response functions are (1) consistency with microscale theory, (2) computational tractability, (3) suitability to capture trends in characterization data, and (4) physics-based judgements about how a material should behave in application domains where controlled experimental data cannot be obtained.

Fundamentally, Kayenta is a generalized and unified plasticity model. Here, the term "plasticity" is defined very broadly to include any mechanism of inelastic deformation. Primarily, the source of inelastic deformation in geological materials (or in rock-like materials such as concrete and ceramics) is growth and coalescence of microcracks and pores. Under massive confining pressures, inelasticity could include plasticity in its traditional dislocation sense or, more generally, might result from other microphysical mechanisms (internal locking, phase transformation, twinning, etc.). Equations governing generalized plasticity a mathematical formalism, as well as solution methods and limitations in shock physics, are summarized in Reference [13].

Kayenta is phenomenological and semi-empirical because the physical mechanisms of inelastic material behavior are handled in an ensemble manner, without explicitly partitioning and modeling each possible contributor to the inelasticity. Kayenta makes no explicit reference to microscale properties such as porosity, grain size, or crack density. Instead, the overall combined effects of the microstructure are modeled by casting the macroscale theory in terms of macroscale variables that are realistic to measure in the laboratory. For example, inelastic compaction followed by shear-enhanced dilatation has long been attributed to an initial phase of void collapse followed later by microcracks opening in shear. Kayenta is exceptionally capable of matching this type of observed compaction/dilatation data, and it does so without demanding that the user supply information about essentially unknowable porosity or microcrack distributions within the material.

Being a generalized plasticity model, Kayenta presumes that there exists a convex contiguous "**elastic domain**" of stress states for which the material response can be construed to be elastic. The boundary of the elastic domain is called the **yield surface**. When loading is severe enough that continuing to apply elasticity theory would produce a stress state lying outside the yield surface, the material response will instead be inelastic and a different set of equations must then be solved. Aside from supporting kinematic hardening, Kayenta is isotropic, which means that the criterion for the onset of plasticity depends only on the three principal values of the stress tensor, $(\sigma_1, \sigma_2, \sigma_3)$, but not on the principal directions. Consequently, as illustrated in Fig. 1.1 (pg. 19), the yield surface may be visualized as a 2D surface embedded in a 3D space where the axes are the principal stresses. The elastic domain is the interior of this surface. The **hydrostat** is the [111] direction, along which all three principal stresses are equal. Any plane that contains the hydrostat is called a **meridional plane**. Any "side view" cross-section of the yield surface on a meridional plane is called a **meridional profile**. Any plane perpendicular to the hydrostat is called an **octahedral plane**, and any cross-section of the yield surface on an octahedral plane is called an **octahedral profile**.

Mathematically, the yield surface may be expressed in terms of a **yield function** $f(\sigma_1, \sigma_2, \sigma_3)$. When hardening is permitted, the yield function additionally depends on **internal state variables** that quantify the underlying microstructure (e.g., porosity). Points on the yield surface satisfy $f = 0$ and therefore, because the equation $f(\sigma_1, \sigma_2, \sigma_3) = 0$ is phrased in terms of three independent

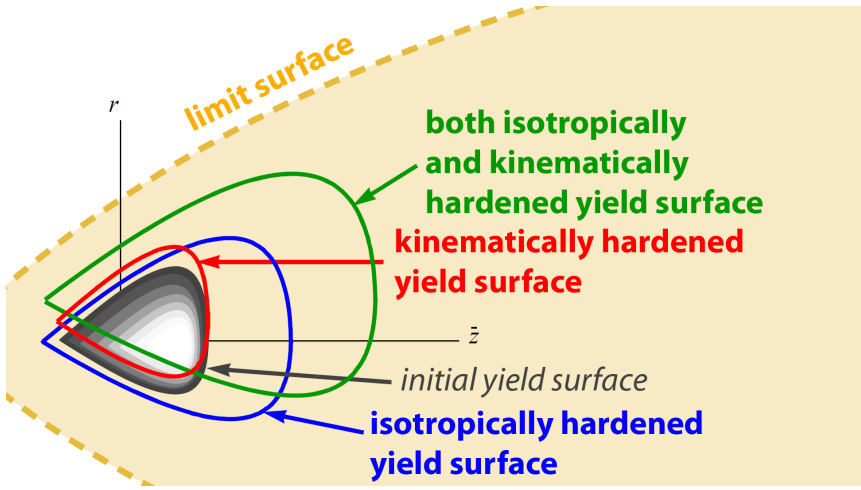

Figure 1.2. Distinction between *a* yield surface and *the* limit surface. This sketch shows meridional profiles of an initial yield surface along with hardened yield surfaces that might evolve from the initial surface. All achievable stress states (and therefore all possible yield surfaces) are contained within the limit surface. Fig. 1.1(b), for example, depicts a family of yield surfaces, all bounded by the limit surface.

variables, the yield surface may be visualized in the 3D Cartesian space, called **stress space**.[2] When the yield function additionally depends on internal state variables, different values for the internal state variables result in different yield surfaces in stress space. Points within the elastic domain satisfy $f < 0$. Brittle materials are very weak in tension, but they can deform elastically under a much broader range of stress states in compression. Consequently, the elastic domain (and therefore its boundary, the yield surface) resides primarily in the compressive part of stress space where all three principal stresses are negative. Thus, the typical rock yield surface shown in Fig. 1.1(a) is actually being viewed from the *compressive* [111] direction. The "cap" part of that yield surface (shown as a wire frame in Fig. 1.1) reflects the fact that, unlike solid metals, inelasticity can occur in rocks even under purely hydrostatic compression as a consequence of void collapse.

A **yield surface** is the boundary of *elastically* obtainable stress states, whereas a **limit surface** is the boundary of stresses that are quasi-statically obtainable *by any quasistatic means*, elastic or plastic. Points *outside* the limit surface can be reached only transiently in dynamic loading via viscoplastic rate dependence. Points outside a yield surface might be attainable through a hardening process, but points outside the limit surface are not attainable via *any* quasistatic process.

Points on the limit surface define the onset of material softening. Consequently, a state on the

[2]Some people prefer that this be called Haigh-Westergaard space [62] so that the phrase "stress-space" may be reserved for the higher-dimensional space defined by the set of all tensors that commute with the stress tensor.

limit surface is attainable at least once, but might not be attainable thereafter. The Sandia GeoModel [33], which was the predecessor to Kayenta, allowed prediction of the material response only up to the limit state. The GeoModel did not simulate subsequent softening because softening induces a change in type of the partial differential equations for momentum balance, which therefore requires a response from the host code to alter its solution algorithm (perhaps by inserting void or by activating special elements that accommodate displacement discontinuities). Shortly after the documentation for the GeoModel was released, a beta, research-only, revision (called BF1[3]) was developed to allow loss of strength and stiffness. This revision, which would have been nonphysical if applied in a local deterministic context, was used in combination with statistical uncertainty and scale effects to mitigate (not eliminate) mesh-dependencies as described on page 109.

By definition, the initial limit surface is regarded as fixed — it does not evolve (i.e., move around in stress space) as a yield surface can. Since the limit surface contains all attainable stress states, it follows that the set of all possible yield surfaces is contained within the limit surface (see Fig. 1.2). Plasticity induces microstructural changes that permit the yield surface to evolve through time, effectively changing the initial material into a mechanically *different* material. A material can have an infinite number of yield surfaces generated via various path-dependent hardening processes, but it can have only one peak limit surface. Limit surface characterization is accomplished by performing numerous experiments all the way to the point of material rupture (catastrophic failure). Each such experiment can have only one peak stress state. Post-peak softening in a material might lead to a stress at rupture that is smaller than at the peak, but it is the collection of *peak* — not rupture — stress states that defines the limit surface. Of course, mapping out the limit surface for a given material requires using a *new sample* for every experiment, which itself introduces uncertainty regarding variability in material composition and microstructure. Within the main Kayenta subroutines, the limit surface (and each yield surface) is treated as a sharp threshold boundary, but Kayenta's theoretical and computational *framework* is specifically designed to allow each finite element to be assigned statistically variable and scale-dependent strength, consistent with laboratory observations. This approach allows these limit and yield thresholds in stress space to be "fuzzy" to better account for natural material variability. Softening is then accomodated by allowing the limit surface to collapse (so that previously attainable stress states are no longer possible).

The set of all possible *yield* surfaces is contained within the peak (pre-softening) limit surface. Porous materials are capable of inelastic deformation even under purely hydrostatic loading. Consequently, porous materials tend to have *closed* convex yield surfaces. Once all pores are crushed out, however, a material can withstand an unlimited amount of pressure. Thus, as indicated in Fig. 1.2, the *limit* surface for any material will always enclose an *open* convex set of attainable stress states.

Despite being originally developed for geological applications, Kayenta is truly a unification of many classical plasticity models. For example, by using only a small subset of available parameters, Kayenta can be instructed to behave precisely like a classical hardening or non-hardening von Mises model, in which case the yield surface becomes a cylinder centered about the [111] direction. Other classical models such as Drucker-Prager plasticity, Tresca theory, maximum principal

[3] which stood for Brannon-Fossum model #1 and was so named to indicate that the aim was to mimic capabilities of the Johnson-Holmquist model [52] called JH1.

stress theory, and Mohr-Coulomb theory are also supported in Kayenta by using the simplified input sets summarized in Appendix B. Replicating analytical results from simplified theories is an important aspect of verification of Kayenta. However, full use of a majority of Kayenta features is often required to adequately *validate* the model for realistic rock-like materials.

To describe in greater detail how Kayenta supports its broad range of micromechanisms of failure in a mathematical and computational framework, Chapter 2 and Chapter 3 first summarize our notation and outline some important concepts and conventions about the nature of stress. Chapter 4 describes Kayenta theory (elasticity, yield surface definition and evolution, etc.). The computational algorithm, subroutines, and plottable output will be discussed in Chapter 8, followed by software quality assurance in Chapter 9. Chapter 10 and Chapter 11 summarize verification and validation tests that have been completed to date for a variety of materials. Model parameters (as well as descriptions of internal state variables and other symbols used in this report) are defined in Appendix B, along with sample input sets for realistic and idealized materials. Instructions for determining appropriate model parameters from laboratory data are provided in Appendix A.

Chapter 2

Notation

Typesetting conventions

Throughout this report, **blue variables** are user input parameters and **green variables** are internal state variables available for plotting in the numerical implementation. At the discretion of the host code in which Kayenta is run, several other field variables (e.g., stress) may be additionally available for plotting.

Vector and tensor equations will be presented using indicial Cartesian notation in which repeated indices within a term are understood to be summed from 1 to 3 while non-repeated indices are free and take values 1 through 3. Upon occasion, vectors and tensors will be written in symbolic or "direct" notation in which the number of "tildes" beneath a symbol equals the tensorial order of that variable. For example, s, $\underset{\sim}{\mathbf{v}}$, and $\underset{\approx}{\mathbf{T}}$ would denote a scalar, a vector, and a tensor, respectively.

Vector and Tensor notation

For this report, the following standard operations and definitions from vector and tensor analysis will be employed:

$$\text{Dot product between two vectors:} \quad \underset{\sim}{\mathbf{u}} \bullet \underset{\sim}{\mathbf{v}} = u_1 v_1 + u_2 v_2 + u_3 v_3 = u_k v_k. \tag{2.1}$$

$$\text{Dot product between a tensor and a vector:} \quad \underset{\sim}{\mathbf{y}} = \underset{\approx}{\mathbf{A}} \bullet \underset{\sim}{\mathbf{x}} \text{ means } y_i = A_{ik} x_k. \tag{2.2}$$

$$\text{Dot product between a tensor and a tensor:} \quad \underset{\approx}{\mathbf{C}} = \underset{\approx}{\mathbf{A}} \bullet \underset{\approx}{\mathbf{B}} \text{ means } C_{ij} = A_{ik} \bullet B_{kj}. \tag{2.3}$$

$$\text{Kronecker delta:} \quad \delta_{ij} = \begin{cases} 1 & \text{if} \quad i = j \\ 0 & \text{if} \quad i \neq j \end{cases}. \tag{2.4}$$

$$\text{Identity tensor:} \quad \underset{\approx}{\mathbf{I}} \text{ is the tensor whose } ij \text{ components are } \delta_{ij}$$
$$\text{and whose component matrix is therefore the } 3 \times 3 \text{ identity matrix.} \tag{2.5}$$

$$\text{Inner product between two tensors:} \quad \underset{\approx}{\mathbf{A}}:\underset{\approx}{\mathbf{B}} = A_{ij}B_{ij}. \tag{2.6}$$

$$\text{Magnitude of a vector:} \quad \|\underset{\sim}{\mathbf{v}}\| = \sqrt{v_k v_k} = \sqrt{\sum_{k=1}^{3} v_k^2}. \tag{2.7}$$

$$\text{Magnitude of a tensor:} \quad \|\underset{\approx}{\mathbf{A}}\| = \sqrt{A_{ij}A_{ij}} = \sqrt{\sum_{i=1}^{3}\sum_{j=1}^{3} A_{ij}^2} \tag{2.8}$$

$$\text{Trace of a tensor } \underset{\approx}{\mathbf{A}}: \quad \operatorname{tr}\underset{\approx}{\mathbf{A}} = A_{11} + A_{22} + A_{33} = A_{kk}. \tag{2.9}$$

$$\text{Deviatoric part of a tensor:} \quad \underset{\approx}{\mathbf{A}}^{\text{dev}} = \underset{\approx}{\mathbf{A}} - \frac{1}{3}(\operatorname{tr}\underset{\approx}{\mathbf{A}})\underset{\approx}{\mathbf{I}}, \quad \text{or} \quad A_{ij}^{\text{dev}} = A_{ij} - \frac{1}{3}A_{kk}\delta_{ij}. \tag{2.10}$$

$$\textbf{First invariant} \text{ (trace) of a tensor } \underset{\approx}{\mathbf{A}}: \quad I_1^A = \operatorname{tr}\underset{\approx}{\mathbf{A}} = A_{kk}. \tag{2.11}$$

$$\textbf{Second invariant} \text{ of a tensor } \underset{\approx}{\mathbf{A}}: \quad J_2^A = \frac{1}{2}\operatorname{tr}[(\underset{\approx}{\mathbf{A}}^{\text{dev}})^2]. \tag{2.12}$$

$$\textbf{Third invariant} \text{ of a tensor } \underset{\approx}{\mathbf{A}}: \quad J_3^A = \frac{1}{3}\operatorname{tr}[(\underset{\approx}{\mathbf{A}}^{\text{dev}})^3]. \tag{2.13}$$

Throughout this report, invariants of the stress tensor $\underset{\approx}{\sigma}$ will be written without the superscript identifier. For example, J_2 means the same thing as ${J_2}^{\sigma}$. Kayenta supports kinematic hardening in which the **shifted stress tensor** $\underset{\approx}{\xi}$ is defined $\underset{\approx}{\xi} = \underset{\approx}{\sigma} - \underset{\approx}{\alpha}$ is the backstress tensor (defined later). The invariants I_1, J_2, J_3 in the non-hardening theory will become $I_1^{\xi}, J_2^{\xi}, J_3^{\xi}$ when kinematic hardening is used.

In materials modeling, tensors are often regarded as higher-dimensional vectors. The inner product between two tensors, $\underset{\approx}{\mathbf{A}}$ and $\underset{\approx}{\mathbf{B}}$, is isomorphic to (i.e., geometrically analogous to) the dot product between two vectors. This permits the "magnitude" of a tensor, the "direction" of a tensor, and the "angle" between two tensors to be defined in manners analogous to ordinary vector definitions. For example, the yield surface is a boundary in six-dimensional stress space, and the normal to this surface is a tensor found by differentiating the yield function with respect to stress. The angle between two tensors can be used to quantify non-normality (i.e., misalignment of the yield normal and flow direction tensor).

The derivatives of a scalar-valued function f that depends on a second-order tensor $\underset{\approx}{\mathbf{T}}$ as well as depending on a scalar are given by s are given by

$$\frac{\partial f}{\partial \underset{\approx}{\mathbf{T}}} \text{ is a second-order tensor with ij components } \frac{\partial f}{\partial T_{ij}}. \tag{2.14}$$

$$\frac{\partial f}{\partial s} \text{ is a scalar.} \tag{2.15}$$

Other derivatives are defined similarly. For example, the derivative of a second-order tensor $\underset{\approx}{\mathbf{A}}$ with respect to another second-order tensor $\underset{\approx}{\mathbf{B}}$ is a fourth-order tensor with *ijkl* components $\frac{\partial A_{ij}}{\partial B_{kl}}$.

The most important fourth-order tensors in Kayenta theory is the plastic tangent stiffness tensor, formally equal to the derivative of the stress rate with respect to the strain rate. In numerical implementations, manipulation and construction of fourth-order tensors is often avoided by exploiting applicable (or presumed) material symmetries.

This page intentionally left blank.

Chapter 3

The Stress Tensor

This section defines the stress tensor, its principal values, its invariants, and its sign convention. This chapter describes four canonical stress paths used to parameterize Kayenta: hydrostatic (HYD), triaxial compression (TXC), triaxial extension (TXE), and shear (SHR). For transient dynamics, Kayenta additionally requires Hugoniot and/or Kolsky (split Hopkinson) bar data to parameterize the viscoplasticity.[1] This chapter defines the distinction between the spatial Cauchy stress and the unrotated "reference" stress. In preparation for a detailed discussion of Kayenta theory, this chapter closes with a detailed description of "stress space" and Lode coordinates.

The **stress tensor** $\underset{\approx}{\sigma}$, is defined such that the **traction** vector $\underset{\sim}{\mathbf{t}}$ (i.e., force per unit area), acting on any given plane with unit normal $\underset{\sim}{\mathbf{n}}$, is given by

$$\underset{\sim}{\mathbf{t}} = \underset{\approx}{\sigma} \bullet \underset{\sim}{\mathbf{n}}. \tag{3.1}$$

Of course, the traction and normal vectors may be described in terms of their Cartesian components, $\{t_1, t_2, t_3\}$ and $\{n_1, n_2, n_3\}$ with respect to an orthonormal basis. The stress tensor has a 3×3 Cartesian component matrix such that the above equation may be written in matrix form as

$$\begin{bmatrix} t_1 \\ t_2 \\ t_3 \end{bmatrix} = \begin{bmatrix} \sigma_{11} & \sigma_{12} & \sigma_{13} \\ \sigma_{21} & \sigma_{22} & \sigma_{23} \\ \sigma_{31} & \sigma_{32} & \sigma_{33} \end{bmatrix} \begin{bmatrix} n_1 \\ n_2 \\ n_3 \end{bmatrix}, \tag{3.2}$$

or in indicial form as

$$t_i = \sigma_{ij} n_j, \tag{3.3}$$

where (recalling the implied summation convention) the repeated index "j" is understood to be summed from 1 to 3 and the non-repeated "free" index "i" appearing in each term takes values from 1 to 3 so that the above equation is actually a compact representation of three separate equations (one for each value of the free index).

The stress is symmetric, which means that $\sigma_{ij} = \sigma_{ji}$. In continuum mechanics, and in this report, stress is taken *positive* in tension. This sign convention can be the source of considerable confusion, especially when discussing stress invariants. For example, the trace of the stress, I_1, is

[1] Until rate dependence is discussed separately in Chapter 7, all incremental or rate equations in this report are understood to apply only under quasistatic loading and may therefore be regarded as "inviscid" equations. Incorporating viscoplastic rate dependence requires, as a pre-requisite, solution of these quasistatic inviscid equations.

positive in tension. However, brittle materials have very low strength in tension. Consequently, most of the functions defined in this report are nontrivial over only a small range of the tensile states where I_1 is positive. On the other hand, most of Kayenta functions are non-trivial over a relatively large range of compressive states where I_1 is negative. To help manage the sign convention problem, we will introduce a new notation that an over-bar on a variable denotes the *negative*. Specifically, for any variable x,

$$\textbf{Definition of the "over-bar"} \quad \boxed{\overline{x} \equiv -x}. \tag{3.4}$$

In our plots of any variable that varies as a function of I_1, we will usually employ an abscissa of $\overline{I_1}$, which (being the negative of I_1) is positive in compression. Any variable typeset with an overbar will be positive more often than negative in most applications.

The **principal** stresses are the eigenvalues $(\sigma_1, \sigma_2, \sigma_3)$ of the stress matrix, positive in tension. Their negatives $(\overline{\sigma}_1, \overline{\sigma}_2, \overline{\sigma}_3)$ are positive in compression.[2] When cast in terms of the principal basis (i.e., the orthonormal eigenvectors of the stress matrix), the diagonal components of the stress matrix will equal the principal stresses, and the off-diagonals will be zero.

The **stress deviator** $\underset{\approx}{\mathbf{S}}$ is the deviatoric part of the stress (see Eq. (2.10)):

$$\underset{\approx}{\mathbf{S}} = \underset{\approx}{\sigma} - \frac{1}{3}(\mathrm{tr}\,\underset{\approx}{\sigma})\underset{\approx}{\mathbf{I}}. \tag{3.5}$$

Loosely speaking, the stress deviator is a *tensor* measure of shear stress. An overall scalar measure of shear will be defined later. The quantity $\frac{1}{3}(\mathrm{tr}\,\underset{\approx}{\sigma})$ is called the mean stress, and we will denote it by p. The negative of the mean stress, $\overline{p} = -p$, is called the **pressure**, and is positive in compression. Noting that the mean stress (or pressure) is simply a multiple of I_1, its value is an invariant, meaning that the sum of diagonal stress components will have the same value regardless of the orthonormal coordinate system used to describe the stress components. The principal directions of the stress deviator are the same as those for the stress itself, and the principal values for the stress deviator are related to the principal stresses by

$$s_1 = \sigma_1 - \frac{1}{3}(\sigma_1 + \sigma_2 + \sigma_3), \tag{3.6a}$$

$$s_2 = \sigma_2 - \frac{1}{3}(\sigma_1 + \sigma_2 + \sigma_3), \text{ and} \tag{3.6b}$$

$$s_3 = \sigma_3 - \frac{1}{3}(\sigma_1 + \sigma_2 + \sigma_3). \tag{3.6c}$$

The trace of $\underset{\approx}{\mathbf{S}}$ is zero, which implies that the numerically largest principal value of any nonzero stress *deviator* will always be positive and the smallest will always be negative. In model parameterization tests, a sufficiently high confining pressure $\overline{p}$ is typically superimposed on the *stress* deviator to make all principal stress components compressive even though the principal deviatoric stresses always have mixed signs (see page 35).

[2] Of course, if principal stresses are ordered such that $\sigma_1 \leq \sigma_2 \leq \sigma_3$, then the barred principal stresses will be ordered $\overline{\sigma}_1 \geq \overline{\sigma}_2 \geq \overline{\sigma}_3$.

Stress invariants

The trace operator is an invariant, which means its value will be the same regardless of which orthonormal basis is used for the stress components. Being symmetric, the stress tensor has a total of *three* independent invariants:

$$I_1 = \operatorname{tr} \underset{\approx}{\sigma} = \sigma_1 + \sigma_2 + \sigma_3, \tag{3.7a}$$

$$J_2 = \frac{1}{2}\operatorname{tr}(\underset{\approx}{\mathbf{S}}^2) = \frac{1}{2}(s_1^2 + s_2^2 + s_3^2), \text{ and} \tag{3.7b}$$

$$J_3 = \frac{1}{3}\operatorname{tr}(\underset{\approx}{\mathbf{S}}^3) = \frac{1}{3}(s_1^3 + s_2^3 + s_3^3). \tag{3.7c}$$

The fact that these invariants are computed from the *stress* tensor $\underset{\approx}{\sigma}$ is sometimes emphasized by typesetting them as I_1^σ, J_2^σ, and J_3^σ. Similarly defined invariants for some *other* tensor $\underset{\approx}{\xi}$ would be typeset as $\{I_1^\xi, J_2^\xi, J_3^\xi\}$. Invariants for a tensor $\underset{\approx}{\alpha}$ would be written $\{I_1^\alpha, J_2^\alpha, J_3^\alpha\}$, and so forth. Any invariant written without a clarifying superscript should be understood to be a *stress* invariant.

The mean stress p is defined to be the average of the principal stresses, whereas pressure $\overline{p}$ is just the negative of mean stress:

$$\textbf{mean stress}\text{: } p = \frac{I_1}{3} \qquad \textbf{pressure}\text{: } \overline{p} = \frac{\overline{I_1}}{3}, \text{ where } \overline{I_1} \equiv -I_1. \tag{3.8}$$

Superimposing an extra pressure $\overline{P}$ on *any* stress state causes the pressure to increase from $\overline{p}$ to $\overline{p} + \overline{P}$, while having no effect on the stress deviator and therefore no effect on the second and third invariants. Because the stress *deviator* $\underset{\approx}{\mathbf{S}}$ has a zero trace, it can be shown that J_3 also equals the determinant of the stress deviator so that $J_3 = s_1 s_2 s_3$, and the second invariant can be written alternatively as $J_2 = -(s_1 s_2 + s_2 s_3 + s_3 s_1)$.

Eq. (3.7b) shows that the invariant J_2 is never negative, which permits us to define a supplemental stress invariant, the **signed equivalent shear stress** τ as

$$\tau = \operatorname{sgn}[\sqrt{J_2}, J_3]. \tag{3.9}$$

The "transfer of sign" operator[3] is defined

$$\operatorname{sgn}[x,y] = \begin{cases} |x| & \text{if} \quad y \geq 0 \\ -|x| & \text{if} \quad y < 0 \end{cases}. \tag{3.10}$$

As defined, the equivalent shear stress will have a numerical sign that is positive in triaxial extension states (defined below), negative in triaxial compression, and it will be identically equal to the applied shear stress if the stress tensor happens to be in a state of pure shear (also defined below).

[3] which is an intrinsic function in most computing languages

For clarity, the values of the invariants have been shown here in terms of the principal values of the stress and its deviator. However, because the trace operation gives the same result regardless of which basis is used, the invariants are computed in practice directly from fully-populated 3×3 component matrices, thereby avoiding the need for an expensive eigenvalue analysis.

Derivatives of the stress invariants

For *isotropic* material modeling, each scalar-values function of stress, $\phi(\underset{\approx}{\sigma})$, is presumed to depend only on the principal stress values, not on the principal stress directions. Equivalently, the function $\phi(\underset{\approx}{\sigma})$ is isotropic if and only if it may be expressed alternatively as a function of the three stress invariants I_1, J_2, J_3. In situations where the derivative of ϕ with respect to stress is required, the chain rule can be applied as follows:

$$\frac{\partial\phi}{\partial\sigma_{ij}} = \frac{\partial\phi}{\partial I_1}\frac{\partial I_1}{\partial\sigma_{ij}} + \frac{\partial\phi}{\partial J_2}\frac{\partial J_2}{\partial\sigma_{ij}} + \frac{\partial\phi}{\partial J_3}\frac{\partial J_3}{\partial\sigma_{ij}}. \tag{3.11}$$

In symbolic tensor notation, this expansion is written as

$$\frac{\partial\phi}{\partial\underset{\approx}{\sigma}} = \frac{\partial\phi}{\partial I_1}\frac{\partial I_1}{\partial\underset{\approx}{\sigma}} + \frac{\partial\phi}{\partial J_2}\frac{\partial J_2}{\partial\underset{\approx}{\sigma}} + \frac{\partial\phi}{\partial J_3}\frac{\partial J_3}{\partial\underset{\approx}{\sigma}}. \tag{3.12}$$

Because the three invariants are each proper functions of the stress tensor, their derivatives may be computed in advance:

$$\frac{\mathrm{d}I_1}{\mathrm{d}\underset{\approx}{\sigma}} = \underset{\approx}{\mathbf{I}} = \text{ the identity tensor} \tag{3.13a}$$

$$\frac{\mathrm{d}J_2}{\mathrm{d}\underset{\approx}{\sigma}} = \underset{\approx}{\mathbf{S}} = \mathrm{dev}(\underset{\approx}{\sigma}) = \text{ the stress deviator} \tag{3.13b}$$

$$\frac{\mathrm{d}J_3}{\mathrm{d}\underset{\approx}{\sigma}} = \underset{\approx}{\mathbf{T}} = \mathrm{dev}(\underset{\approx}{\mathbf{S}}^2) = \text{ the “Hill” tensor} \tag{3.13c}$$

Thus, Eq. (3.12) may be written

$$\boxed{\frac{\partial\phi}{\partial\underset{\approx}{\sigma}} = \left(\frac{\partial\phi}{\partial I_1}\right)\underset{\approx}{\mathbf{I}} + \left(\frac{\partial\phi}{\partial J_2}\right)\underset{\approx}{\mathbf{S}} + \left(\frac{\partial\phi}{\partial J_3}\right)\underset{\approx}{\mathbf{T}}.} \tag{3.14}$$

Of particular interest is the trace of the above expression, $\mathrm{tr}\left(\frac{\partial\phi}{\partial\underset{\approx}{\sigma}}\right)$. Since both $\underset{\approx}{\mathbf{S}}$ and $\underset{\approx}{\mathbf{T}}$ are deviatoric, the result is

$$\mathrm{tr}\left(\frac{\partial\phi}{\partial\underset{\approx}{\sigma}}\right) = 3\left(\frac{\partial\phi}{\partial I_1}\right). \tag{3.15}$$

The factor of 3 appears simply because $\mathrm{tr}\,\underset{\approx}{\mathbf{I}} = 3$. This, by the way, is a good example of the fallibility of indicial notation. Specifically,

$$\mathrm{tr}\left(\frac{\partial \phi}{\partial \underset{\approx}{\sigma}}\right) = \sum_{k=1}^{3} \frac{\partial \phi}{\partial \sigma_{kk}} \neq \frac{\partial \phi}{\partial \sum_{k=1}^{3} \sigma_{kk}}. \tag{3.16}$$

Special stress states

This section defines the four main stress states that are used to parameterize Kayenta. These are hydrostatic loading (HYD), triaxial compression (TXC), triaxial extension (TXE), and shear (SHR). The purpose of Kayenta is to interpolate realistically between known material response at these canonical states to describe material behavior under general stress states.

HYDROSTATIC (HYD)

Loading is "**hydrostatic**" when components of the stress tensor are of the form

$$[\underset{\approx}{\sigma}] = \begin{bmatrix} -\overline{p} & 0 & 0 \\ 0 & -\overline{p} & 0 \\ 0 & 0 & -\overline{p} \end{bmatrix} \qquad \text{for hydrostatic stress states.} \tag{3.17}$$

In practice, the pressure $\overline{p}$ is usually compressive (and therefore positive). Hydrostatic testing is very important to parameterization of Kayenta because it indirectly characterizes the influence of material porosity. When hydrostatically loaded to a high pressure and then unloaded, a *non*-porous material will trace through the same stress states on both the loading and unloading curves. A *porous* material, on the other hand, will unload along a *different* path. If possible, hydrostatic testing for Kayenta should be conducted to sufficiently high pressures to compress out all pores, as indicated in Fig. 3.1.[4]

When a material is loaded under hydrostatic *tension* instead of compression, inelastic response is again possible, but the mechanism of failure is catastrophic growth and coalescence of microcracks, resulting in material softening and, ultimately, complete loss of load carrying ability.

TRIAXIAL (TXC and TXE)

Loading is "**triaxial**" whenever two principal stresses (denoted σ_L and called the "lateral" stresses) are equal to each other, but distinct from the third "axial" principal stress (denoted σ_A).

[4] Kayenta parameter p_3 is the logarithmic (Hencky) residual volumetric strain after full void collapse. It is related to initial porosity ϕ_0 by $p_3 = \ln[1/(1-\phi_0)]$, or $p_3 \approx \phi_0$ if ϕ_0 is small. Assuming the matrix material is plastically incompressible, the time-varying porosity during pore collapse can be inferred from Kayenta output variable ε_v^p (plot keyword **EQPV**). Specifically, $\phi = 1-(1-\phi_0)\mathrm{e}^{\varepsilon_v^p} = 1-\exp[-(\varepsilon_v^p+\phi_0)]$.

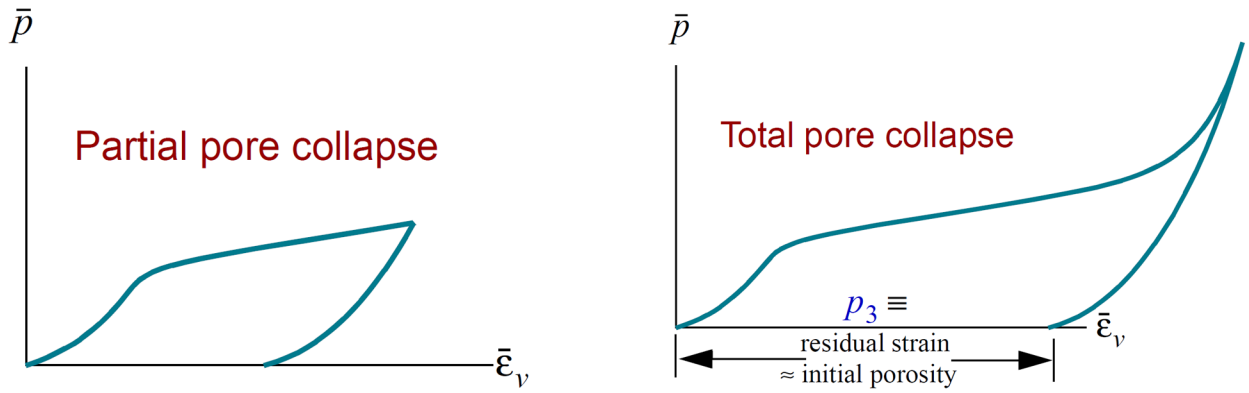

Figure 3.1. Typical hydrostatic (pressure vs. volumetric strain) compression data. Total pore collapse is achieved when the unloading curve (here shown as nonlinearly elastic) is tangent to the loading curve. In this case, the residual volumetric strain approximately equals the initial porosity.

Thus, with respect to the principal basis,

$$[\underset{\approx}{\sigma}] = \begin{bmatrix} \sigma_A & 0 & 0 \\ 0 & \sigma_L & 0 \\ 0 & 0 & \sigma_L \end{bmatrix} \qquad \text{for triaxial stress states,} \tag{3.18}$$

and

$$[\underset{\approx}{\mathbf{S}}] = \frac{\sigma_A - \sigma_L}{3} \begin{bmatrix} 2 & 0 & 0 \\ 0 & -1 & 0 \\ 0 & 0 & -1 \end{bmatrix} \qquad \text{for triaxial stress states.} \tag{3.19}$$

Also,

$$I_1 = \sigma_A + 2\sigma_L \qquad \text{for triaxial stress states,} \tag{3.20a}$$

$$J_2 = \frac{1}{3}(\sigma_A - \sigma_L)^2 \qquad \text{for triaxial stress states, and} \tag{3.20b}$$

$$J_3 = \frac{2}{27}(\sigma_A - \sigma_L)^3 \qquad \text{for triaxial stress states.} \tag{3.20c}$$

The *signed* equivalent shear stress for triaxial loading is

$$\tau = \frac{\sigma_A - \sigma_L}{\sqrt{3}} \tag{3.21}$$

The invariants defined here may be written alternatively in terms of *compressive* stress measures as

$$\boxed{\overline{I_1} = \sqrt{3}\overline{\tau} + 3\overline{\sigma_L}} \tag{3.22a}$$

$$\boxed{J_2 = \overline{\tau}^2} \tag{3.22b}$$

$$\boxed{\overline{J_3} = \frac{2\sqrt{3}}{9}\overline{\tau}^3} \tag{3.22c}$$

where

$$\tau = \frac{\overline{\sigma_A} - \overline{\sigma_L}}{\sqrt{3}}. \tag{3.23}$$

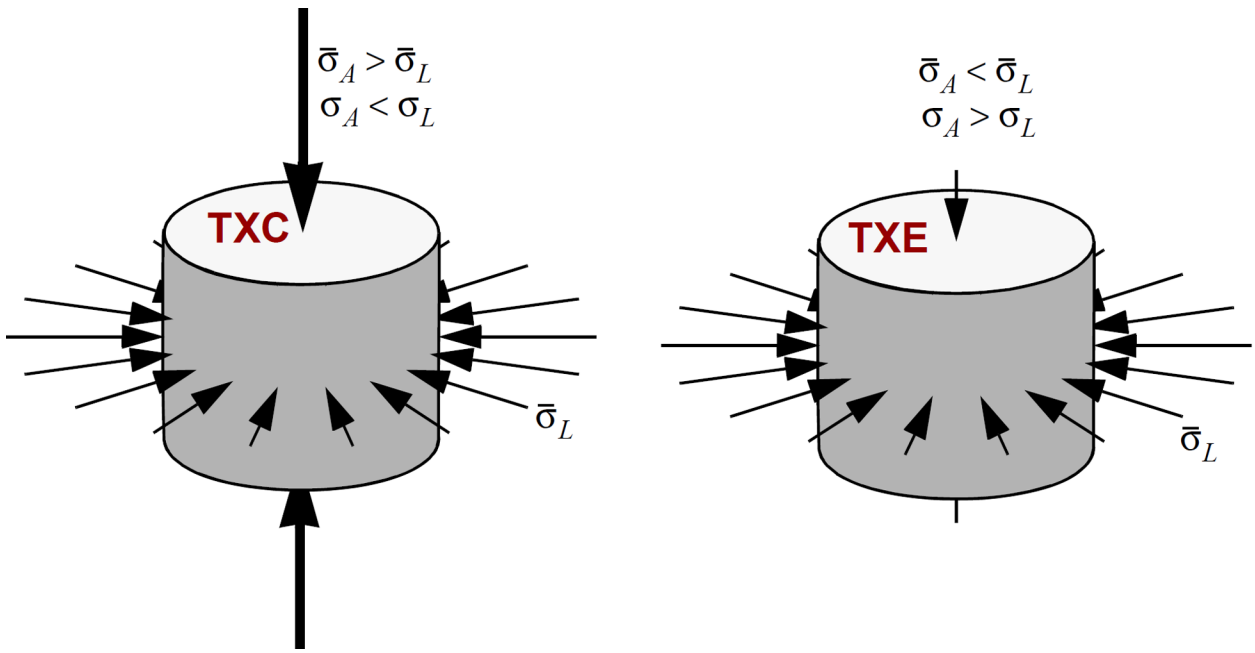

Figure 3.2. Triaxial compression (TXC) and triaxial extension (TXE) Two principal stresses (the lateral stress) are equal. For TXC, the axial stress is more compressive than the lateral stress. For TXE, the axial stress is less compressive than the lateral stress. In the labels, $\overline{\sigma} = -\sigma$; stress σ is positive in tension while stress $\overline{\sigma}$ is positive in compression.

The term "triaxial" is a bit of a misnomer because there are not really three independent loads applied — the lateral stresses are equal. These experiments are normally performed on cylindrical test specimens with the lateral load supplied by a pressure bath. For **triaxial compression (TXC)** the axial stress is more compressive than the lateral stress. For **triaxial extension (TXE)** the axial stress is not necessarily *tensile* — it is merely *less compressive* than the lateral stress. For TXC, the specimen changes shape such that its length-to-diameter ratio decreases. For TXE, the length-to-diameter ratio *increases* even though the length and diameter might *individually* both decrease. Uniaxial stress *compression* (also called **unconfined compression**) is a special form of TXC in which the axial stress is compressive and *the lateral stress is zero*. Uniaxial stress *extension* is a special form of TXE in which the axial stress is tensile and the lateral stress is zero. **Uniaxial *strain* compression**, which is typical in flyer-plate impact experiments is a special case of TXC in which the axial stress is compressive, while the lateral *strain* is zero (making the lateral stress also

compressive, but less compressive than the axial stress). **Biaxial tension** is a special case of TXC in which the lateral stress is tensile and the axial stress is zero. **Biaxial compression** is a special case of TXE in which the lateral stress is compressive and the axial stress is zero. According to Eq. (3.21), the signed shear stress satisfies $\overline{\tau} > 0$ for TXC, whereas $\overline{\tau} < 0$ for TXE. Consequently, Eq. (3.22) shows that $\overline{J_3} > 0$ (and hence $J_3 < 0$) for TXC, while $\overline{J_3} < 0$ (and hence $J_3 > 0$) for TXE. Of course, $J_2 > 0$ for *both* TXC and TXE because it is the *square* of $\overline{\tau}$.

In typical triaxial experiments, the lateral stress is held fixed (via a pressure bath) while only the axial stress is varied. In this case, Eq. (3.22) implies that

$$\frac{\mathrm{d}\overline{\tau}}{\mathrm{d}\overline{I_1}} = \frac{1}{\sqrt{3}} \quad \textbf{for triaxial stress loading with fixed lateral stress.} \tag{3.24}$$

Being easily achieved in the laboratory, TXC and TXE data are essential to parameterize Kayenta. In a typical triaxial test, the material is first loaded hydrostatically in a pressure bath until all three principal stresses reach a compressive pressure $\overline{P}^{\text{bath}}$. Thereafter, the lateral stresses are held fixed at this value ($\overline{\sigma_L} = \overline{P}^{\text{bath}}$) while the axial stress is then increased beyond $\overline{P}^{\text{bath}}$. For some experiments, the axial stress might be increased only until the stress difference reaches a given value, after which all stresses are again increased by equal amounts. These are called **constant stress difference** (**CSD**) experiments. Typically, these experiments are run to the point of material failure. Periodic partial unloading during a test reveals yielding if the unloading stress-strain curve has a noticeably different slope than the loading curve (without unloading, it would be impossible to definitively distinguish plasticity from non-linear elasticity).

As illustrated in Fig. 3.3, a series of TXC experiments at various bath pressures and/or stress differences results in a family of $(\overline{I_1}, \tau)$ stress-at-yield points that map out the TXC meridional profile of Kayenta yield surface. Similar experiments under TXE map out the TXC meridional profile. Usually, the TXE failure envelope will be shaped similarly to the TXC envelope, but lower in magnitude because, at a given value of I_1, the value of $\sqrt{J_2}$at failure is generally lower for TXE than for TXC. A plot of the failure envelope in $\overline{\tau}$ vs. I_1 space is essentially equivalent to the meridional "side" view of the yield surface Fig. 1.1(b), except with the axes scaled differently. The TXE experiments are mapping out the cross-section of the yield surface along which pressure varies while staying on the "base" of the triangular octahedral profile in Fig. 1.1(c) (pg. 19), whereas TXC experiments reveal how the apex of the triangle varies with pressure. For metals, there is little difference between the stress intensity required to initiate failure in TXC compared to TXE. However, for brittle materials, the difference is quite noticeable and (according to idealized microphysical theories) can be attributed to internal frictional resistance to shear crack growth. Because friction increases with pressure, the material strengths in TXC and TXE tend to increase with pressure but in approximately the same proportions so that the ratio of TXC strength to TXE strength is approximately pressure independent. Consequently, the TXE profiles shown in Fig. 3.3 are shaped identically to the TXC profiles except smaller in magnitude.

Another form of triaxial loading, commonly used for dynamic material testing, is **uniaxial strain**, in which the lateral *strain* ε_L is held constant. If the lateral strain ε_L is held constant while continuing to compress axially, the lateral compressive *stress* $\overline{\sigma}_L$ will increase to prevent lateral

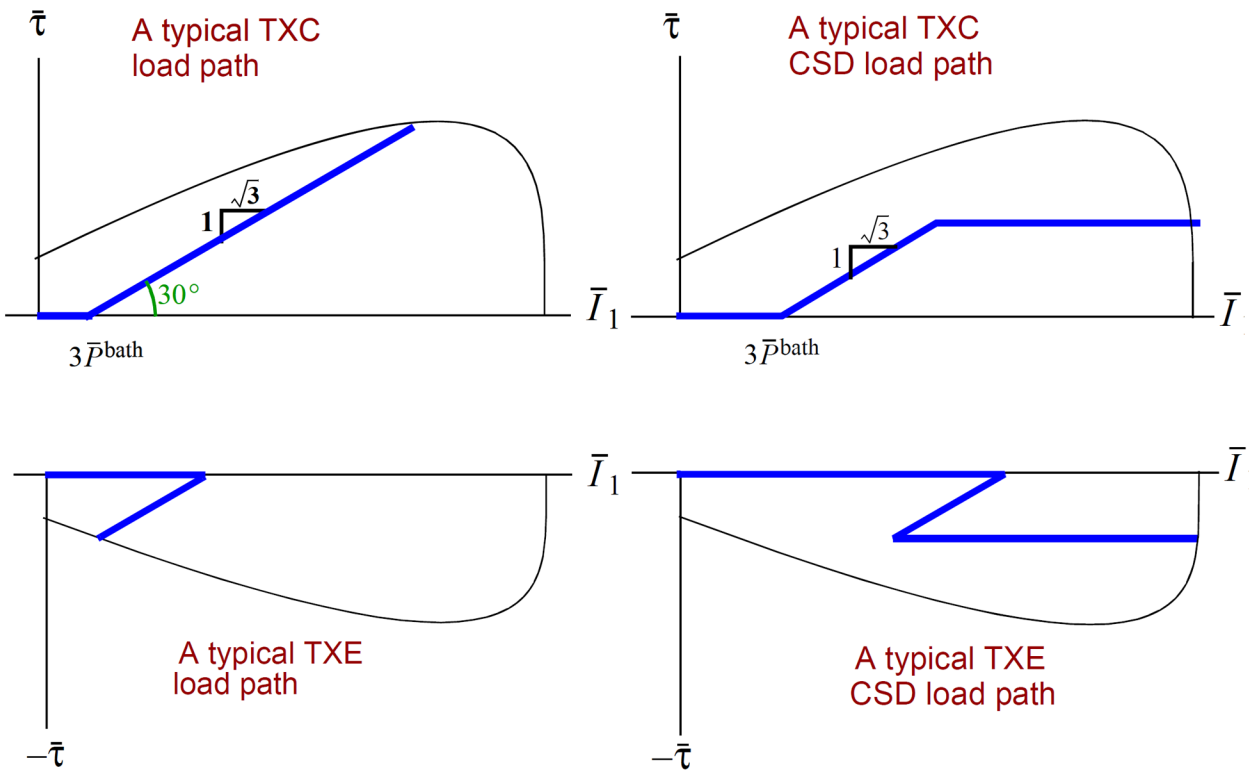

Figure 3.3. Triaxial and CSD load paths. The material is first compressed hydrostatically to a pre-selected bath pressure $\overline{P}^{\text{bath}}$; at this point, the value of the first stress invariant is $I_1 = -3\overline{P}^{\text{bath}}$ and therefore $\overline{I_1} = 3\overline{P}^{\text{bath}}$. When the triaxial leg begins, the lateral stress is held constant ($\overline{\sigma_L} = \overline{P}^{\text{bath}}$) while the axial stress is varied. This causes both the first and second invariants to change such that the path in this stress plot is a straight line with slope $1/\sqrt{3}$. For simple triaxial loading, the stress difference is increased until material failure occurs. For CSD loading, the stress difference is increased to a pre-selected value, and then held fixed while all stress components are thereafter varied equally until failure occurs.

motion. For uniaxial strain, $\dot{\bar{\varepsilon}}_L = 0$, and therefore Hooke's law[5] in rate form reduces to

$$\textbf{Uniaxial strain}: \dot{\bar{\sigma}}_A = \left(K + \frac{4}{3}G\right)\dot{\bar{\varepsilon}}_A \qquad \text{and} \qquad \dot{\bar{\sigma}}_L = \frac{\nu}{1-\nu}\dot{\bar{\sigma}}_A = \left(K + \frac{2}{3}G\right)\dot{\bar{\varepsilon}}_A. \tag{3.25}$$

where K and G are, respectively, the tangent elastic bulk and shear moduli.

For uniaxial strain, the rate of the signed equivalent shear stress and the rate of the first stress invariant are

$$\textbf{Uniaxial Strain}: \dot{\bar{\tau}} = \frac{2G\dot{\bar{\varepsilon}}_A}{\sqrt{3}} \qquad \text{and} \qquad \dot{\bar{I}}_1 = 3K\dot{\bar{\varepsilon}}_A \tag{3.26}$$

and therefore the path through stress space is a straight line with slope

$$\frac{\mathrm{d}\bar{\tau}}{\mathrm{d}\bar{I}_1} = \frac{1}{\sqrt{3}}\frac{2G}{3K} = \frac{1}{\sqrt{3}}\left(\frac{1-2\nu}{1+\nu}\right) \qquad \text{for triaxial stress with fixed lateral strain,} \tag{3.27}$$

where ν is Poisson's ratio. Contrast this with the shallower slop of $\frac{1}{\sqrt{3}}$ in Fig. 3.3. Since Poisson's ratio typically varies between 0 and $\frac{1}{2}$,[6] this result shows that the trajectory in the meridional profile will generally have a shallower slope (and possibly even be curved for non-linear elastic or porous media) under uniaxial strain loading than under uniaxial stress loading. This result should make some intuitive sense. Uniaxial strain experiments are conducted by applying increasing levels of compression in the axial direction while holding the lateral strain fixed. As the axial strain is compressed, the material "wants" to expand laterally, but is not permitted to — a lateral compressive force prevents this outward motion. This constraining lateral compression makes $\bar{I}_1$ larger than it would be when lateral expansion is unconstrained. The larger $\bar{I}_1$ results in a shallower slope in the stress trajectory.

Fig. 3.4 illustrates the distinction between uniaxial stress and uniaxial strain in quasistatic loading of a classical nonhardening von Mises material. The initial slope $C = K + \frac{4}{3}G$ in uniaxial strain (called the constrained modulus) is steeper than Young's modulus E because of the lateral confinement in uniaxial strain. During plastic loading, uniaxial stress response for a nonhardening von Mises material has a zero slope because material is free to flow laterally. However, in uniaxial strain, lateral flow is prevented, causing the slope during plastic loading to equal the bulk modulus K, consistent with compression of a fluid and not to be confused with hardening. The classical nonhardening von Mises model is a useful idealization for performing verification tests of numerical implementations, but it is not usually predictive of realistic behavior of most materials. Most materials are nonlinearly elastic. Furthermore, most materials exhibit some degree of plastic hardening, which would increase the slope during plastic loading in both uniaxial stress and uniaxial strain. Hardening also alters the yield threshold upon load reversal. Consequently, the

[5]The general form of Hooke's law, applicable to any form of triaxial loading, is given in Eq. (4.11). Eq. (3.25) is a special case of Eq. (4.11) in which $\dot{\bar{\varepsilon}}_L = 0$, with Eq. (4.13) used to express Young's modulus E and Poisson's ratio ν in terms of K and G.

[6]Strictly speaking, positive definiteness of the elastic stiffness tensor merely requires $-1 < \nu < \frac{1}{2}$. Whereas negative Poisson's ratio has been observed in man-made materials with re-entrant microstructures, it has not (to our knowledge) been reported for naturally occurring materials. Performance of Kayenta has not been verified for materials with negative Poisson's ratio.

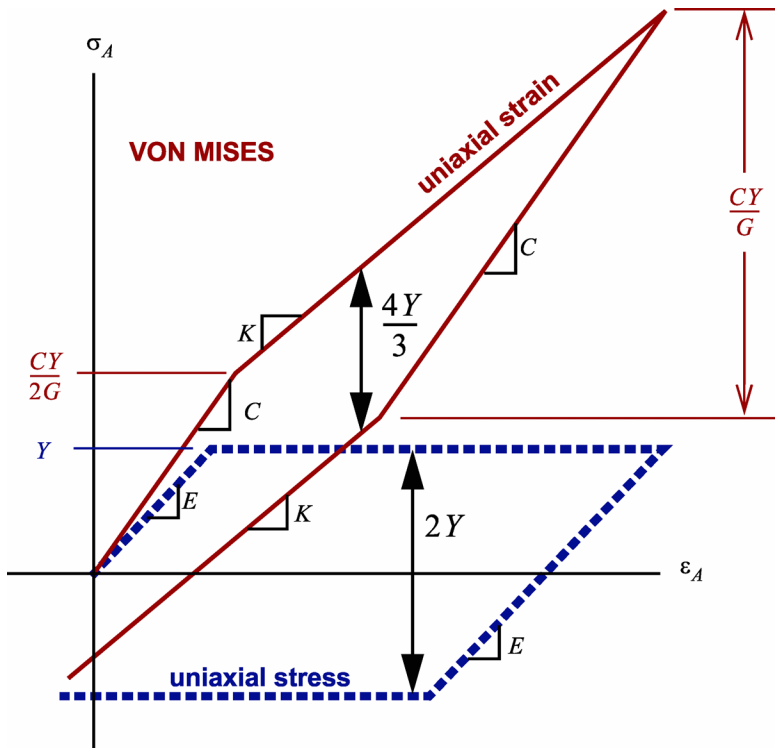

Figure 3.4. Contrast between uniaxial stress and uniaxial strain for quasistatic loading of von Mises material. The initial slope $C = K + \frac{4}{3}G$ in uniaxial strain (called the constrained modulus) is steeper than Young's modulus E because of the lateral confinement in uniaxial strain.

separation between load and unload lines for realistic materials is not determined exclusively by strength, as labeled in Fig. 3.4 for the unrealistic von Mises material. Many materials, especially rocks and concretes, furthermore exhibit pressure-dependence of the yield strength. If the material is nonhardening, then pressure-dependence of yield will alter the post-yield slope in uniaxial strain loading, but it will not affect the slope in uniaxial stress loading.[7]

SIMPLE/PURE SHEAR and PRESSURE-SHEAR LOADING (SHR)

A material is in a state of **simple shear** with respect to a given coordinate system if the stress matrix in that system is of the form

$$[\underset{\approx}{\sigma}] = [\underset{\approx}{\mathbf{S}}] = \begin{bmatrix} 0 & s & 0 \\ s & 0 & 0 \\ 0 & 0 & 0 \end{bmatrix} \text{ for simple shear,} \tag{3.28}$$

where s is the shear stress. The eigenvalues of this matrix are $\{s, -s, 0\}$. In general, any stress state that is deviatoric with one eigenvalue being zero is said to be a **pure shear** [62]. (Thus, simple shear is a special type of pure shear). For an isotropic material model like Kayenta, yield depends only on the principal stresses, so there is no practical difference between simple and pure shear (except when the model is anisotropic because of kinematic hardening, see Fig. 4.1).

For conducting material characterization experiments, **pure shear** of the form

$$[\underset{\approx}{\sigma}] = [\underset{\approx}{\mathbf{S}}] = \begin{bmatrix} s & 0 & 0 \\ 0 & -s & 0 \\ 0 & 0 & 0 \end{bmatrix} \text{ for pure shear,} \tag{3.29}$$

is most convenient. For brittle materials, pure shear is difficult to attain because one of the eigenvalues is always tensile. Frequently, pure shear is superimposed with enough confining hydrostatic pressure to make all principal stresses negative (compressive). Specifically, superimposing the hydrostatic loading of Eq. (3.17) onto the shear stress of Eq. (3.29), gives a state of **combined pressure-shear (SHR)** loading:

$$[\underset{\approx}{\sigma}] = \begin{bmatrix} s-\overline{p} & 0 & 0 \\ 0 & -s-\overline{p} & 0 \\ 0 & 0 & -\overline{p} \end{bmatrix} \text{ for combined pressure-shear loading.} \tag{3.30}$$

The invariants for combined pressure-shear loading are

$$I_1 = -3\overline{p} \qquad \text{for combined pressure-shear loading} \tag{3.31a}$$

$$J_2 = s^2 \qquad \text{for combined pressure-shear loading} \tag{3.31b}$$

$$J_3 = 0 \qquad \text{for combined pressure-shear loading} \tag{3.31c}$$

$$\tau = |s|\,. \tag{3.32}$$

[7]The lack of confinement in uniaxial stress precludes the increase in pressure that would be needed to show the effects of pressure dependence.

Spatial and Reference stress (frame indifference)

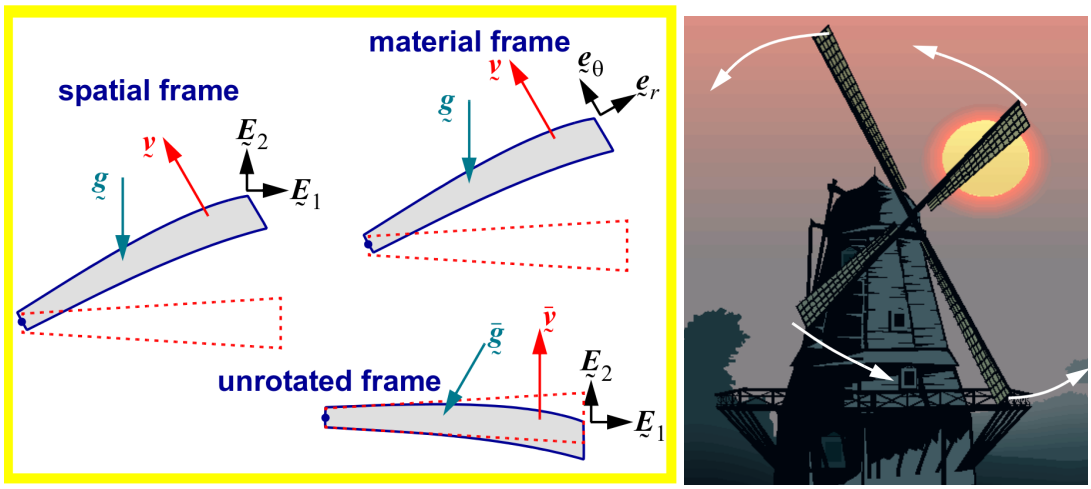

Figure 3.5. Spatial, Material, and unrotated frames. The unrotated frame, in which Kayenta operates at the element level (where the rotation tensor is found from the polar decomposition of the deformation gradient), removes bulk material rotation to keep only material rotation *relative to the material itself.* Once the stresses in the unrotated frame are found, they are re-rotated into the current configuration.

The spatial Cauchy stress tensor defined in Eq. (3.1) is the "familiar" stress tensor used in everyday engineering applications. Let us now denote that stress by $\underset{\approx}{\sigma}^{\text{spatial}}$. The elasticity component of solids models requires knowledge of both the *initial* and *current* configurations. Moreover, the principle of material frame indifference demands that if a *second* problem were considered that had the same initial configuration, but a current configuration that is identical to the current configuration of the first problem, except also rigidly rotated, then the predicted spatial stresses for the second problem should be identical to those of the first problem, except rigidly rotated by the same amount (see Fig. 3.5). This concept is quite different from a mere basis change because the *initial configuration* is identical for both problems.

Satisfying material frame indifference in a *spatial* context can be computationally expensive and error-prone because anisotropic internal state variables (such as directions of material fibers or orientation of the backstress) must be rotated *into* the spatial frame, and special "objective" rates must be integrated in constitutive models. A mathematically equivalent (and numerically more accurate and efficient) strategy instead applies the constitutive model within an *unrotated* reference configuration (see Fig. 3.5). With this approach, rotation of internal variables is not required, and all rates that appear in the constitutive model are more easily integrated *true* rates instead of co-rotational rates.

If $\underset{\approx}{\mathbf{R}}$ is the proper orthogonal tensor (found from a polar decomposition of the deformation) that characterizes the material rotation, then the unrotated stress is simply

$$\underset{\approx}{\sigma}^{\text{unrotated}} = \underset{\approx}{\mathbf{R}}^T \bullet \underset{\approx}{\sigma}^{\text{spatial}} \bullet \underset{\approx}{\mathbf{R}} \tag{3.33}$$

By working in the unrotated reference configuration, Kayenta predicts the stresses for the non-rotating problem. Upon receiving Kayenta's update of the unrotated stress, the host code then rotates the predicted stress back into the spatial frame. Roughly speaking, this approach will give results identical to a spatial constitutive model that is cast in terms of polar objective rates.

For problems involving massive material rotation (e.g., turbine blades, vortices, tumbling rock fragments, etc.), the "unrotation" strategy can give considerably more accurate answers because the host code may, optionally, use the rotation tensor $\underset{\approx}{\mathbf{R}}^n$ at the beginning of the time step when computing the starting value of $\underset{\approx}{\sigma}^{\text{unrotated}}$, but then the host code may use $\underset{\approx}{\mathbf{R}}^{n+1}$ at the *end* of the step when recasting the updated value of $\underset{\approx}{\sigma}^{\text{unrotated}}$ (output of Kayenta) to the spatial frame. Hence, this approach supports so-called *strong objectivity* [76] in a very natural way.

Throughout the remainder of this report, the *stress* $\underset{\approx}{\sigma}$ must be understood to be the *unrotated* stress $\underset{\approx}{\sigma}^{\text{unrotated}}$. Likewise all other vector or tensor variables (such as the strain rate) mentioned in this report are understood to be cast in the unrotated configuration (material frame). Any host code that uses Kayenta must (1) perform these unrotation operations, (2) call Kayenta, and then (3) re-rotate the result back to the spatial frame upon return. For more information, see page 136.

Lode coordinates

By definition, any isotropic yield function may be expressed in terms of the principal stresses $(\sigma_1, \sigma_2, \sigma_3)$. Therefore, the yield surface may be visualized in a 3D space for which the Cartesian coordinates are these principal stresses. The value of the yield function $f(\sigma_1, \sigma_2, \sigma_3)$ must be independent of the ordering of the eigenvalues. Therefore, as seen in Fig. 1.1 (pg. 19), the yield surface must have 120° rotational symmetry about the [111] (hydrostat) direction and reflective symmetry about the TXE and TXC axes in the octahedral plane (i.e., the view looking down the [111] axis).

The **principal Cartesian coordinates** $(\sigma_1, \sigma_2, \sigma_3)$ comprise an adequate choice for characterizing stress space, but the yield function is often cast in terms of different independent variables to exploit the yield surface's natural symmetries optimally. The natural symmetries suggest instead using cylindrical $(r, \overline{\theta}, \overline{z})$ coordinates — called **Lode cylindrical coordinates** — for which the z-axis is parallel with the [111] symmetry axis. We have placed a bar on the symbol $\overline{\theta}$ for the angular coordinate because we intend to define it so that it will be positive in TXC and negative in TXE. A constant $\overline{\theta}$ plane is a **meridional plane**, and a plot of r vs. z at a given value of $\overline{\theta}$ is called a **meridional profile**. Because most of the yield surface resides in the compressive domain where $z < 0$, we will usually display meridional profiles as r vs. $\overline{z}$ (where $\overline{z} = -z$). Any constant-z

plane is an **octahedral plane**, and any cross-section looking down the [111] axis (i.e., on a plane of constant z) is in an **octahedral profile**. Meridional and octahedral profiles are illustrated in Fig. 1.1 (pg. 19).

In this report, the Lode angle $\overline{\theta}$ is defined so that it equals zero in SHR. It varies from -30° in TXE to $+30^\circ$ in TXC. Superimposing pressure on a stress state changes only the axial z-coordinate, leaving the octahedral $(r, \overline{\theta})$ coordinates unchanged, which makes Lode coordinates a natural choice when decomposing tensors in to their isotropic and deviatoric parts. The radial r coordinate equals the magnitude of the stress deviator. The z coordinate is proportional to the mean stress. The angular coordinate is a measure of the relative proportions of the principal values of the stress deviator. Thus, as the Lode angle varies from -30° to $+30^\circ$, the stress transitions through TXE, SHR, and TXC states. Cylindrical Lode coordinates are especially useful because they may be expressed in terms of stress invariants, thereby eliminating the need for an eigenvalue decomposition.

The axial z-coordinate is positive on the tensile part of the hydrostat, so $\bar{z}$ is positive on the compressive hydrostat. We define the Lode angle $\overline{\theta}$ to be positive in TXC and negative in TXE. The change in variables from principal coordinates to Lode coordinates permits the yield function $f(\sigma_1, \sigma_2, \sigma_3)$ to be alternatively expressed in the form $f(r, \overline{\theta}, \bar{z})$. When phrased in terms of Lode coordinates, the yield function needs to be defined only over a 60° sextant on any octahedral plane. The symmetry properties of the yield surface may be used to reconstruct the octahedral profile over the full range from 0° to 360°.

Performing these necessary but tedious coordinate transformations from principal stresses to cylindrical Lode coordinates, it can be shown [62] that the cylindrical Lode coordinates may be determined directly from the I_1, J_2, and J_3 scalar stress invariants, eliminating the need for an eigenvalue analysis. Specifically,

$$\boxed{r = \sqrt{2J_2}} \tag{3.34a}$$

$$\boxed{\sin 3\overline{\theta} = -\frac{J_3}{2}\left(\frac{3}{J_2}\right)^{3/2}} \tag{3.34b}$$

$$\boxed{z = \frac{I_1}{\sqrt{3}}} \tag{3.34c}$$

The square root coefficients are merely by-products of the coordinate transformations. For example, since the z-coordinate is the projection of the stress onto the [111] axis, the $\sqrt{3}$ appears because the magnitude of the [111] vector is $\sqrt{3}$. The Lode radius r is zero if $J_2 = 0$. Also, the Lode angle $\overline{\theta}$ is undefined when $J_2 = 0$, which should not be too disturbing since the angular coordinate for any cylindrical system is undefined when the point in question lies on the symmetry axis (which, in this case, is the [111] hydrostat).

Later, when we give the mathematical formulation for Kayenta yield function, it will be phrased as $f(r, \overline{\theta}, \bar{z})$. Using the above formulas, the yield function is ultimately implemented in the form $f(I_1, J_2, J_3)$. The invariant J_3 influences only the Lode angle. When simpler yield models (Drucker-Prager) are independent of the third stress invariant, they are therefore independent of the Lode

angle, which makes their octahedral yield profile a circle. Kayenta must include a *non-circular* yield profile to reproduce TXE/TXC strength differences clearly evident in the data for geological materials. Thus, Kayenta must necessarily use all three Lode coordinates (equivalently, all three stress invariants).

Octahedral yield profile visualization

Given a yield function $f(r,\overline{\theta},\bar{z})$, yield profiles may be generated by solving $f=0$ to obtain r expressed as a function of $(\overline{\theta},\bar{z})$. A meridional profile is generated by plotting r vs. $\bar{z}$ at a fixed value of $\overline{\theta}$. An octahedral profile, which corresponds to a yield surface cross-section at a given value of $\bar{z}$, describes how the Lode radius at yield varies with the Lode angle. Rather than plotting r vs. $\overline{\theta}$, octahedral profiles are obtained by parametrically plotting Cartesian coordinates

$$x_1 = r\cos\overline{\Theta} \qquad \text{and} \qquad x_2 = r\sin\overline{\Theta} \tag{3.35}$$

Here, Θ is an angle that varies over the full range from 0 to 360°. The Lode angle $\overline{\theta}$, which is permitted to vary only over the range from $-30°$ to $+30°$, is generated from the full-range angle Θ by the sawtooth function

$$\overline{\theta} = \frac{1}{3}\arcsin[\sin(3\overline{\Theta})] \tag{3.36}$$

With $\overline{\theta}$ known, the value of corresponding Lode radius r can be found from the yield condition, and finally, the family of (x_1,x_2) points on the octahedral yield profile may be generated parametrically as Θ varies from 0 to 360°, as illustrated in Fig. 3.6.

Meridional yield profile visualization

To draw a *geometrically accurate* meridional cross-section of the yield surface, the profile should be plotted as r vs. $\bar{z}$ for a given value of $\overline{\theta}$. Typically, we will plot the TXC ($\overline{\theta}=30°$) profile. Using the r and $\bar{z}$ Lode coordinates as the axes in a meridional plot ensures that lengths and angles in the meridional profile will equal corresponding lengths and angles in stress space. Many times, however, we will depict a geometrically *distorted* view of the meridional profile by instead plotting $\overline{\tau}$ vs. $\overline{I_1}$, where the signed equivalent shear stress $\overline{\tau}$ equals $\pm\sqrt{J_2}$, depending on whether the loading is closer to TXE or TXC. Recalling from Eq. (3.34a) and Eq. (3.34c) that $\sqrt{J_2}=r/\sqrt{2}$ and $\overline{I_1}=\sqrt{3}\bar{z}$, a plot of $\overline{\tau}$ vs. $\overline{I_1}$ is equivalent to changing the aspect ratio of an r vs. $\bar{z}$ plot by a factor of $\sqrt{6}=2.45$, as illustrated in Fig. 3.7. Thus, whenever we plot the meridional profile as $\overline{\tau}$ vs. $\overline{I_1}$, keep in mind that the actual meridional cross-section in stress space is smaller in width by a factor of 2.45. Meridional profile distortion is an issue only when ascertaining the direction of the yield surface normal. Fig. 3.7 shows that the normal to the yield profile in a distorted plot does *not* correspond to the normal in stress space.

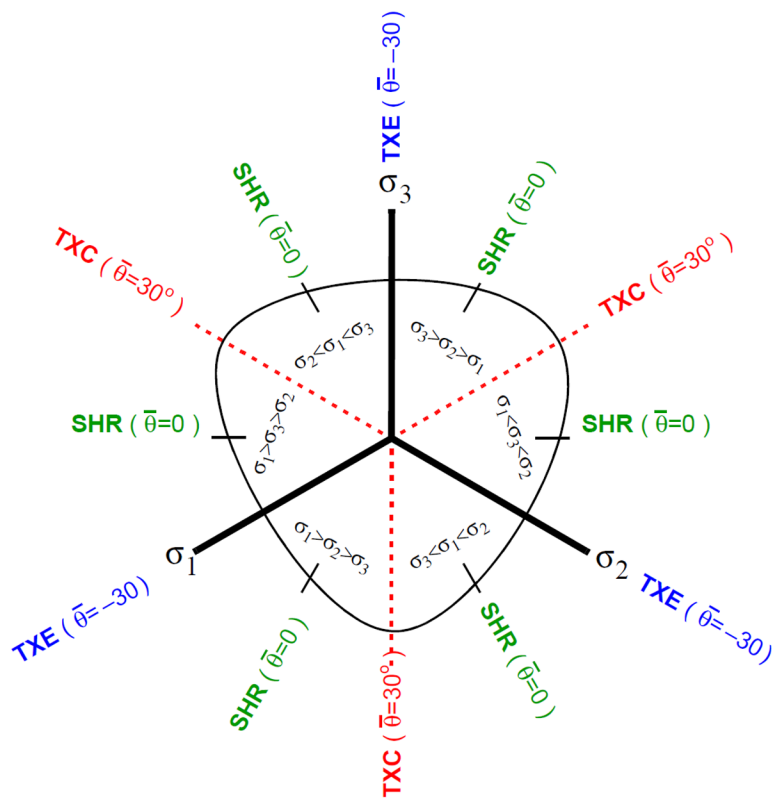

Figure 3.6. An octahedral yield profile. Geological materials tend to be stronger in TXC than in TXE, which is why the TXC axes are always on an apex of the rounded triangle (i.e., farther from the origin, corresponding to higher strength). The Lode angle r alternates cyclically from $-30°$ in TXE to $+30°$ in TXC because the yield threshold must be independent of the eigenvalue ordering.

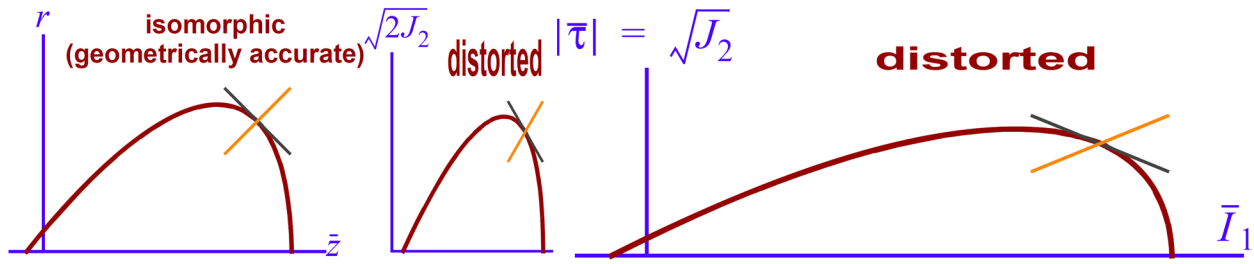

Figure 3.7. Distortion of the meridional profile when using non-isomorphic stress measures. Only a plot of r vs. $\bar{z}$ will result in a geometrically accurate depiction of a meridional cross-section of stress space for which angles and lengths are preserved. The middle plot shows the magnitude of the stress deviator plotted against the pressure, resulting in a plot eccentricity ratio of $1/\sqrt{3} = 0.577$. The last plot shows the equivalent shear stress plotted against the first stress invariant, for a plot eccentricity ratio of $\sqrt{6} = 2.45$.

Closed-form solution for ordered eigenvalues

Recalling that Lode cylindrical coordinates merely represent a coordinate change from the principal coordinates $(\sigma_1, \sigma_2, \sigma_3)$ to a new set of coordinates $(r, \overline{\theta}, \bar{z})$, it follows that inverse transformation formulas should exist for obtaining the principal stresses from Lode coordinates. Each distinct sextant in Fig. 3.6 merely corresponds to a different eigenvalue ordering. Regardless of the sextant in which the stress resides, $\overline{\theta} = 30^\circ$ falls on the pi-plane axis corresponding to the smallest eigenvalue, whereas $\overline{\theta} = -30^\circ$ falls on the axis of the largest eigenvalue. Therefore, transformation formulas that convert cylindrical coordinates back to Cartesian coordinates only need to be defined over the range from -30° through $+30^\circ$ to determine the *ordered* eigenvalues.

Letting the compressive eigenvalues be ordered $\overline{\sigma}_3 \leq \overline{\sigma}_2 \leq \overline{\sigma}_1$, the tensile eigenvalues must be ordered $\sigma_3 \geq \sigma_2 \geq \sigma_1$, and the inverse transformation formulas are

$$\textbf{low}: \boxed{\sigma_1 = \frac{z}{\sqrt{3}} - \frac{r}{\sqrt{2}}\left[\cos\overline{\theta} + \frac{\sin\overline{\theta}}{\sqrt{3}}\right] = \frac{I_1}{3} - \sqrt{J_2}\left[\cos\overline{\theta} + \frac{\sin\overline{\theta}}{\sqrt{3}}\right]} \tag{3.37a}$$

$$\textbf{middle}: \boxed{\sigma_2 = \frac{z}{\sqrt{3}} + \sqrt{\frac{2}{3}}\, r \sin\overline{\theta} = \frac{I_1}{3} + \frac{2}{\sqrt{3}}\sqrt{J_2}\sin\overline{\theta}} \tag{3.37b}$$

$$\textbf{high}: \boxed{\sigma_3 = \frac{z}{\sqrt{3}} + \frac{r}{\sqrt{2}}\left[\cos\overline{\theta} - \frac{\sin\overline{\theta}}{\sqrt{3}}\right] = \frac{I_1}{3} + \sqrt{J_2}\left[\cos\overline{\theta} - \frac{\sin\overline{\theta}}{\sqrt{3}}\right]}. \tag{3.37c}$$

These formulas constitute a closed-form solution for the ordered eigenvalues of any real symmetric 3×3 matrix, not just a stress.[8] Using these formulas, any yield function that is stated in terms of principal stresses, $f(\sigma_1,\sigma_2,\sigma_3)$, can be immediately re-cast into a form expressed in terms of stress invariants, $f(I_1,J_2,J_3)$, which is more convenient for plasticity modeling because it can be differentiated without an eigenvector analysis (see Eq. (3.12)). For example, any material model that seeks to initiate failure when the largest tensile principal stress σ_3 reaches a critical value, σ_3^{crit}, can do so by simply substituting Eq. (3.37c) into the failure criterion, $\sigma_3 = \sigma_3^{\text{crit}}$. The above closed-form solution for ordered eigenvalues is applied in Appendix B (page 229) to convert the Mohr-Coulomb theory of failure into a formulation expressed in terms of stress invariants, as required in Kayenta.

[8]The solution quoted here is equivalent to the closed form solution derived by Malvern [66] via a trigonometric substitution. Malvern's angle α is a Lode angle, but defined to be zero in TXE and 60° in TXC.

This page intentionally left blank.

Chapter 4

Kayenta theory

Being a generalized plasticity theory, Kayenta is founded upon an additive decomposition of the strain rate $\dot{\underset{\approx}{\varepsilon}}$ into separate contributors: $\dot{\underset{\approx}{\varepsilon}}^e$ from elastic straining and $\dot{\underset{\approx}{\varepsilon}}^p$ from inelastic straining:

$$\dot{\underset{\approx}{\varepsilon}} = \dot{\underset{\approx}{\varepsilon}}^e + \dot{\underset{\approx}{\varepsilon}}^p. \tag{4.1}$$

Geomechanics modelers often refer to the inelastic strain as the "plastic strain", so it must be understood that they generalize the term "plasticity" to mean any form of inelastic deformation, including but not necessarily exclusive to the tradition dislocation-based meaning of plastic flow. Kayenta permits the host code to employ any definition of the strain so long as its rate is conjugate to the stress $\underset{\approx}{\sigma}$ in the sense that the work rate per unit volume is given by

$$\underset{\approx}{\sigma} : \dot{\underset{\approx}{\varepsilon}}. \tag{4.2}$$

To satisfy the principle of material frame indifference, the host code must cast the stresses and strain rates in an unrotated configuration. At present, all implementations of Kayenta have approximated the strain rate by the unrotated symmetric part of the velocity gradient:

$$\dot{\varepsilon}_{ij} \approx \frac{1}{2}\left(\frac{\partial v_m}{\partial x_n} + \frac{\partial v_n}{\partial x_m}\right) R_{mi} R_{nj}, \tag{4.3}$$

where $\underset{\sim}{\mathbf{v}}$ is the velocity vector, $\underset{\sim}{\mathbf{x}}$ is the current spatial position vector, and the tensor $\underset{\approx}{\mathbf{R}}$ is the rotation from the polar decomposition of the deformation gradient. The conjugate stress is the unrotated Cauchy stress defined in Eq. (3.33). Henceforth, all references to the stress σ_{ij} and the strain rate $\dot{\varepsilon}_{ij}$ must be understood to be the unrotated stress and strain rate.

All Kayenta material parameterizations to date have been based on the above approximation for the strain rate. Using a different choice for the conjugate stress and strain rate measures would, of course, entail adjusting material parameters appropriately. The strain rate in Eq. (4.3) is an approximation because, for general deformations, it is not precisely equal to the rate of any proper function of the deformation.[1] The approximate strain rate in Eq. (4.3) exactly equals the unrotated logarithmic (Hencky) strain rate for any deformation having stationary *reference* principal stretch directions, and it is an excellent approximation to the Hencky strain rate even when principal stretch directions change orientation as long as the shear strains remain small (volumetric strains

[1] Paths can be devised for which the starting and ending configurations are identical, but the time integral of $\dot{\varepsilon}_{ij}$ does not evaluate to zero [15].

may be arbitrarily large) [16, 17]. For geological applications, material rupture generally occurs well before shear strains become large, so Eq. (4.3) is a prudent choice for the strain rate measure. If, however, the model is to be subjected to significant cyclical loading (e.g., fatigue), then a proper strain rate should be used instead of Eq. (4.3) even if the distortional strains are always small.

Elasticity

Kayenta supports both linear and nonlinear hypoelasticity.[2] Kayenta presumes the material is elastically isotropic and that the elastic stiffness tensor C_{ijkl} is itself isotropic (i.e., deformation-induced elastic anisotropy is not included). Consequently, the stress is governed by a rate form of Hooke's law:

$$\dot{\sigma}_{ij} - \dot{\alpha}_{ij} = C_{ijkl}\dot{\varepsilon}^e_{kl} - \dot{\lambda}^* Z_{ij}. \tag{4.4}$$

Here, the backstress tensor $\underset{\approx}{\alpha}$ is used to define the location of the origin in stress space in order to model the Bauschinger effect (*cf.*[83]). Conventional plasticity models incorporate the backstress only into the definition of the yield function, but Kayenta also includes the backstress in the elastic model to reproduce the experimentally observed phenomenon that plastic loading can become so severe that unloading is actually a partially inelastic process. The above formulation supports this possibility by allowing the origin of stress space to translate so far that the initial origin of stress space falls outside of the evolved yield surface. Accordingly, we include the backstress in *both* the yield model and the elastic model. The Z tensor, which is likewise rarely seen in other plasticity models, accommodates a self-consistent treatment of elastic-plastic coupling as described in [13] Because the elastic tangent stiffness tensor, C_{ijkl}, is presumed to be isotropic, Eq. (4.4) can be written as two separate and much simpler equations, one for the volumetric response and the other for the deviatoric response:

$$\dot{\overline{p}} = K\dot{\varepsilon}^e_v \tag{4.5}$$

and

$$\dot{S}_{ij} = 2G\dot{\gamma}^e_{ij}. \tag{4.6}$$

Here, G and K are the *tangent* shear and bulk elastic moduli; $\overline{p}$ is the pressure (negative of the mean stress); $\dot{\overline{\varepsilon}}^e_v$ is the volumetric elastic strain rate computed by the trace operation,

$$\dot{\overline{\varepsilon}}^e_v = \dot{\overline{\varepsilon}}^e_{kk}, \tag{4.7}$$

S_{ij} is the stress deviator; and $\dot{\gamma}^e_{ij}$ is the deviatoric part of the elastic strain rate, defined

$$\dot{\gamma}^e_{ij} = \dot{\varepsilon}^e_{ij} - \frac{1}{3}\dot{\varepsilon}^e_v\delta_{ij}. \tag{4.8}$$

We have used the overbar (which, recall, simply denotes the negative of a variable) in our equation for the pressure-volume response because the mean stress is typically compressive (negative) in most applications of Kayenta and therefore $\overline{p}$ and $\overline{\varepsilon}^e_v$ are typically positive. Of course, Eq. (4.5)

[2] "Hypoelastic" means the stress can be written as a function of the strain, but is *not* derivable from an energy potential. When a potential exists, then the formulation is "hyperelastic".

remains valid for volumetric expansion ($\overline{\varepsilon}_v^e < 0$) and tensile mean stresses ($\overline{p} < 0$) as well. No overbar is used in Eq. (4.8) because deviatoric tensors always have eigenvalues of mixed signs.

For *linear* elasticity, the user merely specifies constant values for the bulk modulus K and the shear modulus G. For nonlinear elasticity, the moduli are stress-dependent *tangent* moduli (i.e., slopes of the tangents to the stress-strain curves). Three parameters are available for fitting the nonlinear tangent bulk modulus K to laboratory data obtained from unloading curves in hydrostatic compression. Similarly, three parameters are available for fitting the nonlinear tangent shear modulus G indirectly from triaxial test data. Additional elastic parameters are available for materials whose elastic properties are affected by inelastic deformation (see Eq. (4.33) and Eq. (4.34)). Step-by-step instructions for determining elastic properties from measured data are provided in Appendix A.

Nonlinear elasticity

At the user's option, Kayenta supports nonlinear elasticity by permitting the elastic tangent moduli to vary with the stress according to

$$K = b_0 + b_1 \exp\left(-\frac{b_2}{|I_1|}\right) \tag{4.9}$$

$$G = g_0 \left[\frac{1 - g_1 \exp(-g_2\sqrt{J_2})}{1 - g_1}\right]. \tag{4.10}$$

In these equations, the b_k and g_k parameters are material constants determined via nonlinear regression fitting to the unloading portions of hydrostatic compression and triaxial compression experiments, as described in Appendix A.[3] Further descriptions of the physical meanings of the parameters in these equations are given Appendix B. Kayenta's functional forms for the nonlinear elastic tangent moduli are phenomenological to permit tight empirical fits to experimental data for a wide variety of materials. Suitability of these functions for fitting material data is demonstrated in Chapter 10 and Chapter 11, starting on page 195.

Incidentally, it can be shown that an elasticity model of the form in Eq. (4.4) is hyperelastic (i.e., derivable from an isotropic elastic potential) if and only if the shear modulus is constant and the bulk modulus depends at most only on I_1. Because Eq. (4.34) permits the shear modulus to vary, Kayenta is *hypoelastic* if $g_1 \neq 0$.

Assigning values to the elastic constants

The bulk modulus K is determined from the local tangent of the elastic part of a pressure vs. volumetric strain plot obtained from hydrostatic testing. Rather than determining the shear

[3] The generalized nonlinear elasticity formulas on page 63 may be used when elastic properties appear to be affected by inelastic deformation.

modulus directly from a shear loading experiment (where geomaterials tend to be weak), the shear modulus is typically found indirectly from triaxial loading data. For triaxial loading, the stress rates are related to the strain rates by[4]

$$\dot{\bar{\varepsilon}}_A = \frac{\dot{\bar{\sigma}}_A - 2\nu\dot{\bar{\sigma}}_L}{E} \qquad \text{and} \qquad \dot{\bar{\varepsilon}}_L = \frac{-\nu\dot{\bar{\sigma}}_A + (1-\nu)\dot{\bar{\sigma}}_L}{E} \tag{4.11}$$

where E and ν are, respectively, Young's modulus and Poisson's ratio. If E and ν are known, then the bulk modulus K, the Lamé modulus λ, and the shear modulus G may be determined from the well-known elasticity equations [41],

$$K = \frac{E}{3(1-2\nu)} \qquad \lambda = \frac{E\nu}{(1+\nu)(1-2\nu)} \qquad G = \frac{E}{2(1+E)}. \tag{4.12}$$

Because Kayenta casts its elasticity model in terms of the bulk modulus K and the shear modulus G, the following formulas are convenient for converting various combinations of elastic constants into expressions involving only K and G (see, for example, Ref. [41], page 139):

$$\lambda = K - \frac{2}{3}G \qquad \nu = \frac{3K-2G}{2(3K+G))} \qquad E = \frac{9KG}{3K+G} \tag{4.13}$$

$$\frac{E}{\nu} = \frac{18KG}{3K-2G} \qquad \frac{\lambda}{\nu} = \frac{2}{3}(3K+G) \qquad \frac{\nu}{1-\nu} = \frac{3K-2G}{3K+4G} \tag{4.14}$$

$$\frac{E}{1-\nu} = \frac{18KG}{3K+4G} \qquad 2G+\lambda = K + \frac{4}{3}G \qquad G = \frac{3KE}{9K-E} \tag{4.15}$$

$$K + \frac{4}{3}G = \frac{E(1-\nu)}{(1+\nu)(1-2\nu)} \qquad \textbf{Uniaxial } \textbf{\textit{strain}} \textbf{ modulus} \text{ — see Eq. (3.25).} \tag{4.16}$$

Eq. (4.11) implies that triaxial experiments conducted under constant lateral stress ($\dot{\bar{\sigma}}_L = 0$) satisfy

$$\dot{\bar{\sigma}}_A = E\dot{\bar{\varepsilon}}_A. \qquad \textbf{(This applies if lateral stress is constant.)} \tag{4.17}$$

A fixed lateral stress implies that $\dot{\bar{\sigma}}_A = \dot{\bar{\sigma}}_A - \dot{\bar{\sigma}}_L$. Thus, when a stress-strain curve is obtained by plotting the stress difference $\overline{\sigma_A} - \overline{\sigma_L}$ against the axial strain $\overline{\varepsilon_A}$ for a triaxial loading experiment in which the lateral stress is fixed, the local tangent of the curve equals Young's modulus E. With the bulk modulus K having been obtained separately from hydrostatic test data, Eq. (4.15) may then be used to determine the tangent shear modulus G.

The elastic limit (yield surface)

Like most plasticity models, Kayenta begins each solution phase (i.e., each time step) by tentatively presuming that the loading is elastic. This produces a trial elastic stress, which is then

[4]Here, we are writing Hooke's Law in rate form to allow for the possibility that the elastic moduli might be nonlinear. Thus, the elastic properties used here are the *tangent* moduli (i.e., based on the local slope of an elastic stress vs. strain curve).

checked to see if it is inside or on the yield surface. If so, the tentative assumption of elasticity is validated and the actual updated stress is set equal to the trial elastic stress. If, on the other hand, the trial elastic stress falls outside the yield surface, then the tentative assumption of elastic response was wrong, and the solution phase is then solved anew using the equations governing inelastic deformation. Before discussing these inelastic governing equations, we must first characterize the yield surface itself. We will begin by discussing yield surfaces in some generality and then progressively work towards the precise functional form for Kayenta's yield surface.

Mathematically, Kayenta is a generalized plasticity model. The term "plasticity" is broadened to include not only the usual flow of material via dislocations (a phenomenon that has actually been observed in brittle materials when they are loaded under extraordinarily high confining pressure), but also any other mechanisms that lead to a marked departure from elasticity. Examples include crack growth, void collapse, or perhaps even phase transition. Rather than explicitly tracking each of these microscale failure mechanisms explicitly, the "yield" surface itself characterizes *them all* in an ensemble phenomenological manner. If the stress state $(\sigma_1, \sigma_2, \sigma_3)$ is "not too severe", then material response will be elastic and therefore reversible (non-dissipative). Once the stress becomes critically severe, however, the material will undergo irreversible structural changes that manifest as inelastic strains (nonrecoverable upon removal of the load). The material response is elastic whenever the stress is on the *inside* of the yield surface. If continuing to apply elasticity theory would move the stress into regions outside the yield surface, then plasticity equations are applied.

Kayenta's yield criterion and yield function are

$$\textbf{Kayenta Yield Criterion}: \sqrt{J_2^{\xi}} = \frac{[F_f(I_1) - N]\sqrt{F_c(I_1, \kappa)}}{\Gamma(\overline{\theta}^{\xi})}. \tag{4.18}$$

$$\textbf{Kayenta Yield Function}: f(\underset{\approx}{\sigma}, \underset{\approx}{\alpha}, \kappa) = J_2^{\xi}\Gamma^2(\overline{\theta}^{\xi}) - [F_f(I_1) - N]^2 F_c(I_1, \kappa). \tag{4.19}$$

The remainder of this chapter is devoted to motivating the functional forms of these equations and defining the numerous variables that appear in them. Briefly, the yield *function* f is defined such that elastic states satisfy $f < 0$. The yield *criterion* corresponds to $f = 0$. The "building block" functions F_f and Γ are used to describe the elastic limit caused by the presence of microcracks, whereas the function F_c accounts for strength reduction by porosity. Commonly assumed in the damage-mechanics models [22], the function F_f represents the ultimate limit on the amount of shear the material can support (i.e., F_f represents the softening initiation *limit* threshold, sketched in Fig. 1.2, resulting exclusively from microcracks). The material parameter N characterizes the maximum allowed translation of the yield surface when kinematic hardening is enabled, in which case J_2^{ξ} is the second invariant of the *shifted* stress tensor $\underset{\approx}{\xi} = \underset{\approx}{\mathbf{S}} - \underset{\approx}{\alpha}$, where $\underset{\approx}{\alpha}$ is the backstress. When kinematic hardening is disabled (i.e., when N is specified to be zero), the backstress will be zero and therefore J_2^{ξ} would be simply the invariant of the stress deviator. The function F_f describes the *limit* strength, whereas $F_f - N$ defines the *yield* threshold associated with cracks, which can evolve toward the limit surface via kinematic hardening as explained later in the context of Fig. 4.7. The function $\Gamma(\overline{\theta}^{\xi})$, where $\overline{\theta}^{\xi}$ is the Lode angle of the shifted stress, is used to account for differences in material strength in triaxial extension and triaxial compression. By appearing as

a multiple of $[F_f - N]^2$, the function F_c accommodates material weakening caused by porosity. The function F_c depends on an internal state variable κ whose value controls the hydrostatic elastic limit, as explained later in the context of Fig. 4.4, Fig. 4.5, and Fig. 4.16.

The principal goal of this section is to describe the physical motivations of Kayenta's yield criterion cited in Eq. (4.18). This criterion describes the geometrical shape of the yield surface in stress space. For rocks and rock-like materials, the yield surface will have a shape similar to the one illustrated in Fig. 1.1 (pg. 19).[5] Fig. 1.1(b) shows a "side" **meridional profile** of the yield surface in **bold**, along with a family of other profiles from which the yield surface might have evolved over time (via continuously varying values of the κ internal state variable); Fig. 4.7 shows a similar plot when kinematic hardening is allowed. Very little of the yield surface in Fig. 1.1(b) exists in the tensile domain (left side of the meridional plot), implying that materials of this type are very weak in tension.

Fig. 1.1(c) shows the yield surface profile from a perspective looking down onto a plane — called an **octahedral plane** — that is perpendicular to the [111] symmetry axis and therefore represents a cross-section of the yield surface at a given pressure. Since the onset of yield must not depend on the ordering of the principal stresses, the yield surface for *any* isotropic yield model possesses 120° rotational symmetry about the hydrostat (i.e., the [111] axis), as well as reflective symmetry about any of the triaxial compression or triaxial extension axes labeled TXC and TXE in Fig. 1.1(c). As seen in Fig. 1.1(c), the octahedral profile is somewhat triangular in shape. This periodic asymmetry corresponds to differences in the failure limit under triaxial compression (TXC) and triaxial extension (TXE). Because the yield surface is farther from the origin on a TXC axis than on a TXE axis, this material has higher strength in TXC than in TXE. The $\Gamma(\overline{\theta})$ function characterizes the *shape* of the octahedral profile because r is proportional to $1/\Gamma(\overline{\theta})$. The *size* of the octahedral profile at various pressures is governed by the functions F_f and F_c.

Elastic stress states are "inside" the yield surface ($f < 0$). Stress states for which $f = 0$ are said to be "on the yield surface". Like classical plasticity models, the yield surface in Kayenta characterizes the point of departure from elastic to inelastic behavior. If applying elasticity theory would result in an updated stress that falls outside the yield surface ($f > 0$), then plasticity equations must be applied. Recall that the theory outlined these sections pertains to quasistatic loading. Therefore, stress states outside the yield surface are unachievable except through a hardening evolution of the internal state variables (κ and/or $\underset{\approx}{\alpha}$) corresponding to a fundamental change of the underlying microstructure of the material. Stresses outside the *limit* surface are unachievable by *any* quasistatic means.

The internal state variable κ controls the location of the yield cap (wire frame in Fig. 1.1(a) on page 19). When κ increases in response to pore collapse, octahedral profiles that pass through the cap will expand isotropically (i.e., the octahedral profile changes size, but not shape, and it does so without translating in stress space). The amount of isotropic expansion or contraction varies with pressure in such a manner that the family of yield surfaces corresponding to various values of κ is

[5] At the user's option, Kayenta parameters can be set to alternatively duplicate classical idealized von Mises or Mohr-Coulomb theory. Doing this would be inappropriate when modeling real materials, but it can be useful in benchmark testing.

bounded by the shear limit surface, $\sqrt{J_2} = F_f(I_1)/\Gamma(\overline{\theta})$.

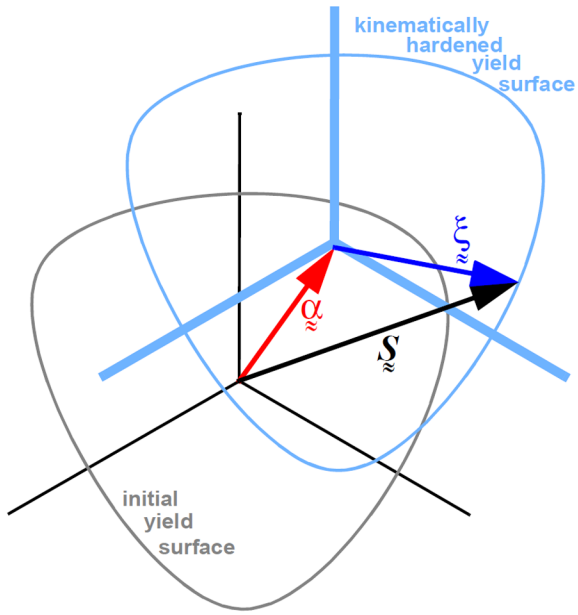

Figure 4.1. Backstress and shifted stress.

Though not needed in many applications, Kayenta supports kinematic hardening for which the symmetry axis of the yield surface is permitted to shift in stress space so that the invariants in the yield function are based on the **shifted stress** tensor, defined

$$\xi_{ij} \equiv S_{ij} - \alpha_{ij}. \tag{4.20}$$

As illustrated in Fig. 4.1, the **backstress** α_{ij} is a deviatoric tensor-valued internal state variable that defines the origin about which the yield surface is centered. When the backstress tensor changes, the yield surface translates in stress space, thereby supporting deformation-induced anisotropy (Bauschinger effect) in a limited capacity. The backstress is initially zero, but then evolves according to an evolution equation described in detail on page 91. Kayenta is otherwise fully isotropic, both elastically and plastically. Consequently, the yield function is isotropic with respect to the *shifted* stress deviator ξ_{ij}, implying that it depends on the invariants of the shifted stress deviator, as well as I_1 and an internal state variable κ that characterizes *isotropic* hardening caused by void collapse or softening caused by porosity increases. Specifically, Kayenta's yield function is of the form

$$f = f(I_1, J_2^{\xi}, J_3^{\xi}; \kappa), \tag{4.21}$$

where

$$J_2^{\xi} = \frac{1}{2}\,\mathrm{tr}\,\underset{\approx}{\xi}^2 \qquad \text{and} \qquad J_3^{\xi} = \frac{1}{3}\,\mathrm{tr}\,\underset{\approx}{\xi}^3. \tag{4.22}$$

In this section, we seek to describe the size and shape of the yield surface at an instant frozen in time. Thus, we will focus on how the yield function depends mathematically on the stress invariants

$(I_1, J_2^{\xi}, J_3^{\xi})$, with the internal state variables (κ and $\underset{\approx}{\alpha}$) regarded as constants. The means by which the yield surface evolves in response to time variation of κ and/or $\underset{\approx}{\alpha}$ is discussed separately.

Before discussing the physical foundations of Kayenta's yield function in Eq. (4.19), we will first discuss qualitative features of any yield function of the more general form in Eq. (4.21). Given that an isotropic yield function possesses alternating 30° symmetry about the [111] direction in stress space, the yield function in Eq. (4.21) is most naturally cast in terms of the cylindrical Lode coordinates as

$$f = f(r, \overline{\theta}, \bar{z}; \kappa), \tag{4.23}$$

where these Lode coordinates are defined with respect to the kinematically *shifted* origin in stress space. For any given values of $\overline{\theta}$, $\bar{z}$, and κ, there must exist only one radius r that is a solution to $f(r, \overline{\theta}, \bar{z}, \kappa) = 0$ (otherwise, the yield surface would not be convex). Thus, without loss in generality, elastic stress states for *any* isotropic yield function always can be characterized in the general functional form

$$r < g(\overline{\theta}, \bar{z}; \kappa), \tag{4.24}$$

where $g(\overline{\theta}, \bar{z}; \kappa)$ is regarded as a material function determined from experimental data and is introduced here only to discuss the structure of isotropic yield functions in generality (i.e., Kayenta has an *implied* "g" function, but does not construct one explicitly). The yield function corresponding to Eq. (4.24) may be written

$$f = r^2 - [g(\overline{\theta}, \bar{z}; \kappa)]^2 \qquad \textbf{(Any isotropic yield function can be written in this form.)} \tag{4.25}$$

At present, Kayenta assumes that the *shape* of the octahedral yield profile is the same at all pressures — only its *size* varies with pressure.[6] Moreover, Kayenta presumes that the *shape* of the octahedral yield profile is constant in time (i.e., it does not evolve to any different shape in response to plastic deformation even though it can permissibly vary in size and translate in stress space). Consequently, Kayenta's yield function is structured such that $g(\overline{\theta}, \bar{z}; \kappa)$ is *separable* into the product of two distinct functions, one depending only on $\overline{\theta}$ and the other depending only on $\bar{z}$ and κ, permitting Eq. (4.24) to be structured in the general form:

$$r < h_1(\overline{\theta}) h_2(\bar{z}; \kappa) \qquad \textbf{(This form results from a \textit{separability} assumption.)} \tag{4.26}$$

As was the case with the g function, h_1 and h_2 have been introduced here only to illustrate the basic structure of Kayenta's yield function. Kayenta's specific formulations will be discussed soon. A degree of ambiguity exists in the definitions of h_1 and h_2 because they may be replaced respectively by ηh_1 and h_2/η for any scalar η without loss in generality. To remove this ambiguity, the function h_1 is scaled such that it merely describes the shape of the octahedral profile (i.e., the view of the yield surface looking down the [111] direction). The function h_2 defines the meridional profile of the yield function, and therefore this function also defines the size of the octahedral profile.

Kayenta aims to model rocks and rock-like brittle materials. The mechanical behavior of such materials is typically driven by two underlying mechanisms: porosity and microcracks. To date,

[6] Some evidence suggests that the octahedral yield profile should in fact vary in shape from strongly triangular at low pressures to nearly circular at extraordinarily high pressures [48]. Consequently, Kayenta's current assumption of a constant octahedral profile shape might change in future releases.

microphysical research has focused on the effects of only one of these mechanisms at a time. Fig. 4.2(a) shows the qualitative shape of the meridional profile typically that is predicted when only porosity is considered. In this case, the meridional yield profile is a "cap" function that is essentially flat like a von Mises profile for a large range of pressures ($\bar{z}$ is proportional to pressure), and then the profile drops to zero when pressure becomes large enough to collapse voids. Fig. 4.2(b) shows the general shape of a meridian profile that is typically predicted for theories that consider only the influence of microcracks *without* considering porosity. Microcracks lead to low strength in tension, but strength increases as pressure is increased because pressure generates additional friction at crack faces, thereby reducing the shear load suffered by the matrix material. Kayenta unifies these separate microscale theories to obtain a combined porosity and microcrack model, as sketched qualitatively in Fig. 4.2(c). Loosely speaking, Kayenta obtains the combined meridional yield function by multiplying the individual porosity and microcrack profiles (and scaling the ordinate appropriately to match data).

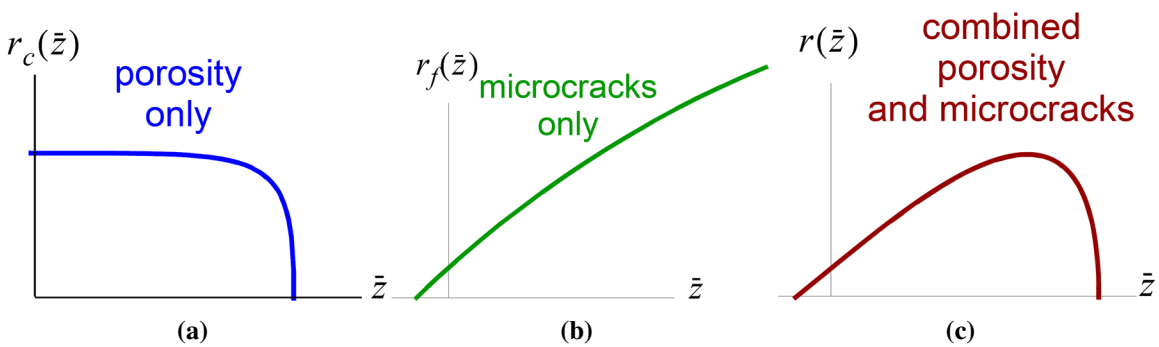

Figure 4.2. Qualitatively meridional profile shapes resulting from (a) porosity alone, (b) microcracks alone, and (c) porosity and microcracks in combination.

To date, the *combined* effect of voids and microcracks remains a poorly developed branch of materials constitutive modeling. Some early models simply asserted that a material is elastic (safe from yield) if and only if it is safe from both crack growth and void collapse, with each criterion tested *separately*. However, as illustrated in Fig. 4.3(a), this approach results in a discontinuous slope in the meridional yield profile and fails to account for interactions between voids and cracks. Kayenta [Fig. 4.3(b)], phenomenologically permits cracks and voids to interact in a way that results in a continuously differentiable meridional profile, making Kayenta better suited for reproducing observed data.

Kayenta achieves a *combined* porous+cracked yield surface by multiplying the fracture function $r_f(\bar{z})$ in Fig. 4.2(b) times the cap function $r_c(\bar{z})$ in Fig. 4.2(a) so that

$$r(\bar{z}) \text{is proportional to } r_f(\bar{z}) r_c(\bar{z}). \tag{4.27}$$

The proportionality factor depends on the Lode angle $\overline{\theta}$ so that the equivalent shear stress at yield (which, recall, is simply a constant multiple of r) can be made lower in TXE than in TXC. Cap

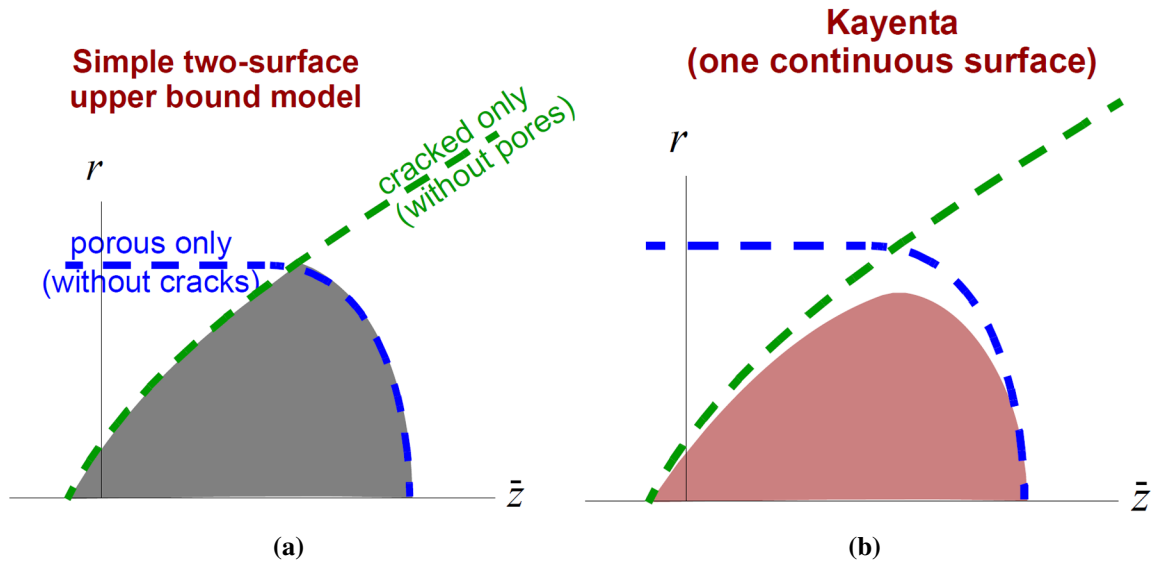

Figure 4.3. Distinction between two-surface upper-bound models and Kayenta.

functions depend on the porosity level (which controls where the cap curve intersects the z-axis). The curvature of a cap function controls the degree to which porosity affects the shear response. Although Kayenta does not explicitly track porosity, it does include an internal state variable κ that equivalently accounts for the *presence* of porosity. As explained later (in page 80), the value of κ and one additional material constant, R, determine both the cap curvature and the location where the cap intersects the hydrostat (the $\bar{z}$ axis). Thus, the cap function $r_c(\bar{z})$ implicitly depends on κ and R.

Recalling that the Lode cylindrical radius r equals $\sqrt{2J_2^{\xi}}$ and the Lode axial coordinate z is proportional to I_1, Kayenta implements the notion of multiplying fracture and cap functions by using Eq. (3.34) to express Eq. (4.27) in terms of stress invariants instead of Lode coordinates, so Kayenta's yield criterion is of the form

$$\sqrt{J_2^{\xi}} = \frac{f_f(\overline{I_1})f_c(\overline{I_1})}{\Gamma(\overline{\theta})}. \qquad [\Gamma \text{ also varies with } \overline{I_1} \text{ if user parameter } \Psi = -1] \tag{4.28}$$

Comparing with Eq. (4.18), the f and F functions are related by

$$f_f = F_f - N \qquad \text{and} \qquad f_c = \sqrt{F_c} \tag{4.29}$$

The invariant J_2^{ξ} is computed using the *shifted* stress tensor $\underset{\approx}{\xi} \equiv \underset{\approx}{\mathbf{S}} - \underset{\approx}{\alpha}$, where is the deviatoric tensor-valued backstress that is nonzero only when kinematic hardening is enabled. Thus, in addition to depending explicitly on the stress tensor, the yield criterion depends implicitly on material constants and on two internal state variables, κ (mentioned earlier) and $\underset{\approx}{\alpha}$.

The fracture function f_f characterizes the cracking-related portion of the meridional yield profile. Kayenta's cap function f_c is normalized to have a peak value of 1. The function $\Gamma(\overline{\theta})$ characterizes the Lode angle dependence of the meridional profile and is normalized to equal 1 in triaxial compression ($\overline{\theta} = 30°$). At different Lode angles, Γ usually has values *greater* than 1, which (because it is a *divisor* in Eq. (4.28) reduces equivalent shear strength. Rather than regarding Γ as a strength reducer, it can be alternatively interpreted as a *stress intensifier*. Qualitatively, these functions are typically shaped as shown in Fig. 4.4.

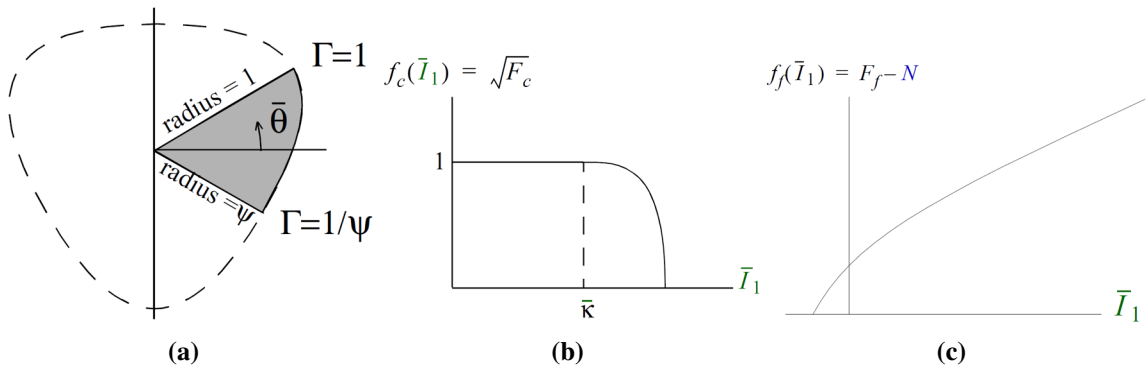

Figure 4.4. Basic shapes of the three key functions that characterize the composite shape of the yield surface. (a) Lode angle dependence, (b) porosity cap curve, (c) limit failure curve. The Lode angle function $\Gamma(\overline{\theta})$ is the *reciprocal* of the radius in the octahedral plane, making it best regarded as a stress intensifier; $\Gamma(\overline{\theta})$ is normalized to equal 1 in triaxial compression, which implies that it must equal $1/\Psi$ in triaxial extension (where Ψ is the TXE/TXC strength ratio). Shear influence on void collapse begins at the point where the cap function branches into an ellipse. Since the cap function is multiplied by the fracture curve, this transition point also marks where the composite Kayenta failure surface branches away from f_f, beyond which macroscale response is influenced simultaneously by *both* cracks and voids. For *pure* (shear-free) hydrostatic compression, void collapse begins at the point where the ellipse intersects the horizontal. Only the function f_f has dimensions of stress (the others are dimensionless).

As explained on page 69, the precise expression for the Γ function is determined by user-specification of two parameters: the TXE/TXC strength ratio Ψ and an integer-valued option (**J3TYPE**), which controls the manner in which the octahedral profile radius varies from the value $1/\Psi$ at TXE to 1 at TXC. As explained below, the porosity (cap) function f_c is defined by two parameters: the initial intersection p_0 on the horizontal axis and the eccentricity or "shape factor" R for the ellipse (i.e., the width to height ratio of the ellipse). As explained on page 81, Kayenta internally computes evolution of the cap function resulting from void collapse. As explained on page 69, the very important f_f function, which reflects influence of microcracks, is determined by fitting triaxial compression data to an exponential spline [up to five parameters (a_1, a_2, a_3, a_4, N)].

Standard experiments (needed to assign values to these parameters) are discussed in Appendix A. The remainder of this chapter is dedicated to providing further details about the three key functions f_c, f_f, and Γ used in Kayenta.

The cap function, f_c

Under compression, the pores in a material can irreversibly collapse, thereby resulting in permanent (plastic) volume changes when the load is removed. Plastic volume changes can occur for porous media even if the matrix material is plastically incompressible. Permanent volume changes can also occur if a material undergoes an irreversible phase transformation. Kayenta supports plastic volume changes, but it does so without explicitly modeling the underlying microphysical mechanisms. Nonetheless, Kayenta does reflect the influence of micromechanical theory by phenomenologically incorporating plastic volume changes observed in hydrostatic loading. To motivate Kayenta's cap theory, we will explain the equations and their qualitative features in the context of porosity, but keep in mind that any other microphysical compactive mechanisms are equally well accommodated by the phenomenological cap model.

The cap function f_c accounts for the presence of pores in a material by controlling where the yield function will intersect the $\overline{I_1}$ axis in compression. This intersection point corresponds to $J_2 = 0$ and, because we are considering compressive states, we will denote the value of $\overline{I_1}$ at the intersection point by $\overline{I_1} = \overline{X}$, where $\overline{X}/3$ is the pressure (positive in compression) at which inelastic deformation commences in *purely hydrostatic* loading for a given level of porosity. As voids compress out, the value of $\overline{X}$ will change, as explained later when we discuss the evolution equations for Kayenta's internal state variable κ. Porosity also degrades material *shear* strength because, recalling Eq. (4.28), the cap function effectively reduces the nonporous yield strength, defined previously by the fracture function f_f.

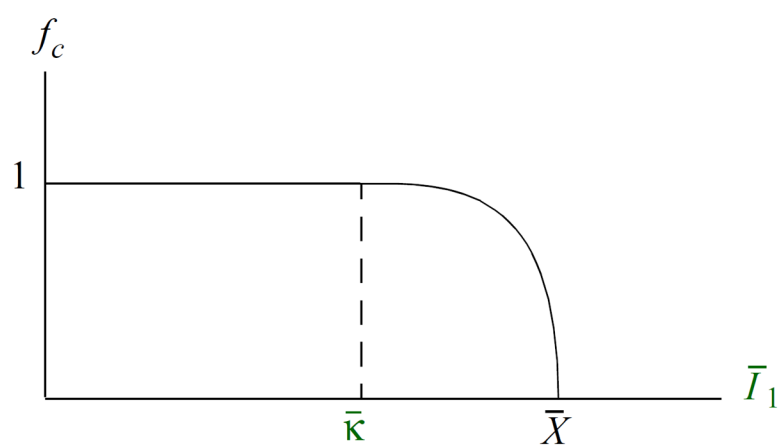

Figure 4.5. Kayenta cap function

Kayenta employs a cap function[7] defined

$$f_c^2(\overline{I_1},\overline{\kappa}) = \begin{cases} 1 & \text{if} \quad \overline{I_1} < \overline{\kappa} \\ 1 - \left(\frac{\overline{I_1}-\overline{\kappa}}{\overline{X}-\overline{\kappa}}\right)^2 & \text{otherwise.} \end{cases} \tag{4.30}$$

Neither $\overline{\kappa}$ nor $\overline{X}$ are user-supplied material parameters. Instead, these variables are computed internally within Kayenta code by enforcing consistency with more intuitive user-supplied parameters obtained from hydrostatic testing (see page 81).

The equation of the elliptical portion of the cap curve is

$$f_c^2 + \left(\frac{\overline{I_1}-\overline{\kappa}}{\overline{X}-\overline{\kappa}}\right)^2 = 1. \tag{4.31}$$

The intersection point $\overline{X}$ will be later related to the value of $\overline{\kappa}$ so that knowledge of the internal state variable $\overline{\kappa}$ will be sufficient to compute a value for $\overline{X}$. For now, while describing the geometry of the yield surface, both $\overline{\kappa}$ and $\overline{X}$ should be regarded as internal state variables whose values are computed internally in Kayenta using evolution equations discussed later. Rather than using f_c directly, recall that Kayenta uses the function F_c that is simply the square of f_c given in Eq. (4.30):

$$F_c = f_c^2. \tag{4.32}$$

Elastic-plastic coupling

The cap model is used when the material being studied contains enough porosity (or highly compliant second phase inclusions) so that inelastic volume reduction becomes possible through irreversible reduction of void space. Intuitively, one might expect the elastic moduli to stiffen as voids collapse, but the material might actually become more elastically compliant as shown in Fig. 10.4 (a phenomenon that might be explained, for example, by rubblization of a ligament network). Regardless of its microphysical origins, the elastic moduli are permitted to vary with plastic strain by generalizing the nonlinear elastic moduli expressions in Eq. (4.9) and Eq. (4.10) to

$$K = f_K \left\{ \left[b_0 + b_1 \exp\left(-\frac{b_2}{|I_1|}\right)\right] - b_3 \exp\left(-\frac{b_4}{\left|\overline{\varepsilon_v^p}\right|}\right) \right\} \tag{4.33}$$

$$G = f_G \left\{ g_0 \left[\frac{1 - g_1 \exp(-g_2\sqrt{J_2})}{1-g_1} \right] - g_3 \exp\left(-\frac{g_4}{\gamma^p_{\text{equiv}}}\right) \right\}. \tag{4.34}$$

In the absence of joints, the scale factors f_G and f_K equal 1.0; otherwise, they are computed internally within Kayenta as described in a separate sequel report [20]. In the above equations,

[7] evaluated in the code by a Pelessone [72] function, $f_c^2(\overline{I_1},\overline{\kappa}) = 1 - \frac{(\overline{I_1}-\overline{\kappa})(\left|\overline{I_1}-\overline{\kappa}\right|+(\overline{I_1}-\overline{\kappa}))}{2(\overline{X}-\overline{\kappa})^2}$

γ^p_{equiv} is the equivalent plastic shear strain (which, for proportional loading,[8] is conjugate to the equivalent shear stress, $\sqrt{J_2}$), and $\overline{\varepsilon^p_v}$ is the plastic compaction volume change. Mathematically,

$$\gamma^p_{\text{equiv}} = \int \sqrt{2}\|\underset{\approx}{\dot{\gamma}}^p\|\mathrm{d}t \tag{4.35}$$

$$\overline{\varepsilon^p_v} = \int \mathrm{tr}(\underset{\approx}{\dot{\varepsilon}}^p)\mathrm{d}t. \tag{4.36}$$

Though defined mathematically as stated, Kayenta computes the plastic volume change, $\overline{\varepsilon^p_v}$ indirectly, as explained later in the context of Eq. (4.69).

Meridional shear limiter function, F_f

In a loose sense, the previous sub-section (page 62) described Kayenta's cap function f_c by considering a material that contained pores, but no cracks. In this sub-section, we describe Kayenta's fracture function f_f by considering a material that contains microcracks *but no porosity*. Numerous microphysical analyses (as well as a preponderance of data) suggest that, for microcracked media, the onset of "yield" depends on all three stress invariants, which implies that the yield function for microcracked media must depend on all three cylindrical Lode coordinates. Kayenta supports this singularly common prediction of microscale damage theory. Though they differ in specific details, microphysical damage theories and laboratory observations for brittle materials also tend to share the following qualitative features:

- At a given mean stress, yield in triaxial extension (TXE) occurs at a lower stress than in triaxial compression (TXC), which implies that octahedral yield profiles are generally triangular (or distorted hexagon) in shape, with the triangle apex being located on TXC axes, as sketched in Fig. 1.1(c) (pg. 19).
- Brittle materials are very weak in tension. This implies that the meridional yield profile will include few if any tensile stress states. Brittle materials are also vulnerable to shear cracking at low pressures, but they become able to support increasingly large shear stresses as pressure is increased because friction at crack faces helps reduce the shear load that must be suffered by the matrix material itself. Thus, in the absence of porosity, the meridional profile is expected to monotonically increase with pressure.
- When microscale theories regard brittle crack fracture to be the *only* failure mechanism, they predict that the material strength (i.e., the Lode radius at failure) will increase monotonically with increasing pressure, so that the meridional profile expands in an ever-expanding

[8] Proportional loading is a movement of stress through stress space along a stratight-line trajectory. Mathematically, the stress varies with time according to $\underset{\approx}{\sigma}(t) = \underset{\approx}{\mathbf{C}} + \beta(t)\underset{\approx}{\mathbf{K}}$ in which $\underset{\approx}{\mathbf{C}}$ and $\underset{\approx}{\mathbf{K}}$ are constant tensors, and $\beta(t)$ is a time-varying scalar loading parameter. Consider, for example, an experiment involving an initial hydrostatic pre-stress pressure p, following by axial loading in which the lateral stresses are held constant at the prestress pressure while the axial stress $\sigma_A(t)$ varies with time. This is proportional loading for which $\underset{\approx}{\mathbf{C}} = -p\,\mathrm{DIAG}[1,1,1]$ for the constant initial pre-stress, $\underset{\approx}{\mathbf{K}} = \mathrm{DIAG}[1,0,0]$ for the axial loading direction, and $\beta(t) = \sigma_A(t) + p$ for the changing axial stress.

cone-like shape like the limit surface in Fig. 1.2. Microphysical idealizations such as Mohr-Coulomb theory predict the meridional profile is a straight line whose slope is directly related to the friction coefficient. When microscale theories allow for both crack growth and ductility of the matrix material, they predict that the increase in strength from friction will continue only until ductile yield (at extraordinarily high pressures) becomes more likely; such theories correspond to a meridional yield profile that is cone-like at low to moderate pressures but asymptotes to a zero slope (like a von Mises cylinder) at high pressures.

Given the wide variety of microscale predictions for the meridional profile, Kayenta is equipped with a four-parameter exponential spline that is capable of replicating any of these microphysical idealized theories, as well as actual observed material yield and rupture response at low and moderate pressures (i.e., at pressures well below the cap elastic limit) so that observed data primarily reflect microcrack damage rather than combined cracking with pore collapse (covered elsewhere in this report).

In the meridional plane (i.e., at a given value of the Lode angle), the **yield surface** characterizes the transition boundary for inelastic flow. Stress states that were, at one time, outside the yield surface might become realizable through hardening evolution of the yield surface. However, the allowable amount of hardening is not unbounded. At some point, the material will fail catastrophically (i.e., rupture). Often, the stress at rupture is *smaller* than the peak stress. Stress-strain curves might or might not exhibit post-peak softening, depending on whether or not the experiment is stress-controlled or strain-controlled.

The peak stress (not the stress at rupture) defines the stress-carrying limit of the material. As first mentioned on page 24, the **limit surface** is the boundary of all stress states that the material is *capable* of supporting. Many of these achievable stress states can be reached only through inelastic processes. Appendix A (STEP 4 on page 220) describes in detail how to determine the limit surface from experimental data. Mathematically, the limit surface is characterized by a limit function that is similar in form to the yield function. Specifically, the limit surface is defined by $F(\underset{\approx}{\sigma}) = 0$, where

$$F(\underset{\approx}{\sigma}) = J_2(\underset{\approx}{\sigma}) - \frac{F_f^2[I_1(\underset{\approx}{\sigma})]}{\Gamma^2[\overline{\theta}(\underset{\approx}{\sigma})]}. \tag{4.37}$$

The limit function $F(\underset{\approx}{\sigma})$ depends *only* on $\underset{\approx}{\sigma}$, not on any internal state variables. A yield function $f(\underset{\approx}{\sigma}, \underset{\approx}{\alpha}, \kappa)$, on the other hand, depends on the backstress tensor $\underset{\approx}{\alpha}$ and on the scalar internal state variable κ. Unlike a yield surface, which can evolve over time because it depends on time-varying internal state variables, the limit surface is *fixed* in stress space. The yield function is presumed to share some qualitative features with the shear limit surface, but depends additionally on internal state variables as follows:

$$f(\underset{\approx}{\sigma}, \underset{\approx}{\alpha}, \kappa) = J_2(\underset{\approx}{\xi}) - \frac{\left\{F_f[I_1(\underset{\approx}{\sigma})] - N\right\}^2 F_c(I_1(\underset{\approx}{\sigma}), \kappa)}{\Gamma^2[\overline{\theta}(\underset{\approx}{\xi})]}, \text{ where } \underset{\approx}{\xi} \equiv \underset{\approx}{\mathbf{S}} - \underset{\approx}{\alpha}. \tag{4.38}$$

When examining experimental data, it is generally easier to determine the maximum limit point than the point at which plasticity first begins. Consequently, Kayenta provides an empirical fitting function F_f for the limit surface in the meridional plane, and the initial meridional yield surface is simply $F_f - N$, reduced perhaps by a cap function F_c if the material initially contains voids. Comparing Eq. (4.38) with Eq. (4.37) reveals that the yield surface inherits its octahedral profile shape (i.e., its Lode angle dependence) from the limit surface. The *size* of the yield octahedral profile is generally smaller than the limit surface profile because of the multiplier (cap) function F_c, which represents the effect of porosity. The yield surface origin is also offset from the limit surface origin by an amount governed by the kinematic hardening backstress tensor $\underset{\approx}{\alpha}$. The limit surface always has a [111] symmetry *axis passing through the actual (not kinematically shifted)* origin in stress space. When kinematic hardening is enabled, the yield surface has a symmetry axis parallel to [111] that is off-set so that it does *not* pass through the origin.

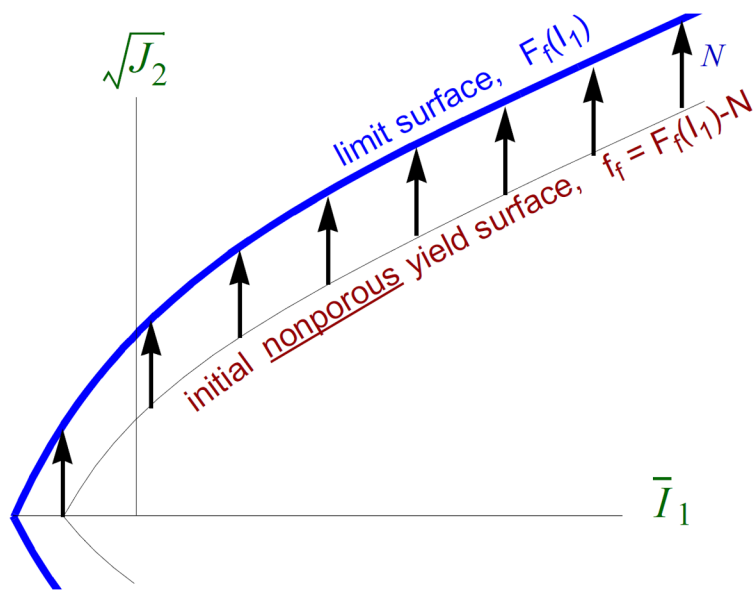

Figure 4.6. Kinematic hardening. The user defines parameters (a_1, a_2, a_3, a_4) for the *ultimate* shear limit surface. The initial yield surface is identical except shifted down by a user specified amount N. Kinematic hardening allows the initial yield surface to translate until reaching the ultimate failure surface (at which point, the host code must initiate "element death" or preferably microphysically justifiable strategy for supporting macroscale softening.

When advancing the solution, the initial meridional profile can harden kinematically and/or isotropically. The equations governing yield surface evolution are designed to permit only a limited amount of hardening. As sketched in Fig. 4.6, the initial yield surface is permitted to translate upward in the meridional plane by no more than a user-specified limit N.

When the yield surface has reached the limit surface *and when the stress itself lies on the limit surface*, the material will begin to soften. At that point, a *constitutive-level* description of material response no longer remains possible; the host code must intervene by inserting void or by invoking special elements capable of supporting displacement discontinuities or by accounting for statistical variability and scale effects as described on page 109. The limit surface marks the point at which a continuum material model is inadequate to characterize macroscale material response because softening localization becomes possible. Before reaching the limit surface, material response is handled entirely by Kayenta with no need for host code intervention.

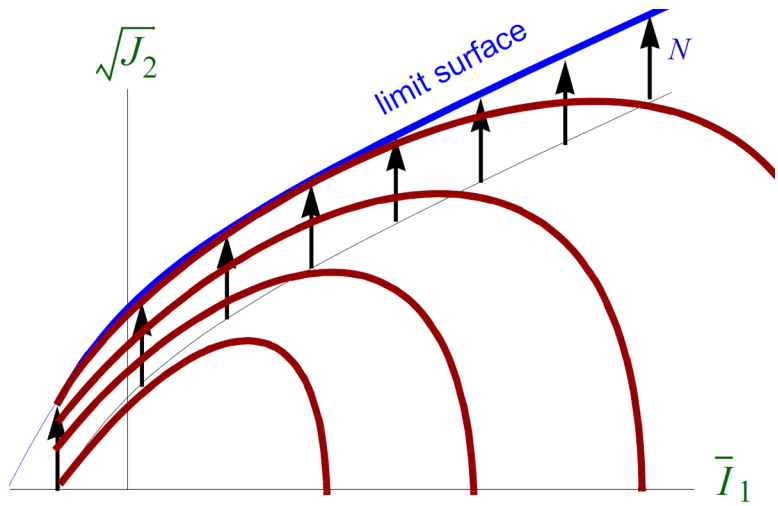

Figure 4.7. Yield surface evolution with both microcracking and porosity. For real materials, that contain both cracks and voids, it is difficult to identify a single envelope for the combined porous/cracked fracture yield function f_f. However, ultimate failure data can be more readily mapped out.

The shifted shear limiter function $F_f(I_1) - N$ defines how the shear stress at yield varies with pressure for a *nonporous*, but microcracked, material in its initial (virgin) state. When this microcrack yield function is combined with the cap function $F_c(I_1, \kappa)$ the actual shear stress at yield is further reduced because porosity makes inelasticity possible even for purely hydrostatic compression (i.e., loading along the $\overline{I_1}$ axis). Kayenta evolves this combined porous yield function in such a way that the yield surface grows up to the limit surface.

Kayenta's behavior *after* reaching the limit surface depends on the value of the user control parameter "**SOFTENING**". Properly, the host code should allow scale-dependent softening and localization as discussed on page 109. If **SOFTENING** $= 0.0$, then Kayenta will treat the limit surface as if it were a nonhardening yield surface (making its post-peak predictions robust and mesh insensitive but probably not realistic). This option is used in many of the Kayenta verification tests where softening is not desired (and nonhardening analytical solutions are available). If **SOFTENING** > 0.0, then Kayenta will allow the material to soften as described in Chapter 5 on

page page 99.

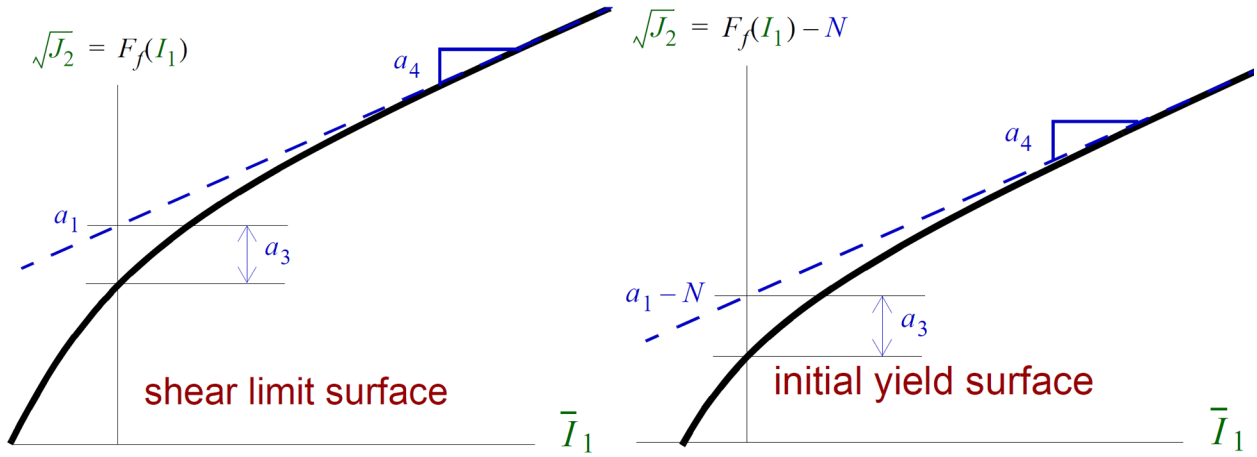

Figure 4.8. Shear limiter function (unshifted and shifted). The shifted function should be regarded as a nominal shape of the yield surface in the meridional plane, although porosity further lowers and distorts the meridional yield profile by multiplying the shifted shear limit function by F_c.

Kayenta supports modeling microcracked material by providing flexible fitting functions that can reproduce octahedral and meridional yield profiles observed for real materials. In particular, the shear limit function used in Kayenta is of the form

$$\boxed{F_f(I_1) = a_1 - a_3 e^{-a_2 \overline{I_1}} + a_4 \overline{I_1}}, \text{ where } \overline{I_1} = -I_1 \qquad \textbf{shear limit surface in TXC.} \tag{4.39}$$

where the a_k are user-specified material parameters determined from experimental data as explained in Appendix A. The initial (nonporous) meridional yield profile is

$$f_f(I_1) = F_f(I_1) - N \qquad \textbf{initial yield surface (non-porous).} \tag{4.40}$$

where N is the user-specified shift parameter. Therefore, $a_1 - N$ is the zero pressure intercept of the nonporous meridional yield surface on the $\sqrt{J_2^{\xi}}$ axis. Frequently, N is taken to be zero. The shear limiter function, Eq. (4.39), asymptotes to a linear envelope, as indicated in Fig. 4.8. To force the material to obey a von-Mises type yield response at extremely high pressures, the slope coefficient a_4 is merely set to zero.

Let us now explain why the shear limiter function has the general shape depicted in Fig. 4.8. Then we will list constraints on the model parameters necessary to achieve this shape. Brittle materials fail at very low shear stresses when the pressure is low, but they are able to sustain higher levels of shear stress without failing if loaded under higher confining pressures. Consequently, the shear limiter function is expected to increase monotonically with pressure. Or, since $\overline{I_1}$ is

proportional to the pressure, F_f is expected to increase monotonically with $\overline{I_1}$. Furthermore, a fundamental tenant from plasticity theory is that the yield function must be semi-convex, which implies that the second partial derivative of $F_f(I_1)$ must be negative or zero. When we speak of the "shear" stress at failure, we are effectively speaking of the value of the Lode radius at failure corresponding to the Lode angle for the stress state. For any cylindrical coordinate system — including the Lode system — the radius must always be non-negative and therefore F_f is defined only over the domain for which it yields positive values. Finally, in its virgin state, any material should be unfailed at zero stress, which means that the origin must fall below the meridional yield profile. All of these physical considerations lead to the following constraints on allowable values for the parameters:

$$a_1 - a_3 - N \geq 0 \qquad \text{unloaded virgin material must be below yield} \tag{4.41a}$$

$$a_2 a_3 + a_4 \geq 0 \qquad \text{non-negative slope at low pressures} \tag{4.41b}$$

$$a_2 \geq 0 \qquad \text{convexity condition} \tag{4.41c}$$

$$a_3 > 0 \qquad \text{positive Lode radius} \tag{4.41d}$$

$$a_4 \geq 0 \qquad \text{non-negative slope at high pressures.} \tag{4.41e}$$

Specific values for these model parameters are determined from triaxial test data, as explained in Fig. 3.3 (pg. 39) (and in Fig. A.4 and Fig. A.5 of Appendix A). Sample fits of Kayenta's shear limit function to data can be found in Fig. 10.1 (pg. 196) and Fig. 10.5 (pg. 200). Incidentally, $a_2 a_3 + a_4 < 1/\sqrt{3}$ for most materials ($1/\sqrt{3}$ is typical for sand). In some cases (as when using automatically determined third-invariant dependence of the model), the lower bound in Eq. (4.41b) is additionally subjected to an upper bound based on the slope for triaxial compression in Fig. 3.3: namely, $a_2 a_3 + a_4 \leq 1/\sqrt{3}$ (this condition, when needed, is imposed by over-riding user-prescribed values for the principal stress cutoff parameter **CUTPS**).

The complete Kayenta yield function

Eq. (4.28) is the yield *criterion*. The yield *function* f must be negative for all elastic states (inside the yield surface), zero for all stress states satisfying the yield criterion (on the yield surface), and positive for all stress states (outside the yield surface) that cannot be reached except through an inelastic process — if at all. For computational reasons, Kayenta's yield function is based on the square of Eq. (4.28):

$$f = \Gamma^2(\overline{\theta}^{\xi}) J_2^{\xi} - f_f^2(I_1) f_c{}^2(I_1, \kappa). \tag{4.42}$$

When kinematic hardening is used, the stress invariants, $\overline{\theta}^{\xi}$ and J_2^{ξ}, are those for the kinematically shifted stress tensor, $\underset{\approx}{\xi} \equiv \underset{\approx}{\mathbf{S}} - \underset{\approx}{\alpha}$. Otherwise, when kinematic hardening is disabled, these are simply the stress invariants. Of course, $I_1$is the first invariant I_1^{σ} of the stress tensor $\underset{\approx}{\sigma}$. (Since backstress $\underset{\approx}{\alpha}$ is deviatoric, $I_1^{\xi} = 0$).

The building block functions f_f and f_c are implemented in Kayenta in a slightly altered form by being expressed in terms of the shear limit function F_f and an alternative (computationally more

efficient) cap function F_f:

$$f_f(I_1) = F_f(I_1) - N \tag{4.43}$$

$$f_c(I_1;\kappa) = \sqrt{F_c(I_1,\kappa)}. \tag{4.44}$$

The first of these equations allows the user to specify a maximum amount, N, that the yield function is permitted to translate under kinematic hardening. Thus, the function F_f can be regarded as a "limit" or "softening" envelope, beyond which stresses can *never* be reached quasistatically (not even via hardening). The second equation recasts the f_c function as the square root of a different function F_c for computational reasons. The second equation also shows explicitly the presence of the internal state variable κ related to the isotropic hardening part of Kayenta associated with void collapse. The internal state variable κ marks the branch point where combined porous/cracked yield surface deviates from the nonporous yield surface. As explained on page 81, this branch point is determined internally within Kayenta in a manner that ensures consistency with measured hydrostatic data.

In terms of the new building block functions, the critical Lode radius in triaxial compression (TXC), where $\Gamma(\overline{\theta}) = 1$, may be expressed as a function of the Lode axial coordinate z as

$$r^{\mathrm{TXC}} = \sqrt{2}\left[(F_f(\sqrt{3}z) - N)\sqrt{F_c(\sqrt{3}z,\kappa)}\right]. \tag{4.45}$$

Plotting r^{TXC} vs. z (at a given value of κ) will produce a *geometrically accurate* visualization of the meridional yield profile. Often we instead plot $\sqrt{J_2}$ vs. $\overline{I_1}$ to label the axes with more broadly recognized stress measures, but in doing so we are actually showing a geometrically distorted view of the yield profile, as explained on page 46.

Substituting Eq. (4.43) and Eq. (4.44) into Eq. (4.42) gives the yield criterion cited at the beginning of this section [Eq. (4.18)].

The "J3TYPE" Lode-angle function, Γ

This section describes available functional forms for the Lode angle dependence function $\Gamma(\overline{\theta})$. This function controls the shape of the octahedral yield profile. Since this function controls only the *shape*, not size, of the octahedral profile, its magnitude is inconsequential. The Γ function is normalized to equal unity in TXC ($\overline{\theta} = +30°$).[9] At other Lode angles, $\Gamma(\overline{\theta}) > 1$. Thus, since $\Gamma(\overline{\theta})$ appears in the yield function as a *multiplier* of J_2^{ξ}, it acts as a pseudo stress *raiser*, causing yield to occur at smaller values of J_2 at Lode angles differing from the fiducial (TXC) angle where $\Gamma(\overline{\theta}) = 1$. To ensure convexity of the octahedral yield profile, the Lode angle function must satisfy

$$\Gamma''(\overline{\theta}) + \Gamma(\overline{\theta}) \geq 0. \tag{4.46}$$

A hallmark trait of rocks and rock-like materials (concrete, ceramics, etc.) is a higher strength in triaxial compression than in triaxial tension at any given mean pressure. Loosely speaking, this

[9] With this normalization, the f_f meridional function then quantifies the pressure-varying *size* of octahedral profiles

characteristic results from friction at crack faces being able to carry a larger portion of the load under compression, therefore sparing the surrounding matrix material from having to carry the entire resolved shear stress at crack tips. Classical Mohr-Coulomb theory, which is supported by Kayenta primarily for comparisons with idealized analytical solutions, has an octahedral profile in the shape of a distorted hexagon, causing considerable computational difficulties when dealing with the vertices. The computational attractiveness of removing yield surface corners has motivated numerous proposals of smoothed three-invariant models for frictional materials [4, 10, 60, 67, 98], and Lade [59] was among the first efforts to additionally include curvature in the meridional plane. According to Borja, et al. [9], there is evidence that smoothed yield surfaces capture mechanical response more accurately than vertex models, but these authors point to no data to back up this claim. Kayenta presently supports three yield-type options (specified by a value of 1, 2, or 3 for the user parameter, **J3TYPE**):

1. Gudehus (an efficient smoothed profile, with restrictions on convexity)

$$\Gamma(\overline{\theta}) = \frac{1}{2}\left[1 + \sin 3\overline{\theta} + \frac{1}{\Psi}(1 - \sin 3\overline{\theta})\right].$$

   To satisfy the convexity requirement of Eq. (4.46), the strength ratio must be between $\frac{7}{9} < \Psi < \frac{9}{7}$.

2. Willam-Warnke (a relatively inefficient smooth profile with no convexity constraints)

$$\Gamma(\overline{\theta}) = \frac{4(1-\Psi^2)\cos^2\alpha^* + (2\Psi-1)^2}{2(1-\Psi^2)\cos\alpha^* + (2\Psi-1)\sqrt{4(1-\Psi^2)\cos^2\alpha^* + 5\Psi^2 - 4\Psi}},$$

   where $\alpha^* = \frac{\pi}{6} + \overline{\theta}$. The Willam-Warnke option is convex for $\frac{1}{2} \leq \Psi \leq 1$

3. Mohr-Coulomb (distorted hexagon polygon)

$$\Gamma(\overline{\theta}) = \frac{2\sqrt{3}}{3 - \sin\Phi}\left(\cos\overline{\theta} - \frac{\sin\Phi\sin\overline{\theta}}{\sqrt{3}}\right).$$

   Here, the **internal friction** angle Φ is the angle of the failure envelope in the Mohr-diagram ($\tan\Phi = \mu$, where μ is the coefficient of friction). Within Kayenta, Φ is determined from the user-supplied strength ratio by $\sin\Phi = 3\frac{1-\Psi}{1+\Psi}$. The Mohr-Coulomb option is convex for $\frac{1}{2} \leq \Psi \leq 2$.

4. Automatic selection of the pressure-dependent strength ratio. If Ψ is set $= -1$, then any value for **J3TYPE** is ignored and instead the octahedral profile is defined by the Willam-Warnke function with a pressure -dependent strength ratio. Specifically, the strength ratio is set to be coupled to TXC meridional profile slope according to Eq. (B.19).

The Gudehus and Willam-Warnke options both correspond to fully differentiable yield functions (no vertices). The Mohr-Coulomb option (which is available principally for comparisons

with analytical solutions) is differentiable everywhere except at triaxial states where yield surface vertices require special numerical handling.[10]

Recognizing logistical constraints of most laboratories, Kayenta presumes that experimental data are available *at most* only for a limited number of canonical loading paths: perhaps triaxial extension ($\overline{\theta} = -\pi/6$), perhaps simple shear ($\overline{\theta} = 0$), and almost certainly triaxial compression ($\overline{\theta} = \pi/6$). Regardless of which yield-type (Gudehus, Willam-Warnke, or Mohr-Coulomb) is selected, the shape of the octahedral yield profile is described, in part, by user specification of a parameter Ψ, equal to the **triaxial extension/compression (TXE/TXC)** strength ratio at a given pressure. Kayenta presumes that only the *size* of the octahedral yield profile — not its shape — varies with pressure. Consequently, the strength ratio Ψ equals its user-specified value at all pressures and throughout the entirety of the simulation (i.e., Ψ is a *constant*, not a time varying internal state variable). Appendix A gives instructions for inferring a value of Ψ from experimental data.

These three options are distinguished by how the octahedral yield profile varies in stress space in the transition from TXE to simple shear to TXC at a fixed pressure. Graphs of the octahedral yield profile corresponding to any of the above options may be constructed by parametrically plotting

$$x = r\cos\overline{\Theta} \qquad\qquad y = r\sin\overline{\Theta} \tag{4.47}$$

$$\text{Here,} r = \frac{\sqrt{2}}{\Gamma(\overline{\theta})}, \qquad \text{where} \qquad \overline{\theta} = \frac{1}{3}\arcsin(\sin 3\overline{\Theta}). \tag{4.48}$$

The angle $\overline{\Theta}$ varies from 0 to 360°, and therefore $\overline{\theta}$ varies between $-30°$ and $+30°$.

As illustrated Fig. 4.9, the Mohr-Coulomb model (**J3TYPE** = 3) interpolates linearly in *octahedral stress space*, resulting in a distorted hexagon if $\frac{1}{2} < \Psi < 1$, a perfect hexagon (Tresca) if $\Psi = 1$, and a triangle if $\Psi = \frac{1}{2}$. For a detailed explanation of the Mohr-Coulomb formulation, see Appendix B (page 229). The Mohr-Coulomb model has yield surface vertices at $\overline{\theta} = \pm\pi/6$, which results in extra computational effort to determine plastic strain rates in triaxial states. The Gudehus and Willam-Warnke options, on the other hand, involve no yield surface vertices, which speeds up computations. The Gudehus option is the default because of its computational simplicity, but it supports only a limited range of TXE/TXC strength ratios, the Willam-Warnke option should be used if a rounded but strongly triangular octahedral yield profile is desired. Appendix A (step 6) provides guidance for selecting the Lode angle option most appropriate for matching experimental data.

Kayenta subsumes many simpler (classical) models as special cases. For example, if failure is hypothesized to occur when the largest principal stress (or strain) reaches a critical value, then the octahedral yield profile will be a triangle. If, on the other hand, failure is presumed when the equivalent shear stress reaches a critical value, independent of the Lode angle (like a von Mises or Drucker-Prager criterion), then the octahedral yield profile is a circle, which can be modeled with

[10] Kayenta averages directions on either side of the vertex if the strain rate points within the limiting (Koiter) fan of unit normals. If the strain rate points within a sextant of the octahedral plane, then the normal in that sextant is used.

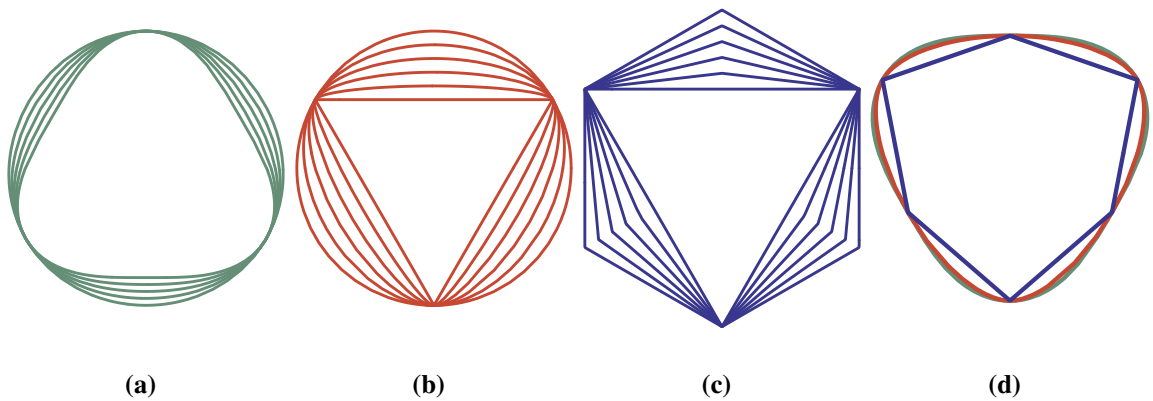

Figure 4.9. Octahedral yield profiles, plotted at allowable values of the strength ratio. (a) *Gudehus*, **J3TYPE** = 1, (b) *Willam-Warnke*, **J3TYPE** = 2, (c) *Mohr-Coulomb*, **J3TYPE** = 3, (d) *Comparison*. The comparison plot corresponds to a strength ratio of $\Psi = 0.8$. The $\Gamma(\overline{\theta})$ function is defined so that all models return a value of 1 in triaxial compression

the Gudehus option. As a rule, any classical failure criterion that is expressed directly in terms of the principal stresses will imply an appropriate **J3TYPE** option (and an appropriate value for the TXE/TXC ratio), but such criteria will *also* imply functional constraints on the meridional failure function f_f as well, which requires appropriate Kayenta inputs to mimic. Simplified Kayenta input sets, corresponding to these classical special-case idealized theories may be found at the end of Appendix B.

Octahedral profile plots like the ones shown in Fig. 4.9 are most illuminating from a qualitative perspective. However, for parameterizing Kayenta to quantitative laboratory data, simple plots of Γ vs. $\overline{\theta}$ are more useful. Fig. 4.11 shows the $\Gamma(\overline{\theta})$ functions for each of the **J3TYPE** options. In all cases, the lower bound on Γ is 1.0 at TXC.

Advancing the solution (groundwork discussion)

So far, we have discussed how some microphysically based, but generally oversimplified theories can be used to predict *theoretical* shapes of yield or failure surfaces. Kayenta implicitly captures microscale phenomena by using *macroscale* measurable variables in phenomenological manner. Direct use of idealized theories would require initializing and evolving microscale quantities (such as porosity) that are impractical to measure in the laboratory. Therefore, the algebraic *structure* of functions used in Kayenta is guided by idealized microscale theories, but recast in terms of directly measurable macroscopic variables. Simplified failure criteria help guide choices for interpolation functions to be fitted to real *observed* data that likely reflect the specific phenom-

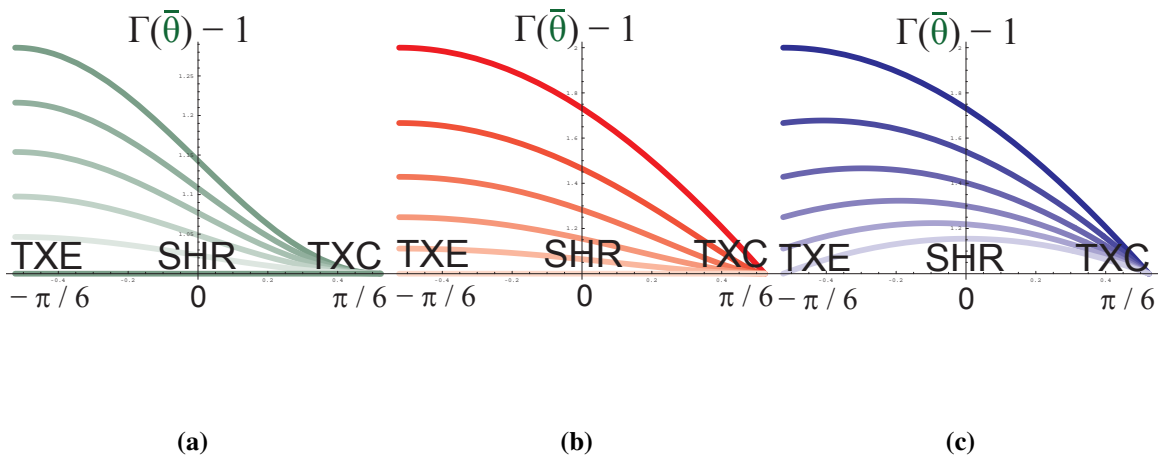

Figure 4.10. Lode angle function (for various y strength ratios) plotted vs. the Lode angle varying from 30° **(TXE) to** $+30^\circ$ **(TXC).** The larger the value of Γ, the smaller the radial distance to the octahedral yield profile and therefore the smaller the shear failure strength. The Gudehus (a) and Willam-Warnke (b) options both predict lowest strength (largest value of Γ) at TXE, whereas Mohr-Coulomb (c) theory predicts lowest strength at an intermediate Lode angle somewhere between TXE and TXC. For example, when $\Psi = 1$, Mohr-Coulomb theory reduces to Tresca theory and the lowest strength (highest Γ) occurs at the zero Lode angle (pure shear).

ena considered in microscale idealizations and possibly some other "unknown" sources of inelastic flow.

Microphysical theories are also used to guide how Kayenta treats the partitioning of inelastic flow, once it begins. For example, most theories of inelastic flow (including Kayenta) presume that the total strain rate $\dot{\underset{\approx}{\varepsilon}}$ can be partitioned additively as

$$\dot{\underset{\approx}{\varepsilon}} = \dot{\underset{\approx}{\varepsilon}}^e + \dot{\underset{\approx}{\varepsilon}}^p, \tag{4.49}$$

where $\dot{\underset{\approx}{\varepsilon}}^e$ represents the elastic (or recoverable) part of the strain rate and $\dot{\underset{\approx}{\varepsilon}}^p$ denotes the "plastic" part of the strain rate. More correctly, $\dot{\underset{\approx}{\varepsilon}}^p$ represents the *inelastic* strain rate, which reflects contributions from any and all sources of inelastic material response. Many classical theories presume that the *direction* of the plastic strain rate is parallel to the normal to the yield surface. In this case, since the normal to the yield surface can be obtained by the gradient of the yield function $f(\underset{\approx}{\sigma}, \underset{\approx}{\alpha}, \kappa)$, the plastic part of the strain rate is presumed to be of the form

$$\dot{\varepsilon}^p_{ij} = \dot{\lambda} \left(\frac{\partial f}{\partial \sigma_{ij}} \right)_{\underset{\approx}{\alpha}, \kappa}, \tag{4.50}$$

where $\dot{\lambda}$ is a multiplier (called the **consistency parameter**) determined by demanding that the stress must remain on the yield surface during inelastic loading. The subscripts on the partial derivative merely indicate that the internal state variables are held constant. When the plastic strain rate direction is determined from the stress gradient of the yield function, as shown here, the model is said to be "associative" (to indicate that the plastic strain rate is associated with the yield function[11]).

While Kayenta does support associativity at user request, many researchers report that normality tends to over-predict the amount of volumetric plastic strain [82]. Therefore, *non*-normality is supported in Kayenta as well. For non-normality, the user specifies a **flow function** $g(\underset{\approx}{\sigma}, \underset{\approx}{\alpha}, \kappa)$ such that[12]

$$\dot{\varepsilon}^p_{ij} = \dot{\lambda} \left(\frac{\partial g}{\partial \sigma_{ij}} \right)_{\underset{\approx}{\alpha}, \kappa}. \tag{4.51}$$

The above references to a yield function or flow function suffer a conceptual shortcoming that neither of these functions is unique [12]. For example, a von Mises yield function can be

[11] For materials that exhibit elastic-plastic coupling, the terms "associativity" and "normality" can have distinct meanings, depending on whether the portion of the total strain rate attributable to rates of elastic moduli is absorbed into the elastic strain rate or the inelastic strain rate. When the coupling terms (from *rates* of elastic moduli) are incorporated into the inelastic strain rate, normality and associativity are *not* interchangeable terms. If the coupling terms are incorporated into the elastic strain rate, then associativity and normality are interchangeable, but at the cost that the elastic strain rate ceases to be an exact differential with respect to deformation.

[12] While considerable data does exist to *suggest* that the inelastic strain rate is *not* directed normal to the yield surface for some materials, such behavior is not well understood. The mathematical validity of assuming existence of a non-associated flow potential function has been called into question by Sandler, Rubin, and Pucik [74, 78]. Burghardt [26] has independently confirmed their assertions that such a model is inherently unstable, nonuniquely liberating energy from quiescent pre-stressed states. The instability arises from the fact that any classically non-associative model admits plastic waves that travel faster than elastic waves [19].

$f(\underset{\approx}{\sigma}) = \sqrt{(J_2)} - k$, where k is the yield stress in shear, or it may be written $f(\underset{\approx}{\sigma}) = J_2 - k^2$. Both of these functions have the same yield surface, which is the set of stress states satisfying $f(\underset{\approx}{\sigma}) = 0$, but these different yield functions have different gradients. Thus, neither the gradient $\partial f / \partial \underset{\approx}{\sigma}$ nor its magnitude $\mathscr{F} := \| \frac{\partial f}{\partial \sigma_{ij}} \|$ is unique. Despite the non-uniqueness of a yield function and its gradient, the *unit normal tensor*, defined by the *ratio* of these two expressions,

$$\underset{\approx}{\mathbf{N}} := \frac{\frac{\partial f}{\partial \sigma_{ij}}}{\mathscr{F}} \qquad \text{where} \qquad \mathscr{F} := \| \frac{\partial f}{\partial \sigma_{ij}} \| \tag{4.52}$$

is unique when evaluated at the yield surface.

Non-uniqueness issues are exacerbated with respect to the flow function since the gradient of the flow function is not usually even evaluated at a zero isosurface. Formally, in analogy to the above equation, we defined a unit flow direction tensor as

$$\underset{\approx}{\mathbf{M}} := \frac{\frac{\partial g}{\partial \sigma_{ij}}}{\mathscr{G}} \qquad \text{where} \qquad \mathscr{G} := \| \frac{\partial g}{\partial \sigma_{ij}} \| \tag{4.53}$$

With this definition, the flow model in Eq. (4.51) may be written as

$$\dot{\varepsilon}^p_{ij} = \dot{\lambda} \mathscr{G} M_{ij}. = \dot{\lambda}^* M_{ij}, \tag{4.54}$$

where we have introduced an alternative consistency parameter defined by

$$\dot{\lambda}^* = \dot{\lambda} \mathscr{G}. \tag{4.55}$$

This alternative consistency parameter is unique, and thus physically meaningful, despite the fact that it is the product of two factors ($\dot{\lambda}$ and $\mathscr{G}$) that are themselves nonunique. This is one of the key differences between Kayenta and its predecessor, the Sandia GeoModel. In the GeoModel, the plottable output variable called **DCSP** was equal to $\dot{\lambda}$. In Kayenta, the output variable of the same name is now $\dot{\lambda}^*$ and thus it has significant physical meaning: it is magnitude of the plastic strain rate tensor!

The first release of the Kayenta User's guide did not discuss issues associated with ambiguity of yield and flow function gradients. As indicated in [12], the nonuniqueness of a yield function does not produce a nonunique final result for updated field variables, but it is nevertheless helpful to instead phrase all equations in terms of the unique part of the yield function gradient (namely, the unit tensor in the direction of this gradient when it is evaluated on the yield surface). The conversion of the old notation to the new notation required, for example, required searching the old documentation for all occurances of $\frac{\partial f}{\partial \sigma_{ij}}$ and making the substitution $\frac{\partial f}{\partial \sigma_{ij}} = \mathscr{F} \underset{\approx}{\mathbf{N}}$, where $\mathscr{F}$ is the magnitude of the yield function gradient (nonunique) and $\underset{\approx}{\mathbf{N}}$ is the unit tensor in the direction of the yield function gradient (which is unique when evaluated on the yield surface). Similar substitutions were made to convert the old User Guide notation to the current version, as listed in Table 4.1

Table 4.1. Substitutions required to convert nonunique plasticity to unique values that can be compared between different codes

Conventional	Preferred
$\frac{\partial f}{\partial \underset{\approx}{\sigma}}$	$= \mathscr{F}\underset{\approx}{\mathbf{N}}$
$\left\Vert \frac{\partial f}{\partial \underset{\approx}{\sigma}} \right\Vert$	$= \mathscr{F}$
$\frac{\partial g}{\partial \underset{\approx}{\sigma}}$	$= \mathscr{G}\underset{\approx}{\mathbf{M}}$
$\left\Vert \frac{\partial g}{\partial \underset{\approx}{\sigma}} \right\Vert$	$= \mathscr{G}$
$\dot{\lambda}$	$= \frac{\dot{\lambda}^*}{\mathscr{G}}$
χ	$= \chi^* \mathscr{F}\mathscr{G}$
$\underset{\approx}{\mathbf{H}}_\alpha$	$= \underset{\approx}{\mathbf{H}}^*_\alpha \mathscr{G}$
h_κ	$= h^*_\kappa \mathscr{G}$

The plastic strain rate $\dot{\underset{\approx}{\varepsilon}}^p$ includes both deviatoric and isotropic parts. If the flow potential depends on the first invariant I_1, then applying Eq. (3.15), the *volumetric* plastic strain rate is

$$\dot{\varepsilon}^p_v = \mathrm{tr}\,\dot{\underset{\approx}{\varepsilon}}^p = \dot{\lambda}^*(\mathrm{tr}\underset{\approx}{\mathbf{M}}) \tag{4.56}$$

The plastic strain rate points normal to the isosurface $g = 0$.[13] If the flow function is associative, then the plastic potential function is identical to the yield function and the plastic strain rate will therefore point normal to the yield surface. Flow surface vertices reside at points where the flow potential is non-differentiable, in which case the plastic strain rate points within a "cone of limiting normals" (Koiter fan) at the vertex and is determined through additionally considering the trial elastic stress rate associated with the total strain rate.

In Kayenta, the functional form of g is the same as that of f, but with different values for material constants. Specifically, the flow potential g can be made to differ from the yield function by assigning values to a_2^{PF}, a_4^{PF}, R^{PF}, and Ψ^{PF} that differ from their counterpart parameters (a_2, a_4, R, Ψ) used to define the yield surface. For associativity, the potential function parameters should be given values identical to their counterparts in the yield function. Nonassociativity is included in Kayenta primarily as a "legacy" feature to allow Kayenta to emulate other classical plasticity models that use nonassociativity to match experimental data for which associativity "over predicts" the amount of plastic dilatation. As pointed out in [14], there are many ways that a constitutive model might *seem* to be nonassociative when, in fact, it is not. A sophisticated *associative* plasticity model can include features such as elastic-plastic coupling [65], thermo-plastic coupling [92], and/or induced anisotropy [64] that would make its predictions *seem* to be non-associative in the

[13] Because the current stress might not reside on the isosurface $g = 0$, Kayenta projects the stress to the nearest point on this isosurface. The need for such revisions is rarely recognized in plasticity programs (and casts doubt on the very notion flow potentials).

context of simpler models. Stated differently, experimental data that appear to be non-associative might actually be simply implying a need for more sophistication in the model used to interpret the data. These and additional cautions about tenuous phyisical foundations of non-associative plasticity are summarized in [18].

If continuing to apply elasticity theory would result in a predicted stress lying outside the yield surface, the governing equations are no longer elastic. At this point, the strain rate is decomposed into two parts, elastic plus plastic, as mentioned in Eq. (4.49). The stress rate is determined by applying elasticity. That is,

$$\dot{\sigma}_{ij} = C_{ijkl}\dot{\varepsilon}^{e}_{ij} = C_{ijkl}(\dot{\varepsilon}_{ij} - \dot{\varepsilon}^{p}_{ij}), \tag{4.57}$$

where C_{ijkl} denotes the isotropic tangent elastic stiffness tensor. In Eq. (4.57), our goal is to compute the stress *rate*. The current state is known, and therefore the instantaneous stress state and elastic moduli are known. In numerical implementations of constitutive models, the strain rate is known (it is provided by the host code after solution of the momentum equation). Thus, the only unknown in this equation is the plastic strain rate. Eq. (4.51) allows us to compute the *direction* of the plastic strain rate from the known instantaneous stress state. Thus, after substitution of Eq. (4.51) into Eq. (4.57), the stress rate can be written

$$\dot{\sigma}_{ij} = C_{ijkl}\dot{\varepsilon}^{e}_{ij} = C_{ijkl}\left[\dot{\varepsilon}_{ij} - \dot{\lambda}^{*}M_{ij}\right]. \tag{4.58}$$

Everything on the right-hand-side of this equation is known except the value of the consistency parameter, $\dot{\lambda}^{*}$.

A recent and fundamental change in Kayenta revises Eq. (4.58) to be instead

$$\dot{\sigma}_{ij} - \dot{\alpha}_{ij} = C_{ijkl}\dot{\varepsilon}^{e}_{ij} = C_{ijkl}\left[\dot{\varepsilon}_{ij} - \dot{\lambda}^{*}M_{ij}\right] \tag{4.59}$$

where α_{ij} are components of the backstress tensor. With this revision, the backstress becomes the center for elasticity as well as the center for the yield surface. This revision allows the yield surface to translate under kinematic hardening in such a way that zero stress might eventually become a point outside the yield surface, as observed in some laboratory experiments [25]. The documentation in this section continues to be based on the formulation in Eq. (4.58).

The consistency parameter is obtained by demanding that, not only must the stress be on the yield surface during plastic loading ($f = 0$), it must also *remain on the yield surface throughout a plastic loading interval*. Thus, $\dot{f} = 0$ during plastic loading. The yield function f depends on the stress, but it also depends on the isotropic hardening internal state variable, κ and (if applicable) on the kinematic hardening backstress state variable tensor α_{ij}. Thus, the assertion that $\dot{f} = 0$ can be written via the chain rule as

$$\dot{f} = \frac{\partial f}{\partial \sigma_{ij}}\dot{\sigma}_{ij} + \frac{\partial f}{\partial \kappa}\dot{\kappa} + \frac{\partial f}{\partial \alpha_{ij}}\dot{\alpha}_{ij} = 0. \tag{4.60}$$

The first term may be simplified through application of Eq. (3.14). The last two terms reflect the fact that the yield surface can evolve in shape and translate in stress space during inelastic loading.

Dividing both sides of Eq. (4.60) by $\mathscr{F}$ gives

$$N_{ij}\dot{\sigma}_{ij} + \frac{\frac{\partial f}{\partial \kappa}}{\mathscr{F}}\dot{\kappa} + \frac{\frac{\partial f}{\partial \alpha_{ij}}}{\mathscr{F}}\dot{\alpha}_{ij} = 0. \tag{4.61}$$

In what follows, we will present "evolution equations" that govern how the state variables change in response to plastic flow. It will be argued that the evolution of each internal state variable should be proportional to the plastic strain rate. Equivalently, these rates must be proportional to our unknown plastic consistency parameter $\dot{\lambda}^*$. By substituting Eq. (4.58) and these soon-to-be-derived evolution equations for the internal state variables into Eq. (4.60) we will be able to solve Eq. (4.60) for the consistency parameter $\dot{\lambda}^*$. Once the consistency parameter is known, it can be substituted into Eq. (4.58) to obtain the stress rate, which may then be integrated numerically to update the stress. With the consistency parameter $\dot{\lambda}^*$ known, then *rates* of internal state variables (ISVs) become known through their evolution equations, allowing the ISVs themselves to be updated to the end of the timestep. Thus, the key to advancing the solution is to now derive in detail the internal state variable evolution equations.

Evolution equations

Eq. (4.60) may be used to determine the plastic consistency parameter $\dot{\lambda}^*$ if hardening evolution laws can be found for which the rate of each internal state variable (κ and α_{ij}) is proportional to $\dot{\lambda}^*$. Once the plastic consistency parameter is known, the evolution laws may be integrated through time to model the time varying hardening evolution of the yield surface.

As indicated in Fig. 4.11, isotropic hardening (governed by κ and related to void collapse) causes a change in *size* of octahedral yield profiles, while kinematic hardening (governed by the backstress tensor α_{ij}) produces a *translation* of all octahedral yield profiles. In general, both types of hardening can occur simultaneously.

In this section, we will derive explicit expressions for an isotropic hardening modulus h^*_κ and a kinematic hardening tensor, $\underset{\approx}{\mathbf{H}}^*_\alpha$, such that the evolution of the internal state variables may be written in the forms

$$\dot{\kappa} = h^*_\kappa \dot{\lambda}^*, \tag{4.62}$$

and

$$\dot{\underset{\approx}{\alpha}} = \underset{\approx}{\mathbf{H}}^*_\alpha \dot{\lambda}^*. \tag{4.63}$$

Later, substituting these expressions into Eq. (4.60) will lead to an expression for the plastic consistency parameter $\dot{\lambda}$. Once the consistency parameter is known, the above equations can be themselves integrated through time to update κ and $\underset{\approx}{\alpha}$.

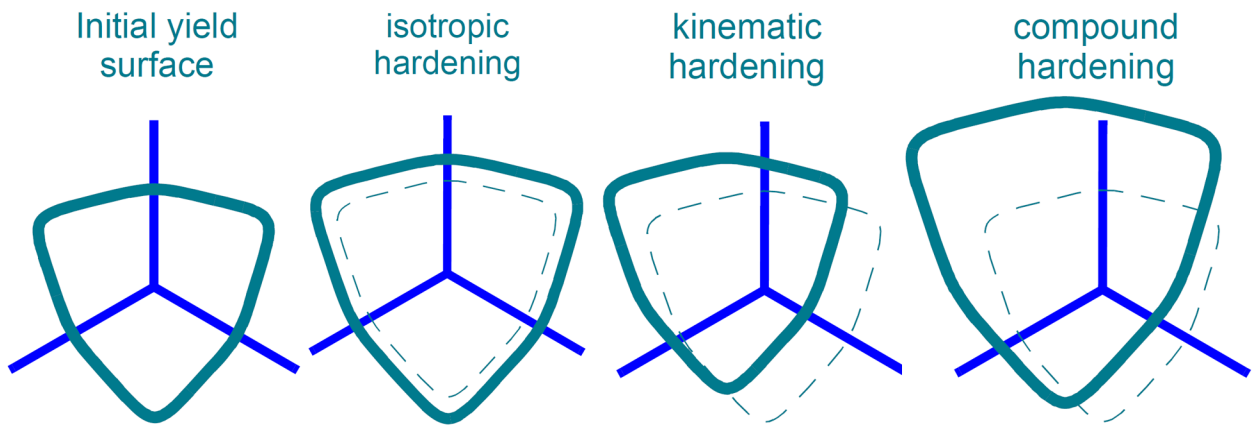

Figure 4.11. Hardening mechanisms. At a given pressure, isotropic hardening entails an increase in size, kinematic hardening translates the yield surface, and compound hardening includes both mechanisms. Softening corresponds to a yield surface *contraction*.

Evolution equation for the porosity-related internal state variable, κ

We begin this section with some background discussion about the meaning of the internal state variable κ, connecting it to some classical microphysical theories for purely porous (non-cracked) materials. Kayenta's re-interpretation of κ for both porous and cracked materials will lead ultimately to an evolution law of the desired form, $\dot{\kappa} = h^*_\kappa \dot{\lambda}^*$ where h^*_κ is called the *isotropic hardening modulus*.

In Kayenta, void collapse commences at different pressures depending on the amount of shear stress present. The effect of shear stress on void collapse is characterized by the cap function illustrate in Fig. 4.5. Even though void collapse depends on shear stress, *characterizing* this effect requires only specification of two numbers $\overline{\kappa}$ and $\overline{X}$ on the hydrostat [see Fig. 4.5]. In Kayenta, $\overline{\kappa}$ and $\overline{X}$ are presumed to be interrelated so that knowledge of $\overline{X}$ is sufficient to compute the value of $\overline{\kappa}$. We will discuss this relationship later. For now, we will focus on how the hydrostat intercept $\overline{X}$ should increase as porosity is reduced.

If a material is capable of permanent volume change (i.e., if hydrostatic testing exhibits nonzero residual plastic volumetric strain $\overline{\varepsilon_v^p}$ upon releasing the pressure), then the material likely contains voids. The hydrostat intercept $\overline{X}$ is proportional to the critical "elastic limit" pressure required to initiate irreversible void collapse. Therefore, the larger the porosity, the smaller $\overline{X}$ will be. As porosity is crushed out, the hydrostat intercept will move to the right so that increasing pressure will be required to continue crushing out the pores. Recognizing that $\overline{\varepsilon_v^p}$ is an indirect measure of porosity changes, our first goal is to describe how the relationship between $\overline{\varepsilon_v^p}$ and $\overline{X}$ can be inferred from hydrostatic test data. Then we will discuss the relationship between $\overline{\kappa}$ and $\overline{X}$. With

these two relationships in hand, we will ultimately assert that

$$\dot{\kappa} = \left(\frac{\partial \kappa}{\partial \overline{X}}\right)\left(\frac{\partial \overline{X}}{\partial \overline{\varepsilon_v^p}}\right)\overline{\dot{\varepsilon}_v^e}, \tag{4.64}$$

from which substitution of Eq. (4.56), during hydrostatic compression or compaction dominated processes, will give the evolution equation in the desired form,

$$\dot{\kappa} = h_\kappa^* \dot{\lambda}^*, \text{ where } \quad h_\kappa^* = \left(\frac{\partial \kappa}{\partial \overline{X}}\right)\left(\frac{\partial \overline{X}}{\partial \overline{\varepsilon_v^p}}\right) \operatorname{tr}(\overline{\underset{\approx}{\mathbf{M}}}). \tag{4.65}$$

During dilatation-dominated processes, a different form is used for h_κ^* (see Eq. (4.76)).

Relationship between $\overline{X}$ and $\overline{\dot{\varepsilon}_v^p}$ (cap curvature model)

If the *matrix* material for a porous medium is plastically incompressible, then it can be shown [68] that the unloaded porosity Π (i.e., the innate porosity at the rest state, not the slightly different porosity that reflects reversible *elastic* porosity reduction under loading) evolves under plastic loading according to

$$\dot{\Pi} = (1-\Pi)\dot{\varepsilon}_v^p, \tag{4.66}$$

where Π is the void volume in a sample divided by the total volume of the sample (both volumes are those in the unloaded state), and $\dot{\varepsilon}_v^p$ is the trace of the logarithmic plastic strain rate. To second order accuracy, Eq. (4.66) implies that the *change* in porosity is approximately equal to the plastic volumetric strain:

$$\Pi - \Pi_0 \approx \varepsilon_v^p. \tag{4.67}$$

Considering *only* hydrostatic loading, early research on pore collapse focused on deriving and/or experimentally measuring so-called "crush curves" in which porosity in a material is plotted as a function of the applied pressure, as in Fig. 4.12. Kayenta uses a similar curve, but inferred directly from hydrostatic stress-strain data so that porosity measurements are not necessary. By using the cap function, Kayenta incorporates the results from this specialized *hydrostatic* experiment into the general theory in such a manner that pore collapse will commence at lower pressures in the presence of *shear*. Recall that the cap function, loosely speaking, represents material response in the absence of microcracks. Porous-only theories typically predict meridional cap profiles similar to Kayenta's cap function. For example, Gurson [43] reported the following upper-bound yield criterion (expressed in terms of Lode cylindrical coordinates):

$$r = k\sqrt{{f_v}^2 + 1 - 2f_v \cosh\left(\frac{z}{\sqrt{2}k}\right)}, \tag{4.68}$$

where k is a constant (the yield stress of the matrix material) and f_v is the porosity. Being independent of the Lode angle, the Gurson yield function is a circle in the octahedral plane; Gurson's *meridional* profile is compared with Kayenta's cap function in Fig. 4.13 for various porosities. As

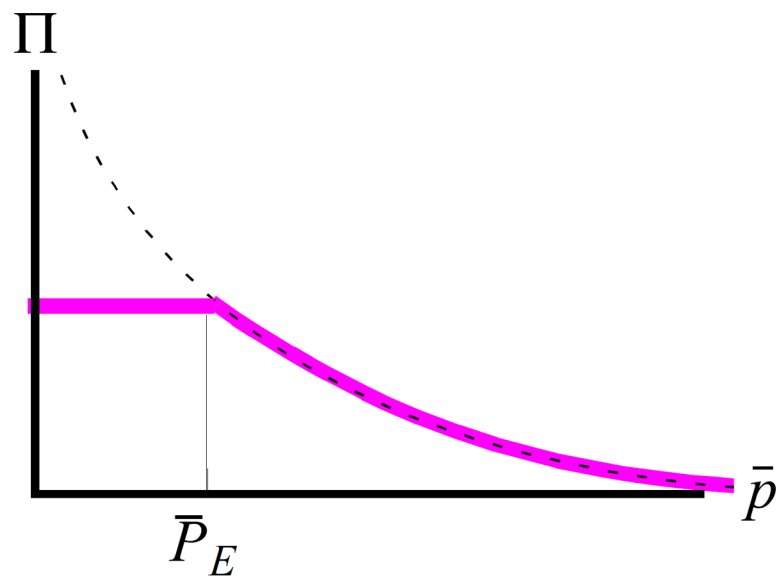

Figure 4.12. A conventional porosity crush curve (dashed) and state path (solid). Porosity is constant until a critical elastic limit pressure is reached. Thereafter, porosity is reduced as pressure is increased.

porosity goes to zero, the meridional profile approaches the pressure insensitive von-Mises profile for the matrix material (in other words, in the absence of microcracks, the yield surface becomes a cylinder in stress space as the porosity goes to zero). This property holds only in the absence of microcracks. When microcracks are later included, the common envelope of yield surfaces will be the shear *fracture* curve F_f.

Under Gurson theory, the key material properties are microphysical (the yield stress k for the matrix material and the porosity f_v), which are difficult to measure directly. To obtain analytical results, these theories must resort to over simplistic assumptions about the matrix material and pore morphology (i.e., Gurson theory presumes perfectly spherical voids arranged in a perfectly periodic array). Finally, microphysical theories are typically *upper bounds*, which are of limited use in applications since the tightness of the bound is unknown.

Rather than *directly* using models like Gurson theory, Kayenta is *guided* by the general trends they predict. Except at extremely high porosity, the Gurson model predicts that the cap surface will be essentially *flat* for a large range of pressures (z-coordinates). The loss in shear strength caused by pores is pronounced over only a small range of pressures near the hydrostatic limit pressure. This region (beyond which the yield surface noticeably branches down to zero) is called the **cap** region. As seen in Fig. 4.13, Gurson theory predicts the yield surface will evolve with porosity in such a manner that the cap essentially translates along the pressure (z) axis — the curvature of the cap region does not change significantly. Kayenta supports these general trends by using a computationally simpler Rubin-Sandler cap function which is simply constant until a critical

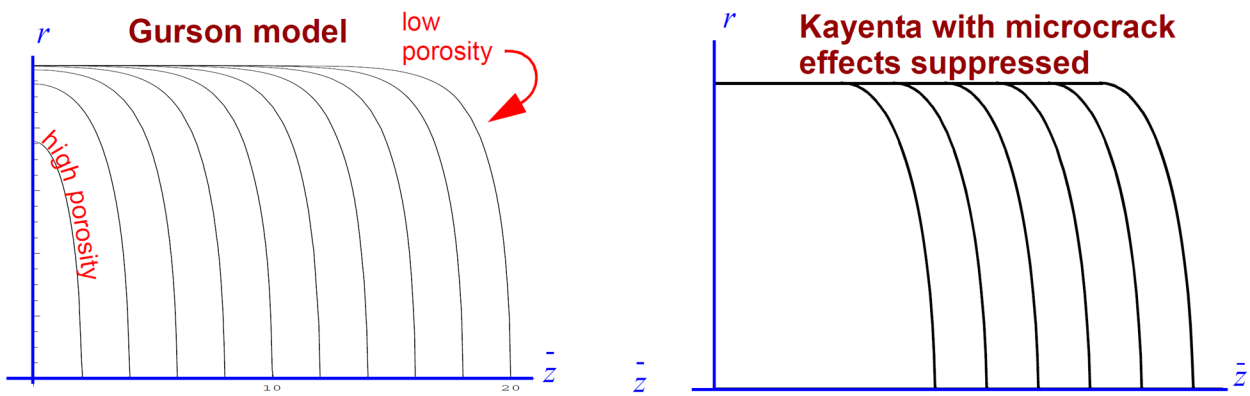

Figure 4.13. The Gurson theory for porous yield surfaces compared with Kayenta cap function at various values of the internal state variable κ. Qualitatively, the theories are similar. When microcrack effects are included, Kayenta forms a *pressure-dependent* envelope, as in Fig. 1.1(b) (pg. 19), instead of the horizontal von-Mises-like envelope shown here.

branch pressure is reached, after which the cap function drops to zero along an ellipse. The cap curve evolves by simple translation along the hydrostat without changes in cap curvature.

In the Gurson model, the current location of the translated cap is a function of the matrix yield stress and the porosity. Rather than using essentially unknowable matrix properties like these as internal state variables, Kayenta recognizes that the appropriate location for the cap can be determined directly from hydrostatic compression test data and the branch point at which shear begins to affect pore collapse is presumed in Kayenta to translate with the hydrostatic limit point. Thus, characterizing how the entire cap function evolves in response to plastic loading boils down to characterizing how the hydrostat intercept point (i.e., where the cap intersects the z-axis) evolves.

Kayenta presumes that it is experimentally tractable to obtain pressure vs. volumetric strain data. If possible, the experiment should be run to the point of total pore collapse (as in Fig. 3.1 on page 36). The elastic response of the material must be first determined by fitting the unloading curve to the nonlinear elasticity fitting function in Eq. (4.9). "Copies" of the elastic unloading function may be superimposed anywhere on the hydrostatic pressure vs. total strain data. As indicated in Fig. 4.14, the elastic unloading curves can be used to determine a shift distance that must be applied at any given pressure to remove the elastic part of the strain. After applying these shifts, the pressure vs. total strain plot is converted to a pressure vs. plastic strain plot, called an X-function. The X-function in Fig. 4.14 asymptotes to infinity when the plastic volume strain (i.e., the change in porosity) has reached its maximum value corresponding to all of the pores having been crushed out. Rotating the X-curve and shifting the origin produces a classical crush curve in which porosity is plotted as a function of pressure. Kayenta never explicitly refers to porosity. Instead, the plastic volumetric strain is employed as an indirect measure of porosity changes.

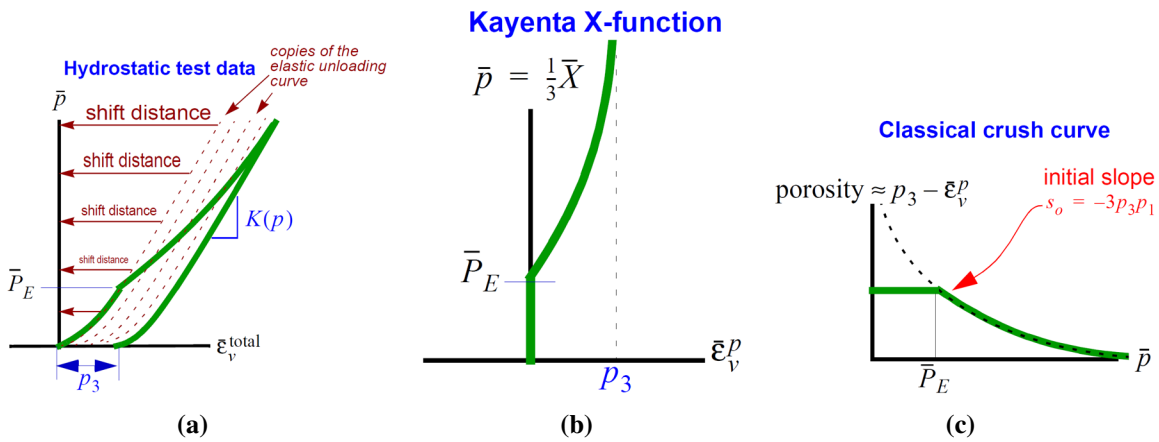

Figure 4.14. Relationship between (a) *hydrostatic pressure vs. volumetric strain data*, (b) *Kayenta X-function*, and (c) *a traditional porosity vs. pressure crush curve*. Test data are pressure vs. total volumetric strain. Once the elastic unloading curves have been parameterized to Kayenta fitting functions, the elastic strain at each pressure value may be subtracted from the total strain to generate the X-function. This function asymptotes to a limit value for the plastic strain when all voids have crushed out (and plastic volume changes therefore become negligible). The limit strain is approximately the initial porosity in the material. Rotating the X-plot 90° and moving the origin as shown will produce a traditional porosity vs. pressure crush curve.

Parameterizing Kayenta so that it will adequately model the changes in the yield surface resulting from pore collapse requires converting hydrostatic pressure vs. volumetric strain data as illustrated in Fig. 4.14 to obtain a classical porosity vs. pressure crush curve in which the porosity is plotted as a function of the pressure $\overline{p}$. Specialized parameterization software is available from the model developers to perform this conversion task and to fit the resulting crush curve to an exponential spline (see Appendix A). The plastic volume strain of a virgin (pre-deformation) material is zero. Therefore the user-specified parameter p_3 is approximately equal to the initial porosity in the material. As pressure is increased from zero, the crush curve (Fig. 4.14(c)) shows that the porosity remains unchanged for a while until an elastic limit pressure $\overline{P}_E$ is reached. Continuing to apply increasing pressure beyond this elastic limit results in irreversible pore collapse and therefore reduction in porosity. Kayenta allows fitting the post yielding part of the crush curve according to the **crush curve spline** formula,

$$\boxed{p_3 - \overline{\varepsilon_v^p} = p_3 \mathrm{e}^{-(p_1+p_2\overline{\xi})\overline{\xi}}}, \text{ where} \qquad \overline{\xi} = \overline{X} - \overline{p_0} = 3(\overline{p} - \overline{P}_E). \tag{4.69}$$

Here, p_0, p_1, p_2, and p_3 are fitting constants. Referring to the porosity vs. pressure crush curve, these parameters are interpreted physically as follows:

- p_0 equals $-3\overline{P}_E$, where $\overline{P}_E$ is the elastic limit pressure at the initial onset of pore collapse.
- p_1 equals $|s_0|/(3p_3)$, where s_0 is the initial slope of the porosity vs. pressure crush curve (see Fig. 4.14).
- p_2 is an optional fitting parameter that may be used if a measured crush curve has an inflection point (i.e., initially concave down, transitioning to concave up at high pressures).
- p_3 is the maximum achievable plastic volume strain, which corresponds approximately to the initial porosity in the material. Complete crushing out of all pores in the material is recognized in the hydrostatic pressure vs. total strain curve if the elastic release curve is tangent to the loading curve.

Eq. (4.69) coincides with hydrostatic test data only during pore collapse. During the initial elastic loading, Eq. (4.69) describes the dashed line in Fig. 4.14, which is *not* required to coincide with the data. At pressures above the elastic limit ($\overline{\xi} > 0$), Eq. (4.69) may be used to compute the plastic volumetric strain according to

$$\overline{\varepsilon_v^p} = p_3 \left[1 - \mathrm{e}^{-(p_1+p_2\overline{\xi})\overline{\xi}}\right], \qquad \text{where} \qquad \overline{\xi} = \overline{X} - \overline{p_0} = 3(\overline{p} - \overline{P}_E) \tag{4.70}$$

This relationship may be differentiated to obtain the derivative $\frac{\mathrm{d}\overline{X}}{\mathrm{d}\overline{\varepsilon_v^p}}$ needed in Eq. (4.65). Now all we need to compute the isotropic hardening modulus h_κ^* is the relationship between κ and $\overline{X}$ so that we can substitute the derivative $\frac{\mathrm{d}\kappa}{\mathrm{d}\overline{X}}$ into Eq. (4.65).

Incidentally, to mimic the crush curve implied in Gurson's porosity model [43], Fossum's parameters should be set as follows:

$$p_1 = \frac{-q_2}{6Y}, \qquad p_2 = 0, \qquad p_3 = \ln\left(\frac{1}{1 - q_1\phi_0}\right) \tag{4.71}$$

where ϕ_0 is the initial porosity (void volume fraction) and Y is the uniaxial yield strength of the matrix material. The parameters q_1 and q_2 are Tvergaard's adjustments [93] to Gurson's model (both equal to 1 in Gurson's original model).

The P2 parameter and its implication on pore growth

Laboratory data for hydrostatic loading is often like that sketched in Fig. 4.14, where the onset of pore collapse corresponds to a smooth change in slope of the stress-strain diagram rather than the abrupt slope discontinuity illustrated in Fig. 4.14. The corresponding crush curve (porosity vs. pressure) is therefore initially concave down before transitioning to concave up. For monotonic compression, this behavior is reproduced in Kayenta by having a nonzero p_2 parameter. The dashed lines, in Fig. 4.14 and Fig. 4.15 are the crush curves defining the relationship between plastic volume strain (which is related to porosity) and pressure for pressures exceeding the elastic limit $\overline{P}_E$.

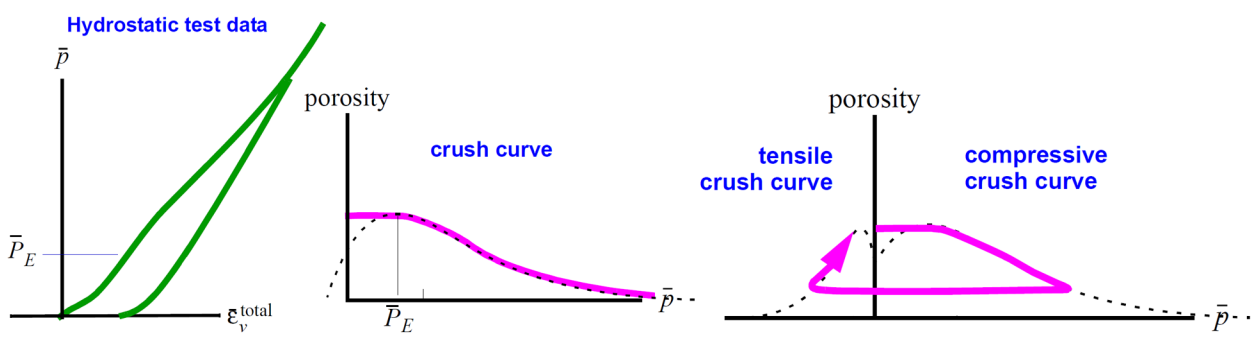

Figure 4.15. A soft "knee" in the onset of pore collapse requires a nonzero value of the p_2 parameter, but the resulting crush curve (dashed line) is reasonable only for $\overline{P} > \overline{P}_E$.

Kayenta faithfully reproduces the crush curve in compression. In practice, however, a load path might involve compression followed by tension, in which case the porosity would need to initially decrease and then subsequently increase. In a traditional porosity model, this is usually modeled by assuming that the tensile crush curve is a copy of the compressive crush curve, (perhaps with a scalar reduction factor applied to pressure, as indicated in the inset figure). In the tensile domain, the porosity would move *upward* along the dashed crush curve. However, when p_2 is nonzero to model the soft bend at the onset of failure, the crush curve has an unrealistic upper bound on porosity — pores cannot grow beyond the initial porosity! The problem lies in the attempt to model the softly bending "knee" in experimental data at the onset of pore collapse. This knee corresponds to heterogeneous material response *at the microscale* in the transition where only a portion of the solid matrix material is deforming plastically [27]. However, Kayenta presumes that deformation is either elastic or plastic, with no transition region. To correctly model the "knee" and tensile pore growth, Kayenta would need to be enhanced to include two yield surfaces: one marking the onset

of plasticity at the microscale and another corresponding to fully developed plasticity throughout the solid matrix.

Relationship between $\overline{\kappa}$ and $\overline{X}$ (cap curvature model)

For a *purely porous* material, Fig. 4.13 suggests that $\overline{\kappa}$ is simply smaller than $\overline{X}$ by a fixed amount. Therefore, knowing $\overline{X}$ is sufficient to determine $\overline{\kappa}$. For a material that contains both pores and microcracks, the relationship between the branch point $\overline{\kappa}$ and $\overline{X}$ is similar, but influenced by the pressure sensitivity of the fracture function. Recall that the continuously differentiable meridional yield function f is constructed by multiplying a function f_f times a cap porosity function f_c. Qualitatively, the fracture function f_f marks the onset of shear crack growth, with significant pressure strengthening being the result of friction at crack faces. This yield envelope function f_f might be lower than the ultimate shear limit envelope F_f if kinematic hardening is allowed. The cap porosity function f_c intersects the hydrostat ($\overline{I_1}$-axis) at $\overline{X}$, marking the point at which pressure *under hydrostatic loading* would be sufficient to induce pore collapse. Variation of the cap function with shear stress (along the ellipse) merely reflects an expectation that pore collapse will commence at a lower pressure than the hydrostatic limit when shear assisted.

Isotropic hardening in Kayenta is cast in terms of the branch point located at $I_1 = \kappa$ (or, equivalently, $\overline{I_1} = \overline{\kappa}$) where the yield function f begins to deviate from the envelope function f_f. The height of the branch point b in Fig. 4.16 is considerably lower than the peak height B.

Between the branch and the peak, material response begins to be influenced by porosity, but is still shear crack (dilatation) dominated, and therefore plastic volume *increases* because of crack bulking. Between the peak and the hydrostatic limit point $\overline{X}$, porosity dominates the material response, resulting in plastic volume *compaction* (from pore collapse). At the critical zero-slope point on the yield surface, material response is influenced equally by both cracks and pores so that no net volume change is apparent at the macroscale.

Two-surface models [i.e., Ref. [79]] typically construct and evolve the yield function by making direct reference to the ratio A/B, which (referring to Fig. 4.16) is typically smaller than unity. Kayenta, however, constructs and evolves its yield function based on the ratio $R \equiv a/b$, which is typically *larger* than unity. This distinction between the two ratios is important to emphasize in publications and presentations to avoid confusion between Kayenta and conventional two-surface models.

Guided both by trends in observed data and by microphysical theories (e.g., Fig. 4.13), Kayenta presumes that hardening proceeds such that the ratio between the distances a and b labeled in Fig. 4.13 remains always equal to a user-specified constant R. The axis labels in Fig. 4.16 indicate that $a = \overline{X} - \overline{\kappa}$ and $b = F_f(\kappa)$. Therefore the **cap eccentricity** (also called the cap **shape parameter**) $R = a/b$ is given by $R = (\overline{X} - \overline{\kappa})/F_f(\kappa)$ or, solving for $\overline{X}$,

$$\overline{X} = \overline{\kappa} + RF_f(\kappa). \tag{4.72}$$

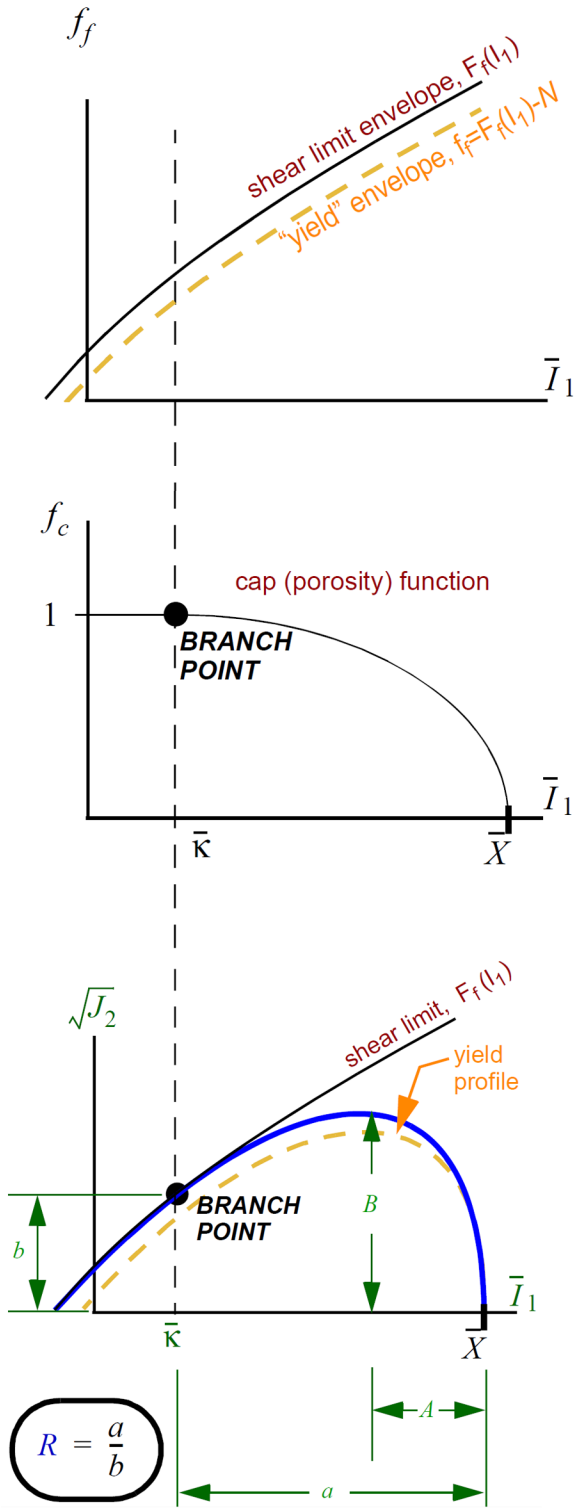

Figure 4.16. Continuously differentiable Kayenta yield function and some characteristic dimensions. The ratio a/b is usually larger than 1, whereas A/B is usually smaller than 1. The bold blue curve is $F_f f_f$. The dashed yield curve is $F_c f_c$.

When written without the overbar denoting the negative, this equation becomes

$$X = \kappa - RF_f(\kappa). \tag{4.73}$$

This expression is evaluated internally within Kayenta coding to determine X as a function of the internal state variable κ. Differentiating both sides of this equation with respect to κ gives

$$\frac{\mathrm{d}X}{\mathrm{d}\kappa} = 1 - RF_f'(\kappa). \tag{4.74}$$

The κ evolution law

Substituting Eq. (4.74) into Eq. (4.65) gives

$$\dot{\kappa} = h_\kappa^* \dot{\lambda}^*, \tag{4.75}$$

where the "isotropic hardening parameter" h_κ^* is

$$\boxed{h_\kappa^* = \mathrm{meld}\left[\overbrace{\mathrm{tr}\underset{\approx}{\mathbf{M}}\left(\frac{\mathrm{d}X/\mathrm{d}\varepsilon_v^p}{1-RF_f'(\kappa)}\right)}^{\text{compaction-dominated hardening modulus}},\ \overbrace{\frac{1}{\mathscr{G}}\left(\frac{I_1-\kappa}{R}\right)\left(\frac{\mathrm{d}X/\mathrm{d}\varepsilon_v^p}{1-RF_f'(\kappa)}\right)}^{\text{dilatation-dominated hardening modulus}}\right]} \tag{4.76}$$

where meld denotes an operator that was, in previous versions of this manual, merely a "min" operator, but which now imposes a smoothed transition from one of the arguments to the other based on a weighted average within the code. As this operation was introduced to smooth the numerical transition, and is currently lacking adequate physical basis, the details of the operator will be omitted in this version of the user's guide, pending subsequent research into understanding the microscale physics of dilatation under triaxial compression. The last term of this hardening model was originally developed to accurately predict dilatation in TXC loading, and it continues to meet that goal quite well. However, the consequence of matching TXC data so well is that the model predicts a hydrostatic strengthening of the material which is almost certainly non-physical. A means to retain good prediction in TXC while avoiding anomalous hydrostatic strengthening is discussed in [64].

Eq. (4.76) is subject to the constraint, $0 > h_\kappa^* > -\infty$.[14] For numerical convenience, this constraint is replaced by $0 > h_\kappa^* \mathscr{G} > -0.01 b_0{}^2$, where b_0 is the initial bulk modulus. The derivative $\frac{\mathrm{d}X}{\mathrm{d}\varepsilon_v^p}$ is found from crush-curve data fitted to Eq. (4.70).

[14] When using the overbar to denote the negative, Eq. (4.75) may be written $\dot{\overline{\kappa}} = \overline{h_\kappa^*}\dot{\gamma}$ subject to $0 < \overline{h_\kappa^*} < \infty$. Thus, since is never negative, this constraint ensures that $\overline{\kappa}$ will never decrease. Physically, this is equivalent to demanding that porosity must always decrease. Increases in porosity (i.e., softening) cannot be accommodated at the material constitutive level — to avoid mesh dependencies of the solution, softening must be handled at the field scale by the host code. See page 99.

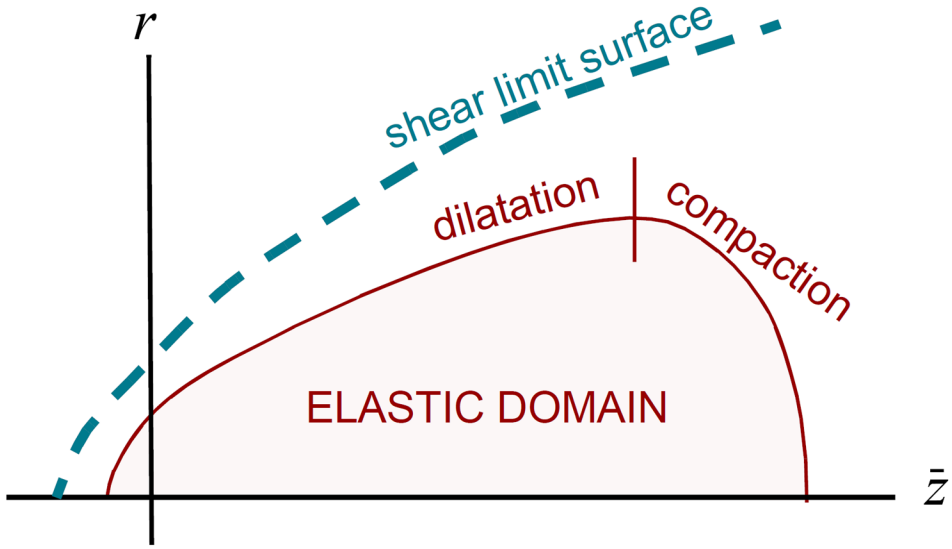

Figure 4.17. Meridional plane in which the magnitude of the stress deviator "r" is plotted against $-z$ (which is proportional to the pressure "p") The yield surface (solid) marks the onset of inelastic flow. Under continued inelastic loading, the yield surface hardens (expands and/or translates) toward the shear limit surface (dashed).

The first term in the meld function of Eq. (4.76) dominates when the stress state falls on the "compaction dominated" part of the yield surface, labeled in Fig. 4.17, while the second term dominates in the dilatation regime. The second term in the minimum function is guided by trends in observed data.

Even under monotonic loading, the relative position of the stress state on the yield surface can move from compaction to dilatation regimes. Fig. 10.6 (pg. 201) shows a triaxial compression load path (angled red arrow) that falls initially on the porosity (compaction) dominated portion of the yield surface, which therefore results in plastic volume reduction and an isotropic expansion of the yield surface. Compaction from void collapse and dilatation from crack bulking are relatively balanced in the vicinity of the critical point. After the stress passes through the critical point, the hardening modulus h^*_κ in Eq. (4.76) transitions from its compaction-dominated value to the dilatation-dominated value.

Evolution equation for the kinematic hardening backstress tensor

Kayenta supports kinematic hardening, but is otherwise isotropic. Kinematic hardening entails using a shifted stress tensor $\underset{\approx}{\xi} = \underset{\approx}{\mathbf{S}} - \underset{\approx}{\alpha}$ in the yield function instead of the actual stress. The tensor internal state variable $\underset{\approx}{\alpha}$ is called the **backstress**, and it is computed using evolution equations described here. In the current version of Kayenta $\underset{\approx}{\alpha}$ is a deviatoric tensor, but it is possible to accommodate effective stress theories for fluid in the pore space by allowing the backstress to include an isotropic part [45].

Recall that the yield criterion with kinematic hardening is given by

$$J_2^\xi = [F_f(I_1) - N]^2 F_c(I_1), \tag{4.77}$$

where J_2^ξ is the second invariant of the shifted stress,

$$\underset{\approx}{\xi} = \underset{\approx}{\mathbf{S}} - \underset{\approx}{\alpha}. \tag{4.78}$$

The backstress tensor $\underset{\approx}{\alpha}$ is initialized to zero. Upon onset of yielding, the backstress evolves in proportion to the deviatoric part of the plastic strain rate:

$$\dot{\underset{\approx}{\alpha}} = HG^\alpha(\underset{\approx}{\alpha})\dot{\underset{\approx}{\gamma}}^p, \tag{4.79}$$

$$\text{where} \quad \dot{\underset{\approx}{\gamma}}^p = \text{dev}\dot{\underset{\approx}{\varepsilon}}^p = \text{dev}\left(\dot{\lambda}^* \underset{\approx}{\mathbf{M}}\right). \tag{4.80}$$

Hence, comparing with Eq. (4.63), the kinematic hardening modulus tensor is given by

$$\underset{\approx}{\mathbf{H}}^*_\alpha = HG^\alpha(\underset{\approx}{\alpha})\text{dev}\left(\underset{\approx}{\mathbf{M}}\right), \tag{4.81}$$

where H is a material constant and $G^\alpha(\underset{\approx}{\alpha})$ is a scalar-valued decay function designed to limit the kinematic hardening such that $G^\alpha \longrightarrow 0$ as approaches the shear limit surface, $F_f(I_1)$. Since the

yield function itself is defined in terms of $F_f(I_1) - N$, the maximum kinematic translation that can occur before reaching the limit surface equals the model offset parameter N. Kayenta uses the G^α function to "slow down" the rate of hardening as the limit surface is approached so that $\underset{\approx}{\mathbf{H}}^*_\alpha$ will equal zero upon reaching the limit surface. Specifically, Kayenta uses the following decay function:

$$G^\alpha(\underset{\approx}{\alpha}) = 1 - \frac{\sqrt{J_2^\alpha}}{N}, \qquad \text{where} \qquad J_2^\alpha = \frac{1}{2}\,\mathrm{tr}\,\underset{\approx}{\alpha}^2. \tag{4.82}$$

Kinematic hardening causes the octahedral profile to translate so that it no longer remains centered at the origin (See Fig. 4.11). Consequently, the yield surface will appear to have translated upward in the meridional plane that contains the backstress (see Fig. 4.18). The translation distance equals $\sqrt{J_2^\alpha}$ and Eq. (4.82) prevents this distance from ever exceeding the user-specified offset limit N. Of course, on the meridional plane *perpendicular* to the backstress, the meridional profile will *not* appear to have translated.

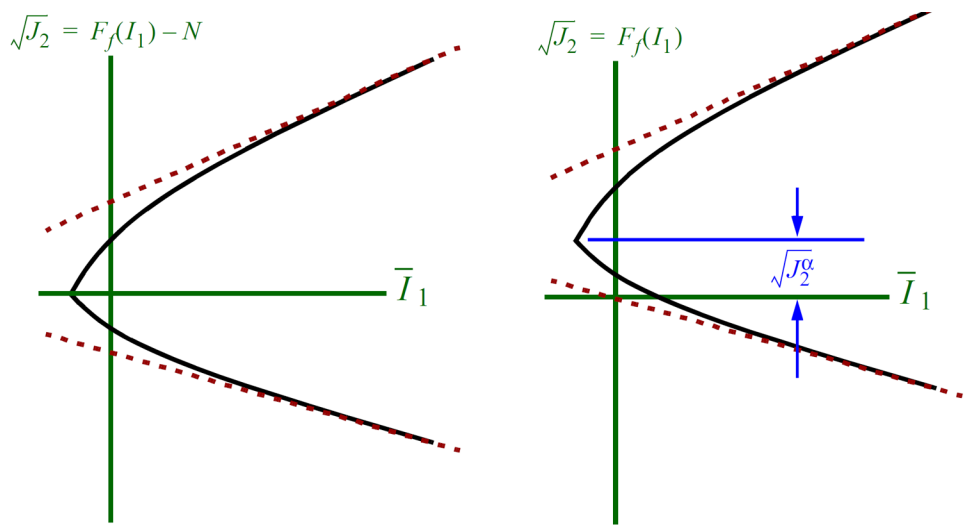

Figure 4.18. The effect of kinematic hardening on the meridional plane that contains the backstress. According to the hardening rule, this meridional profile is permitted to translate in deviatoric stress space by as much as a shift parameter N. This is actually a 2D slice of 6D stress space; think of this as a snow-cone cup shifted away from its original symmetry axis: this view is like a "side view" showing maximum shift distance, but a different view (as from above) might show no shift at all.

Advancing the solution (final step, consistency parameter)

Recall from Eq. (4.61) that the consistency parameter $\dot{\lambda}^*$ is determined from the consistency condition, $\dot{f} = 0$, applied during plastic loading intervals. Specifically,

$$N_{ij}\dot{\sigma}_{ij} + \frac{\frac{\partial f}{\partial \kappa}}{\mathscr{F}}\dot{\kappa} + \frac{\frac{\partial f}{\partial \alpha_{ij}}}{\mathscr{F}}\dot{\alpha}_{ij} = 0. \tag{4.83}$$

Recall the key equations governing the rates of the field and internal state variables:

$$\dot{\sigma}_{ij} = C_{ijkl}\dot{\varepsilon}^e_{kl} = C_{ijkl}\dot{\varepsilon}_{kl} - C_{ijkl}\dot{\varepsilon}^p_{kl} \tag{4.84a}$$

$$\dot{\alpha}_{ij} = H^{\alpha *}_{ij}\dot{\lambda}^* \tag{4.84b}$$

$$\dot{\kappa} = h^*_{\kappa}\dot{\lambda}^* \tag{4.84c}$$

$$\dot{\varepsilon}^p_{ij} = \dot{\lambda}^* M_{ij}. \tag{4.84d}$$

With these, the consistency condition in Eq. (4.60) becomes

$$\mathscr{F} N_{ij}C_{ijkl}\left(\dot{\varepsilon}_{kl} - \dot{\lambda}^* M_{kl}\right) + \frac{\partial f}{\partial \alpha_{ij}}H^{\alpha *}_{ij}\dot{\lambda}^* + \frac{\partial f}{\partial \kappa}h^*_{\kappa}\dot{\lambda}^* = 0. \tag{4.85}$$

From which it follows that

$$\dot{\lambda}^* = \frac{1}{\chi^*}N_{ij}C_{ijkl}\dot{\varepsilon}_{kl}, \tag{4.86}$$

where

$$\boxed{\chi^* = N_{ij}C_{ijkl}M_{kl} - \frac{\frac{\partial f}{\partial \alpha_{ij}}}{\mathscr{F}}H^{\alpha *}_{ij} - \frac{\frac{\partial f}{\partial \kappa}}{\mathscr{F}}h^*_{\kappa}}. \tag{4.87}$$

Numerical implementation for elastic isotropy

The Kayenta subroutines for isotropy exploit the fact that the second-order tensors in the previous section all commute with the stress. For example, $\underset{\approx}{\mathbf{N}} \cdot \underset{\approx}{\sigma} = \underset{\approx}{\sigma} \cdot \underset{\approx}{\mathbf{N}}$. Accordingly, these tensors share a common set of eigenvectors, denoted by $\underset{\sim}{\pi}_1$, $\underset{\sim}{\pi}_2$, $\underset{\sim}{\pi}_3$. Let $\underset{\approx}{\Pi}_1$, $\underset{\approx}{\Pi}_2$, and $\underset{\approx}{\Pi}_3$ denote the corresponding eigenprojectors, defined by

$$\underset{\approx}{\Pi}_i = \underset{\sim}{\pi}_i \otimes \underset{\sim}{\pi}_i \qquad \text{(no sum on } i\text{)} \tag{4.88}$$

Then any tensor $\underset{\approx}{\mathbf{A}}$ having these eigenvectors can be expressed in spectral form as

$$\underset{\approx}{\mathbf{A}} = A_1\underset{\approx}{\Pi}_1 + A_2\underset{\approx}{\Pi}_2 + A_3\underset{\approx}{\Pi}_3 \tag{4.89}$$

where the A_i are the eigenvalues. In this form, the eigenvalues may be interpreted as Cartesian coordinates in a 3D principal space, with the eigenprojectors serving as the corresponding basis.

Since this is true for all tensors that commute with the stress, it is, of course, true for the stress itself:

$$\underset{\approx}{\sigma} = \sigma_1 \underset{\approx}{\Pi}_1 + \sigma_2 \underset{\approx}{\Pi}_2 + \sigma_3 \underset{\approx}{\Pi}_3 \tag{4.90}$$

In this sense, the stress is regarded as a 3D vector within the space spanned by the stress's own eigenprojectors. This geometrical interpretation allows us to depict the yield surface in 3-D in principal stress space, as shown in Fig. 1.1. As is evident in that figure, an isotropic yield surface has a degree of symmetry about the hydrostat, thus motivating a change of basis analogous to setting up a cylindrical coordinate system with the axial direction aligned with the hydrostat. As pointed out in [14], an alternative basis is the Lode basis, $\underset{\approx}{\mathbf{E}}_r$, $\underset{\approx}{\mathbf{E}}_\theta$, and $\underset{\approx}{\mathbf{E}}_z$, which corresponds to a simple change of basis that has $\underset{\approx}{\mathbf{E}}_z$ aligned with the hydrostat. In other words, $\underset{\approx}{\mathbf{E}}_z$ is merely the identity divided by its own magnitude, $\sqrt{3}$. The $\underset{\approx}{\mathbf{E}}_r$ is a unit tensor aligned with the stress deviator. The third base tensor $\underset{\approx}{\mathbf{E}}_\theta$ plays a role similar to the angular base vector in an ordinary cylindrical coordinate system. The unit Lode basis tensors may be found directly from the stress tensor (or shifted stress if using kinematic hardening) by the following formulas taken from [14]:

$$\underset{\approx}{\mathbf{E}}_r = \hat{S}, \qquad \underset{\approx}{\mathbf{E}}_\theta = \frac{\hat{T} - (\sin 3\theta)\hat{S}}{\cos 3\theta}, \qquad \text{and} \qquad \underset{\approx}{\mathbf{E}}_z = \frac{\underset{\approx}{\mathbf{I}}}{\|\underset{\approx}{\mathbf{I}}\|}. \tag{4.91}$$

In terms of the Lode basis, any tensor $\underset{\approx}{\mathbf{A}}$ that commutes with stress may be written as

$$\underset{\approx}{\mathbf{A}} = A_r \underset{\approx}{\mathbf{E}}_r + A_\theta \underset{\approx}{\mathbf{E}}_\theta + A_z \underset{\approx}{\mathbf{E}}_z \tag{4.92}$$

Analogous to the position vector in a cylindrical system, stress tensor has a zero $\overline{\theta}$ coordinate, so that its expansion in terms of the Lode basis is

$$\underset{\approx}{\sigma} = \sigma_r \underset{\approx}{\mathbf{E}}_r + \sigma_z \underset{\approx}{\mathbf{E}}_z \tag{4.93}$$

Other tensors, generally will have a non-zero $\overline{\theta}$ component. This is true, for example, of the yield surface normal if the yield function includes third invariant dependence. The numerical implementation of Kayenta theory strongly draws on this Lode cylindrical basis to improve efficiency of the calculations. In particular, when the elastic stiffness is isotropic (having bulk modulus K and shear modulus G), the operation $C_{ijkl}A_{kl}$ becomes simply

$$\underset{\approx\approx}{\mathbf{C}} : \underset{\approx}{\mathbf{A}} = 3K\text{iso}\underset{\approx}{\mathbf{A}} + 2G\text{dev}\underset{\approx}{\mathbf{A}} = 3KA_z \underset{\approx}{\mathbf{E}}_z + 2G(A_r \underset{\approx}{\mathbf{E}}_r + A_\theta \underset{\approx}{\mathbf{E}}_\theta) \tag{4.94}$$

Moreover, since the Lode basis is a unit basis, the magnitude of $\underset{\approx}{\mathbf{A}}$ is found quite naturally by

$$\|A\| = \sqrt{\underset{\approx}{\mathbf{A}} : \underset{\approx}{\mathbf{A}}} = \sqrt{A_z^2 + A_r^2 + A_\theta^2} \tag{4.95}$$

The inner product between two tensors that commute with stress is similarly written in perfect analogy with the dot product of vectors in cylindrical coordinates. For example, the operation $N_{ij}C_{ijkl}M_{kl}$ in Eq. (4.87) reduces simply to

$$3KN_zM_z + 2G(N_rM_r + N_\theta M_\theta) \tag{4.96}$$

Within the source code itself, recalling that $\underset{\approx}{\mathbf{N}}$ is the unit tensor in the direction of the gradient of f, the three Lode components N_r, N_θ, and N_z are denoted **FR**, **FT**, and **FZ**, and they are normalized such that **FR**^{2} + **FT**^{2} + **FZ**^{2}=1. The Lode components of the flow direction are similarly named with "**F**" replaced with "**G**".

Formal equivalence with oblique return algorithms

With the plastic parameter determined from Eq. (4.87), the stress rate in Eq. (4.84a) may be written

$$\dot{\sigma}_{ij} = \dot{\sigma}^E_{ij} - \frac{A^*_{ij} B^*_{kl} \dot{\sigma}^E_{kl}}{\chi^*}, \tag{4.97}$$

where

$$\dot{\sigma}^E_{ij} = C_{ijkl}\dot{\varepsilon}_{kl} \qquad \textbf{(trial elastic stress rate)} \tag{4.98}$$

$$A^*_{ij} = C_{ijkl} M_{kl} \qquad \text{and} \qquad B^*_{kl} = N_{kl}. \tag{4.99}$$

In Kayenta, the stress state is updated through *direct* integration of Kayenta plasticity equations. However, for our upcoming discussion of rate dependence, it is important to understand that the update formula in Eq. (4.97) implies that the stress may be alternatively integrated through time by first computing a trial elastic stress $\dot{\sigma}^E_{ij}$ at the end of the timestep which may be projected back to the yield surface (which itself has been updated to the end of the step) to determine the final stress. If the trial elastic stress falls outside the yield surface, plastic flow must have occurred during at least part of the solution interval. Therefore, after evolving the internal state variables appropriately to update the yield surface to the end of the step, it can be shown that Eq. (4.97) implies that the stress at the end of the step may be found by obliquely projecting the trial elastic stress back onto the updated yield surface. Because $\underset{\approx}{\mathbf{A}}$ is not generally proportional to $\underset{\approx}{\mathbf{B}}$, the projection is oblique to the yield surface even if plastic normality is used. As explained in Chapter 7, the trial stress is projected only *partly* back to the yield surface whenever rate sensitivity is applied.

Quasistatic inelastic tangent stiffness tensor

For any constitutive model, the inelastic tangent stiffness T_{ijkl} is a fourth-order tensor formally equal to the derivative of the stress rate with respect to the total strain rate. That is,

$$\dot{\sigma}_{ij} = T_{ijkl}\dot{\varepsilon}_{kl}. \tag{4.100}$$

Therefore, comparing this equation with Eq. (4.97) and Eq. (4.98), Kayenta's tangent stiffness is given by

$$\boxed{T_{ijkl} = C_{ijkl} - \frac{1}{\chi^*} P^*_{ij} Q^*_{kl}} \qquad \textbf{quasistatic tangent modulus} \tag{4.101a}$$

where

$$P^*_{ij} = C_{ijkl} M_{kl}, \tag{4.101b}$$

$$Q^*_{kl} = N_{ij} C_{ijkl}, \tag{4.101c}$$

and

$$\chi^* = N_{ij} C_{ijkl} M_{kl} - \frac{\frac{\partial f}{\partial \alpha_{ij}}}{\mathscr{F}} H^* G^\alpha M_{ij} - \frac{\frac{\partial f}{\partial \kappa}}{\mathscr{F}} h^*_\kappa. \tag{4.101d}$$

The tangent stiffness is major symmetric $T_{ijkl} = T_{klij}$ only for associative models ($f = g$).[15]

Stability issues

The last term in Eq. (4.101a) is *subtracted* from the positive-definite elastic stiffness C_{ijkl}, so inelastic flow can potentially make the inelastic tangent stiffness tensor T_{ijkl} non-invertible. In other words, the tangent stiffness tensor might eventually have a zero eigenvalue, marking the onset of softening (yield surface contraction). Whether or not the occurrence of a zero tangent stiffness results in stress-strain softening (i.e., a change from a positive to negative slope in a stress-strain plot) depends on the loading direction. For example, if the strain rate is orthogonal to the null space of a non-invertible tangent stiffness tensor, then no stress-strain softening will be observed and no change in type of the momentum equation will occur even if the yield surface is contracting.

A standing wave (i.e., a non-moving discontinuity in displacement or velocity) is another form of material instability that has been extensively studied in the literature. The acoustic wave speeds (i.e., the speed at which inelastic perturbations can propagate through a material in the direction of a given unit vector $\underset{\sim}{\mathbf{n}}$) are given by $c = \sqrt{x/\rho}$, where x denotes the eigenvalues of the second-order acoustic tensor,

$$a_{jk} = n_i T_{ijkl} n_l. \tag{4.102}$$

Thus, for Kayenta, substituting Eq. (4.101) into Eq. (4.102),

$$a_{jk} = a^e_{jk} - \frac{1}{\chi^*} p^*_j q^*_k \tag{4.103}$$

where

$$a^e_{jk} = n_i C_{ijkl} n_l = \text{the elastic acoustic tensor}, \tag{4.104}$$

and

$$p^*_j = n_i C_{ijkl} M_{kl} \qquad \text{and} \qquad q^*_k = N_{ij} C_{ijkl} n_l. \tag{4.105}$$

If the plastic tangent stiffness T_{ijkl} is not major symmetric, then the acoustic tensor will not be symmetric. In this case, not only are standing waves ($x = 0$) possible, but so are imaginary wave speeds (flutter instability). A complete spectral analysis of acoustic tensors of the form in Eq. (4.103) is

[15] Actually, equivalence of associativity and normality holds only in the absence of elastic-plastic coupling. When elastic moduli can change in response to plastic loading, an associative ($f = g$) model will *not* exhibit normality and will *not* have a major-symmetric tangent stiffness [33].

provided in Ref. [19], where every possible ordering of the inelastic wave speeds relative to elastic wave speeds is derived and where every possible acoustic eigenvector is presented. Physically, the eigenvector characterizes the velocity jump direction. If the eigenvector is parallel to the wave propagation direction $\underset{\sim}{\mathbf{n}}$, then the wave is a compression wave. If the eigenvector is perpendicular to $\underset{\sim}{\mathbf{n}}$, the wave is a shear wave. For elastic materials, these are the only two possible kinds of waves, but for inelastic tangent tensors of the form Eq. (4.101), other modes are possible.

For rate dependent materials, the question of material stability must be examined anew because, as explained in the next section, the *dynamic* tangent stiffness tensor is generally *stiffer* than the quasistatic tangent stiffness.

This page intentionally left blank.

Chapter 5

Softening

In Kayenta, softening refers to a progressive loss of strength and stiffness.

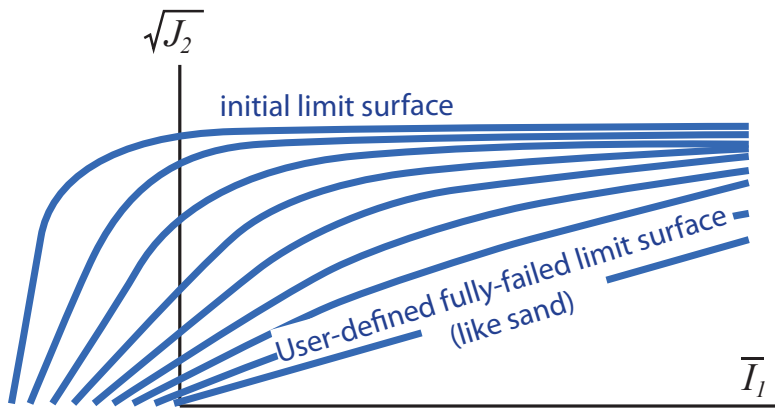

Figure 5.1. Softening regarded as progressive limit surface collapse. Kayenta applies concomitant *damage*, which is progressive degradation of elastic stiffness. By default, the fully failed limit surface emulates cohesionless sand.

The limit surface in Fig. 1.1 (pg. 19) is treated as stationary prior to the onset of softening. As is commonly done in other engineering softening models [22], Kayenta supports softening by allowing the limit surface to collapse as sketched in Fig. 5.1. To initiate softening, the stress state must reach the limit surface. Thereafter, because the limit surface collapses, the stress state cannot reach the same peak state ever again.[1] Once a state on the limit surface has been reached, the material undergoes irreversible softening and damage, thus degrading its load carrying capacity. The fully failed material loses essentially all resistance to loading in tension, but it retains as much strength in compression as is specified by the user. If the user specifies no fully failed limit strength parameters, Kayenta defaults to a limit surface that is typical of sand.

[1]The framework can be modified if, in the future, material healing (i.e., recovery of strength following damage) is desired. However, the current implementation does not support healing.

Strength and Stiffness Degradation in Softening

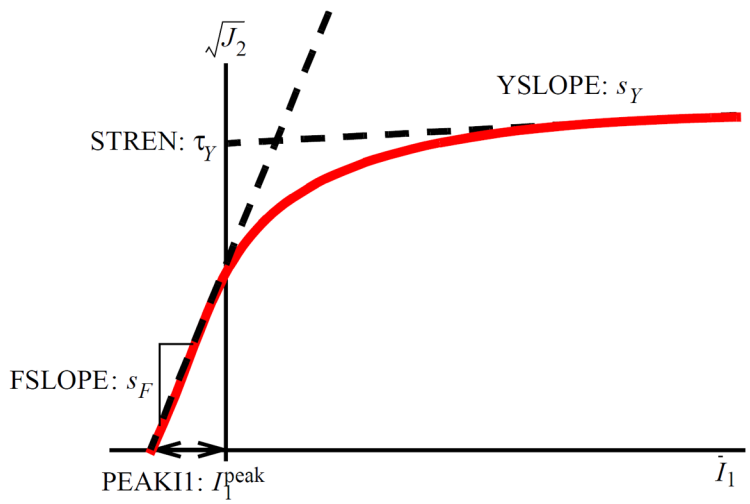

Figure 5.2. Alternative parameterization of the limit curve.

The initial and fully failed limit surfaces are described through user specification of the four parameters labeled in Fig. 5.2.[2] Those slope and intercept parameters are specified via input keywords ending in "I" for the initial limit surface and ending in "F" for the final surface. The dynamically collapsing limit surface is an interpolation between the initial and final surfaces such that

$$\text{FSLOPE} = (1-\mathscr{D}) * (\texttt{FSLOPEI}) + \mathscr{D} * (\texttt{FSLOPEF}) \tag{5.1a}$$

$$\text{PEAKI1} = (1-\mathscr{D}) * (\texttt{PEAKI1I}) + \mathscr{D} * (\texttt{PEAKI1F}) \tag{5.1b}$$

$$\text{STREN} = (1-\mathscr{D}) * (\texttt{STRENI}) + \mathscr{D} * (\texttt{STRENF}) \tag{5.1c}$$

$$\text{YSLOPE} = (1-\mathscr{D}) * (\texttt{YSLOPEI}) + \mathscr{D} * (\texttt{YSLOPEF}) \tag{5.1d}$$

Here, "$\mathscr{D}$" is an interpolation parameter called "damage." Initially, $\mathscr{D} = 0$, and $\mathscr{D}$ goes to 1 as softening progresses. Rather than having any physical significance *per se*, the damage $\mathscr{D}$ is merely an interpolation parameter. The microphysical processes are accommodated indirectly through the evolution equations for $\mathscr{D}$. Internally, the code uses a "coherence" parameter called **COHER**, which is merely $1-\mathscr{D}$.

Evolution of $\mathscr{D}$ should be determined from sound physical arguments and direct fitting of observed softening data to physically justified fitting functions. In practice, however, the evolution of damage might be ad hoc, often because it is recognized that even so-called first-principles models of damage introduce their own non-physical idealizations that fail to realistically account for all

[2] which are internally converted to the four "a" parameters in Eq. (4.39).

sources of microphysical damage.[3] Kayenta falls somewhere in-between these extremes by basing its time-to-failure fitting function on the isotropic part of more complicated microcracking theories (e.g., [28, 70]). Qualitatively, the conventional notion of a damage parameter, $\mathscr{D}$, is

$$\text{damaged elastic stiffness} = (1-\mathscr{D}) * (\text{initial elastic stiffness}) \tag{5.2}$$

In other words, $1-\mathscr{D}$ (which we call "coherance" or **COHER**) is simply the ratio of current stiffness to initial stiffness.[4] This definition, of course, suggests that there should be different levels of damage for different loading modes (such as uniaxial stress contrasted with shear). This expectation is accomodated in the general framework of first-principles self-consistent microcrack damage theories, where the fourth-order elastic *compliance* tensor C^{-1}_{ijkl} (=inverse of the fourth-order stiffness) it typically taken to be related to the initial compliance tensor ${C_{ijkl}}_0^{-1}$ by a formula of the following form [53, 28, 70]:

$$C^{-1}_{ijkl} = {C_{ijkl}}_0^{-1} + \sum_c (\ell^3 A_{ijkl})_c, \tag{5.3}$$

The summation over "c" extends over the number of microcracks within the specimen, ℓ^3 is the crack size cubed (or squared in 2-D problems), and A_{ijkl} is a texture tensor depending only on the intact elastic properties and the crack orientation. This type of statistical crack formulation is clearly more sophisticated than a simple isotropic damage model, but the state-of-the-art for such models still has not matured to the point of being both practical and realistic (e.g., not based on an assumption of an isotropic linear-elatic matrix, not based on simplified crack shapes, not assuming growth of a crack within its own plane, *etc.*[5]). Among the tractibility challenges, for example, practical binning schemes are needed to reduce summations over literally thousands or millions of cracks to sums over a smaller number of "bins" of cracks [91, 46]. This approximate number of cracks in the summation is based on a "rule of thumb" that, at least for armor ceramics, there are $\sim 10^{12}$ cracks per cubic meter (and finite elements in engineering applications are typically larger than a few millimiters in breadth). The actual number of cracks within a specimen is dictated by a Poisson process [91], which (along with statistical variability in orientation and size) represents an irreducible variability in the underlying micromorphology within a representative volume (i.e., a finite element), which in turn gives rise to "aleatory uncertainty" in the stiffness and strength properties of the medium. A theoretical challenge in these models is the need to extend them to include large-deformation effects such as anisotropic nonlinear (and possibily unstable) Poisson expansion effects that would, for example, provide a physical basis for dilatation observed in triaxial compression experiments [64].[6] Kayenta currently supports anisotropy only in its joints option (for intrinsic anisotropy from, say, rock layering [20]) and in its standard backstress kinematic hardening option. It does not currently support induced (i.e., developed) anisotropy caused by oriented

[3]Despite the current non-predictiveness of many "first-principles" damage models, it is nevertheless crucial to support such efforts, as they guide the overall structure of the empiricisms used in Kayenta. Moreover, these models are continuuing to overcome obstacles (such as the need for specialized binning algorithms for tracking evolving crack populations [46]) that currently prevent their widespread use in engineering applications.

[4]Contrast this definiton of damage, which quantifies stiffness degradation, to *softening*, which quantifies strength degradation. Kayenta treats these as concomitant effects, both determined from **COHER**.

[5]These models often address one or two of these limititions, but not all of them.

[6]This dilatation is currently fitted remarkably well via Kayenta's hardening theory, but this might be a simple case of fitting one experiment (triaxial compression) at the cost of being predictive for other loading modes — especially non-proportional loading, where the stress trajectory is tortuous [18].

damage. Accordingly, Kayenta's isotropic damage model is formed by considering the isotropic (non-tensorial) form of Eq. 5.3 and comparing it with Eq. 5.2 along with an assumption that crack size is initially infinitesimal and grows at a fixed rate so that $\ell = \dot{\ell}\, t^{\text{grow}}$ in which $\dot{\ell}$ is a constant and t^{grow} is the total amount of time that a crack has been growing. These simplifying considerations suggest that the time variation of coherence, $1 - \mathscr{D}$, should be of roughly of the form

$$1 - D = 1 - \mathscr{D} = \frac{1}{1 + \left(\frac{t^{\text{grow}}}{t^{\text{fail}}}\right)^k}, \tag{5.4}$$

where (as explained in detail below) t^{fail} is a scale-dependent time-to-failure parameter, k is an exponent controling speed of failure, and t^{grow} is the length of time that the stress state has been at the limit surface (i.e., at the peak attainable stress threshold marking onset of softening and damage). That is, once the stress state has reached the initial limit surface, an internal variable called **TGROW** is incremented such that it equals the amount of time that the stress state has been at the limit surface. As t^{grow} increases, the limit surface itself (and the elastic stiffnesses) are degraded according to microphysically inspired evolution equations that are summarized within this chapter.

By setting **SOFTENING**=1, the time-to-failure parameter, **TFAIL**, marks the point at which the material has lost half of its stiffness and is halfway between its intact and fully-damaged strength capacity. This parameter implicitly provides a scale-dependent and rate-dependent *strain*-to-failure, predicting "dwell" times in impact dynamics that naturally increase with the speed of the projectile. By setting **SOFTENING**=3, Kayenta includes a truly constant strain-to-failure option to facilitate comparing Kayenta with other models that do not include this form of rate-dependent dwell. In that case, **FAIL0** is no longer treated as a constant — it is instead automatically and continually re-set by the code to induce material failure at the user-prescribed strain-to-failure value based on whatever strain rate exists at any given moment in time.

The constant time-to-failure option (invoked by setting **SOFTENING**=1) should be used if damage waves are observed to propagate at a fixed speed, independent of loading rate. In that case, it is helpful to imagine that damage corresponds cracks propagating across a finite domain. If the crack or damage wave growth speed ($\dot{\ell}$) is approximately constant,[7] then t^{fail} may be interpreted as roughly the amount of time required for a steadily growing crack to traverse a distance of one meter. Rather than defaulting to 1 meter, some host codes will require user-supplied values of t^{fail} to also be accompanied by the corresponding spatial scale. Regardless of these syntax details, the host code (in a proper implementation of Kayenta) will automatically scale the value of t^{fail} according to each actual element size. In this way, damage propagates at a mesh-insensitive speed [85]. Confirming proper constant-speed damage propagation is an important verification test to be performed by code *users* (not just developers).

Within Kayenta, the time t^{grow} (called **TGROW** in the source code) is incremented only when the stress state is at the limit surface. Consequently, output graphics colored by **TGROW** can be more interesting and informative than relatively binary (nearly two color) plots of **COHER**. A plot of **TGROW** illustrates the "sequence" of damage through time so that currently failing zones show as a different color from previously failed zones. Hiding material for which **COHER** falls below

[7] This approximation is accurate in impact applications, where the stress-intensity factor is typically high.

some threshold value sometimes effectively illustrates "cracks", but it can give a false impression of loss of load-carrying capacity in zones that (like a comminuted region) are fully damaged but still able to resist compressive loads and to transmit waves. A useful alternative to hiding damaged zones is to simply show them in a darker hue.

The exponent k is referred to by its source code name: **FSPEED**. This exponent controls how rapidly the coherence drops from 1 to 0. Some classical damage theories, such as the first Johnson-Holmquist (JH1) model, impose a nearly instantaneous accumulation of damage after a short delay.[8]. Such theories of "sudden" falure are emulated in Kayenta by using a large (> 10) value of **FSPEED**; a more gradual decay (for which **TFAIL** is the half-damaged time) is acheived by using a smaller value of **FSPEED**. The choice $k = 3$ would correspond to an isotropic version of 3-D statistical damage theories that set the elastic compliance based on randomly oriented "penny shaped" cracks. The choice $k = 2$ would emulate an isotropic version of 2D damage models in which cracks are treated as slits extending out of the plane. Since Kayenta does not include the induced anisotropy of these more sophisticated models, obtaining reasonably predictive simulations from Kayenta requires a fine mesh so that induced anisotropy is captured through explicitly resolved heterogeneity of localized damage on the grid.

In summary, Eq. (5.4) provides a smooth transition from 100% coherent material ($\mathscr{D} = 0$) to complete loss of coherence. The transition has a period of time during which coherence stays nearly 1 (called the "dwell phase," followed by a relatively rapid descent to zero. Our two-parameter coherence-reduction formula allows the user direct control over both the dwell time (through the input parameter **TFAIL**, and the rate of descent (through the parameter **FSPEED**, which is the exponent k). In this way, Kayenta may be made to emulate various damage models in the literature. The **SOFTENING** parameter provides additional support for emulating other damage theories, making Kayenta a convenient multi-purpose framework in which to explore relative merits of competing models. Such freedom is provided because physically derived damage progression equations appear to be an open research question.

By setting **SOFTENING**=1, the user instructs Kayenta to apply a purely time-based damage evolution function based on the previously described notion that cracks tend to grow at a fixed speed regardless of loading rate. If crack growth speed is regarded as constant, a finite amount of time must pass before a crack finishes propagating across a finite element domain. When **SOFTENING**=1, this time delay (t^{fail}) is treated within Kayenta as a material constant. To acheive a constant damage propagation rate on the finite-elment grid, the host code must apply appropriate scaling of this parameter based on the mesh size.

Once the initial limit surface has been reached, the limit surface then begins to collapse. As illustrated in Fig. 5.3, the rate of collapse is controlled by the user through parameters **TFAIL** (t^{fail}) and **FSPEED** (k). The parameter t^{fail} specifies the amount of time that must pass with the stress state at the limit surface before the limit surface collapses to a point halfway between the intact (initial) and fully-failed surfaces. This parameter plays a role similar to the "plastic strain to failure" used by other models such as the Johnson-Holmquist models, JH1 and JH2 [52]. By using a "time to failure" parameter t^{fail}, the Kayenta damage model has the property that apparent

[8]The delay itself is controlled in Kayenta by the values of **SOFTENING** and **TFAIL**

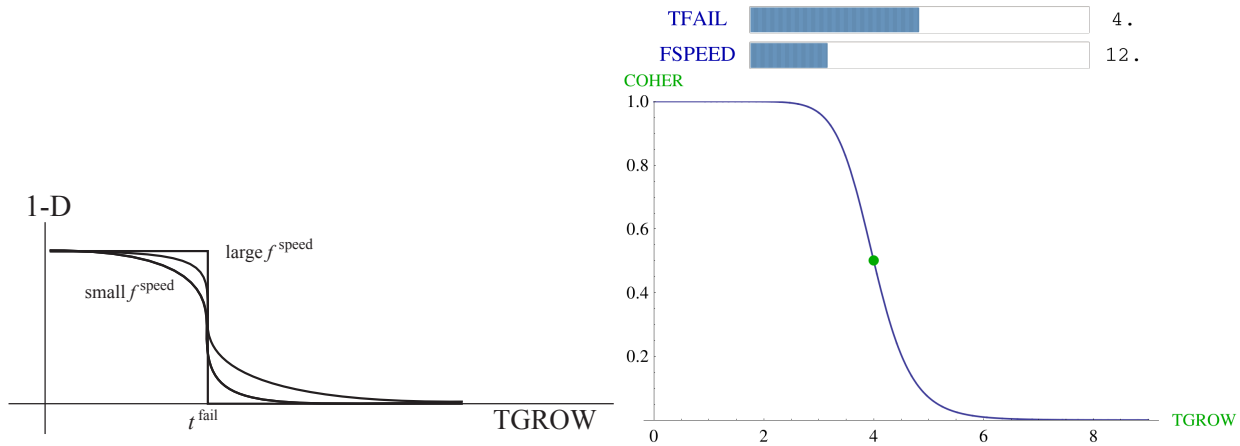

Figure 5.3. Time-based damage evolution. The plottable output variable **TGROW** is the time t^{grow} in Eq. (5.4), and **FSPEED** is the exponent k in the same equation. The first image provides a notional interpretation of t^{fail} and **FSPEED**, while the second image is a specific numerical example.

strain to failure will increase with strain rate. The "failure speed" parameter k is provided merely to allow softening to proceed quickly when k is large (> 30) or more gradually when k is small (< 5). This parameter therefore allows Kayenta's softening to emulate either the JH1 or JH2 models and other similar models. As illustrated in Fig. 5.4(a), the time delay t^{fail} is analogous to the plastic-strain-to-failure used in other dynamic damage models such as the Johnson-Holmquist model [52]. However (unlike these other models), by using a fixed time delay, both plastic-strain-to-failure and energy of failure automatically increase with increased loading rate.

In addition to losing limit strength, a softening material also loses elastic stiffness. At present, the Kayenta model presumes that the stiffness remains isotropic as damage proceeds. An appropriate proposal to improve Kayenta would include support for orthotropic degradation of the elastic moduli. In the current isotropic elastic damage framework, the elastic moduli are degraded using the *isotropic* part of the damaged compliance proposed by Dienes et al. [28], which is very similar to other effective moduli formulations [53, 70]. Dienes's damage compliance is expressed in terms of an overall measure of crack size. As mentioned earlier in the context of limit surface collapse, we contend that the rate of limit surface collapse is also tied to crack growth speed. Therefore, Dienes's compliance reduction formulas are accordingly converted to functions of the damage parameter $\mathscr{D}$. The fact that the limit surface collapses according to the coherence $(1-\mathscr{D})$ is implicitly expressing a critical failure strain model as a stress-based criterion. This approach positions the model well for future enhancements that could introduce anisotropic softening by using a Tsai-Wu transformation of the limit function, wherein the stress sent to an isotropic limit function is replaced by a transformed stress, $\sigma^*_{ij} = L_{ijkl}(\sigma_{kl} - \alpha_{kl})$ in which L_{ijkl} is an anisotropic transformation tensor (equal to the initial stiffness acting on damaged compliance) and α_{kl} is a shift tensor (equal to the kinematic backstress that is already part of Kayenta).

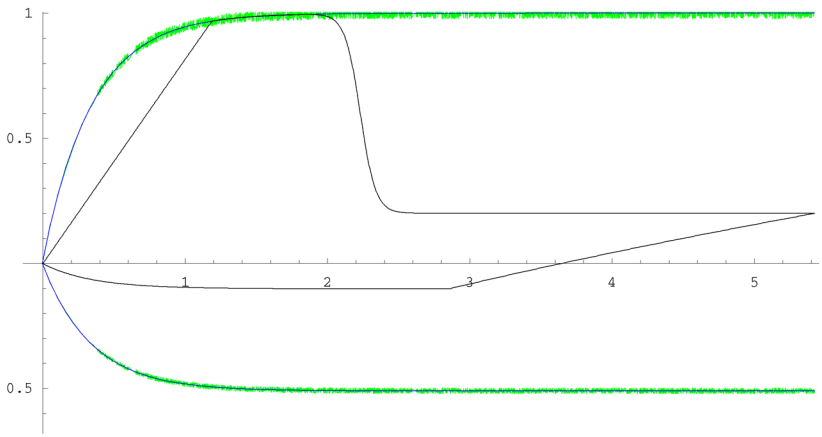

(a) $\sqrt{J_2}$ vs. $\bar{I}_1$ stress space (black line is the uniaxial strain path)

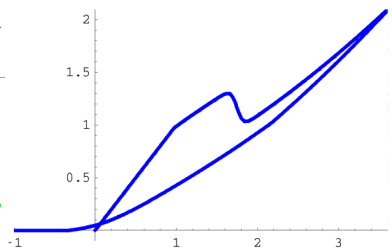

(b) Axial stress vs. axial strain for uniaxial strain loading

Figure 5.4. Demonstration that a time-to-failure criterion leads to apparent plastic-strain-to-failure. For this test case, the failed limit surface was specified to mimic the failed surface in the Johnson-Holmquist ceramic model [52] (namely, the initial limit surface is the green high-strength envelope and the failed surface is the von-Mises-like surface parallel to the I_1 hydrostat at about 1/5 the initial strength). Shown are (a) *path through stress space* and (b) *stress-strain response for uniaxial strain loading*, each illustrating an apparent plastic strain to failure (dwell) with this time-to-failure model.

In addition to the decrease in the elastic stiffness, a pressure dependence is used to give an undamaged response in compression and a softened response in tension. The transition is made between the two using a linear interpolation of the intact and damaged bulk moduli. The interpolation is defined as follows:

$$K = \begin{cases} K_{\text{intact}} & \text{if } I_1 \leq -\frac{K_{\text{intact}}}{100} \\ K_{\text{damaged}} - \frac{I_1}{\frac{K_{\text{intact}}}{100}}(K_{\text{intact}} - K_{\text{damaged}}) & \text{if } -\frac{K_{\text{intact}}}{100} < I_1 < 0 \\ K_{\text{damaged}} & \text{if } I_1 \geq 0 \end{cases} \tag{5.5}$$

The *ad hoc* factor of 100 was included to provide a smooth transition between tensile and compressive responses (i.e., it is not based on any rigorous physics).

Details of the damage evolution equations will not be further discussed here because they are continually undergoing revision to include physics-based evolution models and to achieve better convergence properties when invoking aleatory uncertainty in strength (see [55]).

Accumulated-Damage Framework

The Accumulated-Damage framework is built upon the preexisting time-to-failure softening framework and is automatically used when a strain-to-failure model is selected. It interfaces with the preexisting framework by initializing the time-to-failure user input t^{fail} to unity and by using the state variable **TGROW** as the damage value $\mathscr{D}$.

Models using linear accumulation of damage, such as Johnson-Cook fracture, define the damage variable $\mathscr{D}$ such that $\mathscr{D}$ is initially assigned a value of zero and then is allowed to increase monotonically up to a value of unity; in many of these models, no loss of strength or stiffness occurs until $\mathscr{D} = 1$. Kayenta's "accumulated damage" option mimics these models closely except that $\mathscr{D}$ does not have an upper bound.

The original Kayenta softening framework allows for a relatively gentle transition from a intact material to a failed material. The accumulated-damage framework leverages this implementation so that the sudden loss of strength will not cause instabilities in the simulation. Please see Fig. 5.3 for a diagram depicting the loss of strength.

When the accumulated-damage framework is used k must be set to reflect the expected rate of the loss of strength and the expected loss in strength and stiffness prior to $\mathscr{D}$ equalling unity. A suggested minimum value of k is 10 which corresponds to approximately 75% of the softening to occur within the range $0.9 \leq \mathscr{D} \leq 1.1$. However, for a nearly instantaneous transition it is suggested that k be set to at least 30 which ensures that 90% of the softening occurs within the range $0.95 \leq \mathscr{D} \leq 1.05$.

This approach can be contrasted with cohesive-type (*cf.*[71]) models that might also use a parameter called damage, but which predict material degradation even when $\mathscr{D} \ll 1$. For clarity,

special note should be made that (in Kayenta) the damage parameter $\mathscr{D}$ (actually stored as **TGROW**) does not directly control the loss of strength or stiffness but is used to compute **COHER**.

Implemented Fracture Models

The strain-to-failure models of interest may all be viewed as belonging to the linear accumulation of damage class of models. Models of this class update damage according to

$$\mathscr{D} = \sum \frac{\Delta\varepsilon^p}{\varepsilon^f}, \tag{5.6}$$

where the strain-to-failure ε^f may be a time-varying value and depend on the material state (stress, stress rate, strain, strain rate, temperature, *etc.*).

The Kayenta framework has been expanded to allow the user to mimic a variety of strain-to-failure models by using this implementation (similar strain-to-failure models could quickly be implemented). This is demonstrated by the addition of one contemporary and two classical strain-to-failure fracture models. These three models are distinguished by their theories for setting a value to ε^f:

- Constant Equivalent-Strain-at-Failure: strain-to-failure is, as the name implies, a constant given by a user-supplied parameter $\mathscr{D}_1$.

$$\varepsilon^f = \mathscr{D}_1 \tag{5.7}$$

  The parameters are mapped: $\mathscr{D}_1 =$ **FAIL2**.

- Johnson-Cook Fracture [50]: strain-to-failure is a function of a dimensionless pressure-stress ratio σ^* (which we have been referring to as stress triaxiality η), a dimensionless strain rate $\dot{\varepsilon}^*$ (i.e., normalized by a reference strain rate $\dot{\varepsilon}_0$), and a dimensionless homologous temperature T^*.

$$\varepsilon^f = \left[\mathscr{D}_1 + \mathscr{D}_2 e^{\mathscr{D}_3\sigma^*}\right]\left[1 + \mathscr{D}_4 \ln\dot{\varepsilon}^*\right]\left[1 + \mathscr{D}_5 T^*\right] \tag{5.8}$$

$$\sigma^* = \frac{\sigma_m}{\sigma_e} \qquad \dot{\varepsilon}^* = \frac{\dot{\varepsilon}}{\dot{\varepsilon}_0} \qquad T^* = \frac{T - T_{\text{room}}}{T_{\text{melt}} - T_{\text{room}}} \tag{5.9}$$

  In these formulas, the eight user-supplied parameters are $\mathscr{D}_1 \ldots \mathscr{D}_5$, $\dot{\varepsilon}_0$, T_{melt}, and T_{room}.

  The parameters are mapped: $\mathscr{D}_1 =$ **FAIL2**, $\mathscr{D}_2 =$ **FAIL3**, $\mathscr{D}_3 =$ **FAIL4**, $\mathscr{D}_4 =$ **FAIL5**, $\mathscr{D}_5 =$ **FAIL6**, $\dot{\varepsilon}_0 =$ **FAIL7**, $T_{\text{melt}} =$ **FAIL8**, $T_{\text{room}} =$ **FAIL9**.

- Xue-Wierzbicki Fracture [95]: strain to failure depends on stress triaxiality η, and the Lode parameter

$$\varepsilon^f = \mathscr{D}_1 e^{-\mathscr{D}_2\eta} - \left(\mathscr{D}_1 e^{-\mathscr{D}_2\eta} - \mathscr{D}_3 e^{-\mathscr{D}_4\eta}\right)(1 - \xi^m)^n \tag{5.10}$$

$$\xi = \frac{27}{2}\frac{J_3}{\sqrt{3J_2}^3} \qquad \eta = \frac{\frac{I_1}{3}}{\sqrt{3J_2}} \qquad m = 2\,\text{Round}\left(\frac{1}{2n}\right) \tag{5.11}$$

Here, the five user-supplied material parameters are $\mathscr{D}_1 \ldots \mathscr{D}_4$ and the hardening exponent n (which is assigned the same value as the hardening exponent used in power law plasticity theory).

The parameters are mapped: $\mathscr{D}_1 =$ **FAIL2**, $\mathscr{D}_2 =$ **FAIL3**, $\mathscr{D}_3 =$ **FAIL4**, $\mathscr{D}_4 =$ **FAIL5**, $n =$ **FAIL6**. The Xue-Wierzbicki Fracture model does not allow fracture when the stress triaxiality is below $-\frac{1}{3}$. However, when **FAIL7** is nonzero, then the cutoff is removed.

The parameters in the above equations are all described in the Model Parameters section, Section B.1, of this document.

The value of ε^f can change with respect to the stress state. However, Kayenta supports viscoplasticity and tracks the quasistatic stress and the dynamic stress concurrently. The quasistatic stress always resides within the limit surface while the dynamic stress is not confined by the limit surface. Only when viscoplasticity is used do these two stress values differ. Because of these two potentially different stress values, one of them must be chosen for use in these newly implemented models. At high rates, the dynamic stress is the actual stress being carried by the element, making it the preferred choice for the stress-dependent strain-to-failure theory.

Spall Pressure and Void Insertion

The **SPALLI1** user parameter allows mitigating excessively tensile stress states by limiting the magnitude of **I1**. When set, Kayenta ensures that the value of **I1** does not exceed that of **SPALLI1**. The process by which excessive tensile states are limited is conceptually similar to the radial return of Von-Mises plasticity. However, rather than scale the magnitude of the stress deviator, Kayenta scales **I1** such that **I1** $\leq$ **SPALLI1**. In this way, **SPALLI1** can be conceptualized as a "spall pressure" and the scaling of **I1** as an isotropic return. Unlike the case of radial return, however, the resultant volumetric inelastic strain, given by

$$d\varepsilon^{\text{spall}} = \frac{I_1^{\text{trial}} - \textbf{SPALLI1}}{3K} \tag{5.12}$$

where $3K$ is the current bulk modulus, is not accumulated, but is returned to the host code where it is to be treated similar to void. In this case, $d\varepsilon^{\text{spall}}$ is returned in the **EOS4** variable and **CRACK** set to -1 to alert the host code.

This information is provided to the host code, but Kayenta does not require any specific implementation. Please consult your host code's documentation to determin how, if at all, nonzero values of **EOS4** are handled.

Implementation Requirements for Softening

It is well known that softening induces a change in type of the governing equations An initially quasistatic problem becomes hyperbolic, perhaps marking the onset of localized failure and unstable structural collapse. An initially dynamic problem loses hyperbolicity, marking the onset of localized failure and also resulting in damage waves that propagate slower than shock waves. Without intervention from the host code, the change in type of the governing equations in a local constitutive model will result in non-physical dependency of the solution on the mesh resolution. One means of reducing this problem is to introduce spatial perturbations and scale effects in the strength of the material that are consistent with the following laboratory observations:

- large variability in strength in low-pressure experiments
- a tendency for small specimens to have higher ultimate strength than large specimens
- reduced variability and scale effects at high pressure

These qualitative observations suggest that the deterministic limit surface should be perturbed as illustrated in Fig. 5.5, where all uncertainty and scale effects have been imposed in the $(I_1^{\text{peak}})^{\text{I}}$ limit surface parameter. For details, see [85].

At time zero, before calculations begin, a random number R (uniformly distributed in the range from 0 to 1) is generated at each finite element in the simulation. This random number is converted into a non-uniform scale-dependent Weibull-perturbed realization for $(I_1^{\text{peak}})^{\text{I}}$ at each element by

$$(I_1^{\text{peak}})^{\text{I}} = \widetilde{(I_1^{\text{peak}})^{\text{I}}} \left[\frac{\widetilde{V} \ln R}{V \ln(1/2)} \right]^{1/m} \tag{5.13}$$

where $\widetilde{(I_1^{\text{peak}})^{\text{I}}}$ is the user-defined median value of the tensile spherical strength measured (or inferred) at a known user-specified specimen volume $\widetilde{V}$, and m is the "Weibull modulus" that quantifies the extent of variability. Within a simulation, the volume V is the finite element volume, so this formula accounts for scale effects by assigning a higher strength (on average) to finite elments that are smaller than $\widetilde{V}$. Since this variability is imposed on the "spherical" tensile $(I_1^{\text{peak}})^{\text{I}}$, it produces a non-Weibull scale dependence in *axial* tensile strength as illustrated in Fig. 5.5(b) and Fig. 5.6(b). This non-Weibull character of scale dependence of strength is well known [6].

Some applications of the damage model with statistical uncertainty and scale effects are illustrated in Fig. 5.7 and Fig. 5.8. Although incorporation of uncertainty and scale effects does reduce mesh sensitivity in some cases, one must be warned that it does not eliminate mesh sensitivity altogether. Brazilian indirect tension simulations, in particular, continue to suffer from an unacceptable

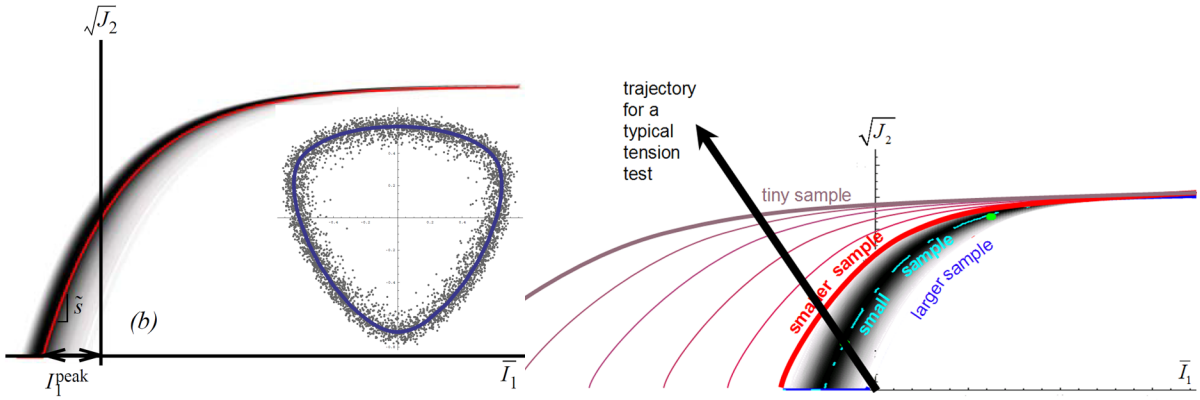

(a) **(b)**

Figure 5.5. Incorporation of uncertainty and scale effects in damage. This figure depicts the character of uncertainty and scale effects expected for a quasibrittle material such as rock. (a) Significantly variability is imposed at low pressure by statistically varying the $(I_1^{peak})^{I}$ parameter. (b) corresponding scale effects ensure that small specimens are stronger, on average, than large specimens.

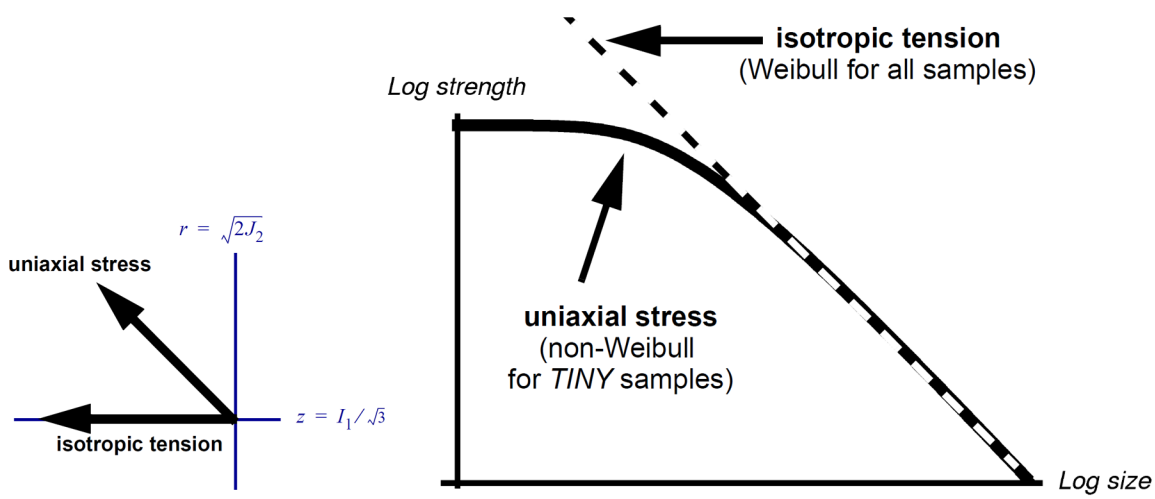

(a) **(b)**

Figure 5.6. The strength size effect in "directed-Weibull" theory varies with stress space trajectory. Whereas strength can increase with bound for small samples in isotropic tension, it saturates to a classical plasticity limit for non-hydrostatic loading of tiny samples (relative to aggregate size).

level of mesh sensitivity [61]. Even though the predictions of trends in the statistics of Brazilian failure are very similar to laboratory observations, the quantitative median strength continues to be mesh dependent and therefore non-predictive. A step towards resolving this problem, at least for the onset of softening, imposes specialized run-time "relocalization" revisions of the element strength are required to compensate for inability of low-order element shape functions to capture stress concentations within an element [55]. This work constitutes a *purely numerical* motivation for nonlocality of material strength.[9]

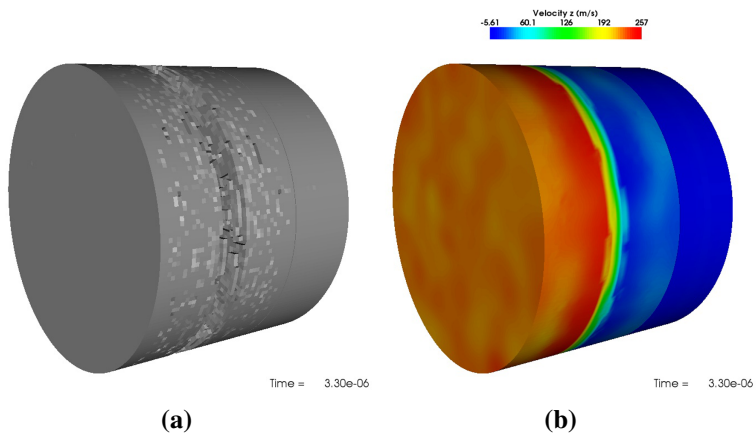

Figure 5.7. Spall with strength variability and scale effects. The left plot shows intact material. The right plot shows material velocity with clear variability.

Further verification and validation of this approach to softening may be found on page 161.

[9]Reference [55] states that using higher-order elements did not significantly reduce errors on coarse meshes, but that assertion might have been errant since its case-study sample simulation essentially treated the Gauss-point stresses as piecewise constant. An appropriate avenue of future work would be to *properly* impose relocalization using the actual non-constant stress field on the element; if successful, this approach would apply a form of nonlocality using information that is local to each element and hence readily parallelized.

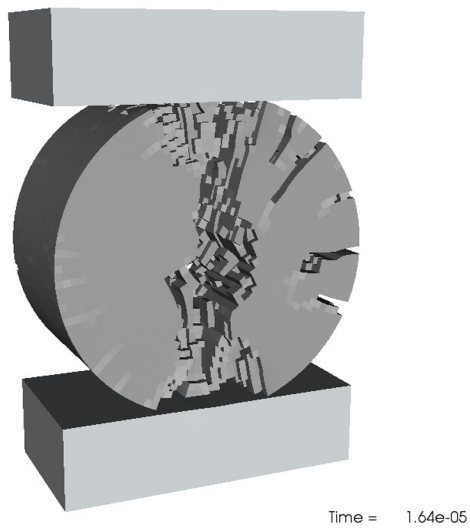

Figure 5.8. Brazilian simulation with variability and scale effects. Plot of intact material.

Chapter 6

Equation of State: Application.

This section outlines the modifications that have been made to Kayenta to include thermal response due to deformation in accordance with the first and second laws of thermodynamics. Currently, the thermal version of Kayenta, referred to as Thermal-Kayenta, can now demonstrated to reproduce single-element response curves for the Johnson-Cook thermoplasticity model with Mie-Grüneisen equation of state under strain-controlled compression, pure shear, and uniaxial strain.

This section is a collection of verbatim or paraphrased excerpts from the Sandia National Laboratories technical report [40] by Fuller et al.; please refer to this report for details on thermomechanics for thermoelastic and thermoplastic solids.

Constitutive Models for Thermoplastic Materials

This chapter reviews the essential aspects of thermal theories for the Sandia National Laboratories' Kayenta plasticity model, Kayenta's option for emulating Johnson-Cook plasticity, and Kayenta's implementation of Mie-Grüneisen equation of state.

Kayenta

Please refer to Chapter 4, for a detailed explanation of Kayenta yield functions and the hardening stress tensors.

Johnson-Cook Plasticity

In classical Johnson-Cook plasticity [49, 50], the flow stress is given by the empirical relation Eq. (5.8). In addition to publishing detailed procedures for choosing values for the material constants $\mathscr{D}_1 \ldots \mathscr{D}_5$ and σ_m, Johnson and Cook published large tables of calibration data for a wide range of materials. This, combined with the model's simplicity, has led to the Johnson-Cook flow

rule to becoming one of the most widely used thermoplasticity formulations today. It is also available as a built in material definition in nearly every commercial finite element code, furthering its use nearly 25 years after its introduction. Regular use notwithstanding, the Johnson-Cook flow stress model is, at its core, a hardening von-Mises type flow rule with strain rate hardening and temperature dependence included through the multipliers $[1+\mathscr{D}_4 \ln \dot{\varepsilon}^*]$ and $[1+\mathscr{D}_5 T^*]$. It is well established that the overly-simplistic Von-Mises flow rule is insufficient for modeling complex phenomena and materials [63, 83]. Wright [101] argues that the temperature term should be considered unsatisfactory because it either vanishes at T_{room} ($m > 0$) or is infinite there ($m < 0$); and that for the common case that $m = 1$, the initial thermal softening is determined solely by the magnitude of the melt temperature T_{melt} All three of these cases are physically unlikely, particularly in the case where the functional form of the temperature dependence of the yield strength changes due to phase changes within the material.

Furthermore, the Johnson-Cook flow stress model is empirical and, thus, its performance is highly dependent on its calibration data. In other words, simulations performed outside of the class of problems used for calibrating the model should be considered highly suspect. This leaves a large hole in the models usefulness as calibration data typically only exists for few [1] of the infinitely many loading paths.

For a comparison of the Johnson-Cook model with other thermoplasticity models as implemented in the University of Utah's Uintah MPM code see [5].

Mie-Grüneisen Equation of State

The outline of the Mie-Grüneisen equation of state closely follows the treatment given by Drumheller [30] which can be consulted for further details. Strictly speaking, the Mie-Grüneisen equation of state is not a thermoplastic model, but an equation of state relating energy, density, pressure, and temperature. However, the Mie-Grüneisen equation of state is an important component in many thermoplasticity models as it is used to compute the bulk response of the thermoplastic material undergoing large compressive deformation.

In the Mie-Grüneisen solid, it is assumed that the internal energy can be decomposed additively into "cold" and "thermal" parts

$$u = u_c(\rho) + u_T(\rho, s) \tag{6.1}$$

It is further assumed that the thermal energy can be decomposed multiplicatively in its arguments so that

$$\ln \frac{u - u_c}{u_0} = \int_{\rho_0}^{\rho} \frac{\gamma(\rho')}{\rho'} \, \mathrm{d}\rho' + \int_{s_0}^{s} \frac{1}{c_v(s')} \, \mathrm{d}s' \tag{6.2}$$

where $\gamma(\rho)$ and $c(s)$ are functional forms of the Grüneisen parameter and the specific heat. [2] Equation Eq. (6.2) now describes the equilibrium energy of the Mie-Grüneisen solid. The partial

[1] Calibration data is typically only available from uniaxial strain, uniaxial stress, and dynamic torsion tests.

[2] In this section γ refers to the Grüneisen parameter, which should not be confused with the shear strain used in

derivative of Eq. (6.2) with respect to J gives

$$\left(\frac{1}{u-u_c}\right)\left(\left(\frac{\partial u}{\partial J}\right)_u - \frac{\mathrm{d}u_c}{\mathrm{d}J}\right) = -\frac{\gamma}{J} \tag{6.3}$$

Simplifying Eq. (6.3),

$$\frac{1}{\rho_0}(\frac{\partial u}{\partial V})_s = \frac{1}{\rho_0}\frac{\mathrm{d}u_c}{\mathrm{d}V} - \frac{1}{\rho_0}c_v T\gamma\rho \tag{6.4}$$

where V is the specific volume and we have used $u-u_c = u_T = c_v T$.[3] Multiplying Eq. (6.4) by ρ_0, the equilibrium pressure in a Mie-Grüneisen solid is defined as

$$\overline{p} = \overline{p}_c + \overline{p}_T \tag{6.5}$$

where

$$\begin{aligned} \overline{p} &= -\frac{\partial u}{\partial V} \\ \overline{p}_c &= -\frac{\partial u_c}{\partial V} \\ \overline{p}_T &= \rho\gamma c_v T \end{aligned} \tag{6.6}$$

Using shock Hugoniot data as a reference instead of the cold state, the pressure in Mie-Grüneisen solid is given by

$$\begin{aligned} \overline{p} &= \overline{p}_H + \gamma_0\rho_0\,(u-u_H) \\ T &= T_H + \frac{1}{c_v}\,(u-u_H) \end{aligned} \tag{6.7}$$

where $\overline{p}_H$, u_H, and T_H are the Hugoniot pressure, energy, and temperature, respectively which are determined from the Hugoniot. The Hugoniot is given by

$$v_s = c_s + s_1 v_p + \frac{s_2}{c_s}v_p^2 \tag{6.8}$$

where c_s, s_1, and s_2 are constants determined by experiment.

A detailed description of the Mie-Grüneisen solid and derivations of Eq. (6.7) and Eq. (6.8) can be found in Chapter 4 of [30].

Incorporating Thermal Effects in Kayenta: Initial Development

In the previous chapters, overviews of thermomechanics of solids, Kayenta, and Johnson-Cook constitutive models were made. As previously noted, the equation of state in previous releases of

other sections.

[3]The relation $u_T = c_v T$ can be seen by taking the partial derivative of Eq. (6.2) with respect to s

Kayenta was purely mechanical and could not adequately predict material response to deformation when thermal effects were non-negligible, as in metals. It also goes without saying, that these previous releases of Kayenta did not satisfy the balance and dissipation laws given in Chapter 2 of [40]. Nevertheless, Kayenta's extensive feature set and ability to reduce to a number of classical plasticity models make it an attractive base model to which thermal effects can be included.

In this section, an overview of the implementation of thermomechanics in Kayenta will be made. To distinguish this version of Kayenta from previous versions which had no thermodynamic considerations, it will be referred to as "'Thermo-Kayenta'". In the sections that follow, descriptions of how thermomechanics is implemented in Thermo-Kayenta will be given.

Thermal Softening

Because Thermo-Kayenta presumes that the material, its stiffness tensor C_{ijkl}, and Grüneisen tensor are isotropic, the stress rate in Eq. (2.40) of Fuller et al. [40], is decomposed additively into isotropic and deviatoric responses

$$\dot{\underset{\approx}{\tau}} = -K^* \dot{\varepsilon}_v \underset{\approx}{\mathbf{I}} + 2G^* \mathrm{dev}\dot{\underset{\approx}{\varepsilon}} \tag{6.9}$$

where K^* and G^* are the effective tangent bulk and shear moduli, respectively and $\mathrm{dev}\dot{\varepsilon}$ is the strain deviator defined in the usual way as

$$\mathrm{dev}\dot{\varepsilon} = \dot{\varepsilon} - \frac{1}{3}\dot{\varepsilon}_v \underset{\approx}{\mathbf{I}} \tag{6.10}$$

The temperature response, in general, is given by

$$\dot{T} = \dot{T}(K, \dot{\varepsilon}) \tag{6.11}$$

The specific forms of $\dot{T}(K, \dot{\varepsilon})$ and the effective bulk and shear moduli are determined by the value of the user input **IEOSID**. If **IEOSID**=0 (default), then the effective moduli are computed by

$$\begin{aligned} K^* &= K(I_1)\left(1 - \frac{\rho^2}{\rho_0} T c_v \gamma^2\right) \\ G^* &= G(J_2) \end{aligned} \tag{6.12}$$

and

$$\dot{T}(K, \dot{\varepsilon}) = -\frac{\rho}{\rho_0} T \gamma \dot{\varepsilon}_v \tag{6.13}$$

where $K(I_1)$ and $G(J_2)$ are the standard non-linear elastic tangent bulk and shear moduli functions already in Kayenta (see Eq. (4.9) and Eq. (4.10)). If $\gamma = 0$, Eq. (6.12) reduces to the same bulk modulus functions used in previous releases of Kayenta.

Note that the effective bulk modulus in Eq. (6.12) is the standard *isentropic* bulk modulus and requires that $K(I_1)$ be the *isothermal* bulk modulus. However, as explained in the Kayenta User's Manual, the nonlinear function $K(I_1)$ returns a value which is an interpolation between the isothermal and isentropic bulk moduli. Thus, if **IEOSID**= 0, it is recommended that either: 1) γ be set to zero if $B1 - B2$ are non-zero, or 2) $B1 - B2$ be set to zero if γ is non-zero.

If **IEOSID**= 0 and $B1 - B2$ are set equal to zero, Thermo-Kayenta reduces to thermoelasticity as explained in [40], Chapter 2 of Fuller et al..

If **IEOSID**= 1, the effective tangent elastic moduli are computed from an equation of state specified in the subroutine EOSMODULI. Currently, Thermo-Kayenta uses SNL's Kerley Mie-Grüneisen equation of state which takes as input the current density and energy and returns the updated pressure, temperature, and soundspeed. K^* and G^* are then computed by

$$\begin{aligned} K^* &= \rho {c_s}^2 \\ G^* &= 3K^* \frac{1-2\nu}{2(1+\nu)} \end{aligned} \tag{6.14}$$

where c_s is the bulk speed of sound in the material and ν is Poisson's ratio and is assumed to be constant.

If **IEOSID** = 3, Kayenta optionally calls the host code for the Elastic moduli (if supported by the host code).

If **IEOSID** = 5 or 6, Kayenta computes the elastic bulk and shear moduli using updated equations of state developed by Tom Dewers and Pania Newell at SNL. These state of these equations of state is currently currently in flux and are under active development. Contact the Kayenta developers for more information.

To date, every installation of Kayenta has approximated the strain rate by the symmetric part of the velocity gradient, $\underset{\approx}{\mathbf{D}}$. Thus, u is updated internally in Thermo-Kayenta by

$$u = \frac{1}{\rho_0} \underset{\approx}{\tau} : \underset{\approx}{\mathbf{D}} \tag{6.15}$$

Thermoelastic Limit

If the trial elastic stress found in the previous section lies outside of the yield surface given by Eq. (4.18), the tentatively presumed elastic loading is invalidated and the solution to the equations governing thermoplastic loading must be solved. For the case of a thermoplastic material, the yield criterion in Eq. (4.28) is modified to allow for thermal softening in a way similar to Johnson-Cook plasticity by including a non-dimensional multiplier in the yield function, as follows:

$$\sqrt{J_2^{\xi}} = \frac{f_f(I_1) f_c(I_1, \kappa)}{\Gamma(\overline{\theta}^{\xi})} \left(1 - (T^*)^m\right) \tag{6.16}$$

For the case that $f_c = 1$ and $\Gamma = 1$, Eq. (6.16) reduces to

$$\sqrt{J_2^{\xi}} = (a_1 - a_3 \exp[-a_2 I_1] + a_4 I_1)\,(1 - (T^*)^m) \tag{6.17}$$

where m is taken to be the same user specified constant as in Johnson-Cook plasticity. T^* is defined in the same way as in the Johnson-Cook plasticity model:

$$T^* = \frac{T - T_0}{T_m - T_0} \tag{6.18}$$

Evolution Equations

Kinematic Hardening Backstress Tensor

If kinematic hardening is enabled, the evolution of the backstress in a thermoplastic material is revised from Eq. (4.79) to include thermal effects as follows:

$$\dot{\alpha} = \dot{\varepsilon} H_\alpha^\star \tag{6.19}$$

where $H_\alpha^\star$ is given by

$$H_\alpha^\star = H g(\alpha^*) \mathrm{dev} \frac{\partial \varphi}{\partial \xi} \tag{6.20}$$

and

$$g(\alpha^*) = g(\alpha)\,(1 - (T^*)^m)\,. \tag{6.21}$$

Plastic Temperature Evolution

Currently, all plastic work is converted to heat, thus the temperature evolves according to

$$\dot{T} = \dot{T}^{\mathrm{trial}} + \frac{1}{\rho_0}\left[\left(\rho_0 T \gamma + \frac{1}{c_v} I_1\right)\dot{\varepsilon}_v^p + \frac{1}{c_v}\mathrm{dev}(\dot{\underset{\approx}{\tau}}) : \mathrm{dev}\dot{\varepsilon}^p\right] \tag{6.22}$$

Chapter 7

Rate Dependence

The governing equations discussed so far are rate independent, so they only apply for quasistatic loading. Under high strain rates, the elastic response of a material occurs almost instantaneously, but the physical mechanisms that give rise to observable inelasticity can *not* proceed instantaneously. Materials have inherent "viscosity" or "internal resistance" that retards the rate at which damage can accumulate. For example, cracks grow at a finite speed — they cannot change instantaneously from one size to another. If a stress level is high enough to induce crack growth, then the quasistatic solution for material damage will not be realized unless sufficient time elapses to permit the cracks to change length. Likewise, void collapse takes finite time. Simple inertia also contributes to rate dependence. During the time that cracks are growing towards the quasistatic solution, the stress will drop down towards the quasistatic solution. Until sufficient time has elapsed for the material to equilibrate, the stress state will lie *outside* the yield surface. If the applied strain is released any time during this damage accumulation (or plastic flow) period, then the total damage (or plastic strain) will be ultimately lower than it would have been under quasistatic loading through the same strain path.

Viscoplasticity model overview

The evolution of the yield function, and the very character of the inelastic deformation itself, can be dramatically altered by the rate at which loads are applied. In the limit of extraordinarily high load rates (as near the source of an explosion), material response is essentially elastic because insufficient time exists for plasticity to fully develop. At high strain rates, the equation of state (i.e., the pressure-volume part of the elasticity) plays the predominant role in material response. To allow for rate dependence, an overstress model is used. The user specifies a *relaxation* parameter governing the characteristic speed at which the material can respond inelastically. If the loads are applied over a time interval that is significantly smaller than the characteristic response time, then essentially no inelasticity will occur during that interval. If, on the other hand, the loads are applied slowly (as in quasistatic testing), then inelasticity will be evident.

Kayenta uses a generalized Duvaut-Lions [31, 14] rate-sensitive formulation, illustrated qualitatively in Fig. 7.1. Consider a loading increment Δt during which the strain increment is prescribed to be $\Delta \underset{\approx}{\varepsilon}$. Two limiting solutions for the updated stress can be readily computed: (1) the low-rate (quasistatic) solution $\underset{\approx}{\sigma}^L$ which is found by solving the rate-independent Kayenta equa-

tions described previously, and (2) the high-rate solution $\underset{\approx}{\sigma}^H$ corresponding to insufficient time for any plastic damage to develop so that it is simply the trial elastic stress. As explained below and illustrated in Fig. 7.1, the Duvaut-Lions rate formulation is based on a viscoplastic differential equation, the solution of which shows that the updated stress will be (approximately) a linear interpolation between the low-rate quasistatic plasticity solution $\underset{\approx}{\sigma}^L$ and the high-rate purely elastic solution $\underset{\approx}{\sigma}^H$. In other words, there exists a scalar η between 0 and 1 that depends on the strain rate such that

$$\underset{\approx}{\sigma} \approx \underset{\approx}{\sigma}^L + \eta(\underset{\approx}{\sigma}^H - \underset{\approx}{\sigma}^L). \tag{7.1}$$

The update for internal state variables is structured similarly, but uses a somewhat different weighting factor, as explained below. For both the stress and internal state variable updates, the interpolation factor η varies from 1 at high strain rates (when Δt is small) to 0 at low strain rates (when Δt is large), as illustrated in the graph inset of Fig. 7.1, where the abscissa is normalized by a factor τ called the material's "characteristic" response time. At the end of this chapter, we will describe how Kayenta assigns a value for the characteristic material response time τ. Incidentally, for simplicity, Fig. 7.1 shows a stationary yield surface. In general, the yield surface will evolve in size or translate according to the hardening rules described earlier.

A time interval Δt is deemed to be "long" if $\Delta t \gg \tau$. A time interval is "short" if $\Delta t \ll \tau$. Soon we solve the viscoplastic equations to prove that, if the initial stress is on the yield surface, then the high-rate scale factor internal state variable (ISV) is

$$\eta = \frac{1 - \mathrm{e}^{-\Delta t/\tau}}{\Delta t/\tau}. \tag{7.2}$$

This is also the rate factor for the stress at the *onset of yielding* when $\underset{\approx}{\sigma}$ and $\underset{\approx}{\sigma}^{\mathrm{low}}$ coincide. At the end of a viscoplastic step, the final stress state will not lie on the yield surface. We will prove that, in this case, the scale factor is smaller than the value cited in Eq. (7.2). Consequently, the "attraction" that the dynamic stress has for the quasistatic solution increases somewhat as the stress moves farther from the yield surface.

Referring to Eq. (7.2), the η weighting factor is large when the time step is significantly smaller than the characteristic time required for the material's plasticity solution to develop. Effects of plasticity are apparent in Kayenta only when the time interval is long or when the characteristic material response time is short so that η will be small. In this case, according to Eq. (7.1), the solution will be near the quasistatic (low-rate) solution $\underset{\approx}{\sigma}^L$.

Fig. 7.1 illustrates that the viscoplastic solution will follow a trajectory that is similar to the quasistatic solution except displaced from the yield surface. Consequently, experimental data for high-rate loading scenarios have the *appearance* of inducing a higher yield stress in the material. Unlike some plasticity models, Kayenta does *not* alter the material yield stress as a function of strain rate. Instead, the overstress model accomplishes the same effect in a much more physically justifiable manner.

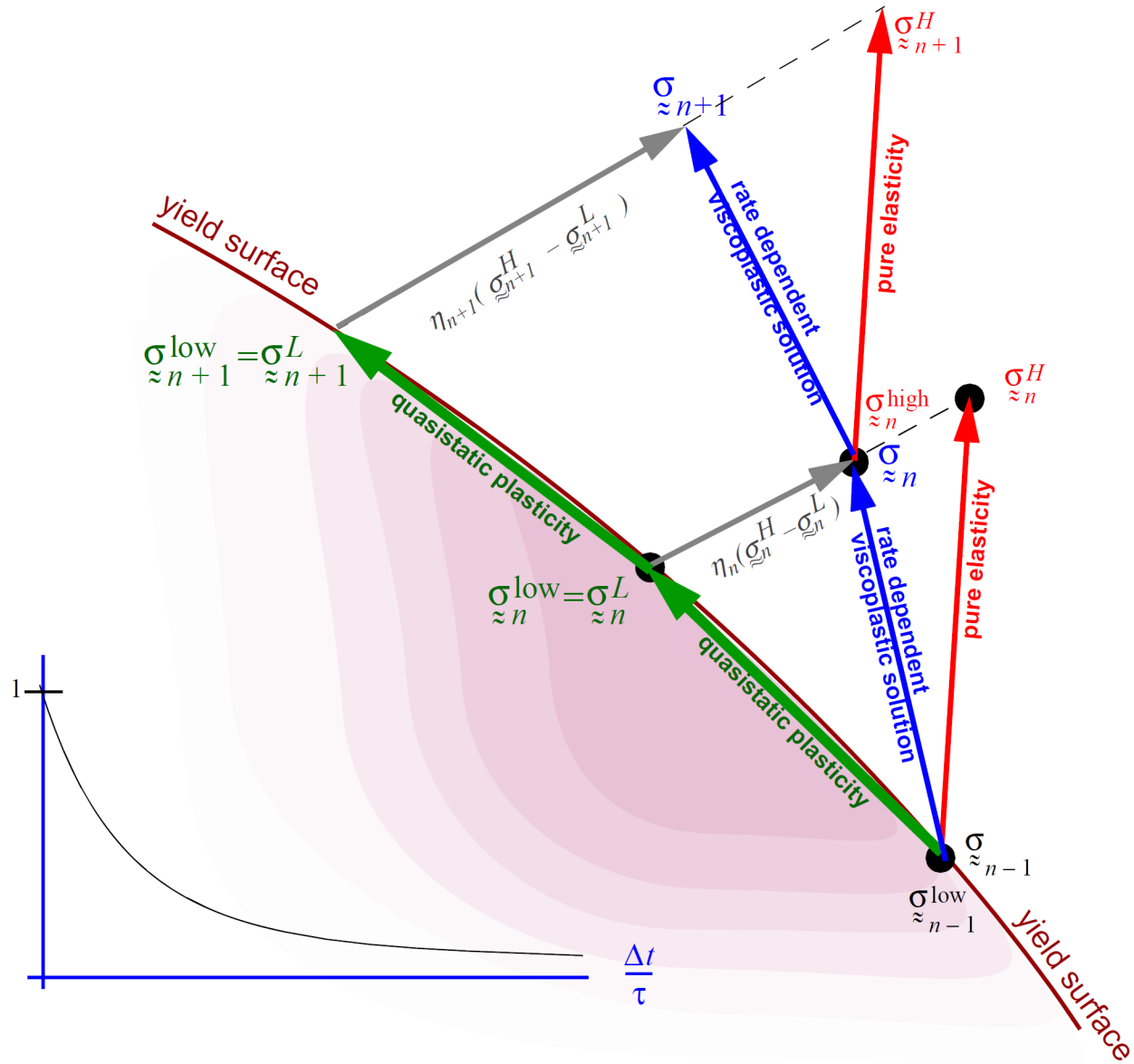

Figure 7.1. Rate dependence. For a given strain increment, two limiting solutions can be readily found. The "low rate" solution $\underset{\approx}{\sigma}^L$, which lies on the yield surface, is the solution to the rate independent Kayenta governing equations. The high rate solution $\underset{\approx}{\sigma}^H$ is simply the trial elastic stress. The actual updated rate-dependent viscoplastic stress $\underset{\approx}{\sigma}$ falls between these two limiting case solutions so that $\underset{\approx}{\sigma} = \underset{\approx}{\sigma}^L + \eta(\underset{\approx}{\sigma}^H - \underset{\approx}{\sigma}^L)$. The inset graph shows how the scale factor η varies with the loading interval. If the loading interval is long relative to the material's characteristic response time τ, then sufficient time exists to fully develop plastic response and the updated solution therefore coincides with the quasistatic solution $\underset{\approx}{\sigma}^L$. If the loading interval is considerably shorter than the material's characteristic response time, then the solution will be the high-rate elastic solution.

Viscoplasticity model derivation

In the context of viscoplasticity, an inviscid (rate-independent) solution $\underset{\approx}{\sigma}^L$ for the stress is presumed to exist. Likewise inviscid (rate-independent) solutions q^L are presumed available for the internal state variables, here denoted collectively by "q". These limiting case solutions are merely the solutions of the rate-independent Kayenta equations described in earlier chapters. Viscous effects are incorporated by presuming that the strain rate is decomposed as the sum of an elastic part $\dot{\underset{\approx}{\varepsilon}}^e$ plus a *viscoplastic* part $\dot{\underset{\approx}{\varepsilon}}^{vp}$:

$$\dot{\underset{\approx}{\varepsilon}} = \dot{\underset{\approx}{\varepsilon}}^e + \dot{\underset{\approx}{\varepsilon}}^{vp}. \tag{7.3}$$

The viscoplastic part of the strain rate includes both the usual plastic strain rate from the quasistatic (low-rate) solution as well as additional (retarding) contributions resulting from viscosity. The viscoplastic strain rate is governed by

$$\dot{\varepsilon}_{ij}^{vp} = \frac{1}{\tau} C_{ijkl}^{-1} [\sigma_{kl} - \sigma_{kl}^{\text{low}}] \tag{7.4}$$

The fourth-order tensor C_{ijkl}^{-1} is the elastic compliance (inverse of the stiffness), τ is a material parameter called the relaxation time, and $\underset{\approx}{\sigma}^{\text{low}}$ is the rate-independent stress solution whose value at the beginning of a time increment Δt is tracked as an extra state variable (called **QSSIGXX**, **QSSIGYY**, etc. in Appendix B).[1] At the end of the time interval, $\underset{\approx}{\sigma}^{\text{low}}$ ultimately has the value $\underset{\approx}{\sigma}^L$, which is found by integrating the rate-independent Kayenta equations from the earlier chapters. During viscoplastic loading, each internal state variable q is presumed to vary according to

$$\dot{q} = \frac{-1}{\tau} [q - q^{\text{low}}]. \tag{7.5}$$

Here q^{low} is the value of the internal state variable (κ or $\underset{\approx}{\alpha}$) throughout the time interval, initially being equal to q_0 at the beginning of the step, and (through application of Kayenta's rate-independent equations in earlier chapters) ultimately equalling the low rate solution q^L at the end of the step. Like the inviscid quasistatic stress, the inviscid quasistatic ISVs (**QSEL**, **QSBSXX**, etc.) must be tracked as distinct extra state variables.

The stress rate is, as usual, given by the elastic stiffness acting on the elastic part of the strain rate: $\dot{\sigma}_{ij} = C_{ijkl}\dot{\varepsilon}_{kl}^e$. Thus, using Eq. (7.3)), the stress rate may be written

$$\dot{\sigma}_{ij} = \dot{\sigma}_{ij}^{\text{high}} - \frac{1}{\tau}(\sigma_{ij} - \sigma_{ij}^{\text{low}}), \qquad \text{where} \qquad \dot{\sigma}_{ij}^{\text{high}} \equiv C_{ijkl}\dot{\varepsilon}_{kl}. \tag{7.6}$$

Here, $\dot{\sigma}_{ij}^{\text{high}}$ is the elastic trial stress rate, and therefore $\sigma_{ij}^{\text{high}}$ is the time varying elastic trial stress that ultimately equals the high-rate solution σ_{ij}^H at the end of the step.

[1] The "low" or "inviscid" stresses must be tracked independently. They cannot be inferred by projecting the actual stress onto the yield surface. Attempting to do so causes undesirable results in rate-dependent load-unload cycles.

Eq. (7.6) is a set of linear first-order differential equations which may be integrated exactly over a time step with the use of integrating factors [42] *provided that* σ_{ij}^{low} *is known as a function of time throughout the time step*. In principle, we would need to solve the rate independent equations analytically over the entire time step to integrate Eq. (7.6) exactly, but this is not tractable in practice. In what follows, we will describe how the time history of σ_{ij}^{low} can instead be well approximated over the step. First, let's introduce a change of variables by defining

$$u_{ij} \equiv \sigma_{ij} - \sigma_{ij}^{\text{high}}, \tag{7.7}$$

so that the governing equation for the stress rate may be written

$$\dot{u}_{ij} = -\frac{1}{\tau}(u_{ij} + \sigma_{ij}^{\text{high}} - \sigma_{ij}^{\text{low}}). \tag{7.8}$$

This equation can be solved exactly if the time variation of $\underset{\approx}{\sigma}^{\text{high}} - \underset{\approx}{\sigma}^{\text{low}}$ is known throughout the time step.[2] Time variation of $\underset{\approx}{\sigma}^{\text{low}}$ is governed by known quasistatic rate equations. Consequently, the dynamic accuracy can be maximized by presuming that the *rate* of $\underset{\approx}{\sigma}^{\text{low}}$ is constant over the step so that $\underset{\approx}{\sigma}^{\text{low}}$ itself is approximated to vary linearly over the step.

Recall that the final solution $\underset{\approx}{\sigma}^{H} - \underset{\approx}{\sigma}^{L}$ can be presumed known at the end of the step because $\underset{\approx}{\sigma}^{H}$ is found by integrating the elasticity equations and $\underset{\approx}{\sigma}^{L}$ is found separately by integrating the inviscid quasistatic plasticity equations. Similarly, the difference $\underset{\approx}{\sigma}^{\text{high}} - \underset{\approx}{\sigma}^{\text{low}}$ is known at the beginning of the step because $\underset{\approx}{\sigma}^{\text{high}}$ is $\underset{\approx}{\sigma}$ at the beginning of the step and $\underset{\approx}{\sigma}^{\text{low}}$ is retrieved from the saved quasistatic stress extra state variable array. The high-rate stress $\underset{\approx}{\sigma}^{\text{high}}$ is simply the elastic trial stress. Thus, it varies linearly through time from its initial to final value (with small higher-order nonlinearities if the strain rate and/or elastic moduli are not constant). The quasistatic stress rate $\dot{\underset{\approx}{\sigma}}^{\text{low}}$ is an oblique projection of the trial stress rate onto the yield surface, so $\underset{\approx}{\sigma}^{\text{low}}$ also varies approximately linearly through time (with nonlinear effects from flow potential surface curvature being higher order). Thus, we may call on the mean value theorem to assert that

$$(\underset{\approx}{\sigma}^{\text{high}} - \underset{\approx}{\sigma}^{\text{low}}) \approx (\underset{\approx}{\sigma}^{H} - \underset{\approx}{\sigma}^{L})\left(\frac{t-t_0}{\Delta t}\right) + (\underset{\approx}{\sigma}_0^{\text{high}} - \underset{\approx}{\sigma}_0^{\text{low}})\left(1 - \frac{t-t_0}{\Delta t}\right) \tag{7.9}$$

With this approximation, the ODE in Eq. (7.8) may be solved exactly. Since $\underset{\approx}{\sigma}_0^{\text{high}}$ equals $\underset{\approx}{\sigma}_0^{\text{low}}$ at the beginning of the step, the initial condition is that $u_{ij} = 0$ when $t = t_0$. Integrating the ODE, evaluating the result at the end of the step, and applying the definition of u_{ij} to obtain the updated solution for σ_{ij} eventually gives

$$\boxed{\underset{\approx}{\sigma}^{\text{FINAL}} = \underset{\approx}{\sigma}^{L} + R_H(\underset{\approx}{\sigma}^{H} - \underset{\approx}{\sigma}^{L}) + r_h(\underset{\approx}{\sigma}_0^{\text{high}} - \underset{\approx}{\sigma}_0^{\text{low}})}, \tag{7.10}$$

where

$$R_H = \frac{1 - \mathrm{e}^{-\Delta t/\tau}}{\Delta t/\tau} \qquad \text{and } r_h = \mathrm{e}^{-\Delta t/\tau} - R_H \tag{7.11}$$

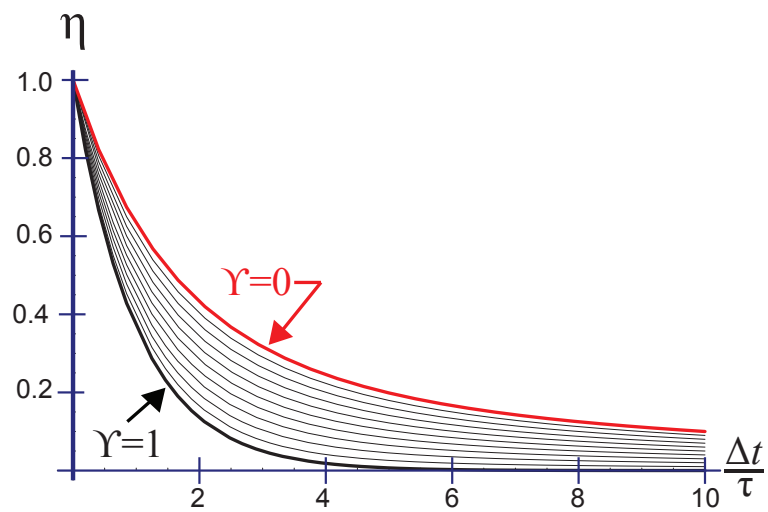

Figure 7.2. High-rate weighting factor at various initial states. The largest weight factor (upper red curve) applies when the initial stress is on the yield surface. The factor is lower if the initial state is already off the yield surface at the beginning of the step.

With the presence of the last term, the solution in Eq. (7.10) is not *precisely* of the form shown in Eq. (7.1) unless $\underset{\approx}{\sigma}_0^{\text{high}} = \underset{\approx}{\sigma}_0^{\text{low}}$. As seen in timestep "$n-1$" in Fig. 7.1, the initial values for the "high" and "low" rate paths coincide only at the *onset* of plasticity. Eq. (7.10) can be put into the form of Eq. (7.1) if we approximate that $\underset{\approx}{\sigma}_0^{\text{high}} - \underset{\approx}{\sigma}_0^{\text{low}}$ is *parallel* to $\underset{\approx}{\sigma}^H - \underset{\approx}{\sigma}^L$. With this assumption, Eq. (7.1) becomes

$$\underset{\approx}{\sigma}^{\text{FINAL}} = \underset{\approx}{\sigma}^L + \eta(\underset{\approx}{\sigma}^H - \underset{\approx}{\sigma}^L), \tag{7.12}$$

where

$$\eta = R_H + r_h \Upsilon \tag{7.13}$$

and

$$\Upsilon \equiv \frac{\|\underset{\approx}{\sigma}_0^{\text{high}} - \underset{\approx}{\sigma}_0^{\text{low}}\|}{\|\underset{\approx}{\sigma}^H - \underset{\approx}{\sigma}^L\|} \tag{7.14}$$

Fig. 7.2 shows how the weighting factor η varies with the stress difference ratio Υ appearing in the last term of Eq. (7.13). For plastic loading, Υ equals 0 only when the initial state is on the yield surface. Otherwise, beyond this onset of yielding moment, Υ increases, eventually asymptoting to 1 under steady strain rates. The lowering of the rate factor η caused by nonzero Υ makes the dynamic stress more strongly attracted to the quasistatic solution as the distance between them increases.

[2]Ref. [14] provides a slightly different formulation for solving the same set of governing equations; that publication might clarify what is given here in this chapter.

For the rate dependent update of internal state variables, Eq. (7.5) can be integrated analytically if the time variation of q over the step is approximated by $q^{\text{low}} = q^H + (q^L - q^H)(t - t_0)/\Delta t$. The resulting solution for q is

$$\boxed{q^{\text{FINAL}} = q^L + R_H(q^H - q^L)}, \tag{7.15}$$

where the high-rate weight factor R_H is the same as in Eq. (7.11). The weight factor R_H for the internal state variables differs from the weight factor η for the stress because the two problems have different initial conditions. Recall that the material responds elastically at extremely high rates. Hence, because the internal state variables can evolve only when plasticity occurs, the high rate solution q^H for any internal state variables is simply its value at the beginning of the time increment.

Limiting case

If a strain rate is held constant for a long enough period then the difference between the dynamic stress σ_{ij} and the inviscid stress σ_{ij}^L will sometimes reach a steady-state value in the laboratory. In this case, the equations outlined in this chapter imply that this steady state stress difference is given by

$$\sigma_{ij} - \sigma_{ij}^L = \frac{\tau}{\chi} P_{ij} Q_{mn} \dot{\varepsilon}_{mn}, \tag{7.16}$$

where χ, P_{ij}, $Q_i j$ are defined in Eq. (4.101).

In the very simplified context of non-hardening von Mises plasticity, this equation becomes

$$\sigma_{ij} - \sigma_{ij}^L = (2G\tau) S_{ij} S_{mn} \dot{\varepsilon}_{mn}, \tag{7.17}$$

where G is the shear modulus and S is a unit tensor in the direction of the stress deviator. For example,

$$[\hat{S}] = \frac{1}{\sqrt{2}} \begin{bmatrix} 0 & 1 & 0 \\ 1 & 0 & 0 \\ 0 & 0 & 0 \end{bmatrix} \text{ for simple shear} \tag{7.18}$$

$$[\hat{S}] = \frac{1}{\sqrt{6}} \begin{bmatrix} 2 & 0 & 0 \\ 0 & -1 & 0 \\ 0 & 0 & -1 \end{bmatrix} \text{ for uniaxial (axisymmetric) loading} \tag{7.19}$$

Therefore, in the case of simple shear for non-hardening von Mises plasticity, Eq. (7.17) implies that

$$\sigma_{12} - \sigma_{12}^L = 2G\tau\dot{\varepsilon}_{12} \qquad \text{for simple shear} \tag{7.20}$$

$$\sigma_1 - \sigma_{11}^L = \frac{4G}{3}\tau\dot{\varepsilon}_{11} \qquad \text{for uniaxial (axisymmetric) loading} \tag{7.21}$$

These simple analytical results can be used to trend-test the numerical implementation of rate sensitivity, as described in Fig. 7.3. See Fig. 3.4 (pg. 41) for an explanation of the post-yield slope even though the material is non-hardening.

Time histories for the overstress and the three strains (elastic, plastic, and total) are contrasted in Fig. 7.4.

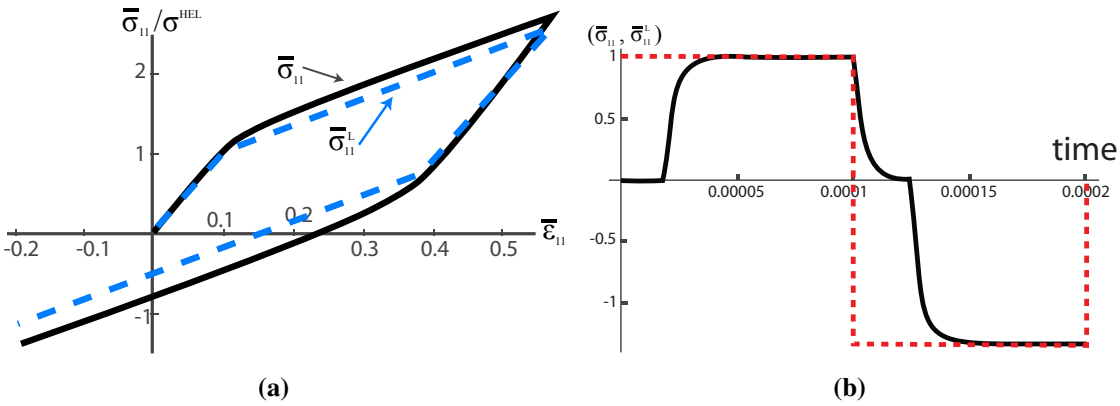

Figure 7.3. Rate dependence in uniaxial strain loading of a nonhardening pressure-insensitive material. In the stress-strain plot, the normalizer is the quasistatic uniaxial yield stress. The dynamic (black) stress-strain plot exhibits an apparent increase in strength relative to the quasistatic (dashed blue) solution. This rate-induced stress difference is plotted in the second figure (normalized by the peak value), where the dashed red line shows the analytical asymptote envelope from Eq. (7.21). This calculation included a lower strength in tension (interestingly, the *difference* between dynamic and quasistatic strengths is higher in tension).

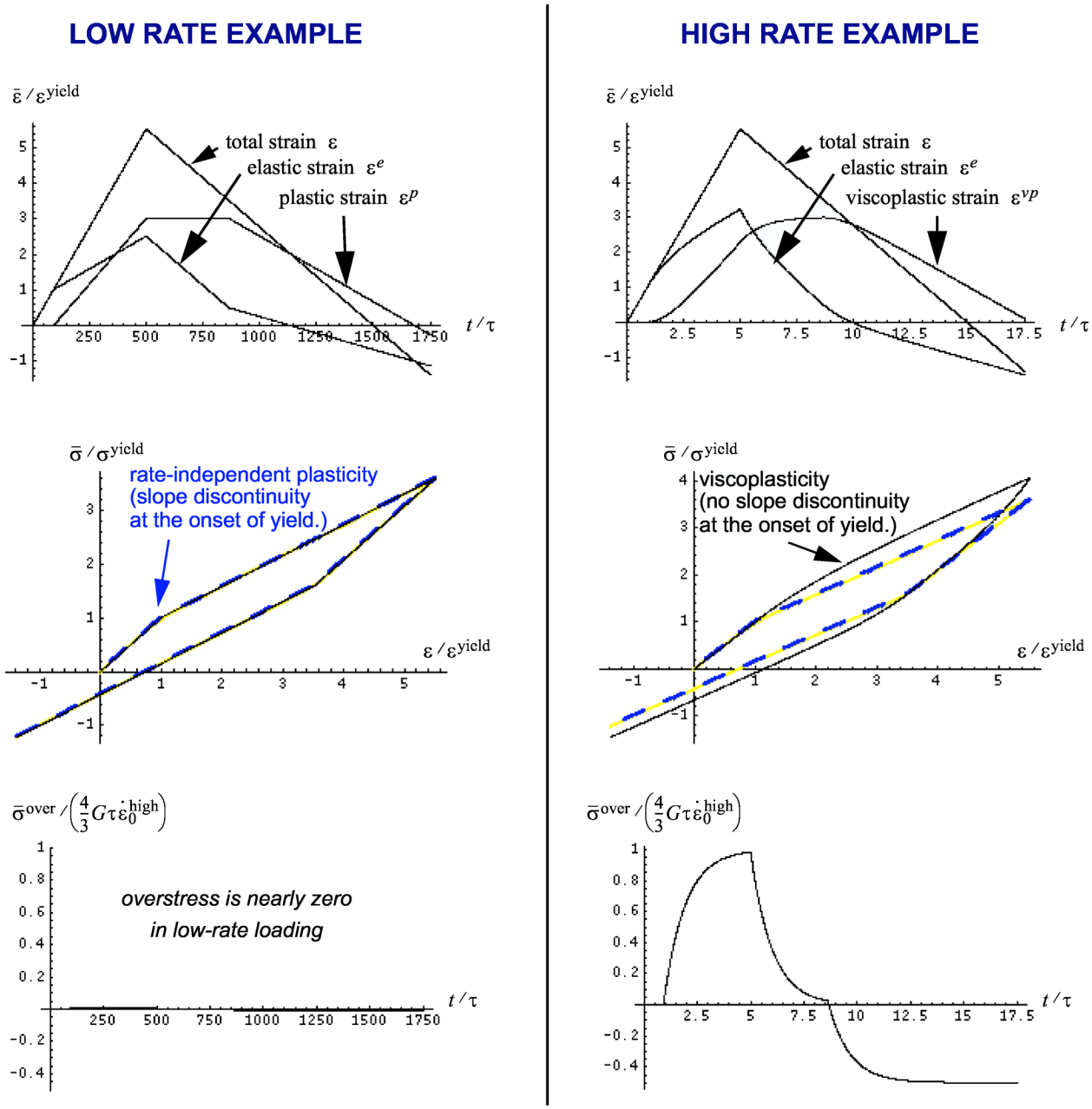

Figure 7.4. **The effect of strain rate in uniaxial strain.**

Assigning a value to the characteristic material time

Kayenta permits the user to control the value of the characteristic time through the use of up to seven parameters, T_1 through T_7. In the present build of Kayenta, these T-parameters are used to assign a value of the characteristic time according to the following formulas:

$$\tau = \begin{cases} f(\dot{\varepsilon}^{\text{equiv}}) & \text{if} \quad \varepsilon_v^p \geq 0 \\ T_6 f(\dot{\varepsilon}^{\text{equiv}})(1 + < T_7(\overline{I_1} + T_5) >^2) & \text{if} \quad \varepsilon_v^p < 0 \quad \text{and} \quad I_1 \leq T_5 \end{cases} \tag{7.22}$$

where

$$f(\dot{\varepsilon}^{\text{equiv}}) = \begin{cases} T_1 & \text{if} \quad T_2 = 0 \\ T_1 \left(\frac{1}{\tau^{\text{ref}} \dot{\varepsilon}^{\text{equiv}}} \right)^{T_2} & \text{if} \quad T_2 \neq 0 \end{cases}, \tag{7.23a}$$

$$\dot{\varepsilon}^{\text{equiv}} = \|\dot{\underset{\approx}{\varepsilon}}\|, \tag{7.23b}$$

and

$$< x >= \begin{cases} 0 & \text{if} \quad x \leq 0 \\ x & \text{if} \quad x > 0 \end{cases} \qquad \text{(Macaulay brackets.)} \tag{7.24}$$

Here, τ^{ref} is a constant equal to 1.0 s. If a *constant* characteristic time τ is desired, then set $T_1 = \tau$, and all other T's to zero. Fig. 7.3 used a constant τ, as did the simple-shear rate-dependent simulation shown in Fig. 9.9(b) (pg. 158). Suitability of this model of rate-dependence for predicting laboratory data is illustrated in Fig. 10.9 (pg. 204). The branch in the above formulas, giving different characteristic times depending on whether the material is plastically dilatating ($\varepsilon_v^p \geq 0$) or plastically compacting ($\varepsilon_v^p < 0$), is motivated by an observation that materials tend to have a greater rate sensitivity in compaction relative to dilatation [35].

Kayenta's formulas for characteristic response time continue to be in a state of flux in order to better support user-specification of laboratory data for the apparent steady-state strength as a function strain rate, which is what is typically available in the literature [90]. These revisions may result in interpretations of the T-parameters that differ from what is documented above. Therefore, since this aspect of the model is in flux, users of 2011 and later builds of Kayenta should consult with the model developers for assigning rate dependence parameter values. Previous versions of this manual warned about incompatibility between softening and overstress modeling, but the current version allows both damage and rate dependence to be active simultaneously.

Thermodynamics considerations

In pre-2009 builds, Kayenta's equation of state was incorporated within the purely mechanical model — it contained no thermal terms (i.e., terms involving material properties such as the

specific heat and Grüneisen parameter). Nonetheless, Kayenta's nonlinear elasticity model had been moderately well fitted to Hugoniot shock data. In thermodynamics, pressure is typically expressed as a function of two variables: the density ρ and a thermal variable (usually temperature or entropy). For example,

$$\overline{p} = f(\rho, T) \tag{7.25}$$

In thermodynamics, you can always use a purely mechanical equation of state if you restrict the class of allowable problems so that one or two of the thermal variables are inter-related in some known way. If, for example, you restrict attention to isothermal loading, then the pressure will be expressible in the form $\overline{p} = F(\rho)$, where the "material constants" in the equation (such as the bulk modulus) must be set to their isothermal values. Likewise, if you can consider only adiabatic loading, then the pressure is again expressible as a mechanical function if the parameters such as the bulk modulus are set to their adiabatic values.

Through the above rather hand-waving reasoning, the pre-2009 builds of Kayenta (called the Sandia GeoModel) were able to perform adequately under high rate shock loading. Recent work has included incorporation of any user-specified equation of state (see page 107). This work has included verification that Kayenta can (with appropriately matched parameters) reproduce the high-rate thermoelastic-plastic material response predicted using the Johnson-Cook plasticity model in conjunction with a Mie-Grüneisen equation of state.

This page intentionally left blank.

Chapter 8

Kayenta Numerical Solution scheme

Aside from kinematic hardening and limited elastic anisotropy from joints, Kayenta is isotropic and therefore the yield function depends only on principal stresses. An eigenvalue analysis is avoided by casting the yield function in terms of stress invariants. The principal stress directions (eigenvectors) are not needed to evaluate the yield function. For any isotropic elasticity model, however, evolution of plastic response must allow for rotation of principal stress directions caused by the elastic portion of the loading. Thus, the governing equations must be cast in incremental tensorial form, requiring all six independent components of symmetric tensors to be passed to the model. Careful numerical integration schemes [9] are required to ensure accuracy and convergence.

This chapter begins with a description of how Kayenta is to be used within a host (finite-element) code, followed by a discussion of the influence of material softening on *field-scale* stability (i.e., stability of the spatial finite-element solution, not stability of Kayenta's internal time integration algorithm). Next, Kayenta installation instructions are provided that describe the public[1] subroutines and memory requirements. Following a summary of plotable Kayenta output, Kayenta's time integration algorithm is briefly summarized.

Role of Kayenta within a finite-element program

Kayenta is designed for use in host codes (typically finite-element programs) that solve the momentum balance PDE,

$$\frac{\partial \sigma_{ij}}{\partial x_j} + f_i = \rho a_i, \tag{8.1}$$

where σ_{ij} is the *spatial* Cauchy stress tensor (denoted $\underset{\approx}{\sigma}^{\text{spatial}}$ in Eq. (3.33)), x_j is the spatial position vector, f_i is the body force per unit volume, ρ is the mass density, and a_i is the material acceleration that is related to the spatial velocity field by material time derivative

$$a_i = \frac{\partial v_i}{\partial t} + \frac{\partial v_i}{\partial x_j} v_j = \frac{\mathrm{D} v_i}{\mathrm{D} t} = \left(\frac{\partial v_i}{\partial t} \right)_{\underset{\sim}{\mathbf{X}}}. \tag{8.2}$$

[1] i.e., called directly from the host code.

Here, $\underset{\sim}{\mathbf{X}}$ is the time-zero reference position vector, which serves to identify Lagrangian material points. The spatial position vector $\underset{\sim}{\mathbf{x}}$ is related to the reference position $\underset{\sim}{\mathbf{X}}$ through the deformation mapping function, such that the deformation gradient tensor is

$$F_{ij} = \left(\frac{\partial x_i}{\partial X_i} \right)_t . \tag{8.3}$$

The stress and velocity fields (as well as displacement or velocity boundary conditions) are known at the beginning of each time step, so that application of Eq. (8.1) permits evaluation of the acceleration field. In most host codes, the updated position of a material particle is computed to second-order accuracy with respect to the time step Δt through application of

$$\underset{\sim}{\mathbf{x}}^{n+1} = \underset{\sim}{\mathbf{x}}^{n} + \left(\frac{\partial \underset{\sim}{\mathbf{x}}}{\partial t} \right)^{n}_{\underset{\sim}{\mathbf{X}}} \Delta t + \frac{1}{2} \left(\frac{\partial^2 \underset{\sim}{\mathbf{x}}}{\partial t^{2^2}} \right)^{n}_{\underset{\sim}{\mathbf{X}}} (\Delta t)^2 \tag{8.4}$$

or

$$\underset{\sim}{\mathbf{x}}^{n+1} = \underset{\sim}{\mathbf{x}}^{n} + \underset{\sim}{\mathbf{v}}^{n} \Delta t + \frac{1}{2} \underset{\sim}{\mathbf{a}}^{n} (\Delta t)^2 . \tag{8.5}$$

Equivalently,

$$\underset{\sim}{\mathbf{x}}^{n+1} = \underset{\sim}{\mathbf{x}}^{n} + \underset{\sim}{\mathbf{v}}^{n+\frac{1}{2}} \Delta t , \tag{8.6}$$

$$\text{where} \qquad \underset{\sim}{\mathbf{v}}^{n+\frac{1}{2}} \equiv \underset{\sim}{\mathbf{v}}^{n} + \frac{1}{2} \underset{\sim}{\mathbf{a}}^{n} \Delta t . \tag{8.7}$$

Different codes might differ in the details.[2]

To date, all installations of Kayenta have approximated the *unrotated* strain rate by the *unrotated* symmetric part of the velocity gradient defined in Eq. (4.3), evaluated at the half-step by using the velocity field in Eq. (8.7). Kayenta integrates the unrotated strain rate to predict the *unrotated* stress at the end of the step, which must then be rotated into the spatial configuration by the host code. As mentioned on page 44 (and clarified later in this chapter), optimizing the accuracy of the *spatial* solution for problems involving massive material rotation requires the host code to apply its un/rotation operations using polar rotation tensors that are consistent with the part of the time step (beginning, half, or end) at which un/rotation operations are required.

Of course, once Kayenta and any other constitutive models in the problem have been applied to determine stresses at the end of a time step, Eq. (8.1) may be integrated again to update the acceleration field, thus launching a new timestep cycle.

[2]For example, material point method (MPM) codes typically solve the momentum equation on an overlaid grid. The grid accelerations from the discretized equations of motion are mapped to particles (using standard FEM mapping on the grid), where particle velocities are updated by integrating particle acceleration. Next, particle velocities are mapped back to the grid to obtain grid nodal velocities for evaluating the velocity gradient needed by the constitutive model. Particle positions are updated by mapping grid velocities to the particles and then integrating the particle velocity through time [86].

Spatial stability (mesh dependence/loss of strong ellipticity)

As rock deforms inelastically, the initial yield surface (lower curve in Fig. 4.17) evolves toward — and is not permitted to evolve *beyond* — the limit surface (upper curve in Fig. 4.17). If the stress reaches the limit surface, the rock has, in a loose sense, failed catastrophically. More correctly, Kayenta has reached the limit of its applicability because large scale cracking and subsequent loss in strength *cannot be modeled locally at the constitutive level*. Material softening generally produces a change in type of the momentum equation, requiring intervention from the host code to change its solution scheme appropriately (for further details, see page 96). In the GeoModel predecessor to Kayenta, the state variable "**CRACK**" was a flag equaling 1.00 whenever a principal stress (or I_1) cut-off has been applied or 2.00 when the stress has reached the limit surface and can harden no further; otherwise "**CRACK**" equals 0.0. In either case, a positive value of "CRACK" marks the onset of softening. In the current version of Kayenta, the meaning of the "**CRACK**" flag is in flux and should be regarded as a developer's flag not of interest to users.

Because Kayenta comes equipped with its own criteria for failure, this model should *not* be used with other fracture models such as a maximum principal stress criterion. Instead, the "**CRACK**" flag should be queried by the host code to determine when it is appropriate to add void (when pressure is tensile) or to apply discontinuous shear displacement element shape functions (when pressure is compressive) or to apply any other appropriate response[3] to material softening that will ensure localization response that converges as the spatial mesh size is reduced. However, since Kayenta's treatment of material softening, along with its update and usage of the "**CRACK**" flag, are under current development, host code owners should consult with the model developers for guidance on proper implementation of material softening. Also see page 109.

If the host code fails to activate any special response when the "**CRACK**" flag becomes nonzero, Kayenta will continue to run, but its predictions are suspect. Without a meaningful host-code response to failure, Kayenta will handle the inelastic response at the limit state in a manner similar to non-hardening plasticity (i.e., rather than properly softening down away from the limit state, Kayenta will force the stress to dwell at the limit state). To summarize, Kayenta is intended to model *only* the portion of material response that is appropriate to compute at the local constitutive level. Kayenta sends flags back to the host code at the *onset* of softening (a non-local phenomenon). The *host code* is responsible for responding appropriately to these flags by initiating material softening.

[3]Chapter 5 describes a field-scale softening strategy that introduces a length scale based on Weibull perturbations of the material strength field, which is especially appealing because (unlike so-called element death or cohesive zone models) it can be easily justified physically. Specifically, softening results from sub-grid-scale flaw clustering, which are expected to have a Weibull (or nearly Weibull) distribution *in spherical loading conditions*. Even if not Weibull-distributed, the statistics and associated scale sensitivity of strength can be parameterized via standard laboratory-scale experiments. Early preliminary investigations [7] have shown that spatial statistics in strength leads to *very* realistic fragment patterns that, with inclusion of scale effects, are less mesh sensitive than purely deterministic theories.

Kayenta files, subroutines, memory requirements, and model installation requirements

This section is a software requirements specification that must be followed by anyone who installs Kayenta into a host code.[4] Kayenta is designed to be implemented into multiple host codes without *any* revision of the source code. As described below, the model has *three* public[5] subroutines (**KAYENTA_CHK**, **KAYENTA_RXV**, and **KAYENTA_CALCS**). To support portability, Kayenta conforms to Sandia's Model Interface Guidelines (MIG) [24]. Therefore, the model presumes that calculations entail three distinct phases, the first two of which are performed at start-up while the last one is applied for every element at every timestep:

1. **User input.** Kayenta requires the host code to acquire user input values and save them into a single array using the keywords and ordering listed in Appendix B. This property array must be passed to the subroutine **KAYENTA_CHK** for "domain certification" (i.e., verifying that input values fall within allowable ranges, as explained on page 143). Additionally, the routine **KAYENTA_CHK** sets defaults for unspecified user inputs; this routine might even change user-specified values if necessary to ensure self-consistency of material properties.

2. **Storage.** To be portable, Kayenta does not actually *allocate* storage for internal state variables (ISVs, also called "Extra Variables") — this is the responsibility of the host because data lay-out varies from code to code. Kayenta provides a *list* of storage requirements by requiring the host code to call subroutine **KAYENTA_RXV**. This routine returns physical dimensions, initial values, plot keywords, and advection requirements for each internal state variable. To use this routine, the host code loops over these "storage-request" lists that were returned by **KAYENTA_RXV** to then actually allocate the storage, define plot options, and initialize the ISV fields.[6]

3. **Execution.** Every cycle, **KAYENTA_CALCS** must be called to update the stress to the end of the step. Detailed descriptions of the input-output arguments are provided below.

Kayenta must, upon occasion, relay messages to the user or terminate the calculation. Log message protocols and bombing procedures vary among host codes. For portability, Kayenta follows MIG guidelines by calling subroutines **LOGMES**, **FATERR**, or **BOMBED** whenever it needs

[4] Any deviation from these model installation instructions (as well as any modification of Kayenta source code itself) may result in loss of technical support. Model installers who believe that a deviation from these instructions is warranted are encouraged to contact Kayenta developers.

[5] i.e., routines that are called directly from the host code. All other routines in Kayenta are *private* and should not be called by the host. To serve codes that re-mesh, one additional public routine, **KAYENTA_state**, is available that will repair advection errors.

[6] Historically, host-code developers have often opted to brute-force Kayenta's internal variable arrays by writing their own native internal variable allocation coding. To our experience, however, this short-term gain has invariably been a poor decision in the long run. Doing this part correctly by looping over output from **KAYENTA_RXV** produces very clean, compact, and easily maintained host-code wrappers that support a plug-and-play paradigm for new Kayenta releases.

to relay messages to the user, log fatal errors, or terminate calculations, respectively. These routines are *not* part of Kayenta source code. Because these actions require host-code responses that vary from code to code, these routines must be written and maintained by the host-code architects. Likewise, a routine called **TOKENS** (explained in MIG documentation and used only in the extra variable request routine) is expected to pre-exist in the host code. Any host code that *already* supports MIG models will already have these MIG-utilities in their repository. Host code architects of non-MIG-compliant codes may request sample MIG-utilities that they may customize to suit their own code's protocols for information passing and code termination.

Kayenta source code is available in both FORTRAN 77 and 90. To date, large-scale production codes have used the F77 version to best ensure portability, so those routines will be described here. The F90 routines, which are not significantly different, are generated from the F77 master files to ensure consistency.

Arguments passed to and from Kayenta's driver routine

The following list describes variables passed between the host code and Kayenta's driver routine (**KAYENTA_CALCS**):

Input

- **NBLK**: The number of cells or finite elements to be processed. Parallel codes send only one cell at a time (**NBLK=1**). Vectorized codes send more than one element at a time (**NBLK>1**).
- **NINSV**: The number of internal state variables for Kayenta.
- **DT**: The time step
- **UI**: the user-input array, filled with real numbers, as summarized at the top of the nomenclature table in Appendix B and also summarized within the source code prolog itself.
- **GC**: Global constants
- **DC**: Derived constants
- **SIG**: The unrotated Cauchy stress tensor at time n. The six independent components of the stress must be passed in the ordering $\{\sigma_{11}, \sigma_{22}, \sigma_{33}, \sigma_{12}, \sigma_{23}, \sigma_{31}\}$. Within the FORTRAN, this array is dimensioned "**SIG(6, NBLK)**" so that the stress components for any given finite element are in six contiguous memory locations.
- **D**: The unrotated strain rate tensor, preferably evaluated at time $n+\frac{1}{2}$ because Kayenta treats the strain rate tensor as constant over the entire interval. Most codes approximate the strain rate tensor as the unrotated symmetric part of the velocity gradient (see Eq. (4.3)). Component ordering and contiguous storage are the same as for stress.

- **SV**: the internal state variable array containing reals, as described in the nomenclature table in Appendix B.

Output

- **SIG**: The unrotated stress tensor at time $n+1$. The component ordering is the same as described above.
- **SV**: The internal state variable array (updated to time $n+1$)
- **USM**: Uniaxial strain (constrained) elastic modulus equal to $H = K + \frac{4}{3}G$. The host code may use the USM output to compute an upper bound on the wave speed ($\sqrt{H/\rho}$, where ρ is mass density) when setting the timestep.

These arguments require unrotation of spatial stress at time n, unrotation of the strain rate at time $n+\frac{1}{2}$, and rotation of the updated stress back to the spatial frame at time $n+1$. For problems involving significant material rotation, this requires using *three* different polar rotation tensors [32]. Even for moderate rotation problems, it is unacceptable to use the rotation tensor evaluated at time $n+\frac{1}{2}$ for all three operations [54, 56].

Plottable Output

In addition to the stress, any variable in the **SV** state variable array is available for plotting. The plot keywords (and ordering of variables in the **SV** array) are listed in Nomenclature Appendix B.

As mentioned earlier, the "**CRACK**" flag may be plotted to visualize softening regions. The "**INDEX**" flag may be plotted to locate regions that are deformed inelastically (the meaning of this output varies to support code debugging; currently it is a flag that indicates what part of the yield surface is active). To visualize regions that are *currently* deforming inelastically, the "**SHEAR**" variable should be plotted.

The "**SHEAR**" variable is an informational output, equal to zero during elastic cycles and equaling a measure of normality of the trial elastic stress rate during plastic intervals. Specifically, as illustrated in Fig. 8.1, "**SHEAR**" ranges from zero when the trial stress rate is tangent to the yield surface to unity when it is normal to the yield surface; an intermediate value of "**SHEAR**" indicates oblique plastic loading relative to the yield surface. While "**SHEAR**" quantifies the plastic loading direction relative to the yield surface, the internal state variable "**DCSP**", which is the plastic consistency parameter $\dot{\lambda}^*$, may be plotted as a measure of the *magnitude* or intensity of plastic loading.

The "**EQDOT**" variable may be plotted to gain an overall sense of intensity of the current strain rate. Small values of "**EQDOT**" correspond to relatively quiescent regions. Plotting "**EQPS**" will

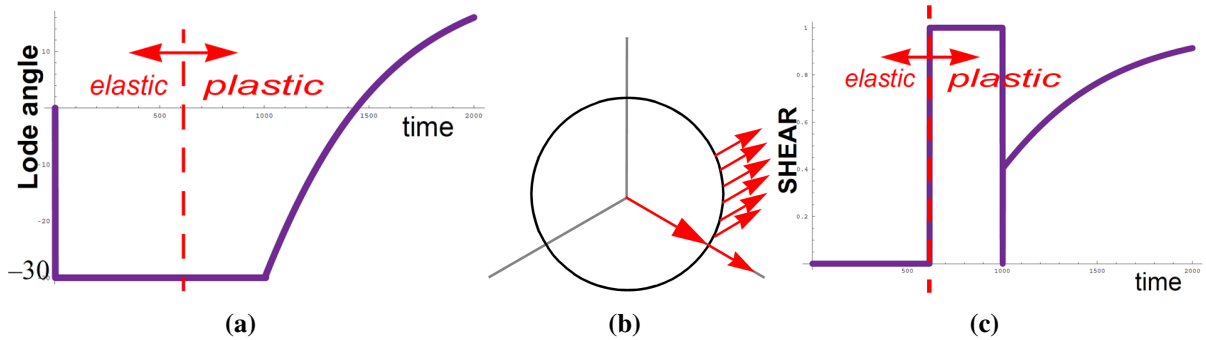

Figure 8.1. Meaning of the "SHEAR" output variable. This calculation uses a von Mises yield surface. The strain rate remains in triaxial extension for half of the calculation, which is why the Lode angle (a) is initially constant at $-30°$. During this interval, the stress reaches the yield surface and continues to push directly against it, which is why **SHEAR** (c) jumps to and holds at 1.0. Halfway through the problem, the strain rate direction is changed in stress space [as indicated by arrows in (b)] to move the stress toward triaxial compression. At the beginning of this transition, **SHEAR** first jumps to 0.5 where the normal and tangential components are equal, and moves back toward 1.0 as the tangential component decays.

show equivalent plastic shear strain, while "**EQPV**" gives plastic volume strain (and is roughly equal to the porosity change from inelastic void collapse).

The stress invariant "**I1**" is three times the negative of pressure. "**ROOTJ2**" may be regarded as a scalar measure of effective shear stress and is proportional to the radial coordinate of the stress in the octahedral plane. The Lode angle, "**LODE**", quantifies the angular location of the stress in the octahedral plane, and it varies from 30 for triaxial compression to -30 for triaxial extension (0 for simple or pure shear). If kinematic hardening is enabled, "**BACKRN**" quantifies the distance that the origin of the octahedral profile has shifted in stress space.

The complete list of other (less useful) plotable output is in Appendix B.

Kayenta algorithm

Kayenta presumes that the strain rate is constant throughout the entire step, and the stress is integrated as follows:

Rate independent (inviscid) part of the viscoplasticity equations

STEP 1 To guard against unpredictable host-code advection errors (or similar corruption of the updated state from the last time step), apply a return algorithm to ensure the initial stress is on or inside the yield surface.

STEP 2 Compute the nonlinear elastic tangent moduli appropriate to the stress at time n. When running the isotropic model, this step evaluates the shear and bulk moduli according to Eq. (4.9) and Eq. (4.10) or Eq. (4.33) and Eq. (4.34). When running with the orthotropic joints option, this step determines the seven independent elastic moduli for the orthotropic fourth-order tensor (see [20]).

STEP 3 Apply Hooke's law in rate form ($\dot{\sigma}_{ij} = C_{ijkl}\dot{\varepsilon}_{kl}$) to obtain the elastic stress rate at time n.

STEP 4 Integrate the elastic stress rate using first-order differencing to obtain an estimate for the trial elastic stress at the end of the step. Compute the invariants of this trial stress for substitution into the yield function.

STEP 5 Evaluate the yield function at the trial elastic stress. If the yield function evaluates to a negative number, the trial elastic stress is accepted as the final updated stress, and the inviscid algorithm returns (i.e., go to STEP 18). Otherwise, continue.

STEP 6 To reach this step, the trial elastic stress state was found to lie outside the yield surface. At this point, the time step is divided into an internally determined number of subcycles (which may be increased by setting **SUBX**>0 or decreased by **SUBX**<0. All subsequent steps described below this point apply to the smaller time steps associated with subcycles.

STEP 7 Evaluate the gradients of the yield function for eventual use in Eq. (4.86).

STEP 8 Evaluate the flow potential gradients for eventual use in Eq. (4.99) and Eq. (4.97)

STEP 9 Evaluate the isotropic hardening coefficient h_κ^* in Eq. (4.75).

STEP 10 Evaluate the numerator in the consistency parameter defined in Eq. (4.86).

STEP 11 Evaluate the denominator in the consistency parameter defined in Eq. (4.86).

STEP 12 Evaluate the G^α function in Eq. (4.79).

STEP 13 Apply Eq. (4.86) to obtain the consistency parameter.

STEP 14 Use forward differencing (within the subcycle) to integrate Eq. (4.75) and Eq. (4.79), thereby updating the internal state variables, κ and α_{ij}. Similarly integrate Eq. (4.97) to advance the stress to the end of the subcycle.

STEP 15 The above steps directly integrate the governing equations through the end of the subcycle, so the updated stress will be *in principle* already on the yield surface. However, guard against slight round-off and integration errors by applying an iterative return correction to place the stress *exactly* on the yield surface.

STEP 16 Increment the subcycle counter, and save the partially updated inviscid internal state variables.

STEP 17 If subcycles remain to be evaluated, go to STEP 7. Otherwise, continue to STEP 18

Viscous part of the viscoplasticity equations

STEP 18 The previous set of steps govern computation of the equilibrium state. Now apply Eq. (7.22) to compute the characteristic material response time.

STEP 19 Using the trial elastic stress corresponding to an update to the end of the time step, apply Eq. (7.10) to compute the dynamic stress. Apply Eq. (7.15) to similarly compute the dynamic values of internal state variables to account for rate sensitivity.

STEP 20 Save the values of the internal state variables into the state variable array.

STEP 21 STOP.

This page intentionally left blank.

Chapter 9

Software "confidence building" activities

This chapter describes progress towards Software Quality Assurance (SQA), which encompasses a broad range of activities including code maintenance, documentation, and (most importantly) code verification. "Code verification" is defined by the IEEE [47] as "formal proof of program correctness" in the sense that the governing equations are numerically solved correctly within a tolerable degree of accuracy. Model *validation*[1] will not be discussed until Chapter 11.

We make no claims at this point that Kayenta software has been exhaustively verified. In other words, we cannot state with *absolute* certainty that the governing equations presented in this report are in fact solved correctly. One might challenge the Verification and Validation (V&V) community to prove that "formal proof of program correctness" is even possible. Realistically, the confidence one can place in the veracity of any model prediction can be based only on the extent to which documented evidence *suggests* that the equations are solved correctly. It seems acceptable, therefore, to speak of varying *degrees of progress* towards verification,[2] or, more generally, varying degrees of SQA. In this sense, Kayenta has undergone a higher level of SQA than is normally applied to modern material constitutive models of comparable complexity.[3] Even though we claim that Kayenta's verification and SQA status is above average, we do *not* assert that such activities have progressed to the point where we consider the job "finished". Here in this chapter, we aim only to build confidence in Kayenta by summarizing some of the SQA activities that have been applied to Kayenta to date (a comprehensive *detailed* discourse would fall well outside the scope of this report).

Once a constitutive model is installed within a host code, it becomes only a single component

[1] Whereas "Verification" seeks to confirm that the equations are solved correctly without questioning their appropriateness, "validation" compares model predictions against experimental data to determine whether or not the equations themselves are indeed suitable for the application.

[2] Suppose, for example, that one constitutive model has been verified for both uniaxial strain and simple shear, whereas another one has been tested only in uniaxial strain. If these are the only tests, *neither* model is "well verified," but the first one is certainly *better* verified.

[3] From a practical (rather than philosophical) standpoint, the complexity of a model must be considered when speaking about how well a model has been validated. With a given level of financial and computational resources, solids models cannot be tested to the same level of certainty as fluids models. Conclusively demonstrating only *first-order* accuracy of an anisotropic solid constitutive model would require more than *twenty* times the effort needed to verify first-order accuracy of a simple fluids model (this follows because a general anisotropic stiffness tensor has 21 independent components, and therefore 21 independent strain paths would be required to conclusively verify accuracy; moreover comprehensive testing for solids models requires coordinate invariance tests that are not needed for scalar fluids models).

of a much *larger* and *different* model (the finite-element code). Constitutive SQA should include ensuring that the model can be installed and run in a variety of host codes, but verification of the installation is primarily a *host code* (not constitutive) responsibility. Constitutive SQA in the context of larger-scale model integration is limited to providing adequate model installation instructions (including operational constraints), delivering correct solutions to the constitutive governing equations, and ensuring that the model will, wherever feasible, "trap" invalid calling arguments (much as a compiler "traps" IEEE errors such as division by zero).

Numerical schemes for solving field PDEs (such as Navier-Stokes equation or Maxwell's electromagnetism equations) have received considerable attention in the V&V literature, while verification of *constitutive models* has been relatively ignored. Constitutive models are *sub-components* within field-scale calculations. As such, a *partitioning* of responsibility for SQA is needed. (As an analogy, note that the quality assurance responsibilities for a turn-signal manufacturer must be different from those of an automobile manufacturer.) *Constitutive* verification aims to build confidence that the model will return correct solutions to the governing equations, *presuming* that the host code sends inputs falling within the admissible domain for the model. SQA may additionally include some checking of the inputs themselves, as long as doing so does not compromise efficiency. When a host code sends inadmissible inputs (such as corrupted strain rates caused by mesh entanglement, advection, or artificial viscosity errors), then correcting such errors is not the responsibility of a constitutive modeler unless it can be proved *by the host code developers* that such errors originated from constitutive model output errors.

Similarly, because Kayenta is a *local* constitutive model (i.e., because it does not solve space-time PDEs), demonstrating convergence with respect to the *spatial* mesh is not a Kayenta verification responsibility. It is well known that mesh dependence can occur when local constitutive models permit material softening. Therefore, we regard *suppression* of softening as an implicit software requirement specification unless our customers (finite-element code teams) have implemented the code infrastructure that is needed to properly handle the change in type of their governing PDEs that occurs upon softening. Unless such enhancements are made *at the host code (not constitutive) level*, Kayenta's applicability domain is limited to predicting only the onset of catastrophic failure, not its subsequent evolution into macroscale fragments and fractures. If host code enhancements are implemented as described on page 109, then Kayenta's applicability domain is marginally expanded into the softening realm, but it must be understood that nonphysical mesh sensitivities might still be present in certain calculations. In short, models for softening continue to be an active research area.

In the lexicon of Ref. [57], "static" SQA testing is a prerequisite to the verification process that encompasses tests that are performed without running the code. To date, Kayenta has undergone the following static SQA:

- **Independent[4] line-by-line review of the source code.** The source code was aggressively

[4]Here, "independent" (which is not synonymous with "unbiased") means that the source code has been inspected by an individual who has not written the code. Kayenta code inspection was first performed by Brannon (the first author of this report) upon joining this modeling effort at the beginning of fiscal year 2003-04. Subsequent new code revisions and enhancements have been reviewed by the member of the Fossum-Brannon team who did not write the

inspected to locate and remove possibilities for IEEE errors (e.g., trying to take the ArcSin of a number larger than unity,[5] dividing by zero, etc.). Another goal was to confirm that the equations being solved in the code were indeed the equations documented in this report.

- **Model domain certification (preventing "Garbage In $\Longrightarrow$ Garbage Out").** No function or set of equations is well posed without a domain of applicability. The domain for Kayenta includes constraints on run-time subroutine arguments (e.g., the backstress must be deviatoric) as well as constraints on the input parameters (e.g., the bulk modulus must be positive). Except where computational efficiency would be degraded, SQA includes appraising quality of both user input and run-time arguments sent from the host code. A new routine (**`KAYENTA_CHK`**) was recently added to Kayenta that terminates calculations if the user-input falls outside allowable ranges. Run-time testing of this routine is discussed in the next section. Direct run-time testing of *time varying* subroutine arguments is computationally inefficient, so Kayenta's domain certification for variable calling arguments relies primarily on our model installation instructions (page 134), which serve as software requirement specifications that must be obeyed by the host code developers.

- **Portability and version control.** Kayenta has been designed such that it can be implemented in multiple host codes *without altering the source code*, thus allowing Kayenta developers to maintain a single master version. A host code owner who faithfully obeys the model installation instructions on page 134 may update Kayenta by simply replacing three fortran files (posted on WebFileShare under keyword "Kayenta") with the latest Kayenta release and then recompiling. Each Kayenta release is identified by a six digit code[6] that prints to the screen at run time. Kayenta has been compiled on multiple platforms (Sun, Dell, and HP workstations or clusters running Linux and/or Windows) in multiple host codes (Alegra, Presto, Pronto, JAS3D, and two independent drivers) using multiple commercial compilers (gnu, pgf77, pgf90, and Compaq visual fortran). The source code compiles without warnings when using stringent SQA options (such as -Wall -O3 in the gnu compiler).

- **Model documentation.** *This report* is the first publication that describes the numerical algorithm, provides input definitions, and gives model installation instructions that describe how SQA responsibilities are partitioned between the model and the host code.

- **Technical support.** Two stand-alone single-cell codes that exercise Kayenta under prescribed strain and stress paths were previously available to help host (finite-element) code owners verify their Kayenta installations and to assist in parameterization. One of these drivers was geared towards code debugging, while the other was more for parameterization. The best parts of these two drivers have now been absorbed into a unified and much-expanded constitutive model driver called "MatModLab" [39]. Kayenta includes a "problem-resolution" feature that generates a debugging file (kmm.barf) and terminates calculations whenever unacceptable solution quality is detected. The debugging file may be emailed to Kayenta team, who can import it into their driver to resolve the problem quickly.

---

new code.

[5] This can happen because of slight round-off errors, as in **`ASIN(1.0000001)`**.

[6] The code's build identification number is simply the release date in the form "yymmdd". For example, "Kayenta version 1.0 build 090217" was released in 2009 on Feb. 17.

So-called "dynamic" SQA refers to tests performed by actually running Kayenta. Some of the dynamic SQA activities to date are summarized here. A detailed documentation of all Kayenta SQA would require a second report itself, so the following list should be regarded as simply an overview. A small number specific examples will be given later.

- **Model domain certification**: The "KAYENTA_CHK" feature for checking quality of user inputs was tested by confirming that Kayenta would abort when *intentionally* sent invalid inputs. As explained below, the "kmmbarf" problem-resolution feature can often *indirectly* trap invalid forcing functions (caused, for example, by mesh entanglement). However, the *responsibility* for sending valid forcing functions to Kayenta remains the onus of the host code, not Kayenta.

- **Run-time monitoring of the solution quality**: The problem-resolution (kmm.barf) feature has been verified to (1) detect "Garbage Out" predictions such as negative plastic work, (2) terminate calculations, and (3) write a debugging file that can be emailed to model developers to determine whether the problem was caused by bad user input, bad arguments passed from the host code, or a bug in the internal coding.

- **Driver regression testing**: Two stand-alone drivers are available for exercising Kayenta in a homogenous deformation field.[7] Considerable dynamic testing was performed using our research (non-production) model driver that allows visualizing (and algebraically processing) the output within Mathematica [99]. The other driver [75], which runs either from a command line or from an Excel front-end (see Fig. 9.1), is now also deployed in the WISDM materials information database [44], allowing the predictions of Kayenta to be compared directly against experimental calibration data. These drivers have been used to assemble a suite of regression tests (hydrostatic loading, two types of shear loading, uniaxial strain, uniaxial stress, biaxial plane stress, and numerous mixed load-unload problems using a variety of input parameters), several of which are simple enough to admit analytical solutions for verification purposes. The driver regression problems (15 problems to date) are all re-run and inspected for undesirable changes whenever *any* change is made to Kayenta.

- **Trend testing**: Engineering judgement was used to ensure that solutions vary as expected when parameters change. For example, Fig. 8.1 depicted a simple trend test in which analytical (exact) arguments could be used to prove that the "**SHEAR**" should equal 1.0 at the onset of yielding and should dwell at 1.0 until the loading direction changes, after which it should drop instantaneously to 0.5 and then asymptote to 1.0. Similarly, Fig. 7.3 and Fig. 9.9(b) confirmed that increasing Kayenta's characteristic response time (see Eq. (7.22)) would indeed produce the analytically predicted increase in the apparent strength of the material. These tests were quite valuable because they allowed correction of a serious bug in an earlier version of Kayenta where the response trend upon *load reversal* was clearly flawed. Trend and robustness testing also demands that Kayenta must predict *qualitatively* reasonable trends when subjected to deformations that exceed what is expected in applications (e.g., massively

[7] Stand-alone testing obviates many constraints and sources of *non-constitutive* errors in production finite-element simulations (artificial viscosity, hour-glassing, time-step control, boundary-condition errors, code compilation and run-time overhead, etc.).

Problem description:

Fossum Geomodel

Salem Limestone

Hydrostatic Compression (Stress-Driven)

****

Path to Fortran MMD executable:

C:\home\data\mdrive\rb\mmd0402c\Debug\mmd0402c.exe

****

Material model:

Index	Name (optional)
11	Fossum Geomodel

****

Material model input parameters:

B0	B1	B2	B3	B4	G0	G1	G2	G3	G4
(Pa)	(Pa)	(Pa)	(Pa)	(ndim)	(Pa)	(ndim)	(1/Pa)	(Pa)	(ndim)
1.30E+10	4.25E+10	4.11E+08	1.20E+10	0.021	9.86E+09	0	0	0	0

RJS	RKS	RKN	A1	A2	A3	A4	P0	P1	P2
(m)	(Pa/m)	(Pa/m)	(Pa)	(1/Pa)	(Pa)	(rad)	(Pa)	(1/Pa)	(1/Pa^2)
0.00E+00	2.00E+13	1.00E+12	8.43E+08	2.73E-10	8.22E+08	1.00E-10	-3.14E+08	1.22E-10	1.28E-18

P3	CR	RK	RN	HC	CUTI1	CUTPS	T1	T2	T3
(1)	(ndim)	(ndim)	(Pa)	(Pa)	(Pa)	(Pa)	(s)	(1/s)	(ndim)
8.40E-02	6	0.72	5.00E+06	9.00E+10	1.00E+11	3.00E+06	0.00E+00	0	0

T4	T5	T6	T7	J3TYPE	A2PF	A4PF	CRPF	RKPF	SUBX
(1/s)	(Pa)	(s)	(Pa)	(ndim)	(1/Pa)	(rad)	(ndim)	(ndim)	(ndim)
0.00E+00	0.00E+00	0.00E+00	0.00E+00	3	2.73E-10	1.00E-10	6	0.72	0

****

Load path specifications:

leg (ndim)	time (s)	npts (ndim)	nprt (ndim)	ltype* (ndim)	c11	c22	c33	c12	c13	c23
0	0	0	0	111111	0	0	0	0	0	0
1	1	100	2	444222	-1.00E+09	-1.00E+09	-1.00E+09	0	0	0
2	2	100	2	444222	0.00E+00	0.00E+00	0.00E+00	0	0	0

*Load type parameter for each component, cij:

1 = strain rate (1/s)
2 = strain (1)
3 = stress rate (Pa/s)
4 = stress (Pa)

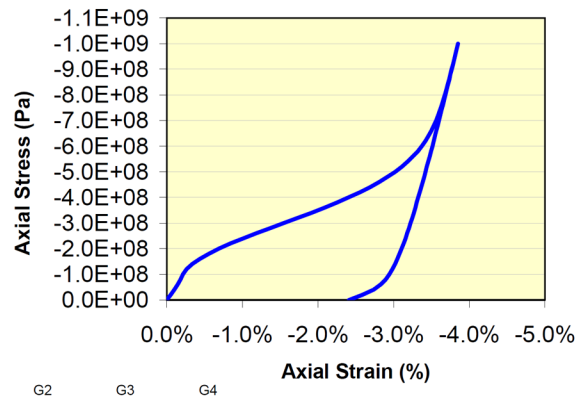

Figure 9.1. Screen shot of the MS Excel interface for Kayenta's material-model driver (MMD). This tool serves as a reliable platform for exercising Kayenta under homogeneous deformations in a simplified host code architecture that is free from solution corruption caused by *unneeded* finite-element code features such as artificial viscosity, wave motion, contact algorithms, etc.

large elongations or pressures). For example, one problem in our driver regression suite verifies that load/unload curves do indeed asymptote toward each other under hydrostatic compression as sketched in Fig. 3.1 and verified in Fig. 9.1. Many other trend tests such as these have been conducted, but (for lack of space) will not be described in detail in this report.

- **Symmetry testing**: Consistent predictions were verified for identical loading applied in different directions (e.g., uniaxial strain in the 1-direction compared with the 2-direction). Consistency has also been tested for stress paths that intersect the yield surface at symmetrically equivalent points and for trial stress rates that by design do not produce tangential stress rates.

- **Extensive comparison testing**:[8] To date, Kayenta has been implemented in five finite-element codes: (ALEGRA [11][100], PRESTO [58], JAS3D [8], EPIC [51], legacy PRONTO3D [88]). A disturbing number of discrepancies (e.g., wave arrival times differing by as much as 10% or peak stresses differing by almost an order of magnitude) have been identified by comparing predictions for the *same problem* simulated by different finite-element codes. In all but a few cases, these discrepancies have been traced to *host-code-level (not constitutive-level)* errors (e.g., hour-glassing, handling of boundary conditions, artificial viscosity, time-step control, etc.). Resolving such discrepancies is the model verification responsibility of the host code owners, not Kayenta developers.[9] The ability of Kayenta to reduce to simpler models (e.g., nonhardening elastoplasticity) has often proved invaluable in determining if a simulation problem originates from Kayenta or elsewhere in the host code. When, for example, an undesired feature in a calculation persists even when Kayenta is run using simplified parameters, a comparison test can be performed using the existing (presumably better verified) independent version of that model within the finite-element code. We have, for example, often compared a host code's standard elasticity model with Kayenta run in an elastic mode. In one instance where a discrepancy was traced to Kayenta, it was attributed to failure of the code owner to follow Kayenta installation instructions (page 134). In a few cases, comparison testing did indeed reveal Kayenta bugs that have since been corrected.

- **Comparison with exact analytical solutions**: Analytical solutions are not available to verify all of Kayenta's features acting *simultaneously*. However, each Kayenta feature has been individually verified to ensure that the promised quantitative material response is delivered (e.g., accurate tracking of a specified porosity crush curve, exact apparent strengthening in high rate loading, etc.). Depending on how the model parameters are set, Kayenta can be idealized to a form for which some problems admit exact solutions. One example is that of a linear Mohr-Coulomb material with an associative or a non-associative flow rule in homogeneous loading. This class of problems was recently studied in a verification and

[8] Testing a numerical model in multiple host codes has been vital to our SQA process. If two codes agree, then no conclusion may be drawn. If, however, two codes predict different answers, then at least one of them is not solving the equations properly (or is not solving the same equations). Resolving such discrepancies has *time and again* expedited bug identification and resolution.

[9] Incidentally, the disquieting frequency of bugs originating within the host code (not the constitutive model) reiterates the importance of specialized constitutive model drivers in constitutive model verification. Constitutive models should *not* use finite-element codes as their primary verification platform.

benchmarking activity sponsored by the Defense Threat Reduction Agency (DTRA) through its Advanced Concepts Technology Demonstration (ACTD) Project. These exercises were part of a larger Verification and Validation (V&V) effort to increase confidence in prediction of low-yield nuclear damage of underground (tunnel) facilities in jointed (in situ) rock mass. The problems are designed to increase in complexity, by invoking additional physics in the material models, until a level is reached that is deemed sufficient to model precision field tests. This work will be described in further detail later in this chapter.

- **Method of manufactured solutions (MMS)**: The MMS method of SQA entails *first* solving an inverse problem in which simple (e.g., quadratically varying) analytical time histories for the *response* functions are substituted into the governing differential operators to obtain (probably with the assistance of a symbolic mathematics program such as *Mathematica*) an expression for the *input* functions that would produce the pre-specified response function [57][77][80]. The numerical model is then sent this *analytically determined* input function to verify that the original (pre-selected) response function is recovered. For Kayenta, using MMS would require pre-selecting an analytically simple stress history to determine a strain history to use as input in the numerical simulation. Solving the inverse problem is usually prohibitively difficult because Kayenta's differential operators are "branched" (one set is used during elastic deformation, while another is used during plastic loading, and the internal state variable evolution equations themselves are coupled to the location of the stress on the current yield surface). However, the inverse problem is tractable for extremely simplified model parameters. In particular, one such exercise (developed as part of an ACTD verification activity [84]) involved plane stress deformation of a non-associative Mohr-Coulomb material. Strictly speaking, this verification problem was an instance of MMS because plane stress entails specification of one of Kayenta's outputs (the out-of-plane stress). An analytical solution was found for the strains required to produce plane stress results. These strains were then used to drive Kayenta in a single element strain-controlled driver, where it was confirmed that the predicted out-of-plane stress was zero (on the order of 10^{-5} relative error, which was comparable error in the prescribed strain table). Moreover, as illustrated in Fig. 9.2, the in-plane stresses agreed with the analytical result (with similar relative error). Details of the strain path and the analytical solution, which are available upon request, are likely to be documented in a future journal article.

- **Order-of-convergence**:[10] Time steps for complicated plasticity models often must be much smaller than the time step used by the host (finite-element) code. Kayenta's governing equations change upon reaching yield, and this transition typically occurs somewhere in the middle of the host code's time step, which implies that the constitutive model must break the step into elastic and plastic parts. Moreover, further subcycling within the constitutive model is required to avoid "drift" of internal state variables into non-physical or inconsistent domains.[11] Subcycling complicates the meaning of a convergence study performed at the host

[10]The term "order-of-convergence" is preferred over "order-of-accuracy" because a converged solution is never necessarily a *correct* solution. For example, if the return direction is incorrect in a classical predictor-corrector plasticity scheme, then the algorithm will converge, *but to the wrong result*. Kayenta, by the way, does not use a return method — it explicitly integrates the equations, using subcycling to assist with the change of governing equations upon yielding.

[11]Of course, higher-order integration is also an option, but the total computational overhead sometimes exceed

code level. Preliminary tests (see page 148) indicate that *each subcycle* within Kayenta is first-order convergent, but (recall the last footnote on page 141) we have not yet performed sufficient tests to consider this claim fully verified for a broad variety of load paths. Subcycling in Kayenta has been massively improved over c2004 versions. Problems that formerly took 2000 code steps to converge to an acceptable accuracy[12] can now be run to the same pointwise accuracy in only 10 apparent *host-code* steps (internally, Kayenta still might run as many as ∼2000 subcycle steps, but this improvement in allowable *host-code* step size is essential in field-scale finite-element simulations). Options for implicit integration in Kayenta (e.g., [36]) have not yet been fully developed.

Preliminary convergence testing

Let $F(x)$ denote a fine-resolution solution curve (e.g., stress as a function of strain) corresponding to N evenly spaced time steps. Let $f(x)$ denote a coarser solution corresponding to $n < N$ time steps. In both cases, the *continuous* curves $F(x)$ and $f(x)$ are here regarded as piecewise linear interpolations between discrete function values at the timesteps. Both curves are normalized by the peak value of $F(x)$.

The "integrated discrepancy" is defined

$$\left(\sum_{K=1}^{N} \left[F(x_k) - f(x_k) \right]^2 \right)^{\frac{1}{2}} \tag{9.1}$$

The "pointwise discrepancy" is defined similarly except that the sum ranges to n instead of N:

$$\left(\sum_{K=1}^{n} \left[F(x_k) - f(x_k) \right]^2 \right)^{\frac{1}{2}} \tag{9.2}$$

Fig. 9.4 shows that the basic algorithm *without subcycling* is first-order accurate. Fig. 9.4 and Fig. 9.3 show that subcycling makes the solution nearly pointwise converged (discrepancy $\approx 2^{-6}$) even for inordinately coarse calculations of 1 to 3 time steps. This highly desirable behavior can be of paramount importance when the model is run in finite-element codes that take large steps.

that of a well-written subcycling algorithm. Moreover, higher-order integration algorithms are notoriously difficult to maintain when the governing equations themselves are being revised during parallel development of the physical theory.

[12] At this stage in our ongoing verification process, it is adequate to use so-called "eyeball norm" assessment of accuracy in which solutions are compared visually by plotting them together. This easy assessment method simply *bounds* the discrepancy between two seemingly overlaying plots to be less than differences perceptible to the human eye relative to the size of the graph.

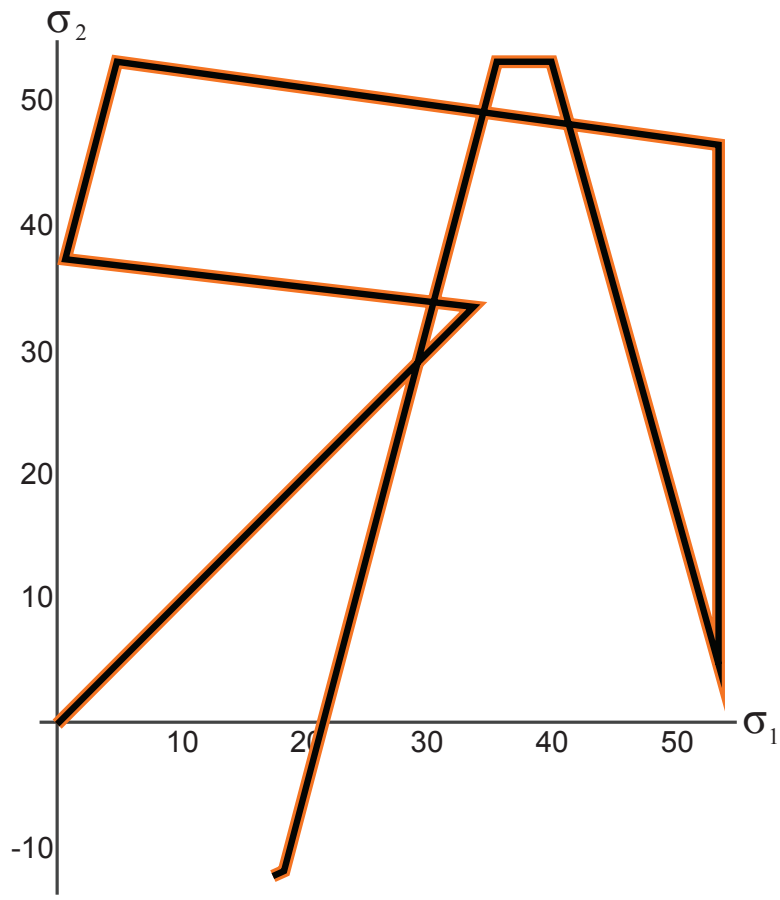

Figure 9.2. MMS verification of Mohr-Coulomb idealization. This plot shows the motion of the principal in-plane stresses in response to a prescribed strain path. The simulation (thin black line) overlays the analytical solution (thick orange line), with computed relative error in the predicted stresses on the order of known error in boundary conditions.

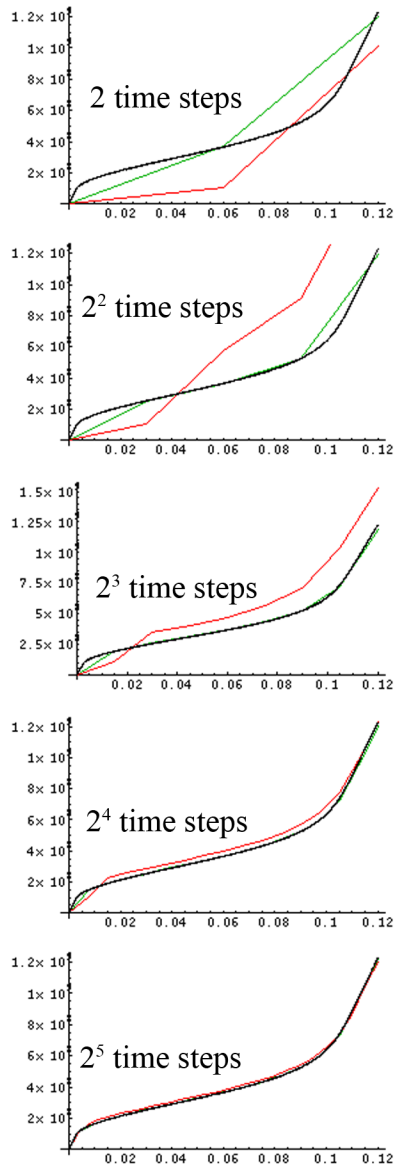

Figure 9.3. Subcycling test for hydrostatic loading. The ordinate is the first stress invariant $\overline{I_1}$ and the abscissa is volumetric strain $\overline{\varepsilon_v}$. Red is without subcycling. Green is with subcycling. Black, $F(x)$, corresponds to 2^{15} time steps.

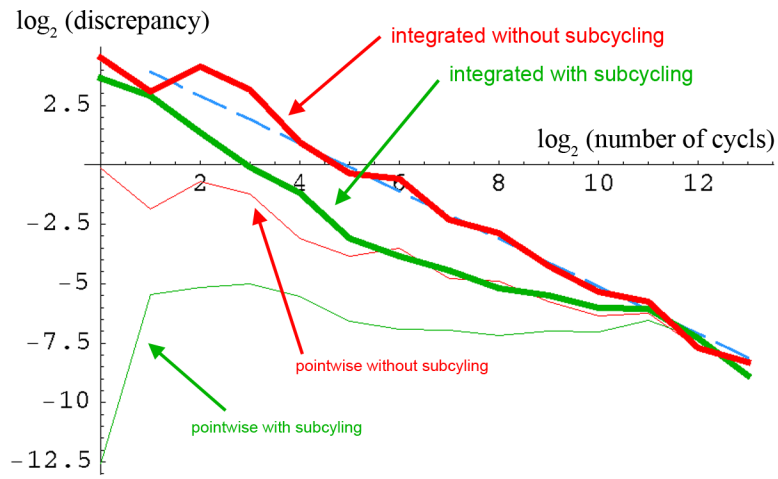

Figure 9.4. Rate of convergence. The dashed blue line (shown for reference) has a slope exactly equal to -1. As seen, subcycling provides significantly reduced discrepancy when the number of code steps is too small to have reached the convergence purely from code stepping. Subcycling therefore allows the host finite-element code to take large steps (usually dictated by a Courant stability condition if it is using an explicit solver), while the Kayenta constitutive model automatically takes smaller steps if it detects very large strain rates; the subcycling is needed to obtain reasonable updates of internal variables and hence accurate predictions of stress at the end of the host-code step.

Verification: single-element problems (regression suite)

A single-element problem is one for which the stress and strain fields do not vary in space. As summarized below, this section presents four different single-element load paths, each separately solved using two different Kayenta parameter sets (associative and non-associative linear Mohr-Coulomb — see Appendix B, page 268). To determine corresponding sets of material parameters for Kayenta, the linear Mohr-Coulomb parameters were used to create simulated data pairs for the limit state and plastic potential functions. Following the instructions in Appendix A, Kayenta was then fitted to these data pairs to determine the limit-state parameters Ψ, a_1, a_2, a_3, a_4 and non-associative material parameters $\{\Psi^{\mathrm{PF}},\ a_2^{PF},\ a_4^{PF}\}$. The compaction parameters $\{R,\ R^{PF},\ p_0,\ p_1,\ p_2,\ p_3\}$ were selected such that no compaction occurred over the stress range specified for the load paths. Likewise, hardening and rate dependence were disabled. Results are summarized in Fig. 9.5 through Fig. 9.8.

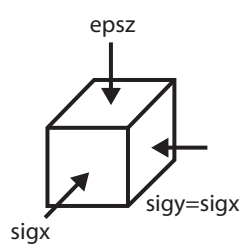

TXC0

Point	sigx=sigy	epsz
1	0	0.000000
2	0	0.005000
3	0	0.003274

TXC20

Point	sigx=sigy	epsz
1	0	0.000000
2	20	0.000310
3	20	0.005000
4	20	0.002060

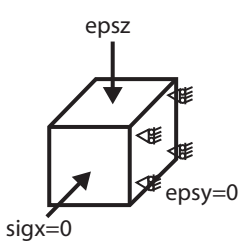

RTX100

Point	sigx=sigy	epsz
1	0	0.000000
2	100	0.001548
3	100	-0.005000
4	100	-0.002295

PSTRN

Point	epsz
1	0.000000
2	0.010000
3	0.008391

- Simple load paths clearly demonstrate basic model response
- Run for both full and partial associativity
- Triaxial Compression
  - Activates compression meridian
  - Same load path as a real lab test
- Reduced Triaxial Extension
  - Activates extension meridian
  - Same load path as a real lab test
- Plane Strain
  - Activates meridians at Lode angle(s) (triaxiality) between compression and extension

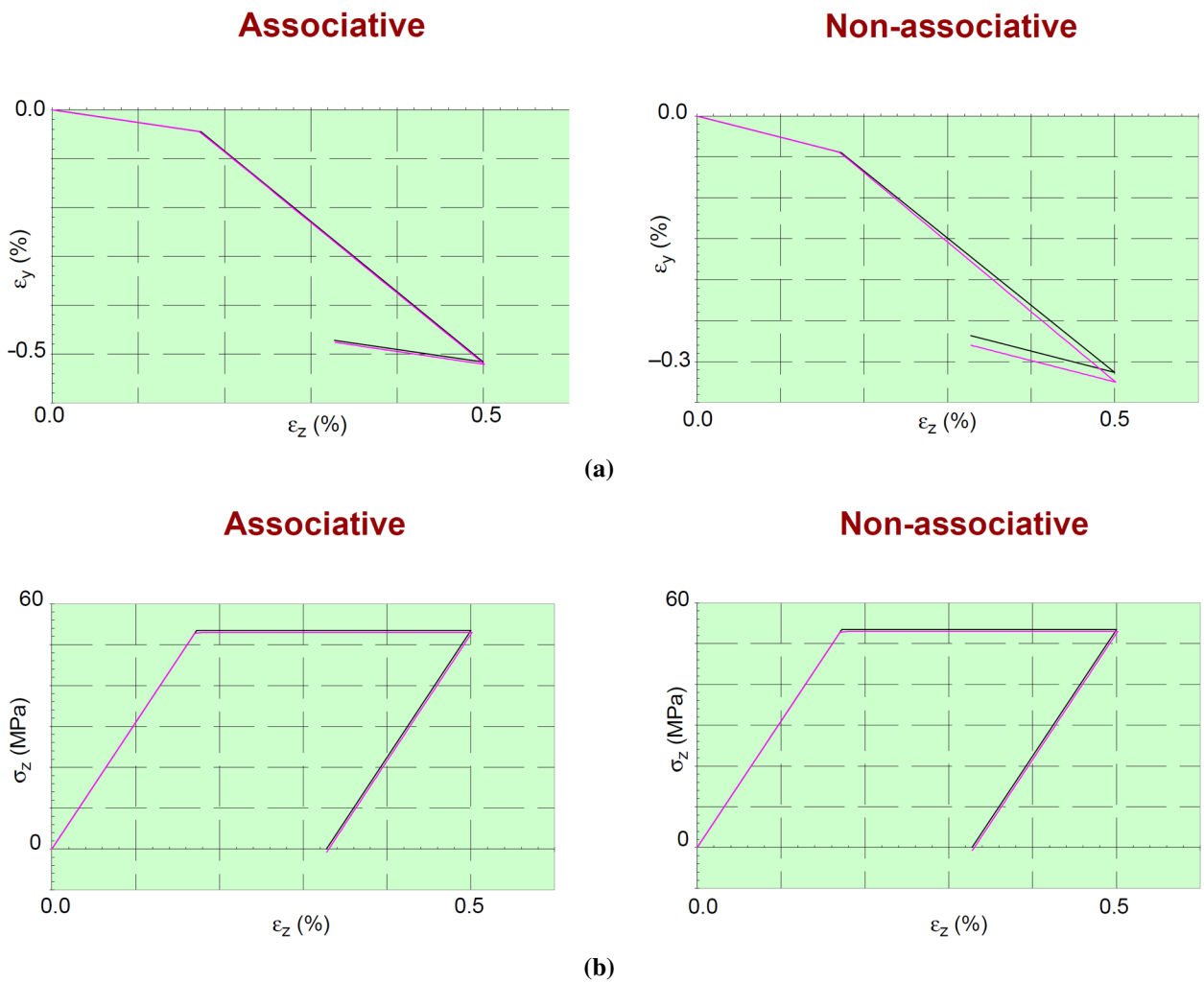

Figure 9.5. Single Element Verification Results, Unconfined compression. Exact (black) solutions compared with alegra Kayenta simulation (pink). (a) lateral strain vs. axial strain (b) Stress vs. strain.

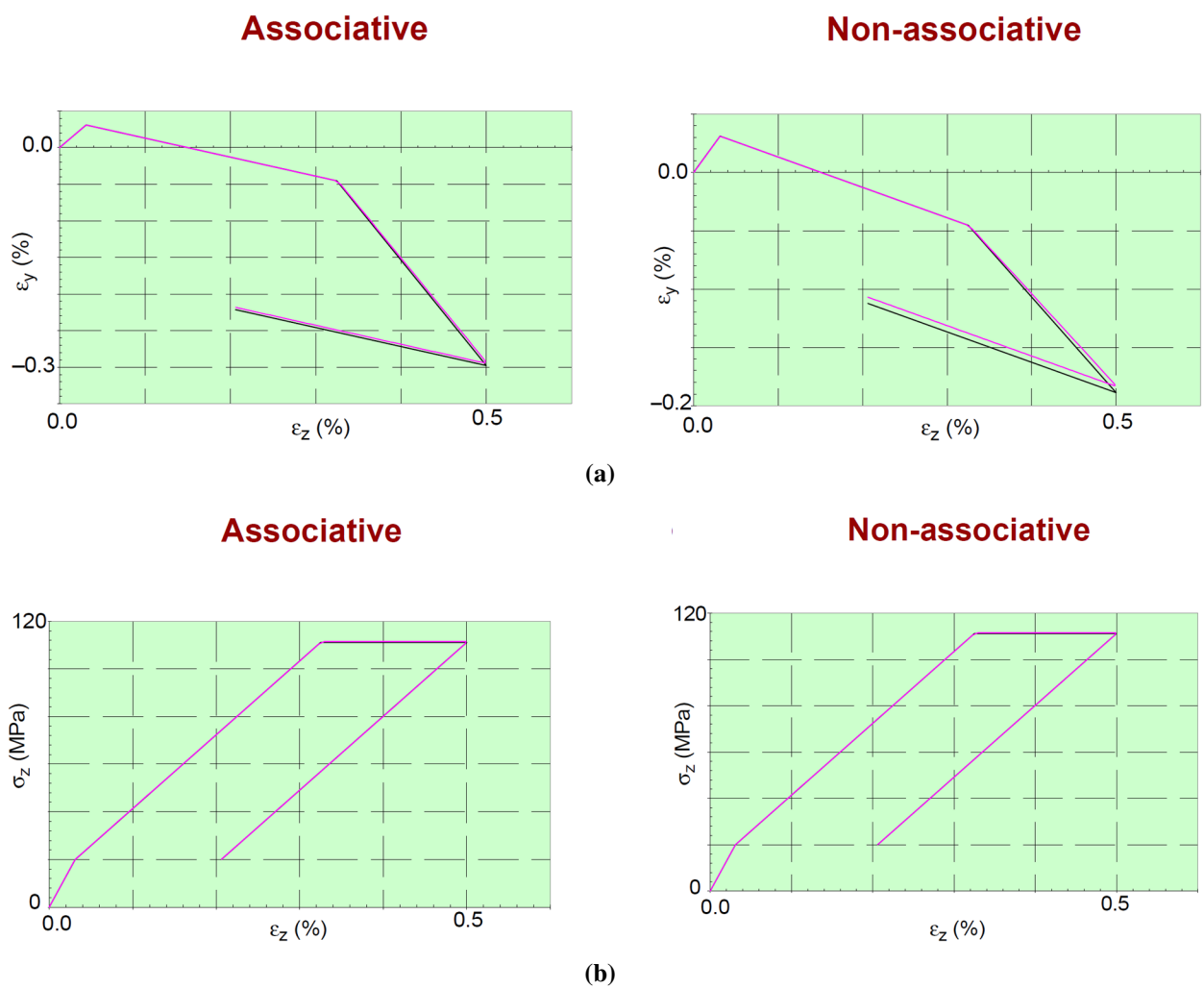

Figure 9.6. Single Element Verification Results, 20 MPa triaxial compression. Exact (black) solutions compared with alegra Kayenta simulation (pink). (a) lateral strain vs. axial strain (b) Stress vs. strain.

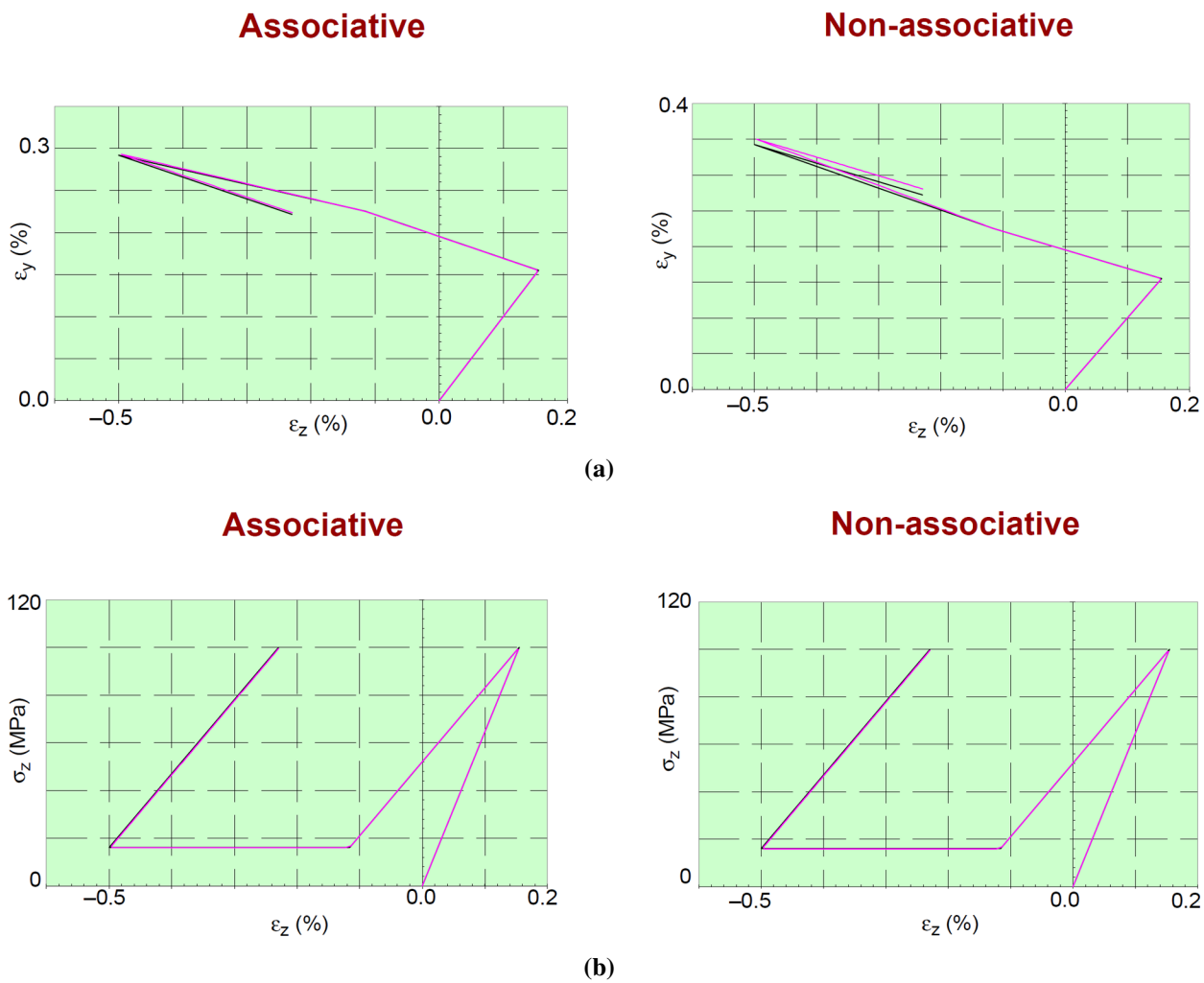

Figure 9.7. Single Element Verification Results, Reduced triaxial extension. Exact (black) solutions compared with alegra Kayenta simulation (pink). (a) lateral strain vs. axial strain (b) Stress vs. strain.

Table 9.1. Mohr-Coulomb Parameters for single-element verification testing

Parameter(material Properties	Symbol	Associative	Non-associative
Young's Modulus	E	31.0 GPa	31.0 GPa
Poisson's Ratio	ν	0.26	0.26
Friction angle	Φ	29°	26°
Dilation angle	ω	29°	14°
Cohesion	S_0	15.7 MPa	15.7 MPa
Dry bulk density	ρ	2.34 MPa$/m^3$	2.34 MPa$/m^3$

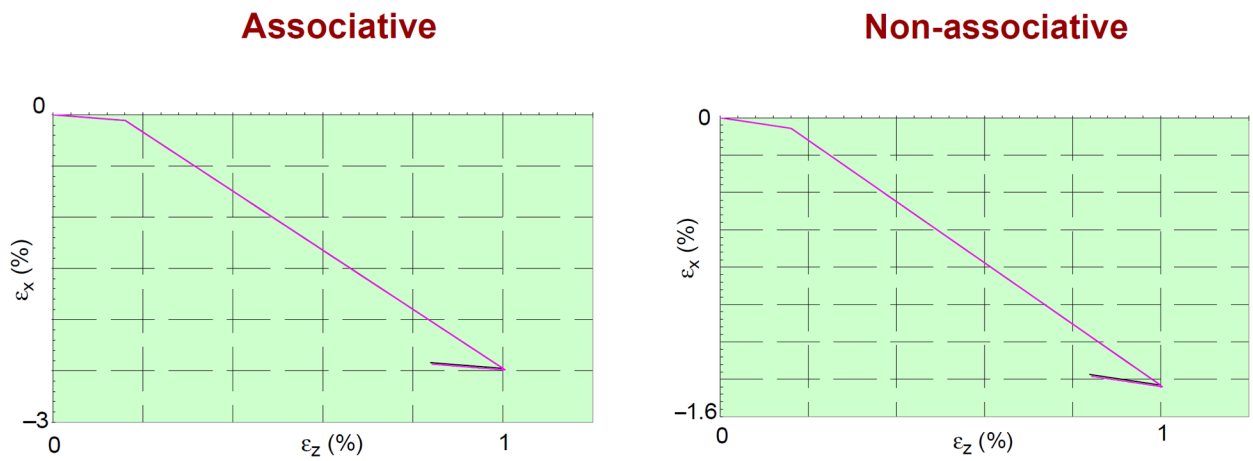

(a)

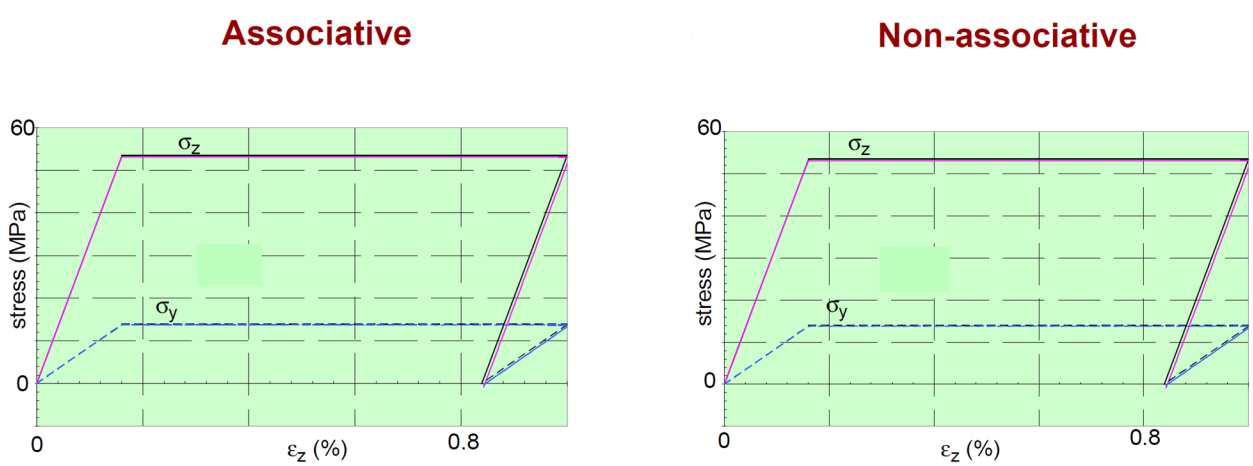

(b)

Figure 9.8. Single Element Verification Results, Plane Strain. Exact (black) solutions compared with alegra Kayenta simulation (pink). (a) lateral strain vs. axial strain (b) Stress vs. strain.

Discussion

In Fig. 9.8, predictions of Kayenta overlay the analytical results.[13] Though not yet proved conclusively, we contend that the slight discrepancy apparent in Fig. 9.5 and Fig. 9.6 arises *not from constitutive model errors*, but instead from host code errors in the handling of stress boundary conditions. The fully strain-controlled problem (Fig. 9.8) exhibits no significant solution discrepancy. However, moderate error is apparent in Fig. 9.5 and Fig. 9.6, which involve *two* stress boundary conditions (the lateral stresses). Like most constitutive models, Kayenta takes strain rate as input and returns updated stress as output. If the host finite-element code handles stress boundary conditions improperly, then it will have slight errors in the strain rate that it sends to Kayenta, thereby causing predictions to deviate slightly from analytical solutions. Such errors are not uncommon when dynamic finite-element codes are used to attempt to simulate homogeneous deformations.[14] To reiterate, we believe boundary condition errors in the host code (not Kayenta) are responsible for the solution errors, and we anticipate re-running these simulations in a true constitutive model driver to verify this claim.

Other single-element tests

Whenever the source code is changed, we perform approximately 20 single-feature single-element verification checks for each of our regression tests performed under loading that is simple enough to admit analytical solutions.

Fig. 9.9(a) depicts results from a hydrostatic loading simulation in which plastic volumetric strain (**`EQPV`**) is plotted against pressure (**`I1`**$/3$). The thick yellow curve in Fig. 9.9(a) is the crush curve [Eq. (4.69)] determined independently by user specified values of Kayenta parameters p_1, p_2, p_3. The *predicted* volumetric strain $\dot{\varepsilon}_v^p$ (black line in Fig. 9.9(a)) is verified to remain zero until the pressure reaches the crush curve, after which it drops along the crush curve as it should. The stress-strain curve (inset in Fig. 9.9(a)) unloads correctly to the user-specified peak strain parameter p_3. For *non-hydrostatic* loading, we have verified (undocumented trend-test) that shear-enhanced pore collapse causes inelasticity to commence *prior* to the pressure reaching the crush curve.

Fig. 9.9(b) simultaneously verifies Kayenta's ability to predict an apparent increase in strength under dynamic loading and its ability to predict different strengths in triaxial extension vs compression. In that problem, pressure dependence of yield was suppressed and the TXE/TXC strength ratio was set to 1/2, resulting in a tensile strength half as large as the compressive strength.[15]

[13] Precisely *quantifying* verification error lags far behind other more important constitutive SQA priorities, so we will be satisfied here and throughout this chapter with assessing agreement between computed and analytical results via a so-called "eyeball metric", where the error is nebulously bounded by what can be perceived visually, given the plot size.

[14] The only way to ensure a precisely homogeneous deformation in a dynamics finite-element code is to bypass solution of the momentum equation. More correctly, homogeneous loading requires a body force $\underset{\sim}{\mathbf{f}}$ identically equal to particle acceleration $\underset{\sim}{\mathbf{a}}$, making the momentum equation trivial.

[15] The TXE/TXC strength ratio applies to TXE and TXC states at the same pressure. When pressure dependence of yield is allowed, the TXE peak in a verification test like this will not *and should not* be 1/2 the magnitude of the TXC

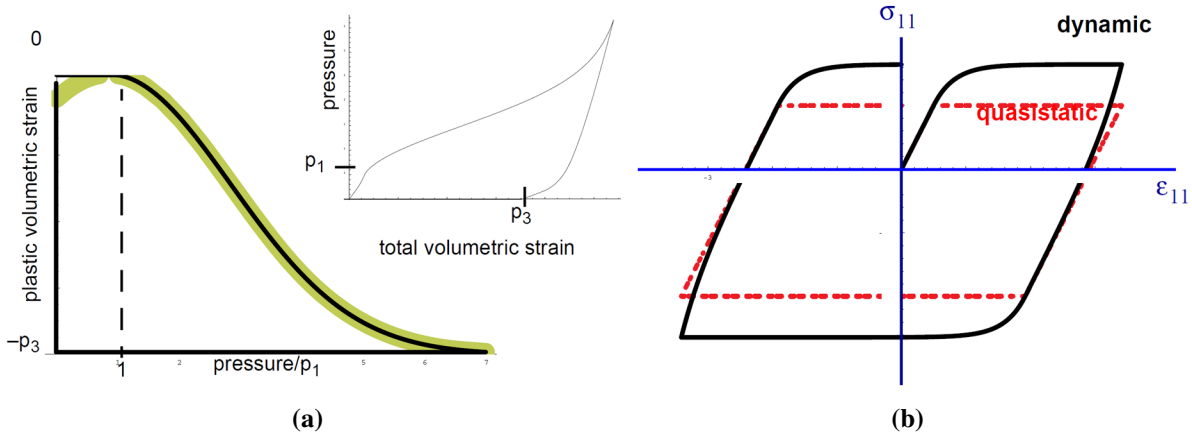

Figure 9.9. Other single-element tests. (a)Crush curve and hydrostatic loading verification. (b) Rate dependence TXE/TXC ratio verification for triaxial load/unload.

Verification: Hendren & Ayier pressurized cylinder

The problem depicted below, solved for subcases of associative and non-associative flow, involves a circular tunnel in a Mohr-Coulomb material loaded in a plane strain configuration. A DTRA contractor provided the analytical solutions. The material parameters are the same as those used in the previous verification problems.

peak.

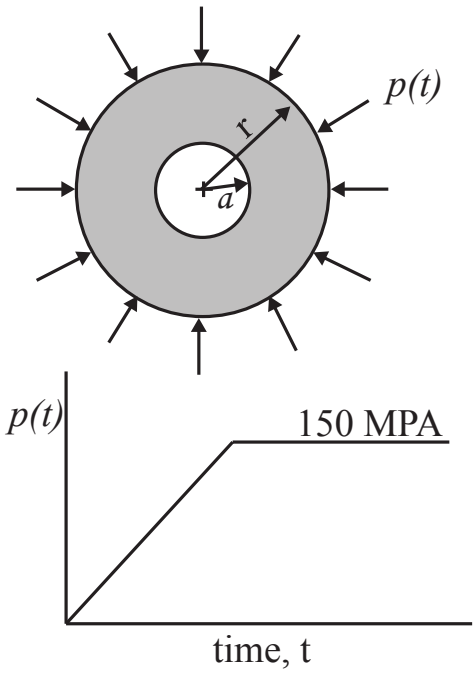

Geometry

Tunnel radius	a	1 m	1 m
Far field radius	b	10 m	10 m

Loading

Internal pressure	p_a	1 m	1 m
Far field pressure	p_b	0 – 50MPa	0 – 150MPa

The results in Fig. 9.10 show that Kayenta solutions agree with analytical results. Though not confirmed conclusively, the very slight discrepancies are hypothesized to result from different strain definitions used in Kayenta and the analytical solution (or possibly host code traction boundary condition issues similar to those discussed earlier).

Elastic free-field wave form (finite-element verification)

This section describes a field-scale test for verifying installation of Kayenta in host finite-element codes. As emphasized earlier, verifying a constitutive model is distinct from verifying its implementation within a finite-element code. After a constitutive model becomes one of *many* components within a much larger finite-element model, the potential sources of solution error expand to now include boundary conditions, artificial viscosity, and other aspects of the host code's method of solving the partial differential equation that governs momentum balance.

As indicated in Fig. 9.11, a time varying velocity (identical to the one later discussed on page 207) was applied at the boundary of a spherical cavity (radius 204 m). Kayenta's yield features were disabled to allow predictions for the velocity at the outer radius (470 m) to be compared with an analytical elasticity solution.[16] Implementations of Kayenta in two finite-element codes were tested. One code was unable to reproduce the correct response because of bugs in roller boundary conditions. Fig. 9.12 demonstrates that the second code (JAS3D) was capable of reproducing the analytical solution well enough to suggest that *Kayenta* is performing correctly. While the moderate solution error might be attributable to the analytical solution's presumption of small

[16] Aldridge's analytical solution [2] is expressed in terms of integrals that are evaluated numerically in the frequency domain using independent software provided by Aldridge.

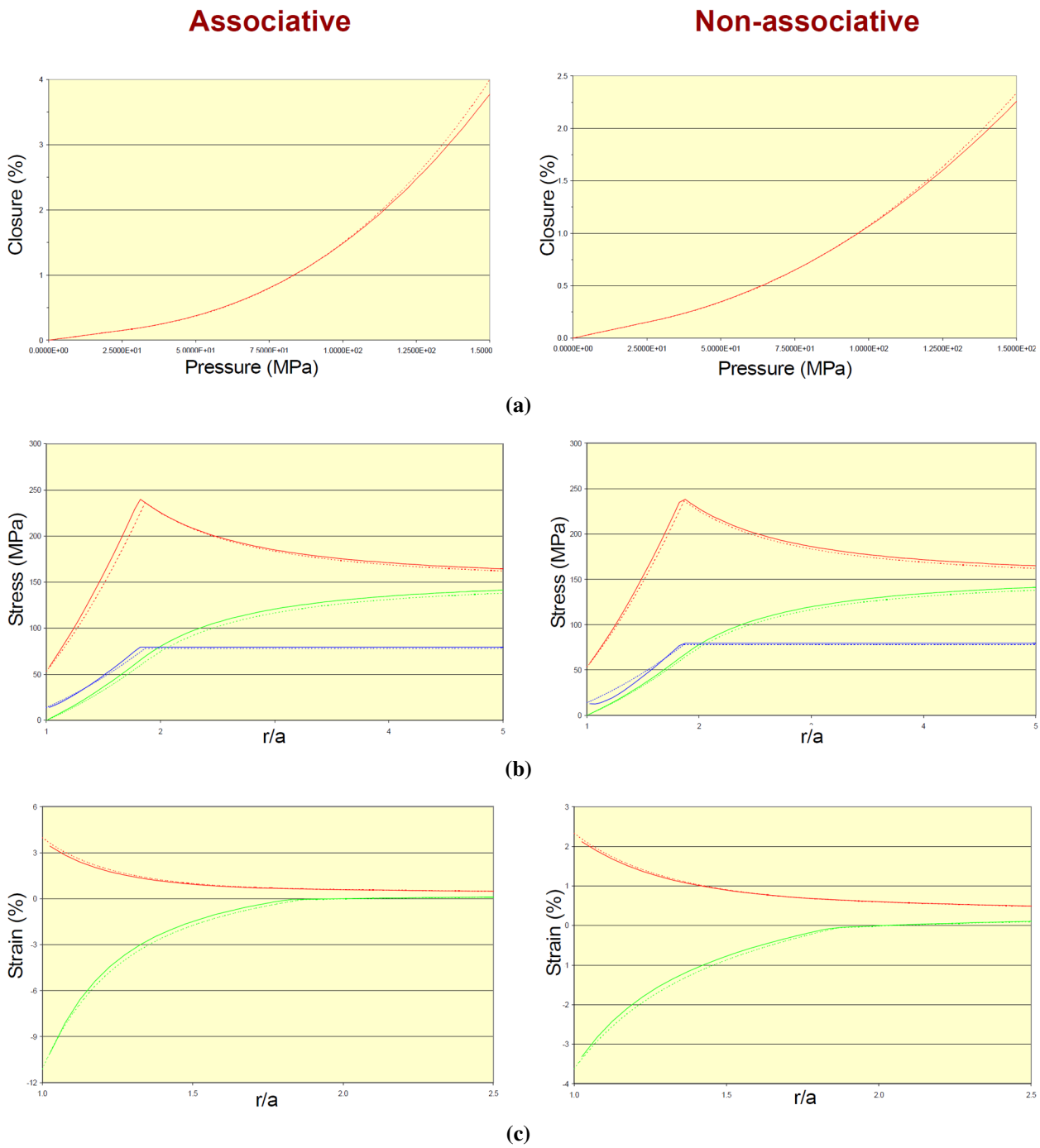

Figure 9.10. Hendron & Ayier verification problem. Exact (dash) solutions compared with alegra Kayenta simulation (solid). (a) Tunnel closure vs. far-field pressure (b) Stress components vs. normalized range, (c) strain components vs. normalized range.

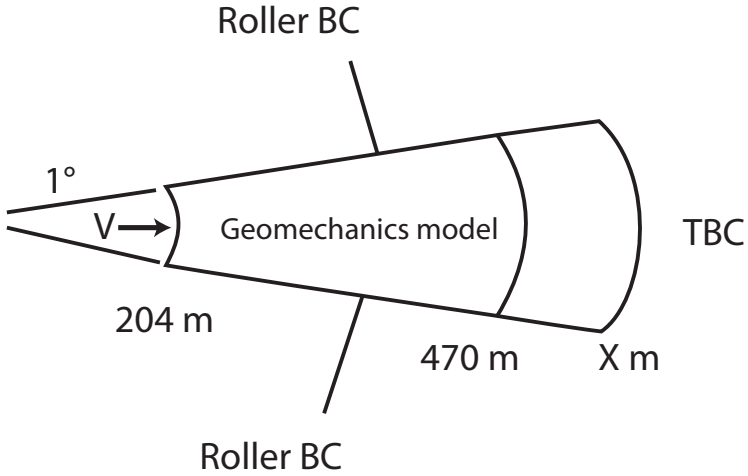

Figure 9.11. Spherical cavity geometry.

strains, further study (by the code owners, not Kayenta developers) is warranted to determine if the solution errors result from under-integration, or some other aspect of the finite-element model such as artificial viscosity (both codes' solutions were strongly affected by artificial viscosity — default settings for artificial viscosity were insufficient to reproduce the analytical results). This elasticity verification problem is revisited and generalized in the *plasticity* validation test on page 207, where code predictions are compared with data.

Softening verification and validation

Softening and failure is a relatively new capability within Kayenta. As such, the softening and failure implementation is still under development, and its verification and validation is incomplete. This section summarizes only some basic trend testing.

The softening capabilities of Kayenta should be used only in conjunction with additional measures taken within the host code to mitigate mesh sensitivity associated with the change in type of the governing equations that occurs upon the onset of softening. As discussed in Chapter 5 and illustrated in Fig. 9.13, one means of mitigating mesh dependence allows development of localized failure by introducing statistical variability and scale effects in strength.

When statistical uncertainty is incorporated in a simulation, verification and validation testing becomes considerably more difficult since one must run a statistically significant number of simulations to check for convergence of results toward an analytical distribution function. One such study, summarized in Fig. 9.14, used the **FAILSTAT** user control parameter (see page page 230) to verify that the onset of failure under nominally homogeneous loading in spherical tension was

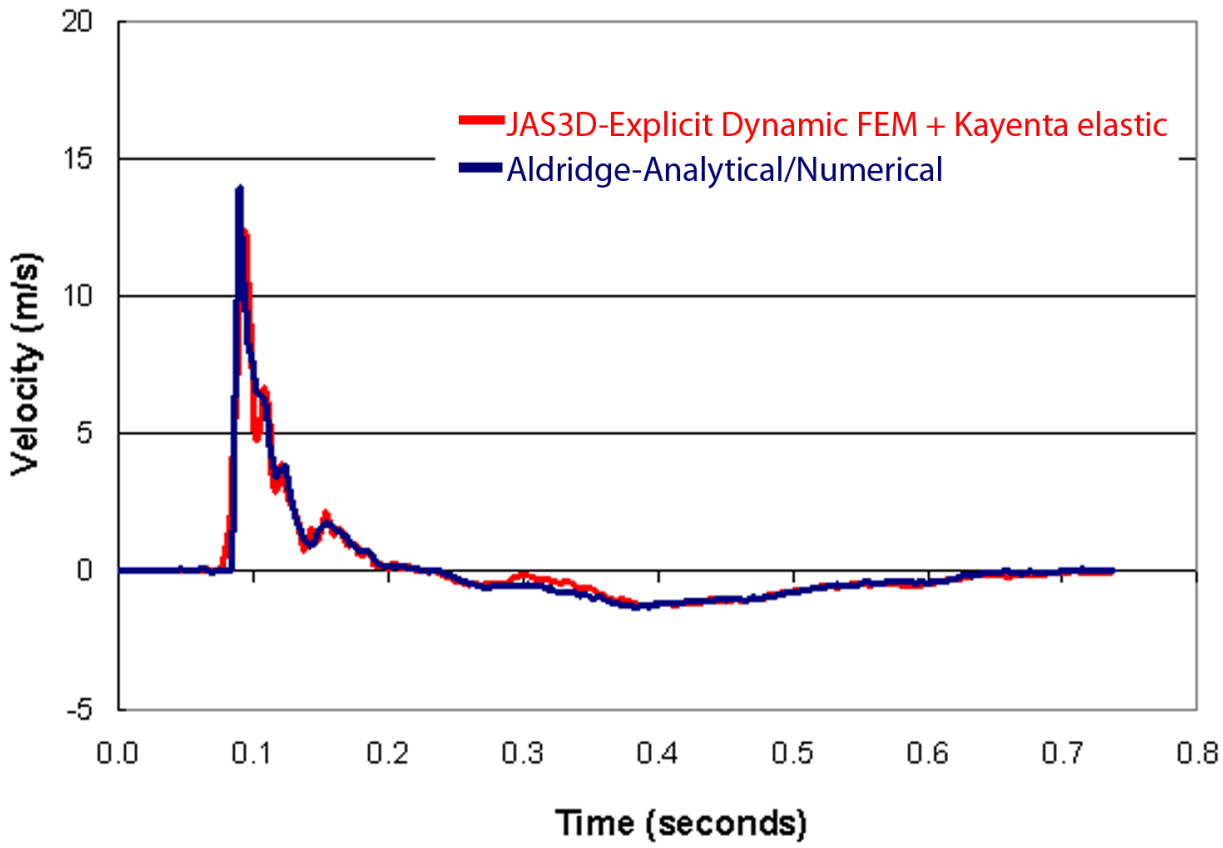

Figure 9.12. Finite-element vs. analytical/numerical elastic wave velocity at 470 meters from a velocity spherical cavity source at 204 meters.

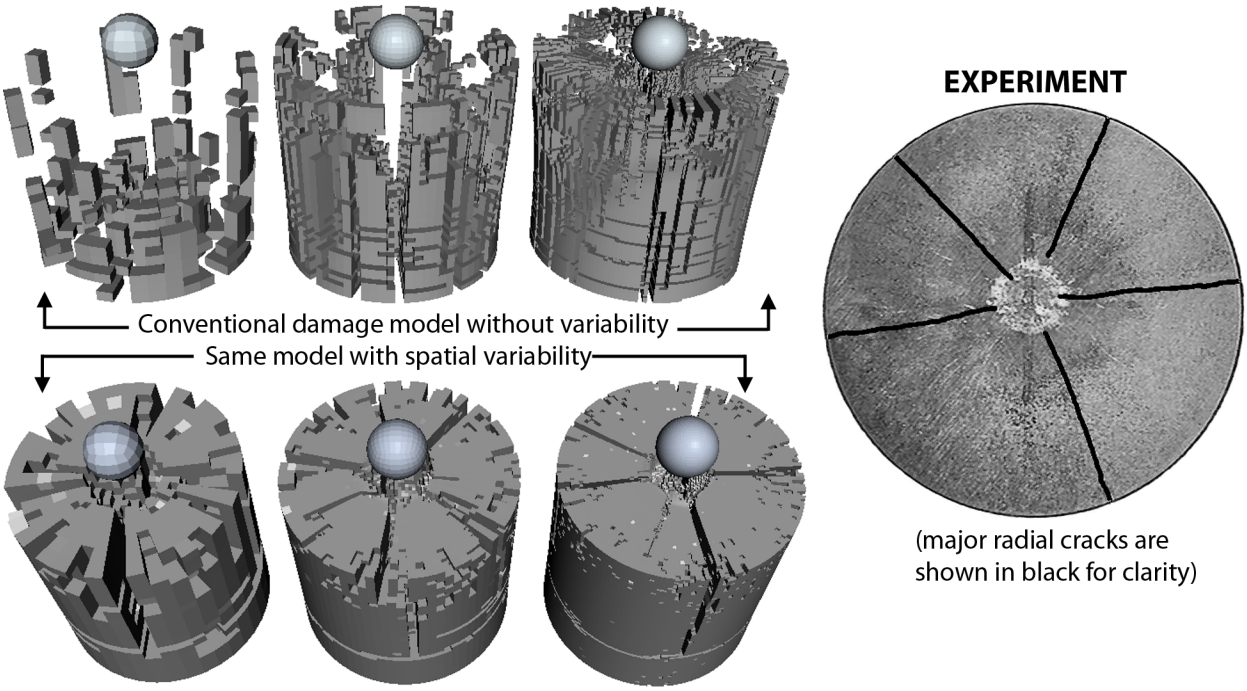

Figure 9.13. Reduced mesh dependence and improved accuracy in dynamic indentation (tungsten carbide sphere impacting SiC-N ceramic at 500 m/s). All simulations show intact material at the same moment in time, but at three mesh resolutions. All use the Kayenta damage model with the same median properties. Simulations in the bottom row merely allow the material properties to deviate from the median based on experimental evidence for aleatory uncertainty and size effects.

indeed consistent with the user specified failure line in Weibull space. The ordinate in a Weibull plot is the indicated transformation of the complementary cumulative probability P_s which may be interpreted as the probability the sample is safe at the specified stress level. The abscissa is the log of the stress normalized by the median failure stress. Fig. 9.14 also shows a very light level of validation by illustrating that observed deviations of measured strength data from a Weibull line are finite sampling effects consistent with similar deviations in finite sampling of *exactly* Weibull distributed data.

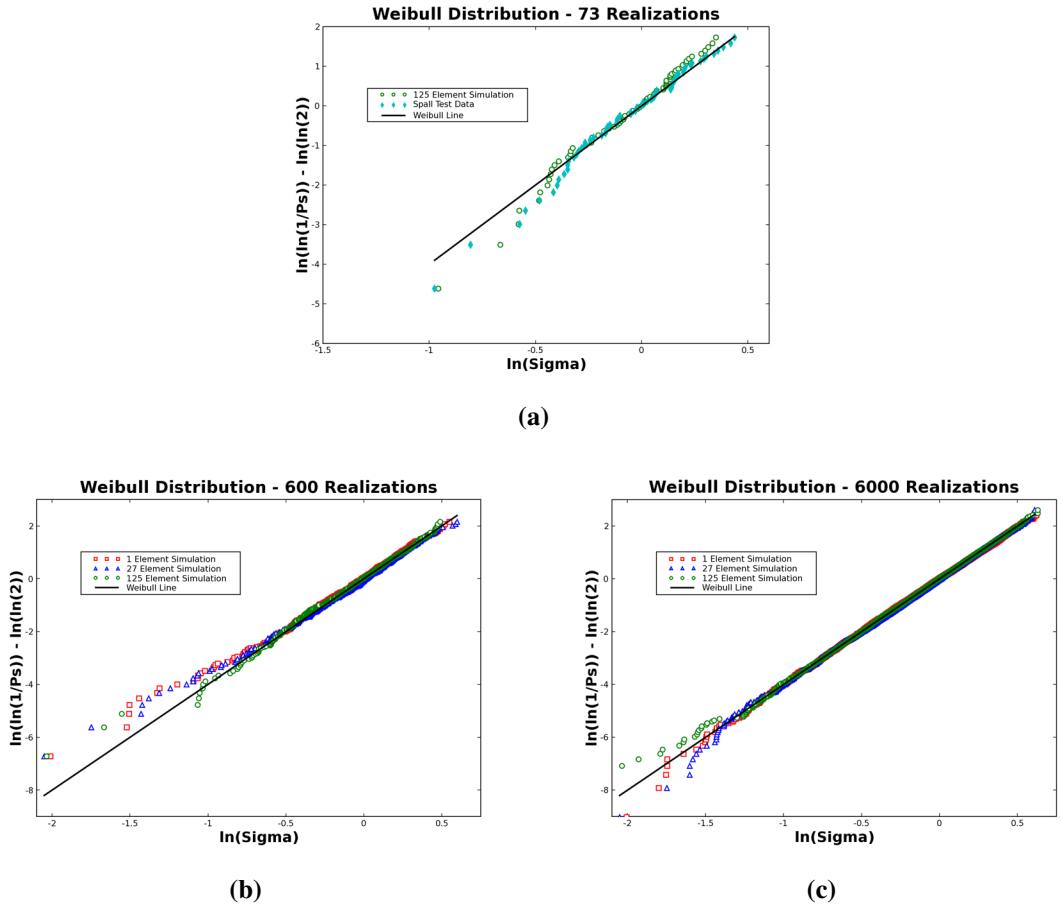

Figure 9.14. Reduction in sampling error with number of data points. (a) compares experimental data against numerically generated failure strengths that are *exactly* Weibull distributed with the same Weibull modulus. (b) and (c) show simulated data for the onset of failure (using the "FAILSTAT" control parameter) for three mesh resolutions to demonstrate that the failure statistics are mesh insensitive and approach the Weibull distribution as the number of realizations is increased.

Users should always assess believability of their simulations by performing mesh sensitivity

analysis. This verification and validation practice is even more essential in any softening or failure simulation. Accounting for statistical variability and scale effects appears to be *necessary* for obtaining realistic predictions of material failure. However, in the interest of full disclosure, it should be noted that variability and scale effects are not *sufficient* to ensure mesh insensitive results. Our simulations of Brazilian failure (see Fig. 5.8) produced failure statistics having trends consistent with laboratory data, but the quantitative median strength was found to be mesh dependent.

Verification of Accumulated Damage Framework

This section explains the verification procedure for the new strain-to-failure damage framework. It is a collection of verbatim or paraphrased excerpts from the thesis [87] by M. Swan.

Any constitutive model, no matter how long it has been in use, should undergo regular verification and validation testing. Verification, in this sense, refers to the act of ensuring that the model has been correctly implemented and connected to the host code while validation ensures that the model's predictions match experimental observations. The importance of verification testing for all usage conditions cannot be overstated. Verification testing proves that a model's predictions can be trusted for the specific usage scenarios where the constitutive assumptions are met. However, when a model is not implemented correctly, its results cannot be trusted; the only way to build confidence in a model is to do verification testing. Ideally, verification testing is done by using the constitutive equations to derive an analytical solution and compare that to the computed approximation to make certain that the model is behaving appropriately. Even when analytical solutions are not tractable, verification testing is applied to confirm expected trends in the results and appropriate numerical behavior such as convergence and stability.

For this research, an integral part of which is to enable fast prototyping of recently developed fracture models with linear accumulation of damage, verification is of the utmost importance as this research lays a foundation for future models to be implemented. Specifically, the new strain-to-failure damage framework (along with the three initial models to be included: the constant equivalent-strain-to-failure (CESF), Johnson-Cook [50] (JC), and Xue-Wierzbicki [95] (XW) fracture models) is being implemented into Kayenta, a computational framework for generalized plasticity models. Kayenta was a natural choice for this research as it is already part of numerous codes in use by private companies and government laboratories domestically as well as abroad. Because Kayenta is already in daily use by many researchers and is installed on many clusters, some of them frequently utilizing thousands of processors per simulation, these models can be implemented and evaluated in large-scale applications with very little time spent on the model/host code interface. However, before running simulations with millions of elements, it is necessary to do extensive single-element testing.

Kayenta's primary benchmarking and single-element testing framework is called `MatModLab` [39]. MatModLab is a flexible, easily extensible framework written in Python that supports a user-defined mixture of stress and strain control, as well as a user-defined electric field (for ferroelectric and piezoelectric models). Because of the great flexibility and ease of use of MatModLab, it is

adopted in this research to verify the implementation of these three fracture models into Kayenta. In the case of the JC and XW fracture models, it is very important to maintain proportional loading along a constant stress triaxiality and Lode angle (which corresponds to the set of stress states falling on a straight line passing through the origin in Haigh-Westergaard principal-stress space). Because the verification problems that we are looking at involve softening (loss of strength and stiffness), it is very difficult to maintain proportional loading throughout the simulation while maintaining a nonzero strain rate because of the collapsing limit surface.

Given that constitutive models are invariably written such that strain or strain increment is the input, with updated stress and internal variables being the outputs, MatModLab can iteratively solve an inverse problem to determine the strain increments required to achieve a prescribed stress or stress increment. In the verification plots to follow, it will be seen that MatModLab performs well in prescribed-stress proportional loading cases of triaxial extension, triaxial compression, and pure shear. However, maintaining proportional loading for stress states that are not in the preceding list is much more difficult for specific values of stress triaxiality. Artifacts from this shortcoming of MatModLab (not Kayenta or the implementation of the fracture framework) can be identified by noise in the **EQPS** value at a given **COHER** value. Fig. 9.18 (which will be shown later) depicts this instability well as all the failure strain realizations from the single element tests for the CESF model should be at an intersection of the grid lines representing the analytical solution.

Table 9.2. A list of values used to parameterize the models for the verification plots. The fracture models all used parameters published in Ref. [95]. All values in MKS.

Material Parameters for Al 2024-T351					
von Mises	K		G		Y
	71.5×10^9		28×10^9		283×10^6
CESF	ε^f				
	0.21				
JC Fracture	D_1	D_2	D_3	D_4	D_5
	0.13	0.13	-1.5	0.0	0.0
XW Fracture	D_1	D_2	D_3	D_4	n
	0.87	1.77	0.21	0.01	0.153

The verification tests in this chapter are analyzed in much the same manner as the laboratory tests used to calibrate the Xue-Wierzbicki model [95]. Also, these analyses use the user inputs that Wierzbicki proposed for Aluminum 2024-T351 and are included in Table 9.2. In particular, most of the verification tests in this chapter are performed on states of plane stress since Wierzbicki states that all of his specimens failed in states of plane stress. The primary measurement from a given simulation or experiment is the equivalent plastic strain at failure. Wierzbicki [95] makes the assumption that all strains (volumetric and deviatoric, elastic and plastic) are plastic, but classic fracture models (e.g., the Johnson-Cook [49] and Wilkins [97] fracture models) use only the deviatoric part of the plastic strain to compute the equivalent plastic strain. Because of this precedent, the Kayenta implementation of the three fracture models will be based on the equivalent deviatoric

plastic strain.

Equivalent strain at failure is often plotted against the two most likely independent variables, namely the stress triaxiality and the Lode parameter. These two values loosely represent $J_2$and J_3 dependence, respectively. While the dependence of fracture on $J_2$is well known, current publications are increasingly reporting that J_3 dependence is nonnegligible for fracture prediction.

Though some research efforts using servo-controlled axisymmetric loading have shown promise in achieving controlled movement of the stress state through stress space [18], triaxiality and the Lode parameter are difficult to keep constant (as required for proportional loading) during laboratory tests. Because of this, the averages of both the triaxiality and Lode parameter are computed (in both the experiment and simulated analysis) through an equivalent-strain-weighted average:[17]

$$\eta_{\text{avg}} = \frac{1}{\varepsilon^f} \int_0^{\varepsilon^f} \eta \, d\varepsilon \tag{9.3}$$

$$\xi_{\text{avg}} = \frac{1}{\varepsilon^f} \int_0^{\varepsilon^f} \xi \, d\varepsilon \tag{9.4}$$

The XW and the quasi-static, isothermal JC fracture models both assume proportional loading to failure for the analytical solution to be valid. As Wierzbicki and others have used the strain-weighted average technique to parameterize the models, we will use it to include the effects of slight nonproportional deviations in loading for the single-element tests.

In many of the verification figures to follow, there is a comparison of the effect of k on the accuracy of the fracture prediction. As discussed earlier, k controls how quickly the material loses strength; low values of k dictate that softening proceeds slowly while large values implies near-instantaneous softening. The gradual nature of the loss of strength calls into question when, precisely, a material transforms from intact to fractured. The upcoming figures and discussion compare the value of plastic strain when **COHER** $= 0.5$ with the failure strain ε^f in the three fracture models. For each single-element test reported in the upcoming figures, there are three points that convey the range over which the material is softening. As the loss of strength occurs over relatively few time steps, we use a linear interpolation of the independent variable **COHER** to determine the equivalent plastic strain at exact values of coherence. Time step size has been reduced to help in minimizing errors from the linear interpolation, but some small amount of error still exists.To generate plane stress states, the ratio of the nonzero stresses was determined by realizing a distribution of equally spaced angles ranging from $[\pi/4, 5\pi/4]$ and using each angle realization ϕ in

$$\frac{\sigma_1}{\sigma_2} = \frac{\cos\phi}{\sin\phi} \tag{9.5}$$

This gives a ratio of unity for both $\pi/4$ and $5\pi/4$, which correspond to biaxial tension and biaxial compression, respectively (see Table.(2.1), in [87]). Because the material is isotropic, it is

[17] In Eq. (9.4), (ξ) is the *deviatoric state parameter* and not to be confused with the *shifted stress* used in the other parts of the document. (η) is a measure of triaxiality.

not necessary to generate angle realizations for the full circle. However, the framework has been tested extensively to verify that material isotropy is maintained. For states of plane stress with the ratio of the nonzero stresses as defined above, the stress triaxiality η is given by

$$\eta = \frac{\cos(\phi) + \sin(\phi)}{3\sqrt{1 - \frac{1}{2}\sin(2\phi)}} \tag{9.6}$$

As seen in Fig. 9.15, stress triaxiality η is nearly linear with respect to ϕ. However, the slight nonlinearity (especially at the extremes) will produce slightly nonuniform spacing in triaxiality realizations when the angle ϕ is sampled uniformly. This accounts for the minor spacing irregularities in many of the upcoming figures.

The root-mean-square error (RMS error or the standard deviation of error) is presented as a quantitative method to determine the accuracy of the framework. For each triaxiality realization, a single element simulation was performed. The analytical value of ε^f (as determined by the triaxiality realization) is compared with the simulated value of ε (**EQPS**) when **COHER** $= 0.5$. Thus, the RMS error encompasses the errors introduced by the proportional stress implementation of MatModLab as well as the fracture framework error.

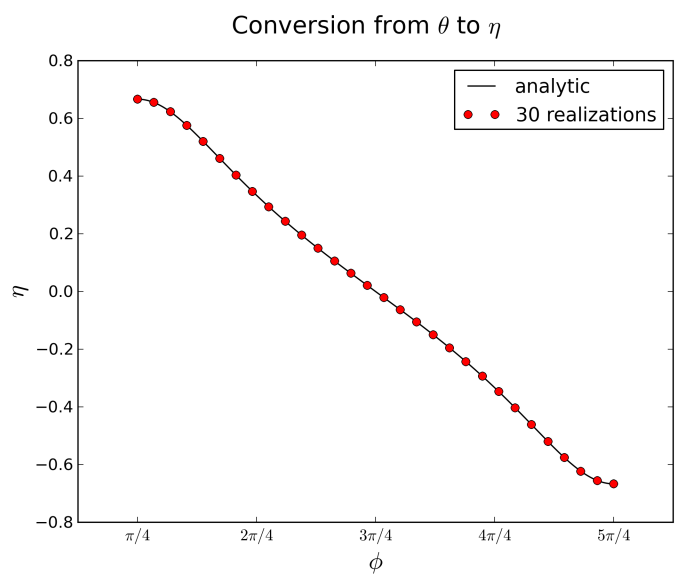

Figure 9.15. A comparison of triaxiality versus proportionality angle for plane stress states.

Constant Equivalent-Strain-at-Failure Verification

The scatter evident in Fig. 9.16, where $k = 5$, is caused by the previously mentioned difficulty of maintaining proportional loading for those particular values of the Lode parameter. When $k = 50$ the accuracy and precision of predicted equivalent plastic strain at fracture are much increased, giving excellent agreement with the analytical solution (in this case $\varepsilon^f = 0.21$, shown by the black line) considering that, during the loss of strength in prescribed stress simulations, strain rate increases dramatically. The RMS error between the analytical solution and the **EQPS** values when **COHER** $= 0.5$ and $k = 50$ in Fig. 9.18 is 0.000059, or approximately 0.03%.

This model is a very good indicator of the overall accuracy of the fracture framework, especially as it is a simple model without peaks or cusps in ε^f versus η and ξ space.

As previously mentioned, the triaxiality realizations were generated by varying the angle ϕ in the plane stress (σ_2 vs. σ_1) space. As ϕ is varied, not only does triaxiality change, but the Lode parameter varies as well. Therefore, Fig. 9.16 and Fig. 9.17 show variation of strain-to-failure with respect to both triaxiality and the Lode parameter.

Johnson-Cook verification

As seen in Fig. 9.19, Fig. 9.20, and Fig. 9.21, the JC fracture model verification results are similar to those of the CESF model. The same difficulties in maintaining proportional loading (and the corresponding scatter in predictions) are encountered, particularly for low values of k. The single-element tests and the analytical solution agree within a standard deviation of 0.0032. As the ε^f value varies with respect to η, this error can be approximated as 1.0% assuming an average ε^f value of 0.3. As it is necessary for the new code to be considered well-verified for these problems, the analytical solution (black line in Fig. 9.19) lies within the range of **EQPS** between **COHER** = 0.75 and **COHER** = 0.25 for the entire domain of interest. This test of the quasi-static, isothermal JC model shows that, for a more complicated model with η dependence, the framework can still predict failure close to analytical solution.

Xue-Wierzbicki Verification

The XW model posed some challenges to the verification framework. While the form of the fracture locus in η space is functionally similar to that of the JC model, the coefficients in the exponential are much larger and predict unreasonably high fracture strains for Lode angle parameters extremely close to $+1$ or -1 (see Fig. 9.23; this accounts for the anomalous strain spikes in Fig. 9.22).

In the verification realizations in Fig. 9.22(a), Fig. 9.22(b), and Fig. 9.24 the cusps of the analytical solution are difficult to reproduce. This is due, in part, to the averaging process (see Eq. (9.3) and Eq. (9.4)) to determine the values of η and ξ to plot the computed **EQPS** against.

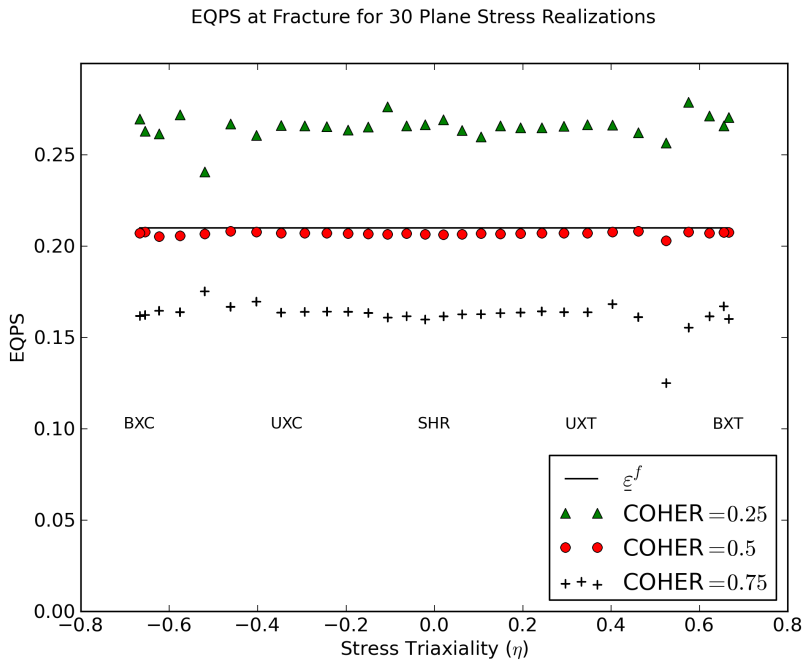

(a)

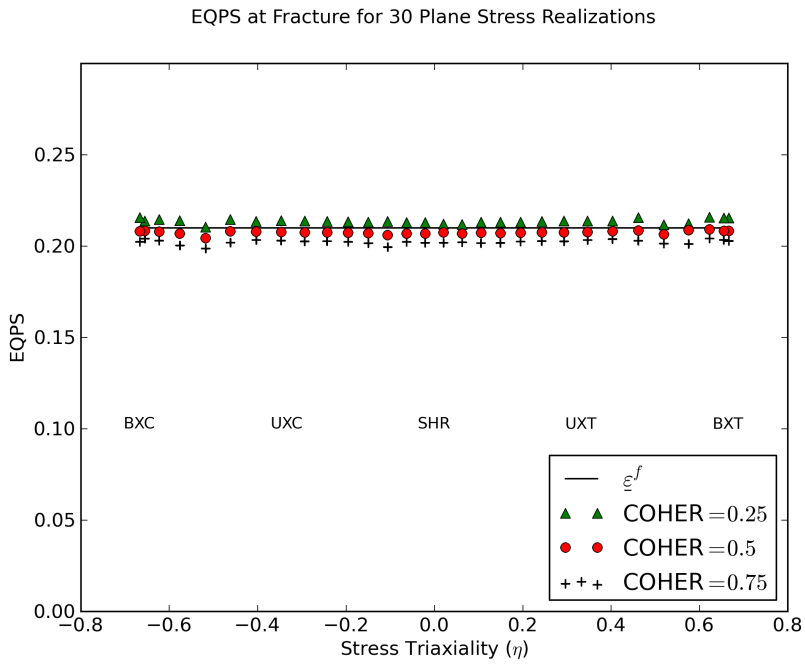

(b)

Figure 9.16. A comparison of accuracies of equivalent plastic strains (**EQPS**) at failure for different values of k using the constant equivalent-strain-at-failure fracture model.(a) $k = 0.5$. (b) $k = 50$.

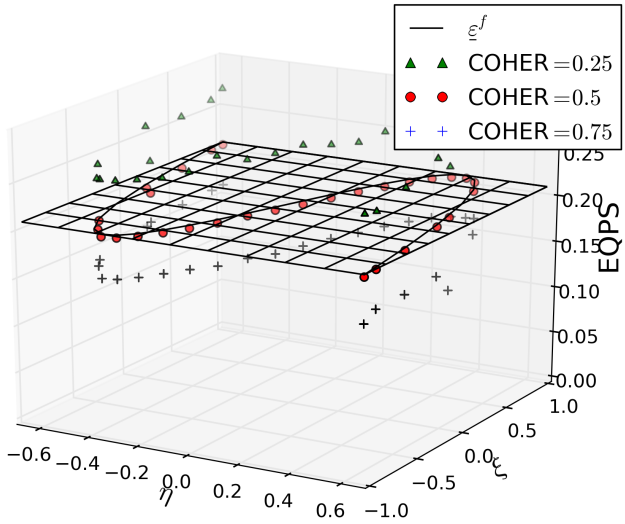

(a)

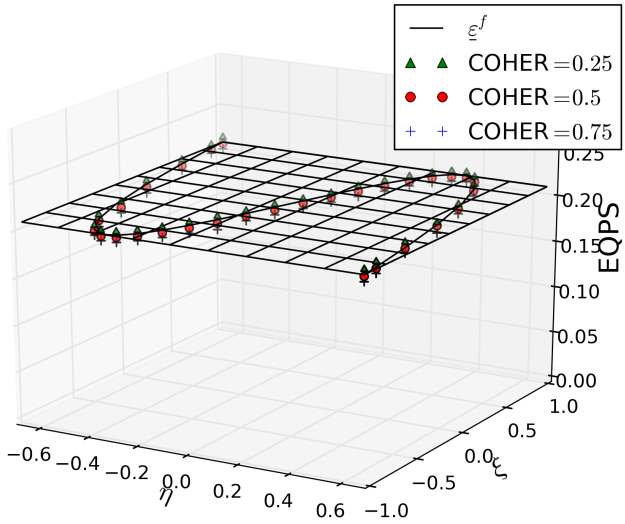

(b)

Figure 9.17. 3D Comparison of equivalent plastic strain (**EQPS**) at failure for different values of k versus strain-averaged triaxiality and Lode parameter using the constant equivalent-strain-to-failure fracture model.(a) $k = 5$. (b) $k = 50$.

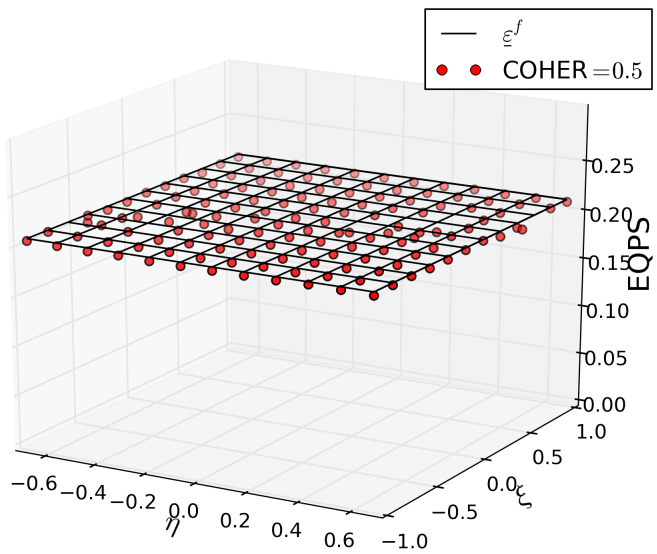

Figure 9.18. This plot demonstrates the limitations of MatMod-Lab in maintaining proportional loading for certain values of η and ξ (with $k = 50$). However, for verifying the accuracy of the fracture framework, the results are very good for all points displayed (the RMS error is approximately 0.03%).

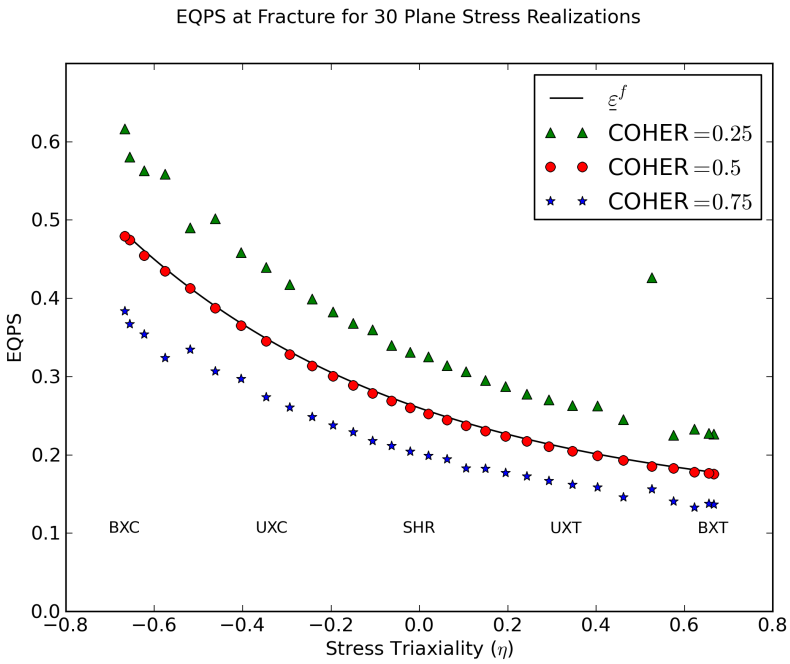

(a)

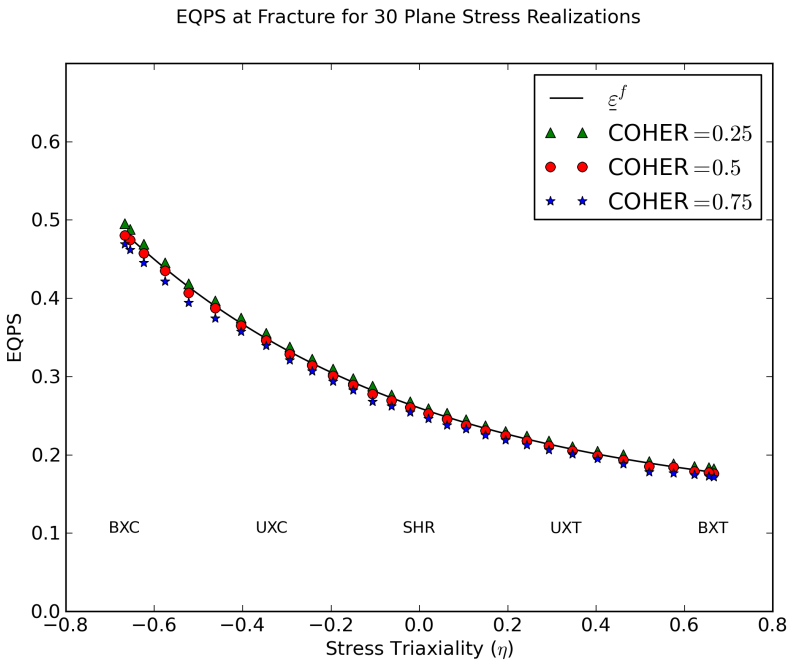

(b)

Figure 9.19. Comparison of accuracies of equivalent plastic strains (**EQPS**) at failure for different values of k verses strain-averaged triaxiality using the Johnson-Cook fracture model.(a) $k = 0.5$. (b) $k = 50$.

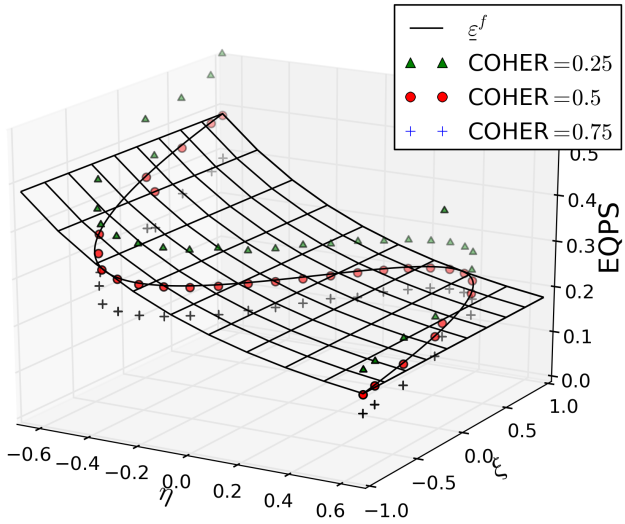

(a)

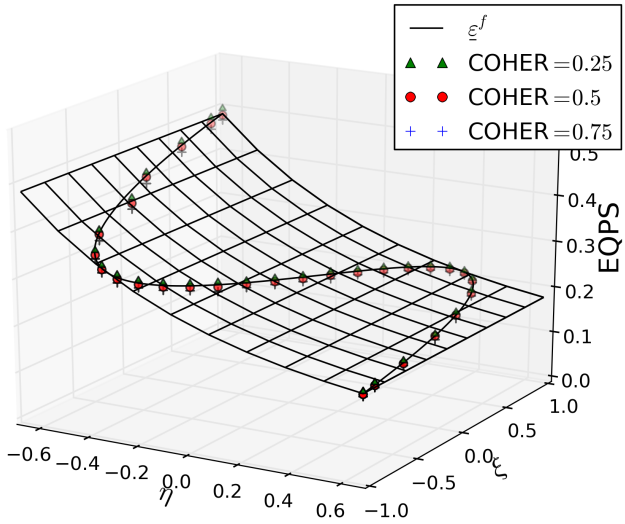

(b)

Figure 9.20. 3D Comparison of equivalent plastic strain (**EQPS**) at failure for different values of k versus strain-averaged triaxiality and Lode parameter using the Johnson-Cook fracture model.(a) $k = 5$. (b) $k = 50$.

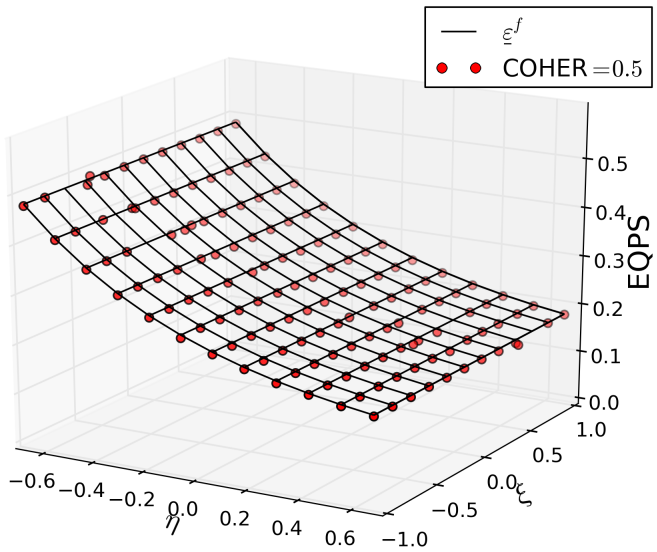

Figure 9.21. This plot demonstrates the limitations of MatModLab in maintaining proportional loading for certain values of η and ξ (with $k = 50$). However, for verifying the accuracy of the fracture framework, the results are very good for all points displayed (the RMS error is approximately 0.93%).

The bulk of the cause of the discrepancies at the cusps is the linear accumulation of damage with slight deviations in η and ξ. This difficulty is reflected in the RMS error (error $= 0.027$) between the realizations and the analytic solution. However, the **EQPS** error goes down to 0.0028 when values on the cusps ($\varepsilon^f > 0.5$) are neglected.

Verification for the XW model at stress triaxialities below $-\frac{1}{3}$ is entirely academic as the model assumes a fracture cutoff at $\eta = -\frac{1}{3}$. As this is primarily a verification for the strain-to-failure framework, this region was included to push the limits of reasonable **EQPS** values at fracture for highly specific stress states.

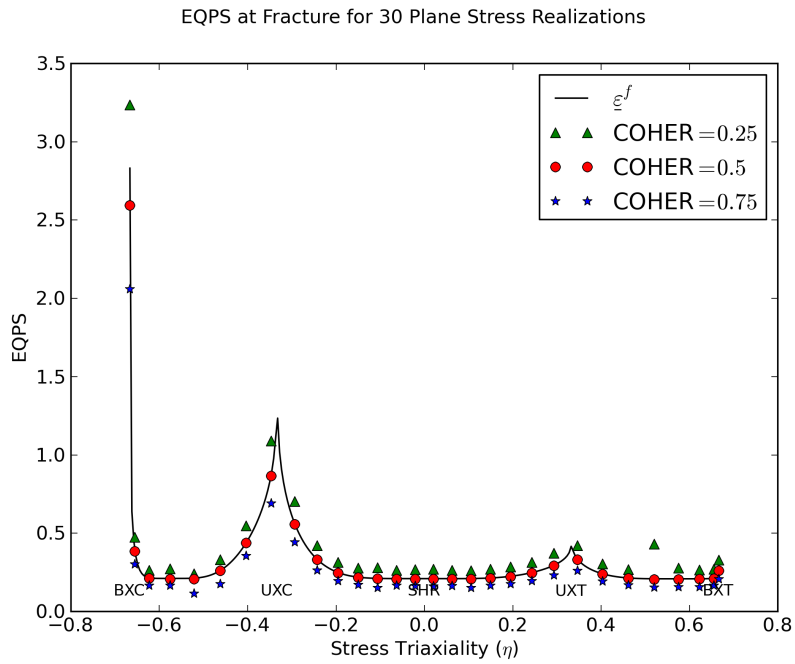

(a)

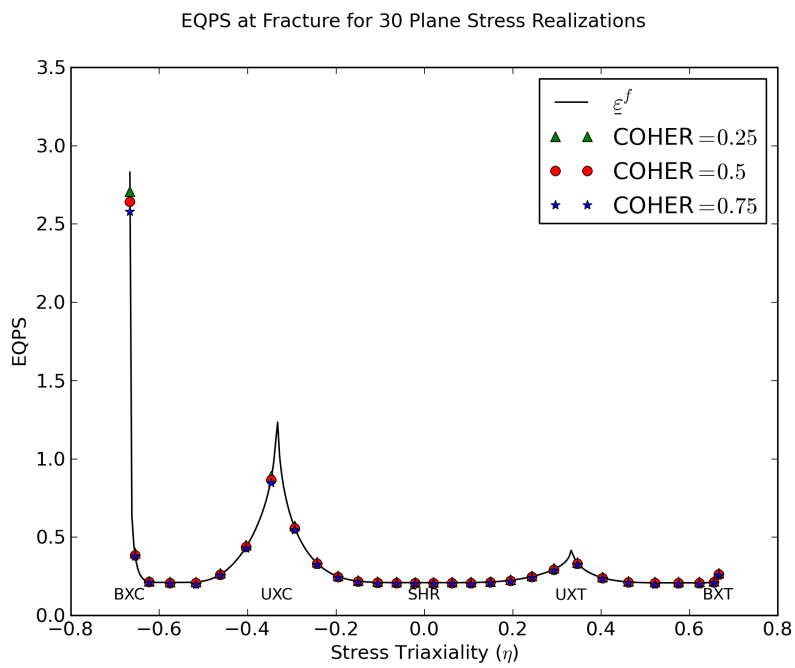

(b)

Figure 9.22. Comparison of accuracies of equivalent plastic strains (**EQPS**) at failure for different values of k using the quasi-static, isothermal Xue-Wierzbicki fracture model.(a) $k = 0.5$. (b) $k = 50$.

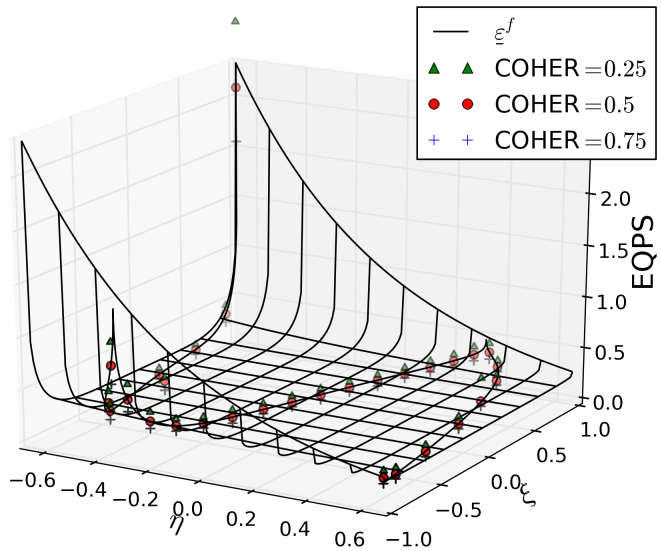

(a)

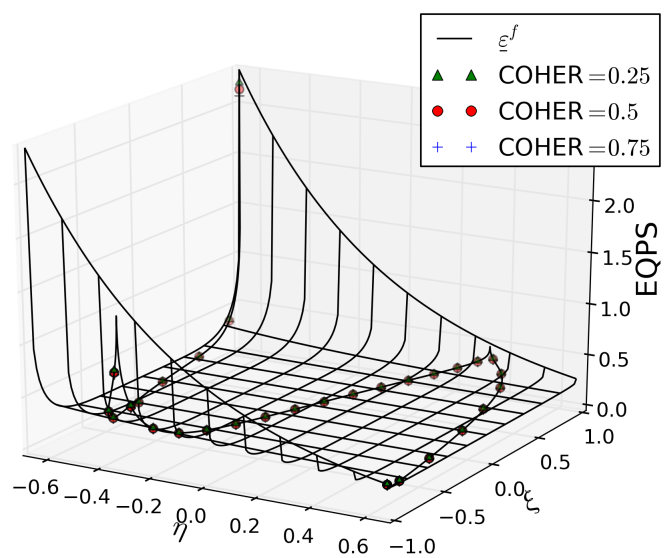

(b)

Figure 9.23. 3D Comparison of accuracies of equivalent plastic strain (**EQPS**) at failure for different values of k versus strain-averaged triaxiality and Lode parameter using the Xue-Wierzbicki fracture model. (a) $k = 5$. (b) $k = 50$.

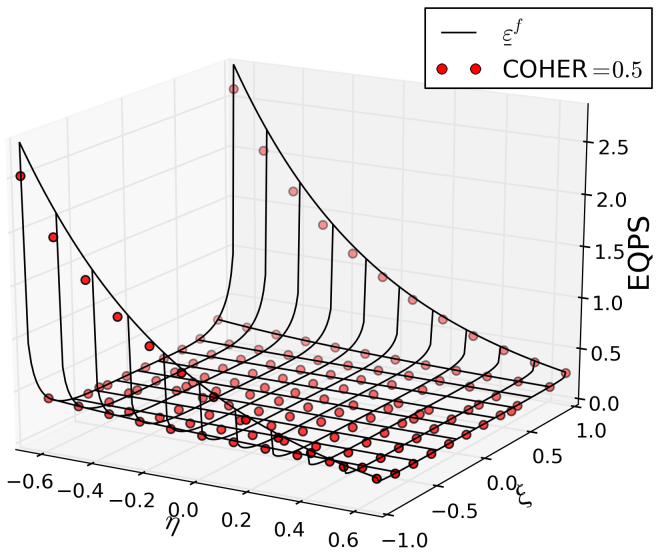

Figure 9.24. For proportional loading, the plotted dots are expected to lie on the gridlines. Clearly, this plot demonstrates the limitations of MatModLab in maintaining proportional loading for certain values of η and ξ (with $k = 50$). However, for verifying the accuracy of the fracture framework, the results are very good for all points displayed (the RMS error is approximately 0.022%).

Thermo-Kayenta Verification

We now review the results of simulations using Thermo-Kayenta and verify those results against identical simulations run using the Johnson-Cook plasticity model. Two types of verification tests were run: single element simulations using uniaxial, isotropic, and isochoric displacement controlled strain paths and a multi-element Taylor impact simulation.

All single element Johnson-Cook simulations were performed by Joseph Bishop on SNL's ALEGRA using identical Mie-Grüneisen equation of state subroutines while the single element Thermo-Kayenta simulations were performed in Prof. Rebecca Brannon's stand alone material driver, MED. Both the Johnson-Cook and Thermo-Kayenta Taylor impact simulations were performed in LS-Dyna.

In the following simulations, the following material properties were used in the models indicated:

A	B	C	m	n	T_0	T_m
90 MPa	292 MPa	0.025	1.09	0.31	298 K	1356 K

Table 9.3. Material properties used in the Johnson-Cook flow model

K	G	A_1	R	H	T_1
137 GPa	53.0 GPa	112.5 MPa	22.5 MPa	750 Gpa	-

Table 9.4. Material properties used in Thermo-Kayenta

ρ_0	c	s_1	γ_0	c_v
8960.0 kg/m^3	-	1.5	1.99	383.0 J·kg/K

Table 9.5. Material properties used in the Mie-Grüneisen equation of state

Isotropic Deformation

Since Thermo-Kayenta, as does SNL's installation of Johnson-Cook plasticity in ALEGRA, presumes plastic incompressibility, comparison of isotropic deformation is used to verify calculations and installation of the equation of state in Thermo-Kayenta. For each of the following comparisons, the following prescribed volumetric strain path was used:

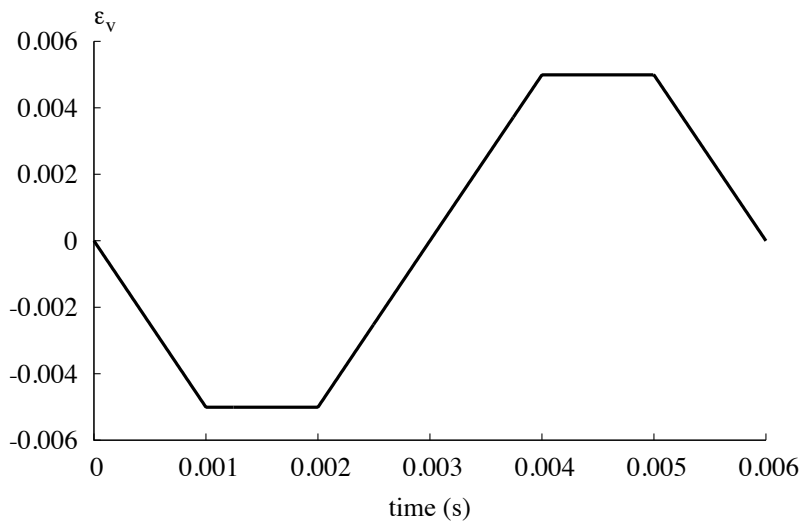

Figure 9.25. Prescribed isotropic strain path for Thermo-Kayenta.

The results, shown in Figure 9.26, show a high level of agreement between the two models, which is not surprising since both use identical Mie-Grüneisen equation of state subroutines.

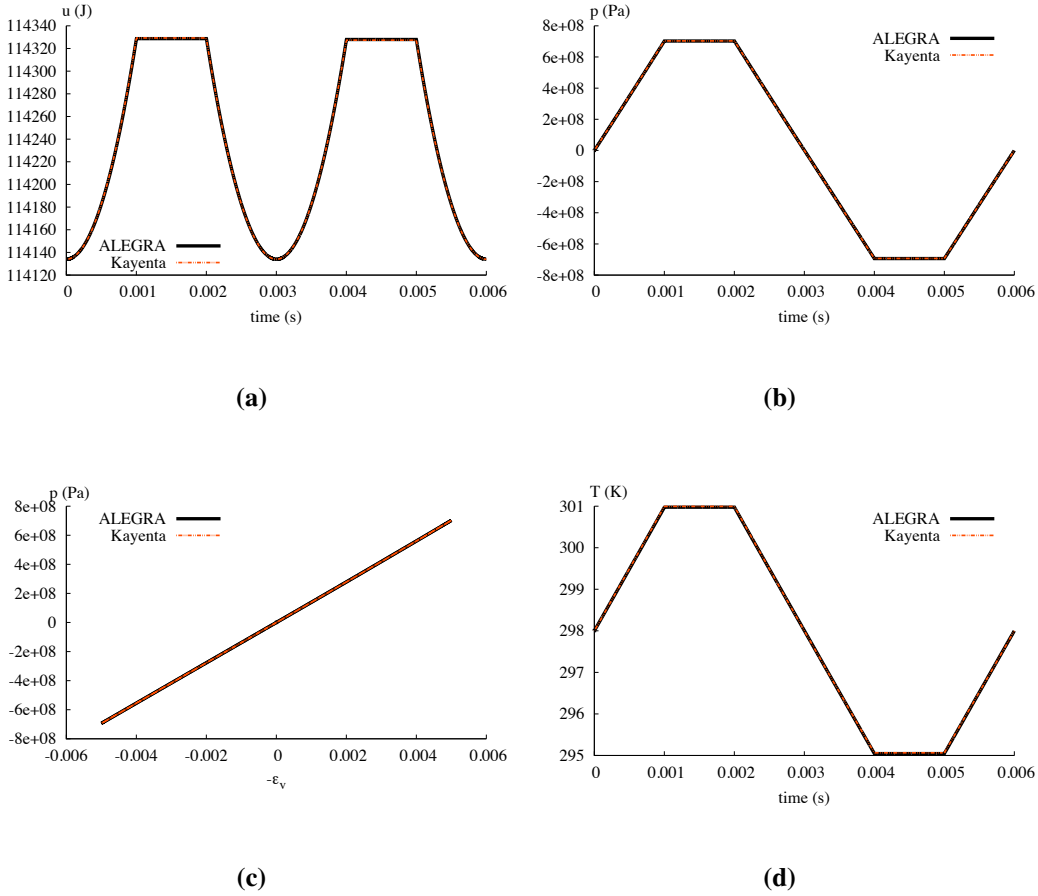

Figure 9.26. Isotropic deformation - comparison of material response. Comparison of Thermo-kayenta with ALEGRA for isotropic deformation. (a) Energy. (b) Pressure. (c) Pressure Vs. Volumetric strain. (d) Temperature.

Isochoric Deformation

In the previous comparisons, the response of the equation of state dominated the material response because of the isotropic nature of the deformation. In the following comparisons, an isochoric deformation is compared and the strength model will dominate the results. Isochoric deformation is also a good indicator if the deviatoric energy is being updated properly. The following strain path was used in each simulation:

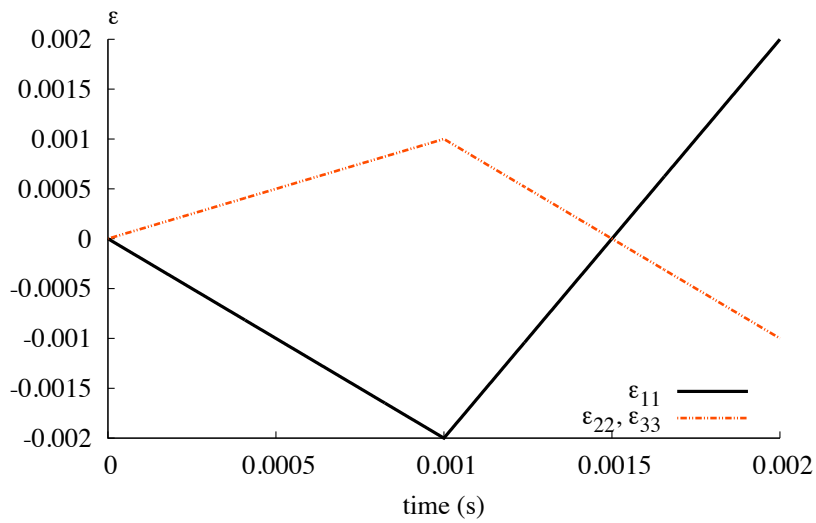

Figure 9.27. Prescribed isochoric strain path for Thermo-Kayenta.

In the following pages, the following features of Thermo-Kayenta will be compared with simulations run in ALEGRA through the same strain path. Each feature is enabled by adjusting the previously given parameters as indicated.

- Elastic response, $A = 10^{90}$ MPa
- Yield, $B = 0$ MPa, $C = 0$, $T_m = 10^{90}$ K
- Yield with thermal effects, $B = 0$ MPa, $C = 0$
- Yield with thermal and hardening effects, $C = 0$
- Yield with rate effects, $B = 0$ MPa, $T_m = 10^{90}$ K

We will begin, however, with a comparison of each of the separate features in Thermo-Kayenta.

In Fig. 9.28, hardening, thermal, and rate effects on yield in Thermo-Kayenta are compared.

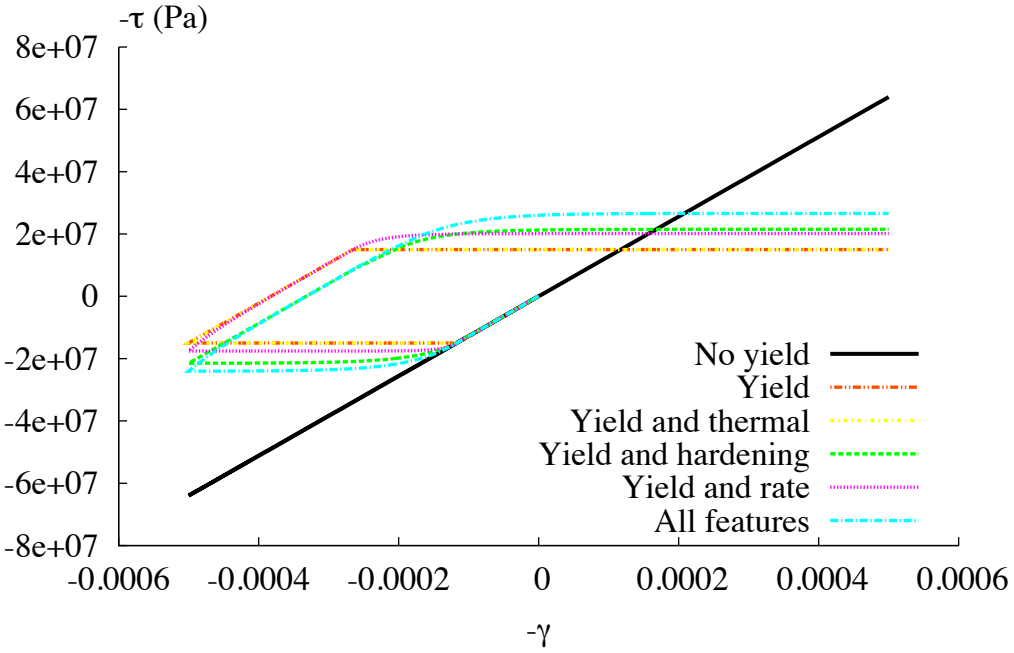

Figure 9.28. Comparison of features in Thermo-Kayenta for isochoric deformation.

The following trends are observed in Fig. 9.28:

- Because of the limited final strain, the change in temperature is negligible for this simulation, thus, the difference between yield and yield with thermal effects is also negligible.
- When hardening is enabled, the strength of the material increases with plastic strain.
- When rate dependence is enabled, the apparent strength is higher than when not enabled.

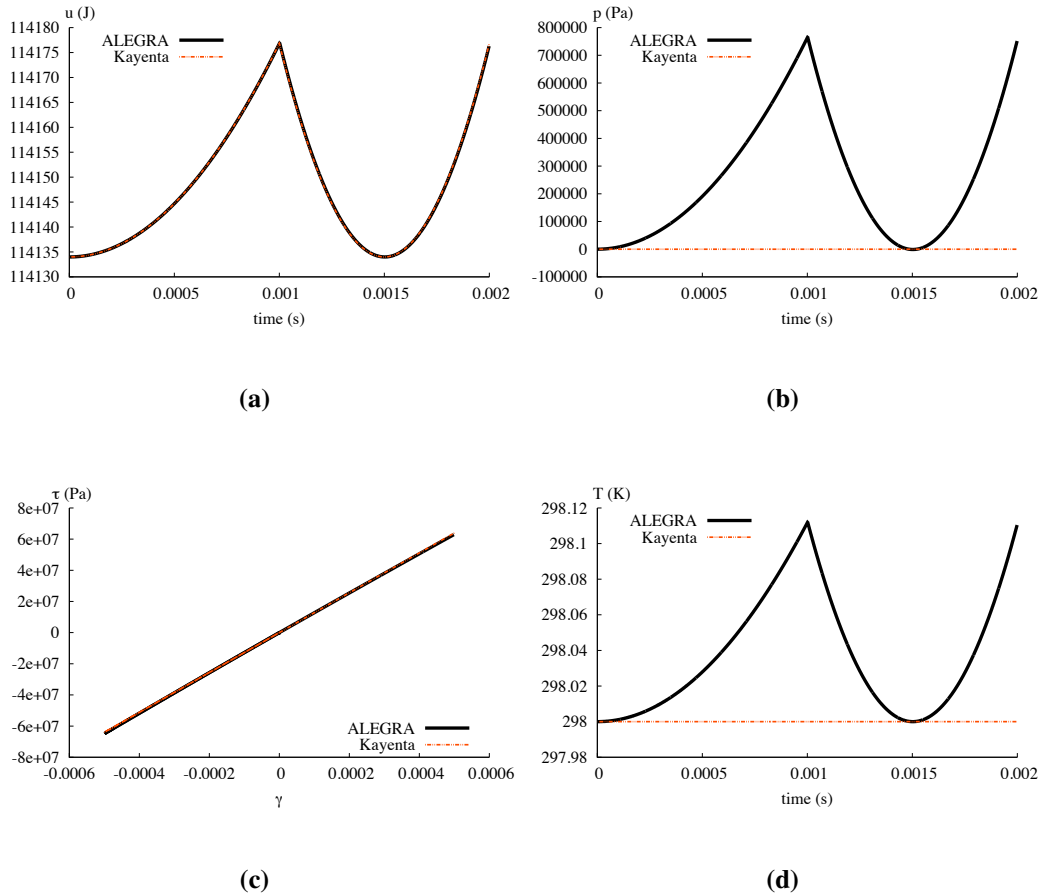

Figure 9.29. Comparison of the elastic response in Thermo-Kayenta with ALEGRA for isochoric deformation. (a) Energy. (b) Pressure. (c) Maximum Shear stress Vs Shear strain. (d) Temperature.

In these, and all of the plots of isochoric strain that follow, the non-negligible pressure in the ALEGRA simulations is due to the pressure being updated directly by the Mie-Grüneisen equation of state, where pressure is allowed to vary with energy, even in the absence of volumetric strain. In Thermo-Kayenta, the pressure is updated according to $\dot{\bar{p}} = K\varepsilon_v$, thus no pressure change is seen in the Thermo-Kayenta simulations. Similarly, in ALEGRA, the temperature is computed from the equation of state, whereas the temperature is computed from (6.22) in Thermo-Kayenta. With the exception of these two plots, all other quantities are in good agreement.

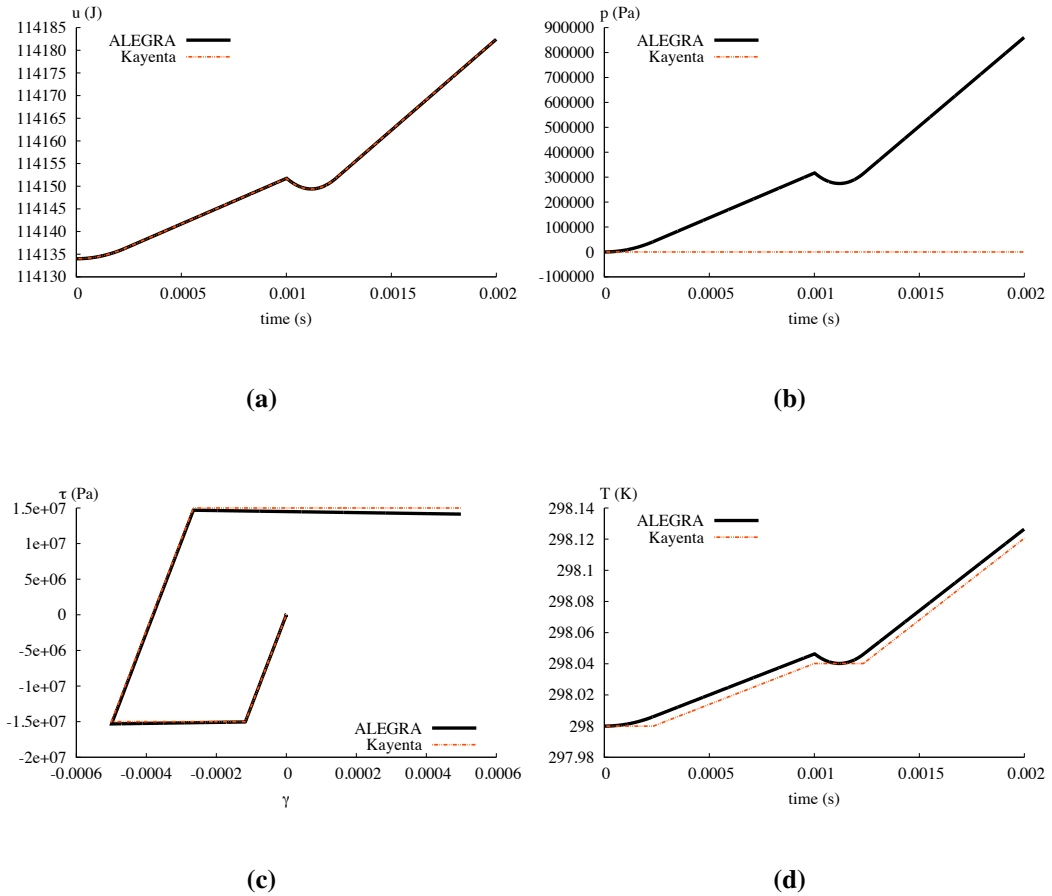

Figure 9.30. Comparison of the yield response in Thermo-Kayenta with ALEGRA for isochoric deformation. (a) Energy. (b) Pressure. (c) Maximum Shear stress Vs Shear strain. (d) Temperature.

Again, there is near perfect agreement between the two simulations, with the exception of the pressure and temperature plots, due to the reasons previously outlined. In the regions of plastic deformation, the temperatures in the two simulations increase identically, indicating that ALEGRA, like Thermo-Kayenta, converts 100% of plastic work to heat.

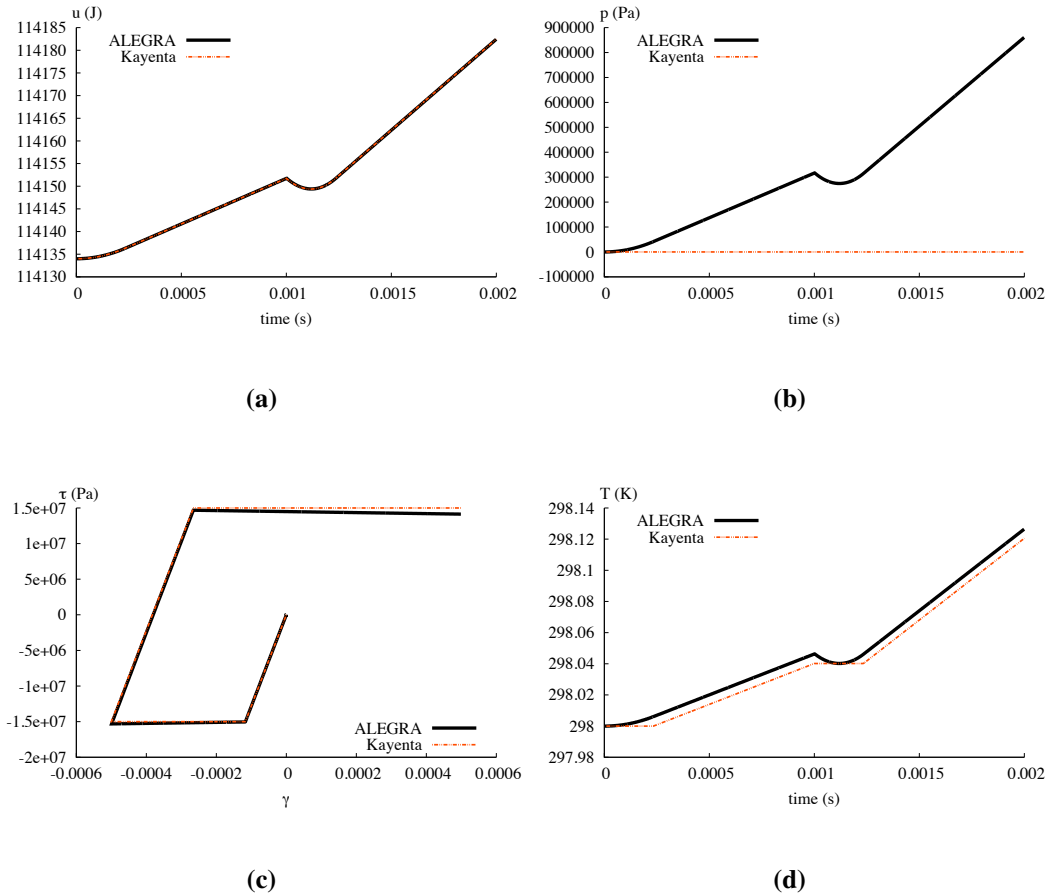

Figure 9.31. Comparison of Thermo-Kayenta with ALEGRA for isochoric deformation with yield and thermal effects enabled. (a) Energy. (b) Pressure. (c) Maximum Shear stress Vs Shear strain. (d) Temperature.

With thermal effects enabled, near perfect agreement is again obtained.

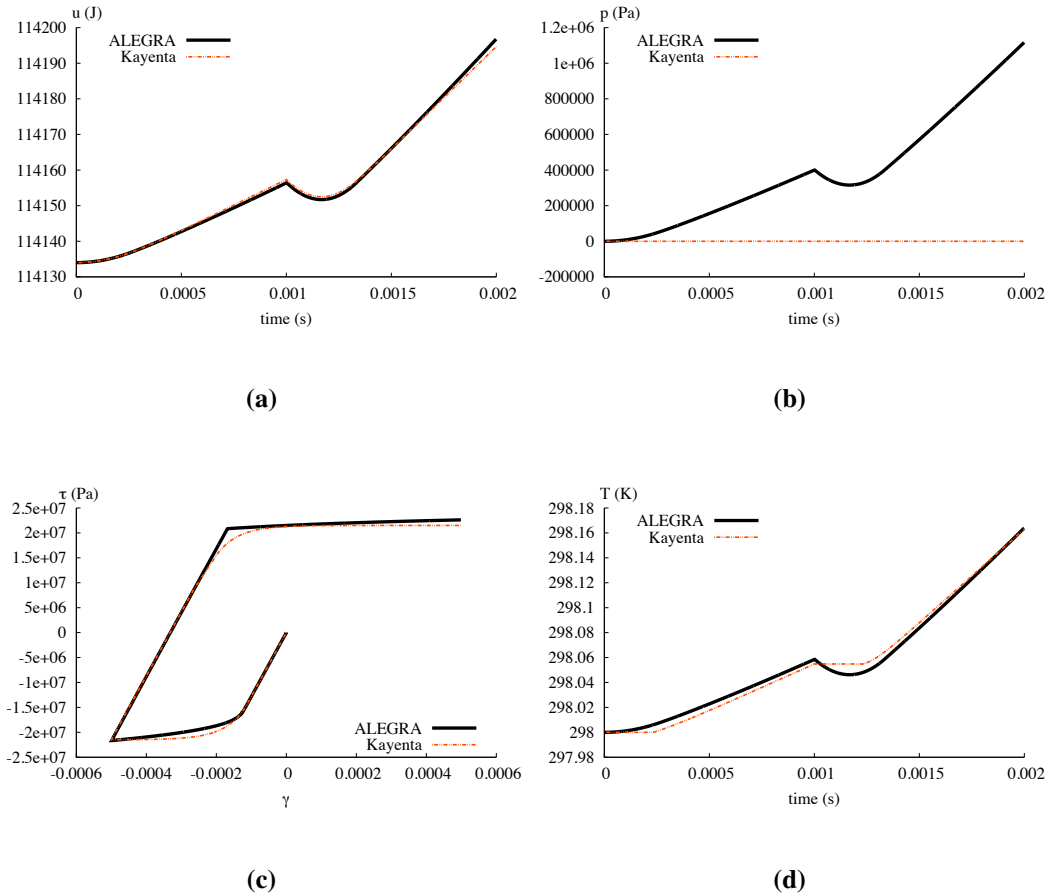

Figure 9.32. Comparison of Thermo-Kayenta with ALEGRA for isochoric deformation with yield and hardening effects enabled. (a) Energy. (b) Pressure. (c) Maximum Shear stress Vs Shear strain. (d) Temperature.

As in the previous isochoric simulations, the pressure and temperature results from ALEGRA are not agreement with those calculated from Thermo-Kayenta, due to reasons already described. In this simulation, however, there is also a discrepancy in the shear stress response. This is attributed to the difference in the implementation of material hardening in the two models. Because Thermo-Kayenta has its roots in modeling geological materials, the material is only allowed to harden to a limiting surface, at which points the hardening saturates. This behavior is responsible for the asymptoting stress response in Fig. 9.32(c). In Johnson-Cook plasticity, the material is allowed to harden with plastic strain indefinitely. Power-law hardening (cf., [14]), which would allow for the stress state to harden beyond what is currently possible in Kayenta is currently being tested in Thermo-Kayenta.

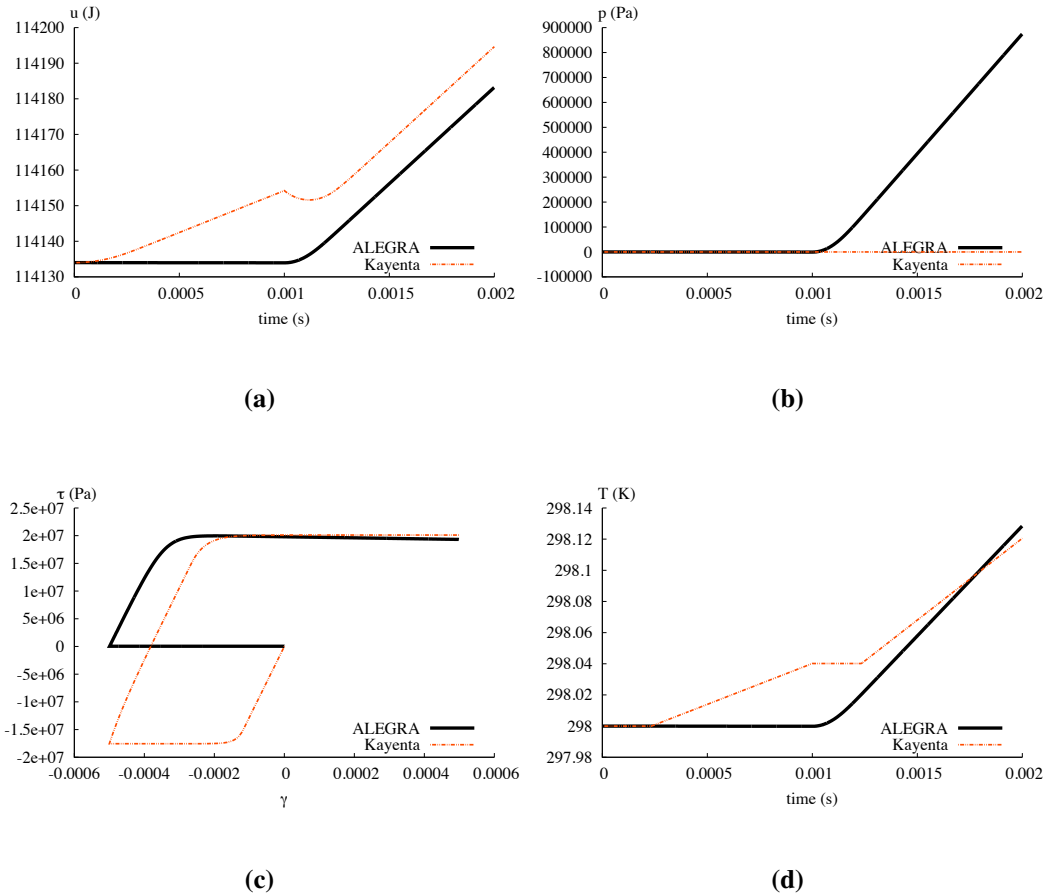

Figure 9.33. Comparison of Thermo-kayenta with ALEGRA for isochoric deformation with yield and rate effects enabled. (a) Energy. (b) Pressure. (c) Maximum Shear stress Vs Shear strain. (d) Temperature.

With rate effects enabled in ALEGRA, plastic deformation commences immediately, resulting in much smaller values for energy, temperature, and axial stress than expected. Surprisingly, after unloading, the material response seems to correct itself and return to expected values. This behavior is due, in part, to the fact that the Johnson-Cook elastic-plastic model does not have a cutoff value for the strain rate, meaning that for strain rates less than one, the rate term, $[1 + \mathscr{D}_4 \ln \varepsilon^*]$, can possibly return a negative value depending the value of $\mathscr{D}_4$. In fact, if $\mathscr{D}_4$ is large enough, the negative rate term can cause the yield stress to vanish or become negative, which is what occurred in these simulations. A cutoff value for ε^* of one will be implemented in future releases of ALEGRA to avoid this situation.

Taylor Impact

Thermo-Kayenta was installed in LS-Dyna and Taylor impact simulations were performed. The following plots compare the results from Thermo-Kayenta with LS-Dyna's built in Johnson-Cook using LS-Dyna's Mie-Grüneisen equation of state for identical simulations. The results of each are compared against experimental data measured by Wilkins and Guinan [96]. The following data were used for each simulation:

Material	Copper
Initial temperature	298 K
Initial length	23.47 mm
Initial diameter	7.62 mm
Impact velocity	210 m/s
Physical time simulated	100 μs

Table 9.6. Data used in for Taylor impact simulations performed in LS-Dyna

Results

Comparisons of the results from the end of the simulations using Thermo-Kayenta with Johnson-Cook and experimental data are shown in Figures 9.34 to 9.36. In Fig. 9.34, temperature contours for Thermo-Kayenta and a comparison of the displacement profile with experimental data are shown. In Fig. 9.35 and Fig. 9.36, displacement profiles and temperature contours from Thermo-Kayenta and Johnson-Cook are compared.

While the discrepancy in the height and width of the deformed profile is not significant between the two simulations, the discrepancy in the peak temperature ($\approx 31\%$) is. The source of the discrepancies is most likely related to the limiting value placed on the stress due to the hardening scheme in Thermo-Kayenta. Since $\dot{T} \propto \boldsymbol{\tau}\!:\!\dot{\boldsymbol{\gamma}}$, it is expected that the temperature will be lower in the Thermo-Kayenta simulations as the stress reaches this limiting value. When the hardening scheme in Kayenta is adjusted to allow for power law type hardening we expect the temperature levels to be in better agreement.

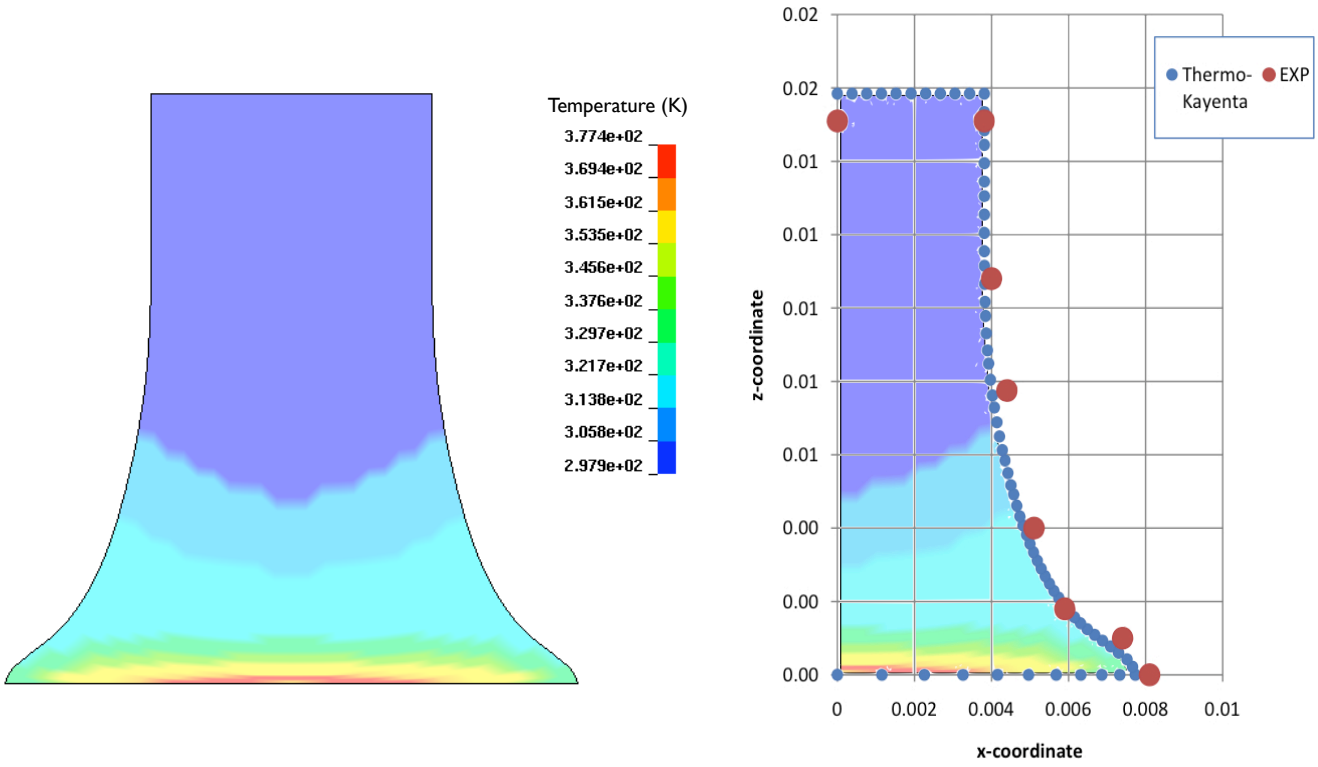

Figure 9.34. Displacement profile for Thermo-Kayenta at the end of the simulation. The red dots represent the experimental profile as given in [96].

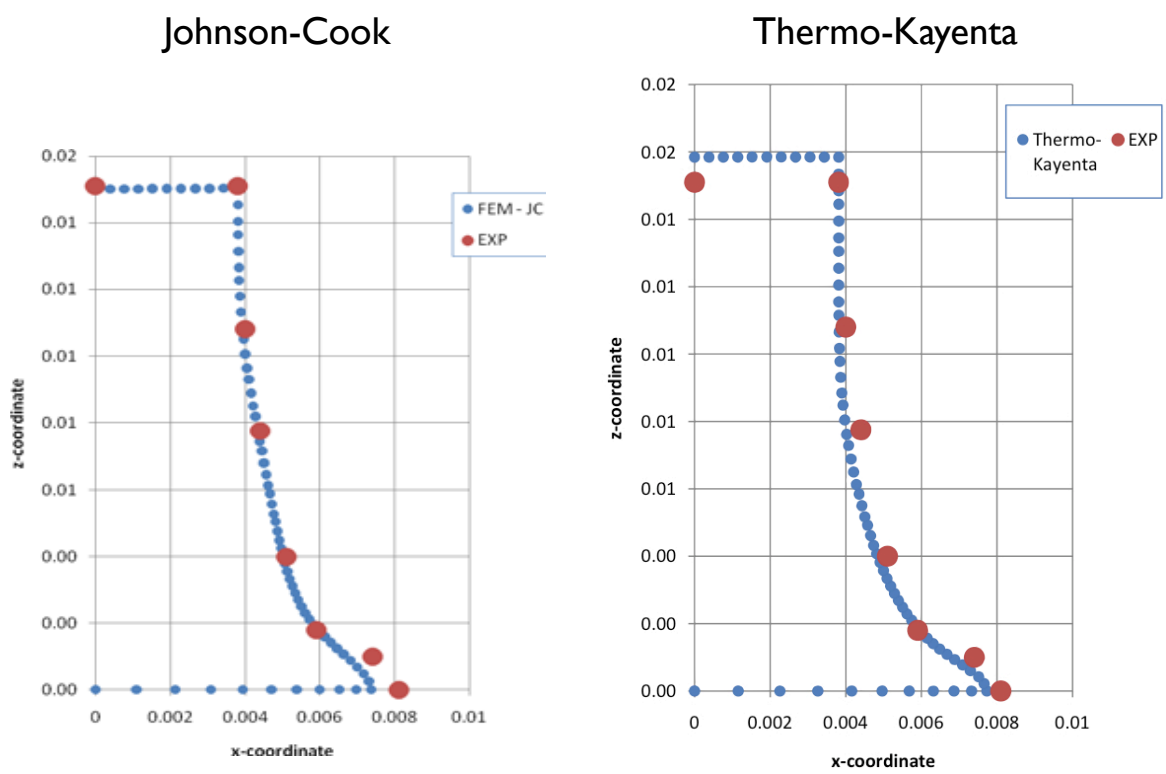

Figure 9.35. Comparison of the displacement profile for Thermo-kayenta and Johnson-Cook. The red dots in each plot represent the experimental profiles as given in [96].

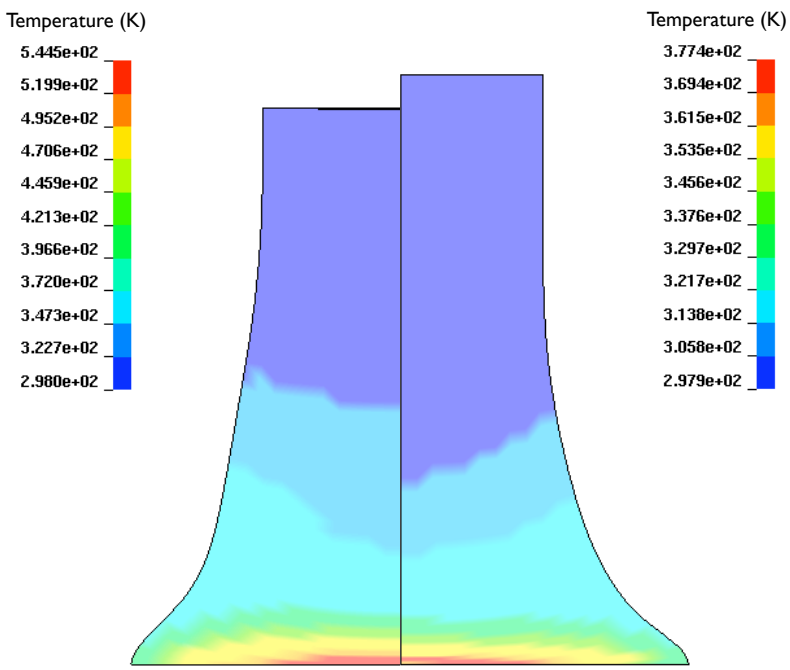

Figure 9.36. Comparison of the temperature contours for Thermo-Kayenta and Johnson-Cook.

This page intentionally left blank.

Chapter 10

Parameterization (calibration)

Appendix A provides some step-by-step guidance on experiments and analysis procedures required to characterize (calibrate) a material for Kayenta. This chapter summarizes the results of applying those procedures to find parameter sets for a variety of materials. This chapter offers laboratory evidence that has served to motivate our choices of fitting functions. If you are working with a simplistic material (or a complex material subjected to simple loading conditions), then only a small subset of Kayenta's available material parameters are needed, so it is important to realize that Kayenta's number of parameters varies with the complexity of the problem. Typical values for Kayenta's material constants are found in the material-specific datasets of Appendix B.

Nonlinear elasticity

Figures 10.2 and 10.3 demonstrate the ability of Kayenta's nonlinear elasticity fitting functions [Eq. (4.10) and Eq. (4.9)] to reproduce nonlinear elasticity data. Parameters were assigned using the least-squares model calibration tools described in Appendix A.

Elastic-plastic coupling

For some materials, elastic moduli are unaffected by inelastic deformation. However, Fig. 10.4 shows data for a material whose elastic properties are affected by inelasticity. Modeling this effect requires using the enhanced moduli fitting functions, Eq. (4.33) and Eq. (4.34), which permit the shear and bulk moduli to vary with equivalent plastic strain (determined from data by the residual strain upon unloading to a zero stress, as explained in Appendix A). For Kayenta to be considered a good fit to data, the simulated unloading curves merely need to be parallel to experimental unloading curves (not necessarily overlapping unless the data and simulation unload from the same strain).

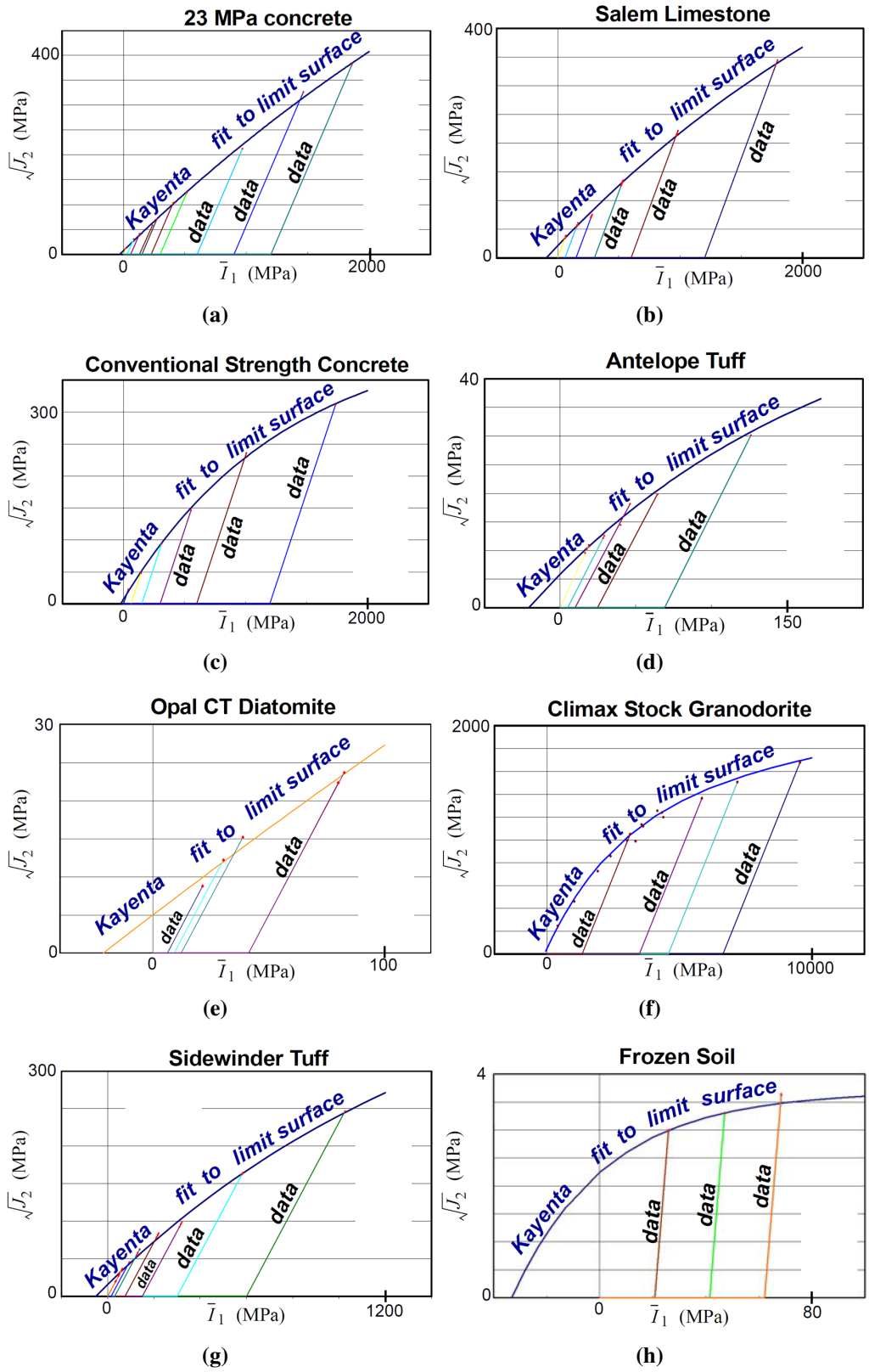

Figure 10.1. Meridional limit curves for some materials already parameterized to Kayenta

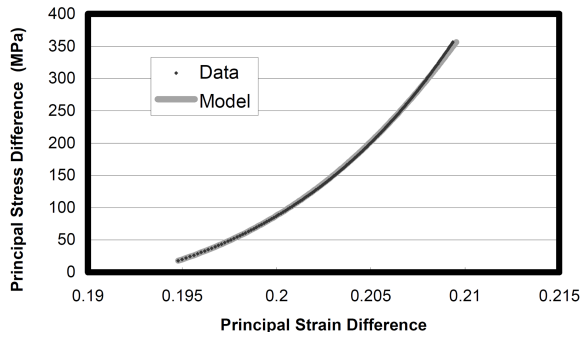

Figure 10.2. Nonlinear elasticity in shear. This figure shows Kayenta's fit to concrete data [94] from the unload portion of a triaxial compression test conducted at a confining pressure of 200 MPa. Here, the principal stress difference is plotted against the principal strain difference, thereby making the slope equal to twice the shear modulus.

Triaxial Compression

The most important set of experiments to fit a model to Kayenta is triaxial compression at a variety of confining pressures, which determines the **A** parameters for the limit surface. Results of such fitting efforts are summarized in Fig. 10.1 (compare these with Fig. 1.2 and Fig. 3.3).

Triaxial compression (TXC) and triaxial extension (TXE) testing is integral to parameterization of Kayenta. By performing a series of tests, as described in Fig. 3.3, the limit state (onset of softening) can be mapped out. For example, Fig. A.6 (pg. 222) shows raw data from a a suite of TXC tests, indicating how the peak values in each test provide one data point on Kayenta's limit surface Fig. A.6. Data from a similar set of experiments for concrete, along with Kayenta's least-squares fit of Eq. (4.8) are shown in Fig. 10.5. Fig. 10.1 shows similar plots for other materials. Appendix A describes the least-squares fitting procedures in more detail.

Recall that triaxial testing normally begins with a hydrostatic "load-up" phase, indicated by the horizontal red arrow Fig. 10.6 (where $\sqrt{J_2} = 0$). During the hydrostatic leg, deformation is initially nonlinearly elastic until the virgin yield surface is reached, at which time microscale stress concentrations caused by the presence of pores become too large to resist elastically. Continuing to push the hydrostatic stress to higher levels results in inelastic pore collapse with associated hardening (expansion) of the yield surface. In Fig. 10.6, the target hydrostatic stress state for a given experiment (which marks the transition from the hydrostatic leg to the triaxial leg) was $P = 400$MPa, giving an I_1 value of -1200MPa. Pressure-volume data taken during the hydrostatic leg may be used to determine Kayenta parameters $\{p_0,\ p_1,\ p_2,\ p_3\ \}$ by following instructions in Appendix A. Because multiple triaxial experiments must be performed to fully characterize a geological material, variations observed during hydrostatic loading from different tests can be used to quantify the material property variability.

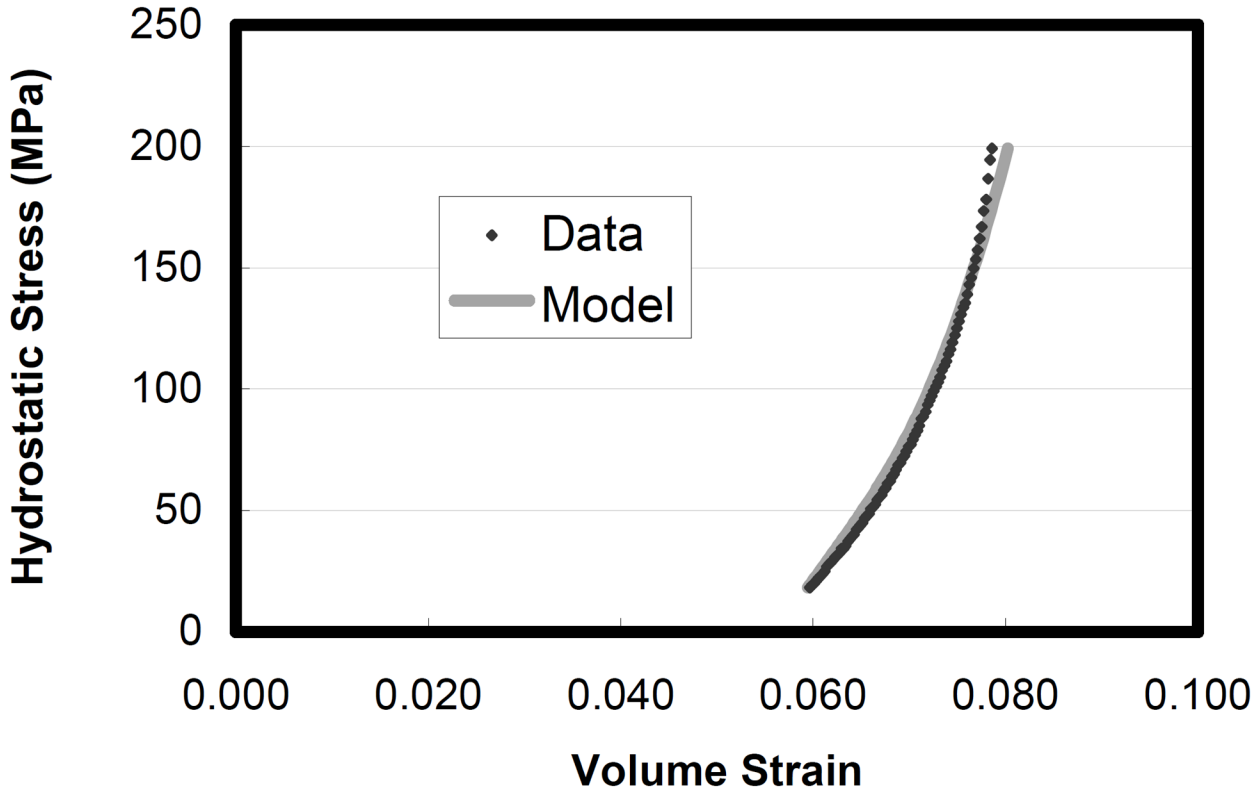

Figure 10.3. Nonlinear elasticity in hydrostatic loading. This figure shows Kayenta's fit to concrete data [94] from the unload portion of a hydrostatic compression test from 200 MPa. Here, the slope equals the bulk modulus.

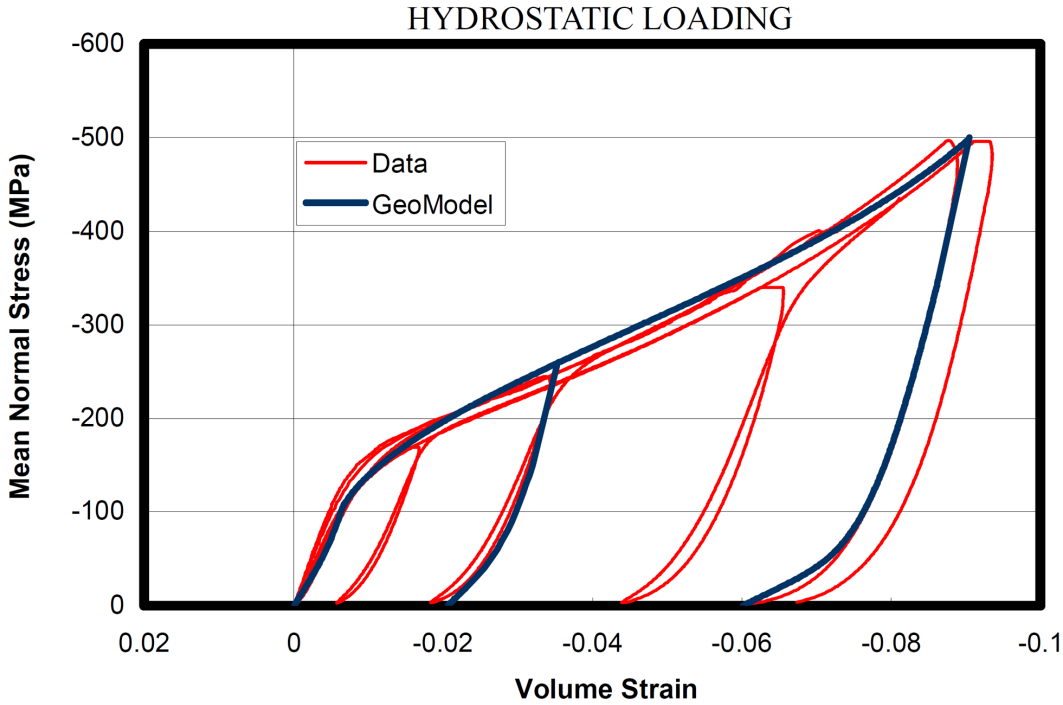

(a)

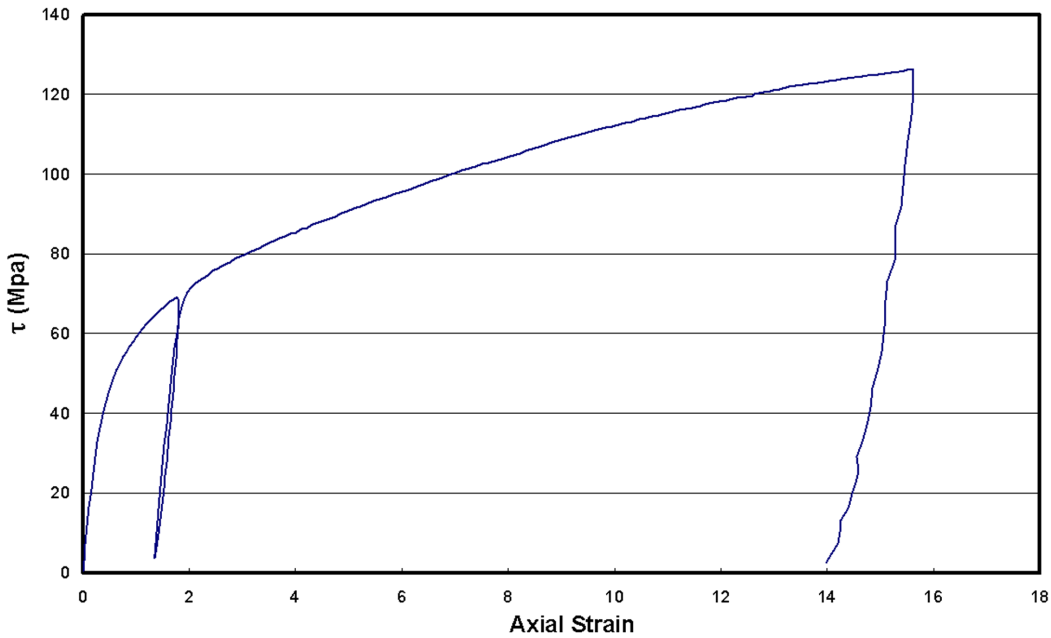

(b)

Figure 10.4. Elastic-plastic coupling: deformation-induced changes in elastic moduli (Salem Limestone). (a) the tangent bulk modulus can change in response to changes in porosity (i.e., volumetric plastic strain). (b) Likewise, the tangent shear modulus, especially at low shear stresses, can change in response to plastic deformation.

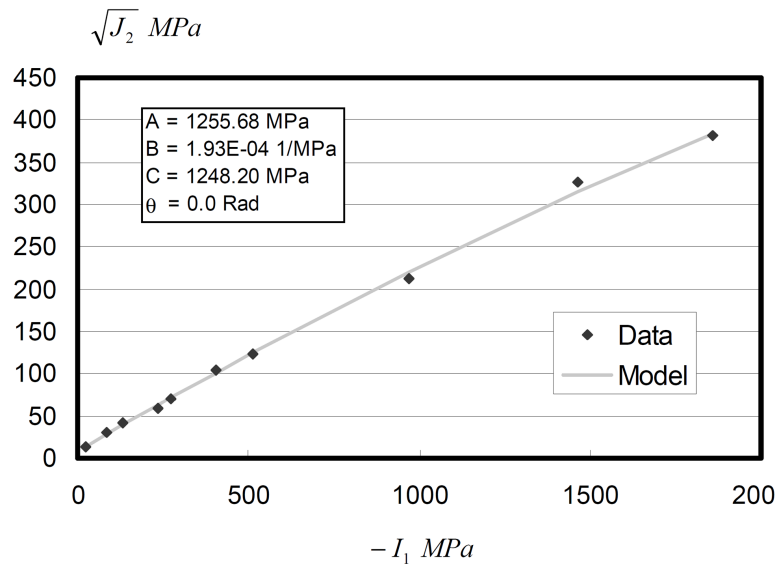

Figure 10.5. Shear failure limit curve compared with concrete data. Ref. [94].

After the hydrostatic leg, the triaxial leg (angled red arrow in Fig. 10.6) commences by increasing the axial load on the specimen while holding the lateral stress constant. As explained on page 39, the stress path follows a straight trajectory in the meridional plane with a slope given by

$$\frac{\mathrm{d}\sqrt{J_2}}{\mathrm{d}\overline{I_1}} = \frac{1}{\sqrt{3}} \tag{10.1}$$

The transition from hydrostatic to triaxial loading is reflected by a pronounced change in slope in the stress-strain plot of Fig. 10.6. As the axial stress is increased during the triaxial leg, the yield surfaces continues to harden outward even more, now further assisted by the presence of a nonzero stress deviator. In Fig. 10.6 the slope of the yield surface is initially negative at the stress state (i.e., where the straight red load path and curved blue yield surface lines intersect). Consequently, the outward *normal* to the yield surface during this early part of the triaxial phase has both a deviatoric component *and a* ***compressive*** *isotropic component*. When the normal to the yield surface is compressive, the inelastic volumetric strain will be compressive as well. However, the isotropic component of the yield surface normal *changes direction* towards the end of the triaxial leg (i.e., the local slope of the yield surface changes sign), which means that the inelastic volumetric strain is *dilatational* (expanding) even though all stress components are compressive. The "critical state" at which the yield surface has a zero local slope on the load path marks the onset of shear-enhanced dilatation. Thus, as illustrated qualitatively in Fig. 10.7 and explained in detail in Appendix A, triaxial loading is used to determine parameters in Kayenta that govern yield surface evolution and cap curvature.

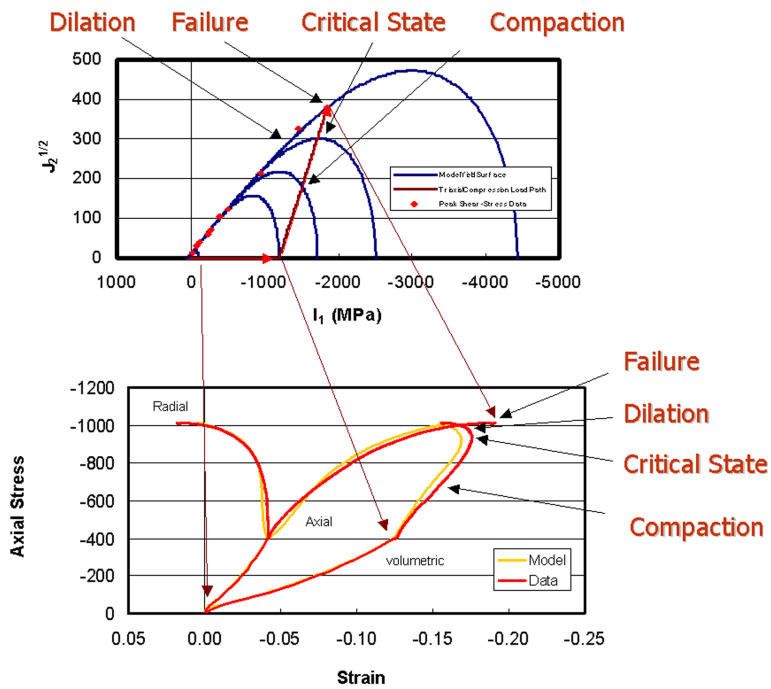

Figure 10.6. Progression of the hardening yield surface (family of blue lines) under a triaxial compression test (red path), illustrated with correspondence of the meridional plane to the stress-strain diagram. The straight red line segments shown show this two-stage stress trajectory (hydrostatic loading followed by triaxial loading) in the meridional plot of $\sqrt{J_2}$ (which is proportional to the effective shear) versus $\overline{I_1}$. Shear-enhanced dilatation corresponds to reaching a zero local yield slope.

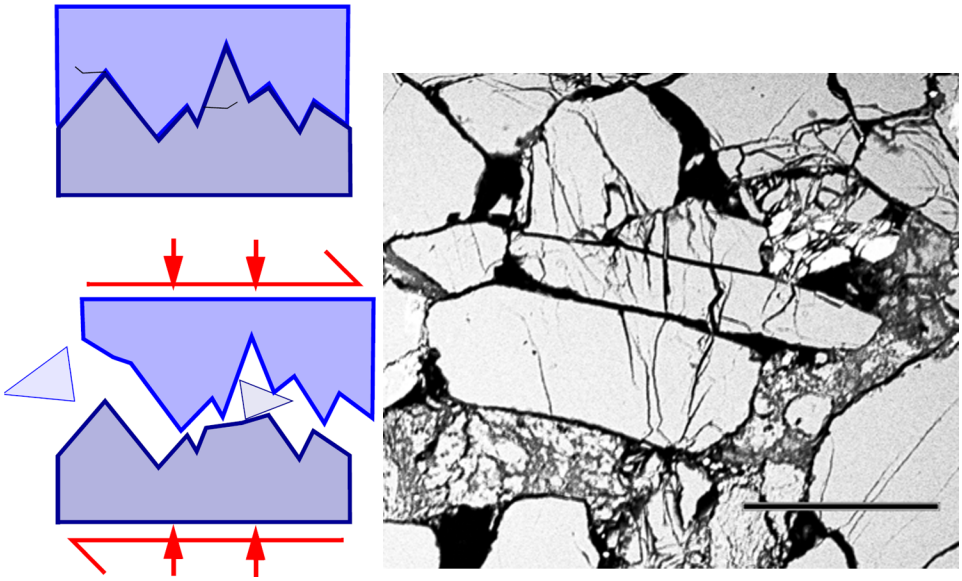

(a) **(b)** DiGiovanni & Fredrich [29]

Figure 10.7. Shear-enhanced dilatation under compression. The exaggerated schematic shows that crack faces must overcome surface incompatibilities — they cannot slip over each other without opening even if they are in compression. Moreover, fragments of broken material can become lodged in the crack face and cause crack opening by their rotation. Crack kinking (in the direction of Mode I loading) further contributes to the dilatation associated with crack opening. The dark regions in the micrograph [29] are pores (which collapse under sufficient pressure). The cracks in inclusions produce "micro-rubble" that ultimately generates, through rotation, inelastic volume increase under shear loading even if all principal stresses are compressive.

Physically, an increase in inelastic volume during compression (which is quite commonly observed for brittle materials) is typically attributed to the growth of microcracks under shear. As the surfaces of these cracks move relative to one another, the crack must open up (dilatate) both to overcome geometric incompatibilities in their surface roughness and to permit crack kinking. This interpretation of shear-enhanced dilatation is illustrated schematically and through SEM imaging in Fig. 10.7.

Parameterization: Rate dependence

Kayenta's relaxation parameters $\{T_1, \ldots, T_7\}$ may be determined through a series of lab-scale laterally-confined Kolsky bar tests (Fig. 10.8) in which a sample is subjected to uniaxial compression at various strain rates.

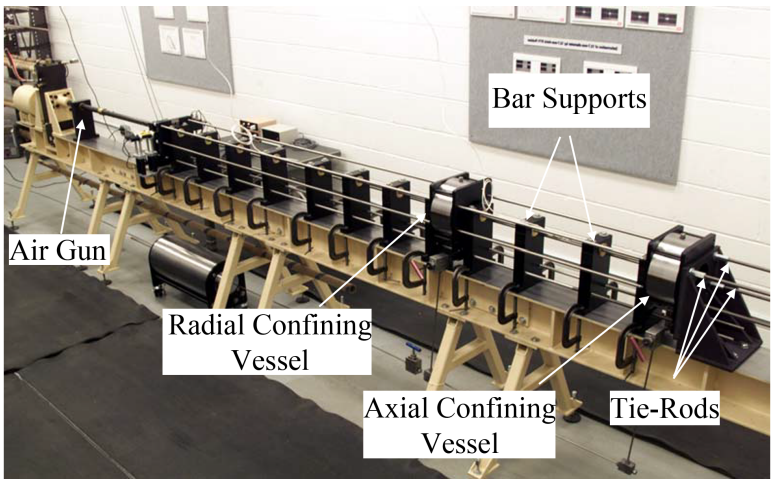

Figure 10.8. Kolsky (split Hopkinson) bar apparatus used to obtain data in Fig. 10.9

Fig. 10.9 shows results for a series of Kolsky (split Hopkinson) bar strain-rate tests conducted on unconfined compression specimens of Salem Limestone [37]. The peak stress in each experiment is used to assign values of Kayenta relaxation parameters to properly correlate apparent strength with strain rate. As seen, the unconfined compressive strength increases with strain rate and is well accommodated by Kayenta theory.

For a discussion of how the data in Fig. 10.9 are used to assign values to $\{T_1, \ldots, T_7\}$, see Appendix A.

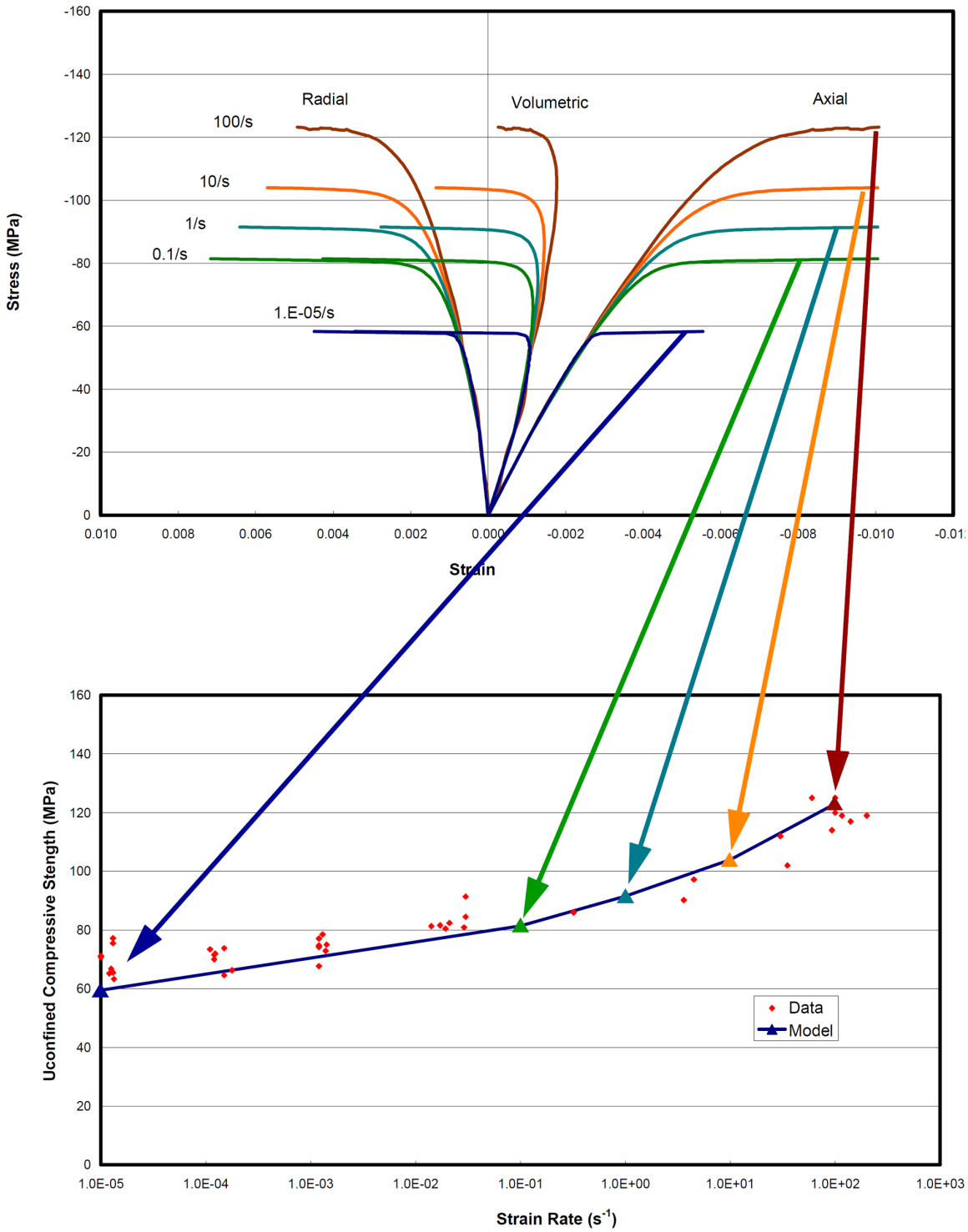

Figure 10.9. Suitability of Kayenta's overstress rate-dependence model to match observed data. The top plot shows model predictions of stress-strain behavior at various strain rates. The bottom plot shows corresponding Kolsky (Hopkinson) bar unconfined compressive strength as a function of strain rate

Chapter 11

Building confidence in the physical theory

In a weak sense, demonstrating (as we did in the previous chapter) that Kayenta is capable of being parameterized from controlled laboratory data lends some credibility to the physical foundations of the model. However, truly *validating* a model after its parameters have been determined from standard laboratory data requires showing that the model can, *without any change in pre-calibrated parameters*, predict material response under different (non-calibration) loading scenarios. Ideally, to validate *a constitutive model* (not its implementation into a host finite-element code), one would prefer to compare the model predictions against test data from homogeneous loading experiments that were different from the homogeneous loading tests conducted for calibration.

Thorough testing of any material constitutive model *along with its implementation in a host code* must, of course, include simulation of applications for which model predictions can be compared with structural response measurements. The goal is to assess the degree to which the integrated model (i.e., its installation into a host code) is capable of predicting material system response to non-trivial loading scenarios.

Parameterization entails fitting to a subset of discrete points in parameterization data tables (e.g., as described on page 197, the limit function is parameterized by using only the *peak* stress values, not all values measured in the test). Model validation therefore includes assessing the fitted model's ability to interpolate well between *other* points in these stress-strain response curves (i.e., points that were *not* used in calibration). Similarly, Kayenta's rate dependence parameters are determined by using only the *peak* stress values in Kolsky bar experiments. Therefore, the model's ability to match the *other* data points in those experiments is a validation test.

In addition to merely ensuring that all data in parameterization tests are well modeled, a better validation test should exercise the model in application domains in which multiple physical mechanisms are acting simultaneously. The goal is to assess whether or not Kayenta parameterization instructions in Appendix A can lead to a high-quality set of material model properties that are *predictive* in general loading scenarios. This chapter describes some validation problems that have been studied to date. In all cases, these problems were run *using only the single Kayenta parameter set obtained from calibrating to* ***other*** *data for the material — no parameter adjustments were made to improve model agreement for these tests*.

Post-calibration Triaxial loading

The nonlinear elasticity Eq. (4.9) and Eq. (4.10) are parameterized from shear and hydrostatic unloading data. The shear limit function Eq. (4.39) parameterized through *peak states* in triaxial testing. The crush curve Eq. (4.69) parameterized through purely hydrostatic testing. Once parameterized in this way, Kayenta may be applied to predict the irreversible plastically-hardening stress-strain response at a *variety* of other stress paths. For example, Fig. 11.1 compares Kayenta predictions with simple triaxial data at various confining pressures (these simulations all use *a single set* of Kayenta parameter values).

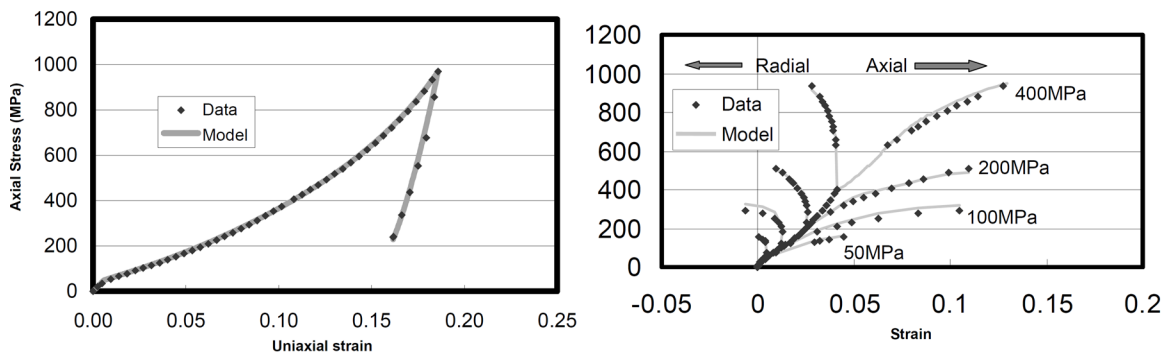

(a) **(b)**

Figure 11.1. Post-calibration Triaxial loading (a) *Kayenta prediction of uniaxial strain loading.* (b) *Kayenta predictions of triaxial stress-strain response at various confining pressures.* From Ref. [94]. The ability of a single parameter set to agree so remarkably well with this suite of data is a validation.

Field-scale penetration

Fig. 11.2 shows results from a *pre-test* prediction of depth of penetration and displacement histories. In tests like these, material constitutive models are often considered "above average" if they are predictive within 20%. As seen, Kayenta performed exceptionally well by this metric. However, attaining even marginally good agreement with laboratory data for dynamic fracture and fragmentation historically has required setting material properties to values appropriate to the scale (i.e., physical size) of the problem and the size of finite elements used in the simulation, which precludes any ability to assert convergence of such simulations with mesh refinement. This problem was addressed by Strack, Leavy, and Brannon [85] by including *automated* statistical variation in Kayenta's strength properties, with concomitant scale effects so that (as observed in laboratory experiments for virtually any brittle or quasi-brittle material; cf. [6]). As seen in Fig.

11, statisical perturbation and scale effects permit Kayenta to predict realistic symmetry-breaking radial fracture patterns.

Free field wave form for spherical shock loading

Fig. 11.6 shows displacement and velocity histories for an underground test in which a wave propagates from an explosive point source. A measured velocity history at a point 204 meters from the source was used as the velocity boundary condition of the simulation. The goal was to predict a second measured velocity history at a point 470 meters from the source (see Fig. 11.5). Unlike the similar elasticity verification test described on page 207, this validation test used elastic-*plastic* field-scale parameters that were determined by applying Kayenta's calibration procedures described in Appendix A (*back-fitting alteration of these independently determined calibration parameters was disallowed, as should be the case for any validation test*).

Kayenta (along with its implementation within the host finite-element code, JAS3D) comes far closer to matching data than simpler models such as non-hardening von Mises plasticity, indicating that Kayenta's advanced physical features (especially pressure sensitivity) are important. Because Kayenta falls short of a *compelling* agreement with data, further study is warranted. Unlike the verification study presented on page 207, this validation simulation is over-predicting peak velocity. As was the case in the verification study, code predictions were strongly affected by artificial viscosity, suggesting that disagreement with data *might* be rooted in host code problems as much as shortcomings of Kayenta. Of course, natural spatial variability of in-situ rock (which is neglected in the simulation) may play a role, as might the response time of gauges used to acquire the data, or myriad other possible error sources.

This concludes our overview of preliminary validation testing. More extensive model validation activities have been ongoing, results of which are available in the open literature.

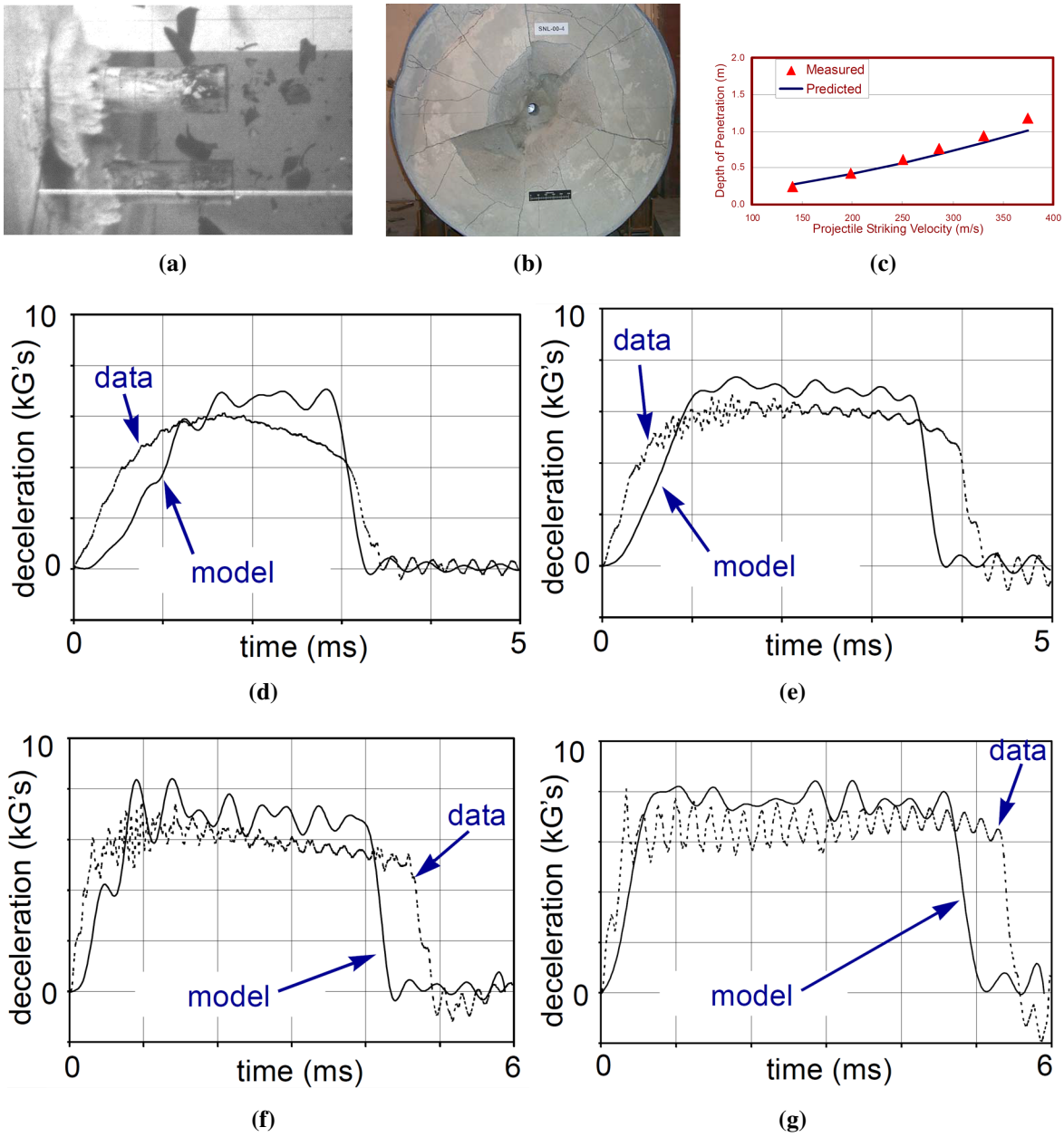

Figure 11.2. After Kayenta was fitted to laboratory-scale material property tests, it was used to predict projectile penetration depth using spherical cavity expansion analysis.

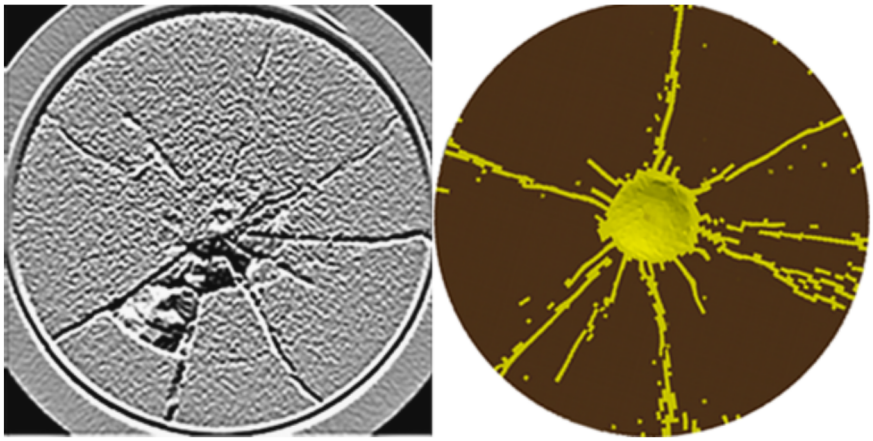

Figure 11.3. Radial cracking in dynamic indentation. X-ray computed tomography image of top surface cracking and corresponding simulation (right) from a 385 m/s impact of a WC sphere on a SiC-N cylinder. Of paramount imporantance is the demonstration that the general character of these predictions (i.e., the number and spacing of radial cracks) is much less sensitive to mesh size and mesh texture than deterministic simulations using the same model [61, 85].

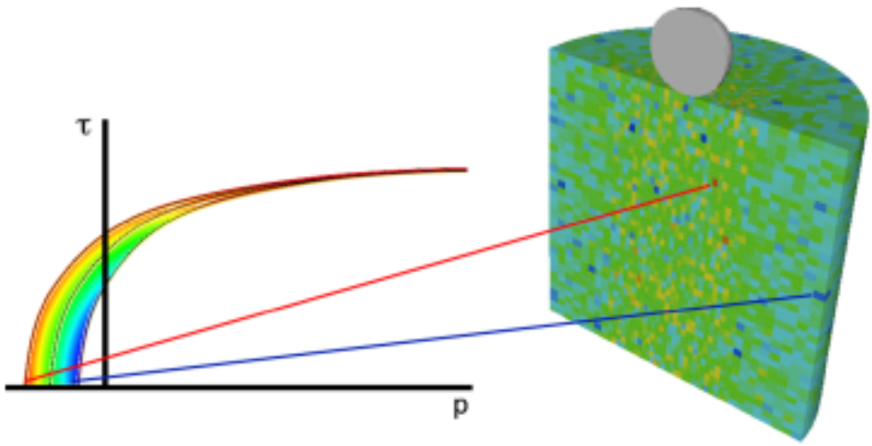

Figure 11.4. A notional depiction of statistical variability in strength used in Fig. 11 and similar simulations. Instead of a single set of strength parameters, corresponding to a single deterministic limit surface, a damage-capable installation of Kayenta is required to use statistically variable strength such that small elements are stronger, on average, than large elements. As seen in this sketch, the imposed variability decreases with increasing confining pressure. Details of this advanced use of the Kayenta model are provided in [85].

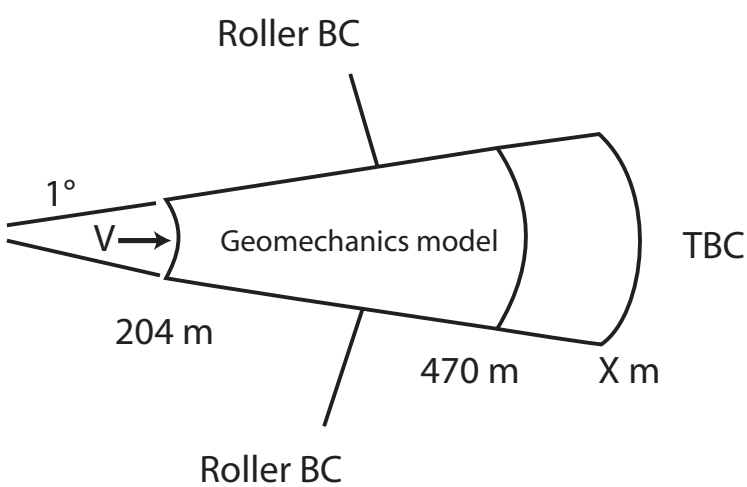

Figure 11.5. Spherical cavity geometry.

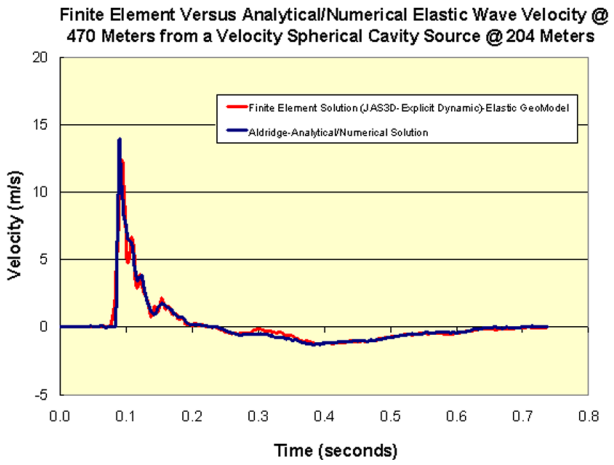

Figure 11.6. Kayenta + JAS3D finite-element prediction (blue) vs. measured (red) velocity and displacement at 470 meters from a spherical cavity velocity source at 204 meters.

This page intentionally left blank.

Chapter 12

Closing Remarks

This user's guide has elucidated the physical foundations, domain of applicability, numerical methods, and user inputs for Sandia's general-purpose Kayenta plasticity and damage model. This model was developed in response to the need for a predictive model that could be used for a wide range of applications while maintaining numerical tractability in the context of Sandia's solid mechanics finite-element software. A significant advantage (and simultaneously drawback) of Kayenta is that it includes a large selection of model features (hardening, damage, first and third invariant dependence, etc.) that are commonly found in other models; having these all available in a single model permits users to explore importance of various potentential constitutive behaviors to various applications of interest.

Three key applications for this work are in projectile penetration research, analysis of hard and deeply buried targets, and reservoir-scale modeling of formation compaction caused by pore pressure drawdown during oil or gas production. With the emergence of the capability to simulate the large-scale mechanical behavior of complex geosystems by virtue of recent advances in software and hardware, Sandia recognized the need to enhance the material modeling capabilities for geomaterials. A large-scale, long-term effort was begun that brings together activities in laboratory testing, basic research, software development, verification, validation, documentation, and quality assurance. The goal is to provide a rock mechanics predictive capability that fully accounts for the complex nature of in situ rock masses. The Kayenta model additionally includes constitutive features common to (and increasingly common to) plastic flow and fracture of metals.

Kayenta is a genuine unification and generalization of simpler models. As such it is capable of meeting the needs of almost any structural application involving geomaterials. So-called "first-principles" microscale theories have influenced the general model framework, but it is recognized that such formulations themselves include unrealistic assumptions (such as linear matrix materials, non-interactions, non-phase transformations, etc.). Accordingly, physically motivated phenomenological judgements about relations between stress and strain have been given ultimate priority to more accurately match observed laboratory behavior.

In the laboratory, most rocks exhibit nonlinear elastic deformation upon unloading and reloading, hysteresis loops, different behavior in extension than in compression, strain-rate sensitivity, pressure dependence, and post-peak softening. Moreover, high porosity rocks under compressive mean stresses and non-zero deviatoric stresses, involve a complex interplay of deformations from competing mechanisms including pore collapse and microcrack-microvoid development, which occur simultaneously allowing macroscopic pre-failure dilatation to occur even as

pores continue to collapse. In addition, the strain-rate sensitivity of some porous rocks depends on the predominant deformation mechanism, e.g., the strain-rate sensitivity of shear and extensional failure is different from that of pore collapse, and the strain-rate sensitivity itself may be pressure dependent. This report summarizes the progress toward achieving a realistic rock constitutive theory that can be calibrated via standard laboratory experiments and is numerically tractable for massively parallel calculations using tens of millions of three-dimensional finite elements and loading conditions that involve ground shock and other non-quiescent processes. Some recent model enhancements (not documented in previous Kayenta documentation) include: pressure dependence of the extension/compression strength ratio, softening and failure (fracture), anisotropic jointed rock behavior (as observed in situ), and natural spatial variability resulting observed scale sensitivity of strength, localization of failure (such as radial cracks in an an otherwise axisymmetric indentation), and accommodation of any user-specified nonlinear thermal equation of state for high-pressure applications. While Kayenta has achieved many stated objectives to date, there is still much to be accomplished. Current model-enhancement activities (to be documented in future reports) include: effective stress theory to accommodate fluid in pore space, induced elastic and inelastic anisotropy (which supplements the existing Kayenta formulations for intrinsic rock-joint anisotropy and kinematic hardening (backstress).

Appendix A

Parameterizing Kayenta

The following steps describe how to determine values for parameters used in Kayenta. Previously available parameterization software (e.g., **HYDROFIT**, **SHEARFIT**, etc.) is no longer maintained; any modern spreadsheet application can perform the same tasks of nonlinear constrained least-squares fitting. In MS Excel, the relevant plug-in function is called "SOLVER". Freely available optimization software, such as DAKOTA [1] at http://dakota.sandia.gov/documentation.html, might also be convenient.

STEP 1 **Use hydrostatic pressure vs. total volumetric strain data to obtain the nonlinear elastic bulk modulus parameters (b_0, b_1, and b_2) as well as the crush curve parameters p_0, p_1, p_2, p_3.**

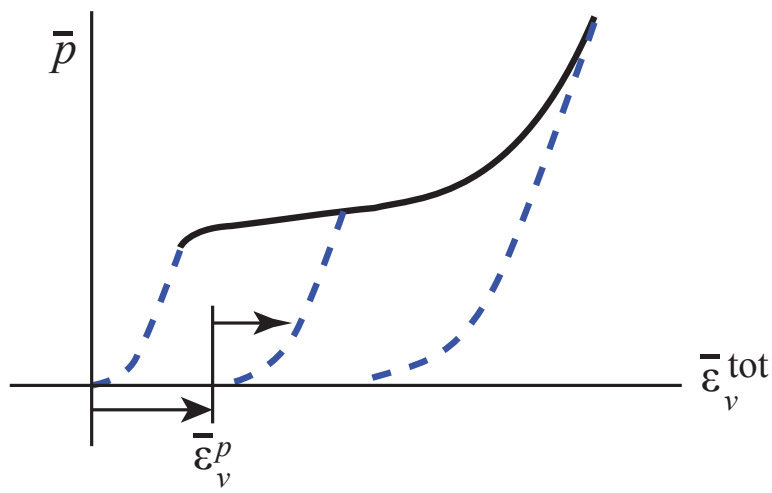

Figure A.1. Elastic legs (dashed) and plastic legs (solid) in hydrostatic loading.

It is assumed that tabular data from hydrostatic loading are available such that one column is total volumetric strain ε_v^{tot} and another column is pressure $\overline{p}$. It is also assumed that the experiment includes elastic unloading curve(s), which are the dashed lines in the sketch of

Fig. A.2. Referring to Fig. A.2, the first step is to separate the data for elastic legs (dashed) and plastic (solid) legs.

The elastic data must be fitted to the bulk modulus parameters in Eq. (4.9),

$$K = b_0 + b_1 \exp\left(-\frac{b_2}{3\overline{p}}\right), \text{ where } 3\overline{p} = \overline{I_1} \tag{A.1}$$

For each elastic leg (dashed lines in Fig. A.2), subtract the plastic strain for that leg (i.e., the strain at zero pressure) to create an elastic strain column ε_v^e. Using only the data from elastic legs, generate a new column containing the local slope $K = \Delta\overline{p}/(\Delta\varepsilon_v^e)$. The slopes at successive points should be averaged to retain data alignment, so that the two data columns K and $\overline{p}$ can be fitted to Eq. (A.1) via nonlinear least squares fitting of the parameters b_0, b_1, and b_2. Each elastic leg should be separately fitted in this way. If it is found that the values for b_0, b_1, and b_2 are significantly different for different elastic legs, then additional fitting parameters, b_3 and b_4, in Eq. (4.33) of the main text are available to improve the fits.

The inelastic legs (solid line in Fig. A.1) are used to determine the parameters in the crush curve, Eq. (4.70) of the main text:

$$p_3 - \varepsilon_v^p = p_3 \mathrm{e}^{-(p_1 + p_2\overline{\xi})\overline{\xi}}, \text{ where } \overline{\xi} = \overline{X} - \overline{p_0} = 3(\overline{p} - \overline{P}_E) \tag{A.2}$$

Using the data from inelastic legs, create a data column $\overline{X} = 3\overline{p}$. To fit to the above function, a new data column must be generated for the plastic volume. To do so, interpolate data on the nearest elastic leg to find the elastic strain ε_v^e associated with the pressure. Subtract the elastic strain, ε_v^e, from total strain, ε_v^{tot}, to obtain the plastic strain ε_v^p. Now that you have data columns for ε_v^p and $\overline{X}$, apply nonlinear least squares fitting of Eq. (A.2) to obtain p_0, p_1, p_2, p_3. To assist with initial guesses for the fitting, note that the peak inelastic volume strain, p_3, roughly equals the initial porosity. Refer to Fig. 4.14 for guidance on how to set initial guesses for the other crush parameters.

STEP 2 **Use triaxial compression data to obtain the shear modulus parameters g_0, g_1, and g_2.** This step determines the parameters in Eq. (4.10),

$$G = g_0 \left[\frac{1 - g_1 \exp(-g_2\sqrt{J_2})}{1 - g_1}\right] \tag{A.3}$$

Arrange the triaxial data as a two-column table, the first column being the axial strain ε_A and the second column being the stress difference $(\sigma_A - \sigma_L)$. Then use nonlinear least squares regression analysis to obtain the shear modulus parameters g_0, g_1, and g_2.

As illustrated in Fig. 3.3 in the main text, triaxial testing is typically performed as a two-stage process in which the material is first compressed hydrostatically to a given pressure. Then, during the second (triaxial) leg, the lateral stress is held fixed while the axial stress is varied. Only the elastic *unloading* data in triaxial legs should be used for determining the nonlinear elastic shear modulus parameters. As explained on page 54, the plot of stress difference $(\sigma_A - \sigma_L)$ vs. axial strain ε_A will have a slope equal to Young's modulus E. Rather than

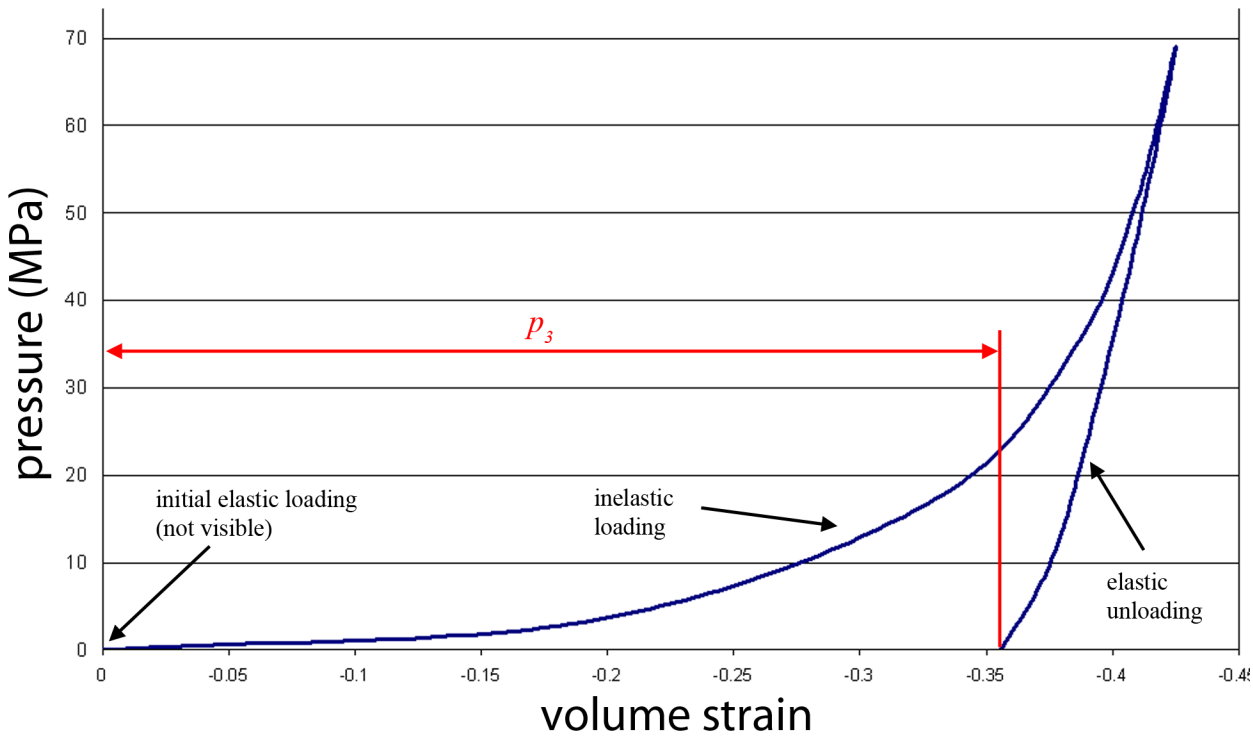

Figure A.2. Ideal hydrostatic parameterization data. The unloading portion is used to obtain the elastic bulk modulus parameters b_0, b_1, and b_2. With these parameters, the loading portion of the data can be converted to a crush curve (see Fig. 4.14) to obtain the crush parameters p_0, p_1, p_2, and p_3 For this material (a ceramic powder, zircoa), the initial elastic loading curve is so small in comparison to the scale that it is not visible.

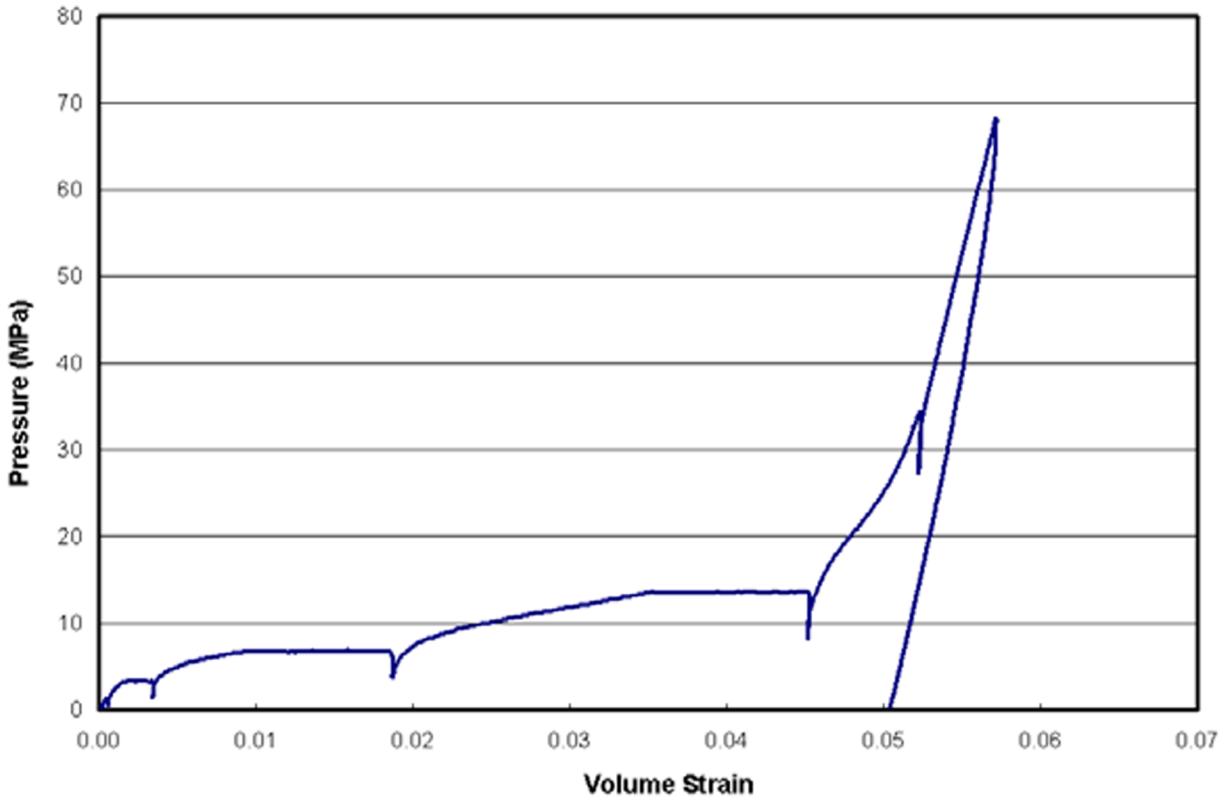

Figure A.3. Less-preferable hydrostatic parameterization data. Like the data for the material shown in Fig. A.2, this hydrostatic compression test (for frozen soil) was conducted nearly to full pore collapse, but the loading curve shows signs of material creep, which is not included in Kayenta.

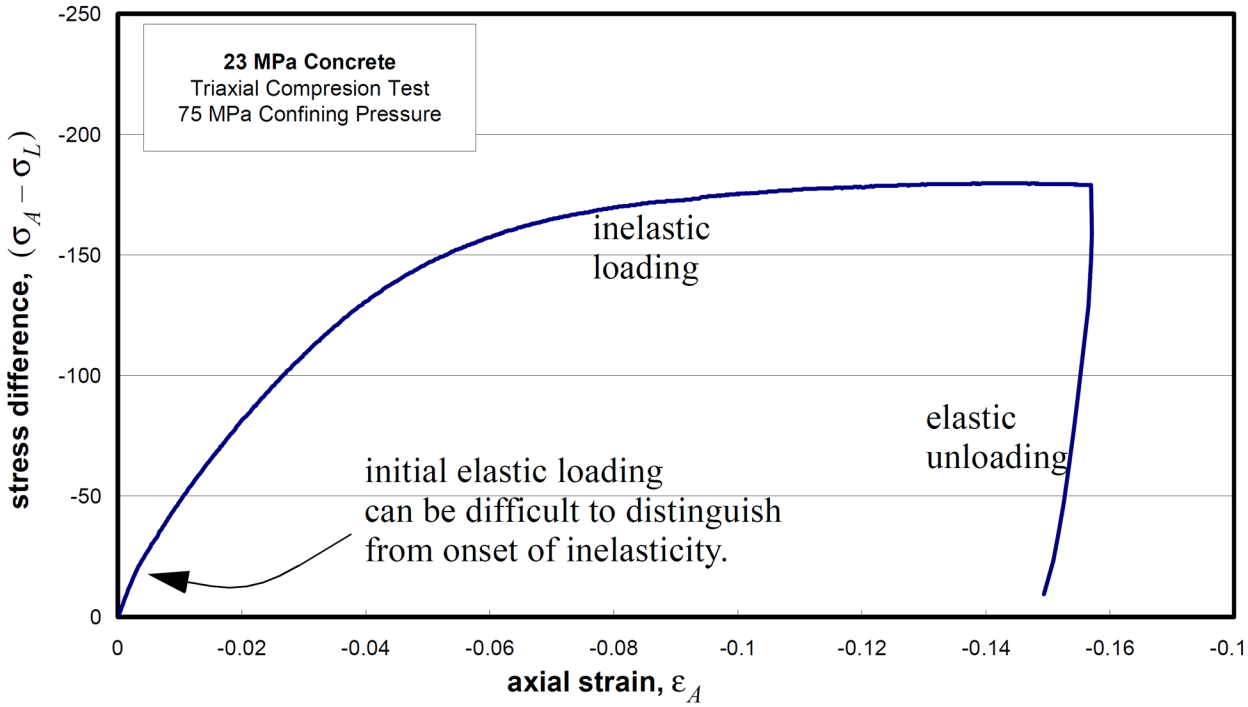

Figure A.4. Data representative of a triaxial compression parameterization test. The slope of the unloading curve is the nonlinear tangent Young's modulus. Through standard moduli conversion formulas from linear elasticity, the previously determined bulk modulus parameters are used to obtain the elastic *shear* modulus parameters g_0, g_1, and g_2.

directly using Young's modulus E as a user-specified material parameter, Kayenta requires the *shear modulus* G. Recall that the nonlinear elastic bulk modulus K was found previously in STEP 1. The shear modulus G can be found from K and E by using the standard linear elasticity formula, $G = \frac{3KE}{9K-E}$, cited in Eq. (4.15). If fitting to rock data, Poisson's ratio, $\nu = \frac{3K-E}{6K}$, is typically in the neighborhood of 0.2 (this is a useful *sanity* check).

STEP 3 **(optional) maintain a record of *all* peak stress states ever measured for every available quasistatic load-to-failure experiment ever performed for the material of interest.** The softening threshold (peak limit) envelope is the boundary of any and *all* stress states quasistatically achievable for the material, including both elastically obtainable stress states and stress states that can be reached only through inelastic deformation. Unlike a yield surface, which is the boundary of *elastically* obtainable stresses (and which therefore will, in general, evolve as the microstructure is altered in response to inelastic deformation), the limit envelope is fixed in time (see Fig. 1.2 on page 24). All achievable yield surfaces (an infinite set) are contained within the *single* limit envelope. Characterizing the limit envelope requires numerous different experiments. Typically, each *individual* experiment has precisely one stress state at which the second stress invariant J_2 achieves a peak value. If the material softens before rupturing, the value of J_2 at failure might be lower than $J_2{}^{\text{peak}}$. It is the *peak* that is of interest, not the post-softening value at failure.

For every available quasistatic load-to-failure experiment, find the stress state at which J_2 is larger than for any of the other stress states in that experiment. Construct a table of data triplets $(\overline{I_1}^{\text{peak}}, \sqrt{J_2^{\text{peak}}}, \overline{\theta}^{\text{peak}})$, where $\overline{I_1}^{\text{peak}}$ and $\overline{\theta}^{\text{peak}}$ are the values of $\overline{I_1}$ and $\overline{\theta}$ at the stress state for which J_2 is at its peak value. The number of entries in your peak stress table will equal the number of experiments run to failure. The goal here is to gather sufficient data to parameterize both the Lode angle function $\Gamma(\overline{\theta})$ and the shear limit envelope in Eq. (4.39),

$$\boxed{F_f(I_1) = a_1 - a_3 \mathrm{e}^{-a_1 \overline{I_1}} + a_4 \overline{I_1}}, \text{ where } \overline{I_1} = -I_1 \textbf{ shear limit surface in TXC.} \tag{A.4}$$

STEP 4 **Use peak stresses from a family of triaxial compression tests to determine the shear failure envelope parameters a_1, a_2, a_3, and a_4.**

Recall that the F_f function represents a peak shear limit envelope in the meridional plane for which $\sqrt{J_2}$ is plotted against $\overline{I_1}$ for triaxial compression (TXC) stress states. Thus, the set of all stress states ever observed in TXC (Lode angle $\overline{\theta} = +30^\circ$) must fall below the curve $\sqrt{J_2} = F_f(I_1)$, modulo experimental scatter. Stated differently, this curve defines boundary of all stress states that ever have been (or ever *can* be) observed in quasistatic TXC loading. A sufficient number of TXC experiments must be conducted under various confining pressures so that the bounding surface begins to take form. On other meridional planes (i.e., at other Lode angles), Kayenta presumes the bounding curve is adequately described by $\sqrt{J_2} = \frac{F_f(I_1)}{\Gamma(\overline{\theta})}$, which simply means that Kayenta presumes that the limit function at *non*-TXC Lode angles is simply a scalar multiple of the TXC function. Once the F_f function has been determined in this parameterization step, the peak stress data at other Lode angles will be used later to determine the Γ proportionality function.

Using only the TXC ($\overline{\theta} = 30°$) data create a scatter plot of all ever-achieved TXC values of $J_2$and $\overline{I_1}$. A scatter plot of all TXC stress data measured at various confining pressures might look somewhat as sketched below:

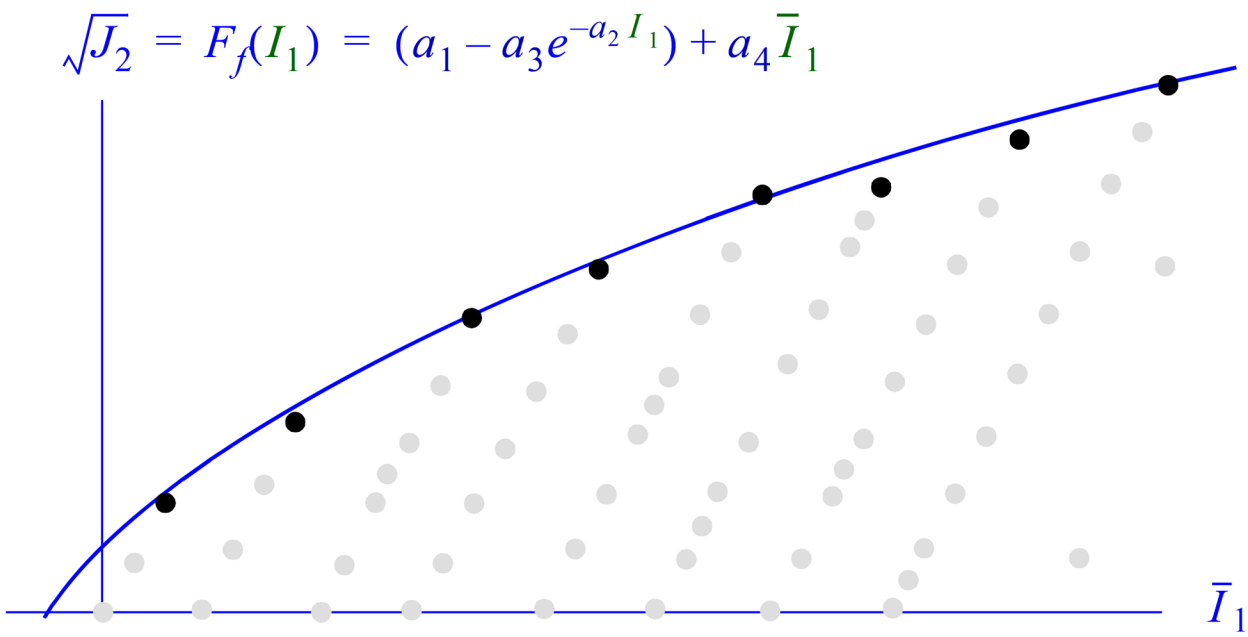

Figure A.5. A family of TXC tests conducted to failure. The boundary of data points defines the F_f function. All other (sub-peak) data points fall below this line. Plots like the are shown for various materials in Fig. 10.1

In Fig. A.5, the *peak* data pairs (darkened dots) correspond to the $\overline{\theta}^{\text{peak}} = 30°$ values from your table of peak-stress invariants collected in STEP 3. A suite of actual TXC experiments for porcelanite is shown in Fig. A.6, along with further illustration of how discrete peak points from these experiments are transferred to a limit surface meridional plot for fitting to Eq. (A.4).

Once enough TXC experiments have been conducted for a well-defined shear limit boundary to emerge, the next step is to determine values of a_1, a_2, a_3, and a_4 that best fit the F_f function to this boundary.

Given triaxial stress difference $\overline{\sigma_A} - \overline{\sigma_L}$ vs. axial strain data, Eq. (3.22) and Eq. (3.23) show that value of J_2 at peak is given by $\sqrt{J_2^{\text{peak}}} = \frac{|\overline{\sigma_A} - \overline{\sigma_L}|^{\text{peak}}}{\sqrt{3}}$ and the value of I_1 (i.e., the trace of the stress) at peak equals $\overline{I_1}^{\text{peak}} = 3\overline{\sigma_L} + (\overline{\sigma_A} - \overline{\sigma_L})^{\text{peak}}$, where $\overline{\sigma_L}$ is the (constant) lateral confining pressure. The ($\overline{I_1}^{\text{peak}}$, $\sqrt{J_2^{\text{peak}}}$) data pairs from TXC experiments (i.e., those for which $\overline{\theta}^{\text{peak}} = +30°$) are used to fit the parameters in Eq. (A.4) via constrained optimization software of your choice. The software must include the constraints on page 69 of the main

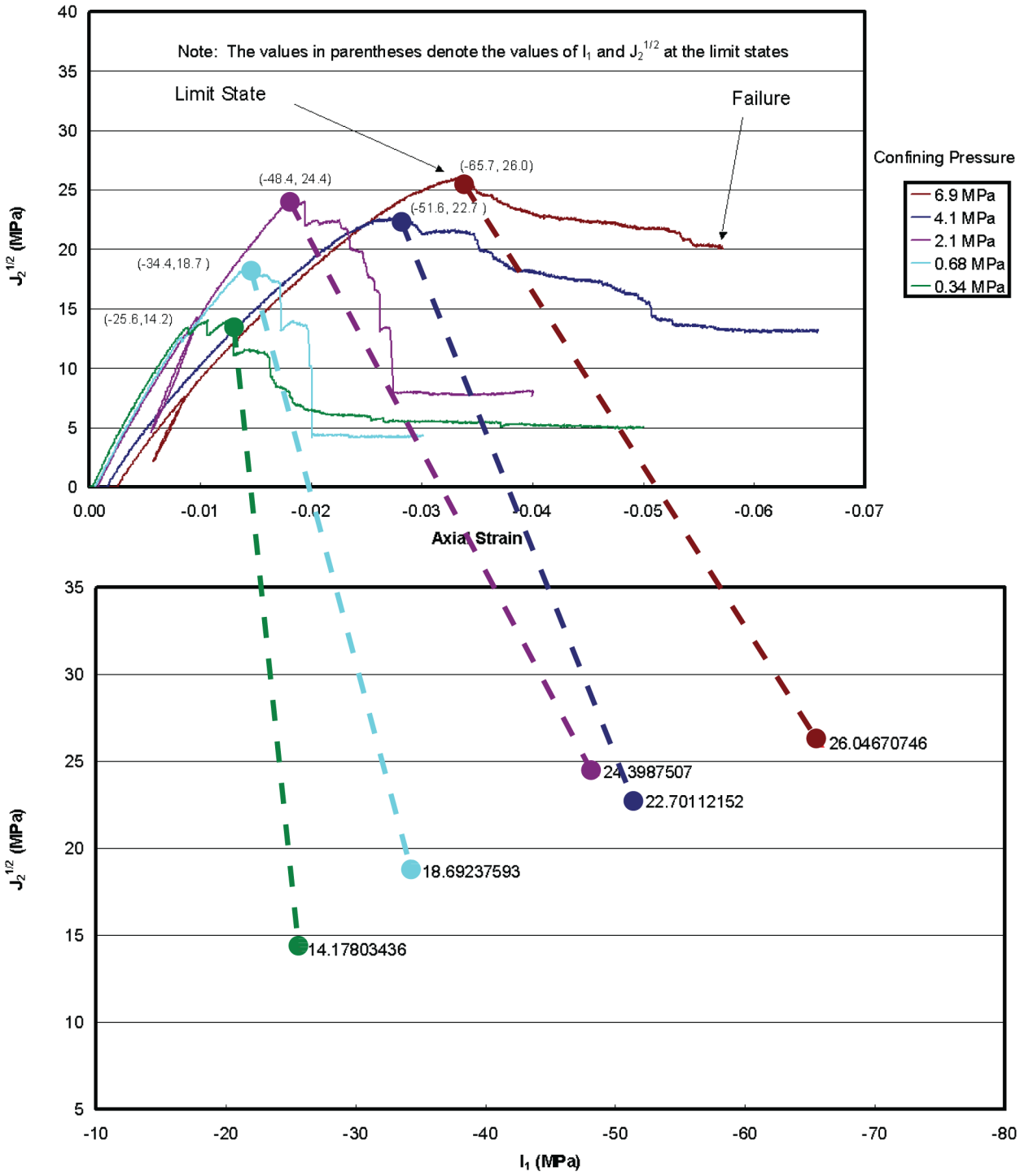

Figure A.6. TXC stress-strain plots and extraction of their peak values to construct the meridional limit curve (data are for porcelanite). Top plot, each shear stress $\sqrt{J_2}$ vs. axial strain plot has exactly one peak value, as labeled. The value of I_1 at this peak is found by applying Eq. (3.22), $\overline{I_1} = \sqrt{3}\tau + 3\sigma_L$ with $\tau = \sqrt{J_2^{\text{peak}}}$ and σ_L equal to the lateral confining pressure for the test. Bottom plot, the peak states are transferred to a plot of $\sqrt{J_2}$vs. $\overline{I_1}$ for fitting to the F_f meridional limit function.

text. Refer to Fig. 4.8 to help decide appropriate initial guesses for a_1, a_2, a_3, and a_4. If the data suggest a linear envelope at high pressures, then your first guess for a_4 should be an approximation of the slope of this envelope. If in doubt, take $a_4 = 0.0$ (i.e., assume the data asymptote to a constant value as pressure goes to infinity). Your first guess for a_1 should approximate the zero-pressure value of the linear asymptote line (extrapolate visually if necessary). Set a_3 to equal a_1 minus your best estimate for the *actual* ordinate intercept of the low-pressure data (again, extrapolate if necessary). Finally, set a_2 to equal an estimate for the initial (low-pressure) slope of the data divided by a_3.

STEP 5 **Use peak stresses from a family of triaxial extension tests to determine the extension to compression ratio Ψ.** This step applies only if you have data for triaxial *extension* TXE, which is rare.

Sometimes, it might be *impractical* — or overly expensive — to obtain TXE data. In this case, an engineering approach for *estimating* Ψ presumes that it obeys the same coupling to the meridional profile slope as predicted in classical Mohr-Coulomb theory. Using Eq. (A.4) to set the TXC slope in Eq. (B.19) in Appendix B, an estimate for the pressure-varying strength ratio is

$$\Psi = \frac{1}{1+\sqrt{3}\left[a_4 + a_2 a_3 \mathrm{e}^{-a_2 \overline{I}_1}\right]} \tag{A.5}$$

When TXE data are unavailable, set the parameter Ψ equal to -1 to instruct Kayenta to use this formula as a "best guess" of the strength ratio.

If TXE data are available, then (as was done above for TXC tests) construct a table of ($\overline{I}_1^{\text{peak}}$, $\sqrt{J_2^{\text{peak}}}$) data pairs corresponding to peak attained stresses in triaxial *extension* (TXE). These are the data pairs in your peak data table from step 3 that correspond to $\overline{\theta}^{\text{peak}} = -30°$. For each of these TXE data pairs, compute

$$\Psi = \frac{\sqrt{J_2^{\text{peak in TXE}}}}{F_f(\overline{I}_1^{\text{ peak in TXE}})} \tag{A.6}$$

where F_f is the TXC shear limit function parameterized in the previous step. Of course, each TXE experiment is likely to result in slightly different values for Ψ. At present, Kayenta presumes that the TXE/TXC ratio Ψ is constant. Therefore, set the Kayenta parameter Ψ equal to the average of each Ψ computed using Eq. (A.6) for each available TXE experiment. Alternatively, compare the measured data with the theoretical prediction in Eq. (A.5). If the prediction from Eq. (A.5) fits the data better than an assumption of a constant strength ratio Ψ, then simply specify the strength ratio as -1 in the model input.

STEP 6 **Determine the appropriate Lode function option `J3TYPE`.** This step applies only if data are available for the peak stress under non-TXC loading. If such data are unavailable, then choose `J3TYPE` $= 2$.

Recall that Kayenta's function $\Gamma(\overline{\theta})$ defines the shape of the octahedral profile shape for Lode angles spanning the range from TXE ($\overline{\theta} = -30°$) to TXC ($\overline{\theta} = +30°$). Kayenta's parameter **J3TYPE** (see page 70) dictates the functional form to be used for the Γ function. Non-triaxial data are difficult to acquire. If no such data are available, you will need to use engineering judgement as to an appropriate choice for **J3TYPE**. This parameterization step aims to guide the choice in the happy circumstance that non-triaxial data *are* available.

As illustrated in Fig. 4.10, Kayenta's Γ function is defined to equal 1 in TXC and $1/\Psi$ in TXE. Large values of Γ correspond to small shear strengths. In this model parameterization step, all available peak-state data obtained in *non-triaxial* loading paths are considered to help decide an appropriate choice for the **J3TYPE** option. Looping over your table (collected in STEP 3) of "all-observed" peak stress invariant triplets ($\overline{I}_1^{\text{peak}}$, $\sqrt{J_2^{\text{peak}}}$, $\overline{\theta}^{\text{peak}}$), especially those at non-triaxial states, create a new two-column table of ($\overline{\theta}$, Γ) data pairs, where

$$\Gamma = \frac{F_f(\overline{I}_1^{\text{peak}})}{\sqrt{J_2^{\text{peak}}}} \tag{A.7}$$

By comparing a scatter plot of these ($\overline{\theta}$, Γ) data to the graphs in Fig. 4.10, an appropriate choice for **J3TYPE** should be more clear. To assist in the decision, it might be easier to instead scale the ordinate as shown in Fig. 4.7. By overlaying data with the family of plots in Fig. 4.7 an appropriate choice for **J3TYPE** should be apparent, as illustrated in Fig. 4.8. If non-triaxial data are unavailable (a common problem), select **J3TYPE** $= 1$ if the material is judged to be moderately ductile; otherwise, select **J3TYPE** $= 3$.

STEP 7 **Hardening parameters.** In the previous steps, we determined Kayenta parameters that define the outer limit surface. No stress state outside this fixed (non-evolving) limit surface can be achieved through *any* load path. Consequently, the infinite set of all possible *yield* surfaces must be contained within this limit envelope. Unlike the limit surface, which bounds *all* possible stress states, the yield surface merely bounds the set of *elastically* obtainable stress states. Unlike the limit surface, a yield surface evolves (hardens) through time as a result of microstructural changes induced in the material under inelastic loading. The initial yield surface is typically much smaller than the limit surface (see Fig. 1.2 in the main text). Isotropic hardening permits the *initial* yield surface to expand on octahedral planes (by amounts that vary with pressure) up until the limit surface is reached. Kinematic hardening permits the yield surface to translate in stress space until the limit surface is reached. Both types of hardening may occur simultaneously.

As a rule, the amount of kinematic hardening relative to total stress is high at lower pressures. Therefore, kinematic hardening data are best inferred from unconfined compression tests. In the previous parameterization steps, we determined crush parameter values (p_0, p_1, p_2), elastic parameters , the limit surface parameters (b_0, b_1, b_2, g_0, g_1, g_2), and **J3TYPE**. Now these values should be used in a finite-element (or single cell driver) implementation of Kayenta, to obtain a simulated table of axial stress vs volume strain to compare with available experimental data. The goal is to determine values for unknown Kayenta parameters through

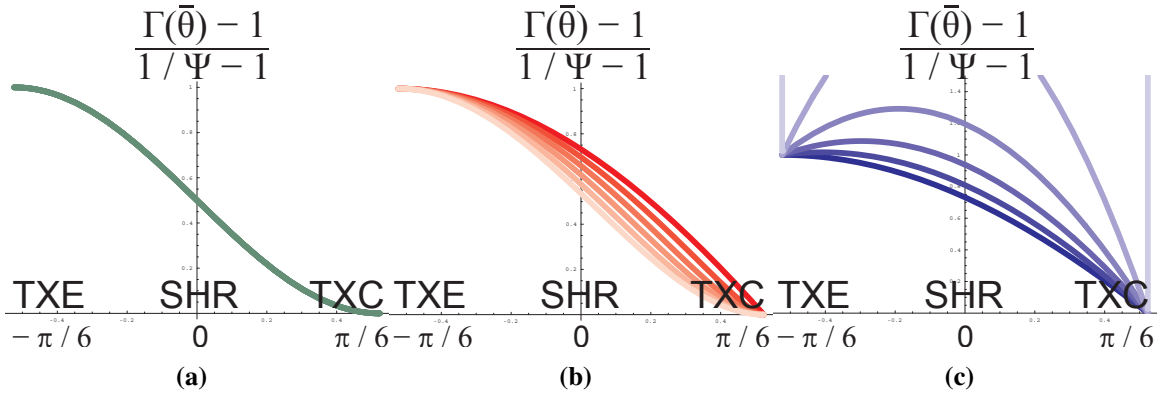

Figure A.7. The Lode function information originally shown in Fig. 4.10 of the main report, now displayed with a transformed ordinate. Knowing that $\Gamma = 1/\Psi$ in TXE and $\Gamma = 1$ in TXC, it makes sense to scale the ordinate as shown so that, regardless of the value of Ψ, the scaled ordinate equals 1 in TXE and 0 in TXC. With this scaling, all Gudehus Lode functions overlap; the others vary with Ψ.

a systematic simulation sequence. As a first guess, set the "yet-to-be-determined" Kayenta parameters as follows:

- offset **RN** $= N = 0$ (i.e., suppress hardening)
- kinematic hardening parameter **HC** $= 1e5$
- shape parameter **CR** $= R = 10$
- plastic potential function parameters for non-associativity **A2PF**==A2, **A4PF**==A4, **RKPF**=RK, **CRPF**=CR (i.e., tentatively assume associativity)
- joint spacing **RJS** $= \ell_s = 0.0$
- rate sensitivity parameters **T1** through **T7** $= 0.0$ (no rate sensitivity).

Run the finite-element code for unconfined compression and output axial stress vs. volumetric strain (**EVOL**). It is unlikely that this result will replicate observed unconfined compression data on the first try. We ultimately hope to assign values to the above parameters so that the volume strain will "turn around" as Fig. 10.6 (even though axial strain increases monotonically, the *volume* strain turns around because of the lateral bulking strains).

The phenomenological fitting functions employed in Kayenta are designed to extrapolate reasonably well into regions where data are not available, but these functions are also selected in part for computational tractability and they therefore serve only as approximations. Consequently, there will be modeling error. Ideally, one should use regression fitting procedures to select Kayenta hardening parameters that minimize modeling error relative to

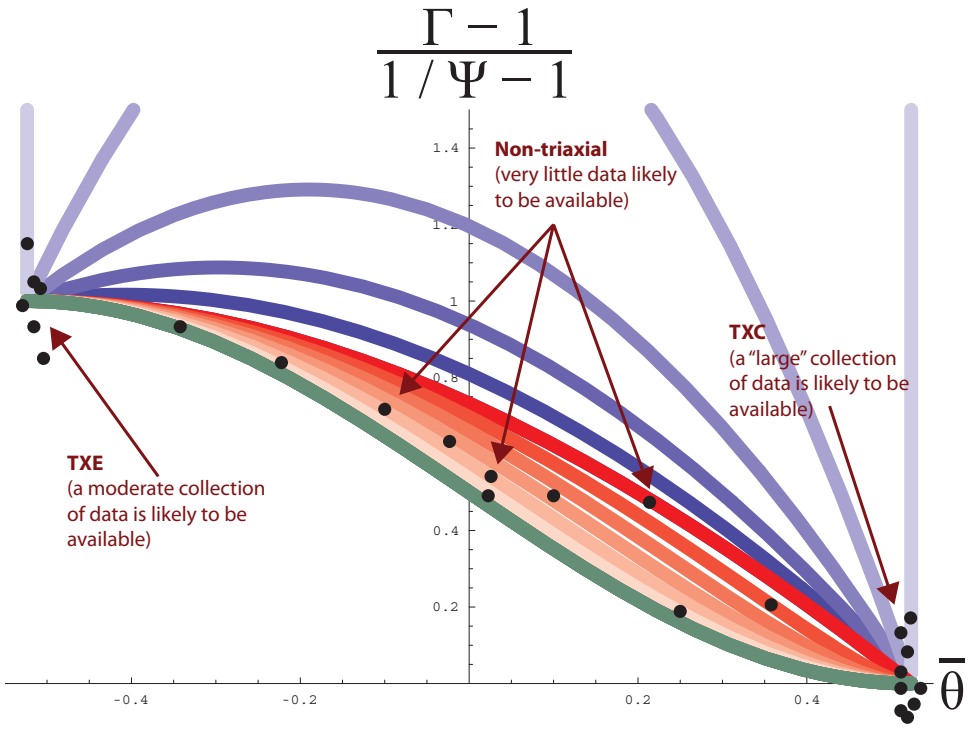

Figure A.8. A sketch of how data might be distributed at non-triaxial states. In this contrived example, most of the data at non-triaxial states falls in the **red** Willam-Warnke region and therefore **J3TYPE** = 2 would be appropriate for this material. In practice, data at non-triaxial Lode angles are rarely available. In this case, the user must resort to engineering judgement to decide which **J3TYPE** option to select.

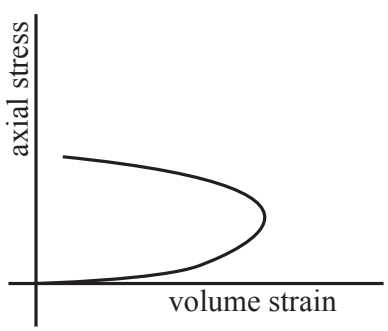

Figure A.9. Sketch of axial stress vs. strain.

available data. We have already described the systematic process for fitting the elastic data, the crush curve data, and the limit state data. However, no similar fitting procedure has yet been developed to determine the hardening parameters. Consequently, for these parameters, exploratory manual "trial and error" must be used. For this step, a means of running Kayenta in "single element" (homogeneous loading) must be available. The single element driver must be able to support stress boundary conditions similar to the boundary conditions used in the laboratory for triaxial compression testing.

In the following, we will be exploring adjustments of CR, RN, and HC to try to achieve a strain "turn around" at the correct (observed) strain and stress for triaxial loading.

If no turn around is apparent in your simulation of the TXC experiment, try decreasing CR. Continue decreasing CR until turn around occurs. If you still get no turn around, bring down the initial yield surface. The intercept on the ordinate on the meridional profile is located at $\sqrt{J_2} = a_1 - a_3$. Try increasing N to a value no larger than $a_1 - a_3$ (our initial guess of $N = 0$ presumed that the initial yield surface coincided with the shear limit surface. By setting N to a nonzero value, we are now permitting kinematic hardening). You will likely see "turn around" start to occur.

Now that a turn-around is visible, the parameters need to be adjusted to fit the compression and dilatation phases. Try changing HC. Increasing (say, doubling) HC will increase the strain value at which turn-around occurs. Lowering HC lowers the turn-around strain. If you continue to have trouble getting turn around, double check that you have correctly entered the previously determined (*known*) parameter values. If the turn-around stress is too high, try lowering HC.

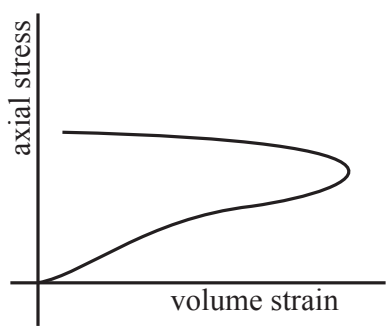

Figure A.10. Sketch of axial stress vs. strain.

Once shear-induced dilatation (turn-around) has been adequately modeled for unconfined TXC, go then to high-confinement data. Try changing CR (e.g., from 7 to 10 if computed peak strain is too large).

Go back to unconfined, and work on HC and RN.

Continue to go back and forth until you are satisfied with both confined and unconfined results.

Below: There is a stand-alone model driver that can provide a so-called "shotgun" exploration of the effect of changing a variety of model parameters at once to predict several response curves from which the user can select the one that best matches data. As mentioned earlier, this procedure clearly could benefit from automation!

STEP 8 **RATE DEPENDENCE PARAMETERS**: Unlike rate-dependence theories that treat strength as a *function* of strain rate, Kayenta's Duvaut-Lion overstress model treats strength as a *functional* of strain rate.[1] Figure 10.9 shows that high-rate loading causes the stress to asymptote to a higher values. Under conditions of *constant* strain rate, the stress asymptotes to a steady-state value, which is (under such conditions) an actual function of strain rate, from which Kayenta's **T**-parameters may be found. As mentioned in the main text on page 203, it is hoped that future revisions of Kayenta will have the rate dependence parameters be taken directly from standard data for rate dependence that reports apparent steady-state strength as a function of strain rate in uniaxial loading (*cf.*dynamic increasing factor "DIF" curves in [90], which are essentially fits to data such as in the bottom plot of Fig. 10.9). Kayenta's rate dependence parameters currently must be set via trial end error, but the procedure for doing so is fairly straightforward. For each stress-strain plot in Fig. 10.9, for example, you would begin by set all **T**-parameters to zero except T_1, and then you would find the value of T_1 that best matches the steady-state strength. After this is done for each of the different curves (each at different strain rates), you will have obtained values of T_1, which is equivalent to finding values of the characteristic time τ needed at each strain rate. Once this information for τ as a function of strain rate is determined, you simply fit it to Eq. (7.22) to obtain proper values of T_1 and T_2 to match the entire suite of tests with a single parameter set (i.e., without having to change T_1 for each strain rate as was done during the fitting process). We know that we are dealing with the $\varepsilon_v^p > 0$ branch of Eq. (7.22) because the volumetric curves in Fig. 10.9 are showing an increase in volumetric strain. Other loading scenarios, such as plate-slap experiments or Kolsky bar tests with high lateral confinement, might involve compaction (in which case, the characteristic time might be longer by a factor as much as 3); such data would be fitted in a similar manner (i.e., finding the constant τ required to fit each experiment, and then fitting those constant values to the second branch of Eq. (7.22) to the actual conditions of each experiment. In summary, the fitting procedure is straightforward, which means that the steps ar moderately clear without necessarily being easy.

This concludes our guidance for parameterizing new materials to Kayenta. Further revisions of this manual will likely include additional tips and parameterization experiment suggestions.

[1] A model that has strength as a *function* of strain rate generally cannot predict the transient (curved) parts of the stress-strain plots in Fig. 10.9. A model that treats strength as a *function* of strain rate would go straight up to the apparent steady-state strength without any bend in the curve. Such behavior is not only clearly at odds with observations, but it also causes numerical problems if the strain rate is suddenly "cut off" to zero because that would put the strength instantly to a lower value and thus would make the stress state itself fall in the inadmissible domain outside of the yield surface. This is why most models of this sort impose an artificial requirement that the stress must drop down over a few computational time steps. Overstress models, on the other hand, automatically drop the stress over a finite physical time.

Appendix B

Nomenclature and Data Sets

This appendix contains three tables defining (1) model parameters, (2) plottable variables, and (3) other symbols or acronyms used internally within this manual. In each table, the first column shows the typeset symbol for the variable. The next column contains the ASCII string used for the variable in code input files and/or within the source code. In the SI units column, a "1" indicates that the variable is dimensionless. A "—" indicates that dimensions vary, while N/A means dimensions are not applicable. The defining equation (or page number) in the last column of the tables cites the location in this report where the quantity is defined or discussed.

Reminder: in mechanics, stress and strain are typically taken positive in tension. However, in applications, they are taken positive in compression. To manage this potentially confusing conflict of conventions, recall

Definition of the "over-bar" $\boxed{\overline{x} \equiv -x}$ (B.1)

For example, I_1denotes the trace of stress (positive in tension). Therefore, $\overline{I_1} \equiv -I_1$ is positive in compression.

MODEL DEVELOPERS: The keywords and their placement in the user input array of the source code is defined in the header file called Kayenta_pnt.h. That file is the master file for defining user inputs and also for defining pointers to variables in the internal state variable array.

B.1 Model Parameters (User Input)

Symbol	ASCII Name	Name and meaning	SI Unit	Defining Equation
b_0	**PROP** (1) **(B0)** **BKMOD**	Initial elastic bulk modulus. The tangent bulk modulus is given by $$K = b_0 + b_1 \exp\left(-\frac{b_2}{\lvert I_1 \rvert}\right)$$ This formula is for a non-jointed material without elastic-plastic coupling. The entry for b_3 shows the more general formula that accounts for these additional effects.	Pa	Eq. (4.9) Eq. (A.1) page 273
b_1	**PROP** (2) **(B1)**	High pressure coefficient in nonlinear elastic (intact) bulk modulus function (see above formula). For linear elasticity, set $b_1 = 0$. For nonlinear elasticity, set b_1 so that the Bulk modulus K will asymptote to a value $b_0 + b_1$ at high pressures.	Pa	Eq. (4.9) Eq. (A.1)
b_2	**PROP** (3) **(B2)** **SMOD**, **SHMOD**	Curvature parameter in nonlinear elastic (intact) bulk modulus function (see above formula). For linear elasticity, set $b_2 = 0$. For nonlinear elasticity, set b_2 to a small value to transition rapidly from the low pressure bulk modulus to the high pressure modulus. Larger values of b_2 will result in a broader transition range.	Pa	Eq. (4.9) Eq. (A.1)
b_3	**PROP** (4) **(B3)**	Coefficient in nonlinear elastic bulk modulus to allow for plasticity-induced changes in the elastic properties. To neglect this effect, set . When this parameter is nonzero, the elastic tangent bulk modulus is computed by $$K = f_K \left\{ \left[b_0 + b_1 \exp\left(-\frac{b_2}{\lvert I_1 \rvert}\right) \right] - b_3 \exp\left(-\frac{b_4}{\lvert \varepsilon_v^p \rvert}\right) \right\}$$	Pa	Eq. (4.33)
b_4	**PROP** (5) **(B4)**	Power in nonlinear elastic bulk modulus to allow for plasticity-induced changes in the elastic properties. To neglect this effect, set $b_4 = 0$. Otherwise, see above formula.	1	Eq. (4.33)

g_0	**PROP** (6) **(G0)**	Initial elastic shear modulus. The tangent shear modulus is computed by $$G = g_0 \left[\frac{1 - g_1 \exp(-g_2 \sqrt{J_2}}{1 - g_1} \right]$$ This formula is for a non-jointed material without elastic-plastic coupling. The entry for g_3 shows the more general formula that accounts for these additional effects.	Pa	Eq. (4.10) Eq. (A.3)
g_1	**PROP** (7) **(G1)**	Parameter used to define the elastic (intact) shear modulus at large shears (see above formula). Specifically, the shear modulus will asymptote to a value $g_0/(1-g_1)$ as shear stress increases. Must be less than 1.0. For linear elasticity, set $g_1 = 0$. For the shear modulus to increase with shearing, set $0 < g_1 < 1$. For the shear modulus to decrease with shearing, set $g_1 < 0$.	1	Eq. (4.10) Eq. (A.3)
g_2	**PROP** (8) **(G2)**	Curvature parameter in nonlinear elastic (intact) shear modulus function (see above formula). Must satisfy $g_2 \geq 0$. For linear elasticity, set $g_2 = 0$. For nonlinear elasticity small values of g_2 cause the shear modulus to transition *rapidly* from its initial value g_0 to its high shear value $g_0/(1-g_1)$. Larger values of g_2 make this transition more gradual.	Pa^{-1}	Eq. (4.10) Eq. (A.3)
g_3	**PROP** (9) **(G3)**	Coefficient in nonlinear elastic shear modulus to allow for plasticity-induced changes in the elastic properties. To neglect this effect, set $g_0 = 0$. When nonzero, the tangent shear modulus is computed by $$G = f_G \left\{ g_0 \left[\frac{1 - g_1 \exp(-g_2 \sqrt{J_2})}{1 - g_1} \right] - g_3 \exp\left(-\frac{g_4}{\gamma^p_{\text{equiv}}} \right) \right\}$$	Pa	Eq. (4.34)
g_4	**PROP** (10) **(G4)**	Power in nonlinear elastic shear modulus to allow for plasticity-induced changes in the elastic properties. To neglect this effect, set $g_4 = 0$. Otherwise, see above formula.	1	Eq. (4.34)

ℓ_s	**PROP** (11) **(RJS)**	Joint spacing. Set this parameter to zero if the material has no geological (or rock-like) faults.	m	cf. [20]
G_s	**PROP** (12) **(RKS)**	Joint shear stiffness. Set this parameter to zero if the material has no geological (or rock-like) faults.	$\mathrm{Pa\,m^{-1}}$	cf. [20]
K_s	**PROP** (13) **(RKN)**	Joint normal stiffness. Set this parameter to zero if the material has no geological (or rock-like) faults.	$\mathrm{Pa\,m^{-1}}$	cf. [20]
a_1	**PROP** (14) **(A1)**	Constant term in the fitting function for the meridional profile, $F_f(I_1) = a_1 - a_3 \mathrm{e}^{-a_2 \overline{I_1}} + a_4 \overline{I_1}$, for the ultimate shear limit surface. Here, $\overline{I_1} = -\operatorname{tr} \underset{\approx}{\sigma}$ and therefore $\overline{I_1}$ is three times the pressure. At zero pressure, $F_f(I_1) = a_1 - a_3$ while at high pressure (large $\overline{I_1}$), $F_f(I_1) \sim a_1 + a_4 \overline{I_1}$. Thus, a_1 is the vertical intercept of the linear *asymptote*, whereas is the vertical intercept of the limit function *itself*. These parameters define the ultimate limit curve, at which the maximum possible hardening has occurred and softening is imminent. The *initial* onset of *yield* is described by $f_f(I_1) = F_f(I_1) - N$. Thus if fitting to data for yield onset, recognize that the constant term will be lower than a_1 by an amount N.	Pa	Eq. (4.39) Eq. (A.4)
a_2	**PROP** (15) **(A2)**	Curvature decay parameter in the fitting function for the meridional profile, $F_f(I_1) = a_1 - a_3 \mathrm{e}^{-a_2 \overline{I_1}} + a_4 \overline{I_1}$. Keep in mind that $I_1 = -3\overline{p}$, where $\overline{p}$ is pressure. Set $a_2 = 0$ for a linear meridional profile as in Mohr-Coulomb theory. Assign a_2 a large value to quickly asymptote to the high-pressure profile slope.	Pa^{-1}	Eq. (4.39) Eq. (A.4)
a_3	**PROP** (16) **(A3)**	Parameter in the shear limit meridional fit function, $F_f(I_1) = a_1 - a_3 \mathrm{e}^{-a_2 \overline{I_1}} + a_4 \overline{I_1}$.	Pa	Eq. (4.39) Eq. (A.4)

a_4	**PROP** (17) **(A4)**	High-pressure meridional slope parameter in the fit function, $F_f(I_1) = a_1 - a_3 e^{-a_2 \overline{I_1}} + a_4 \overline{I_1}$.	1	Eq. (4.39) Eq. (A.4)
p_0	**PROP** (18) **(P0)**	Value of I_1 at the onset of pore collapse for hydrostatic compression of virgin material. This parameter will be negative because I_1 is negative in compression. In the lexicon of traditional p-α crush models, this variable would equal $-3P_E$, where P_E is the elastic limit pressure in hydrostatic compression. In early (pre-2003) publications about Kayenta, this parameter is denoted X_0.	Pa	Eq. (4.69) Eq. (A.2)
p_1	**PROP** (19) **(P1)**	One third of the slope of a porosity vs pressure crush curve at the elastic limit. In early (pre-2003) publications about Kayenta, this parameter is denoted D_1.	Pa^{-1}	Eq. (4.69) Eq. (A.2)
p_2	**PROP** (20) **(P2)**	Extra fitting parameter for hydrostatic crush curve data, used when the crush curve has an inflection point. In early (pre-2003) publications about Kayenta, this parameter is denoted D_2.	Pa^{-2}	Eq. (4.69) Eq. (A.2)
p_3	**PROP** (21) **(P3)**	Asymptote (limit) value of the absolute value of the plastic volume strain. This parameter is approximately equal to the initial porosity in the material and may be inferred from hydrostatic crush data. In early (pre-2003) publications about Kayenta, this parameter is denoted W.	1	Eq. (4.69) Eq. (A.2) page 35
R	**PROP** (22) **(CR)**	Shape parameter that allows porosity to affect shear strength. R equals the eccentricity (width divided by height) of the elliptical cap function, so it is the ratio a/b (not A/B) in Fig. 4.16. This parameter affects the stress level at which dilatation will occur in triaxial compression. If dilatation is occurring too soon, increase the value of R. Decreasing R will decrease the influence of porosity on shear strength and therefore enhance the effect of void space creation associated with crack growth. To replicate older classical pore collapse models (which initiate pore collapse only at a critical pressure, regardless of the level of shear stress), set R to a very small number.	1	Eq. (4.72) page 273

Ψ	**PROP** (23) **(RK)**	TXE/TXC (triaxial extension to compression) strength ratio. Convexity of the yield surface requires that $1/2 \leq \Psi \leq 2$ (or $7/9 \leq \Psi \leq 9/7$ if using **J3TYPE**=1). Real materials generally satisfy $1/2 \leq \Psi \leq 1$. To instruct Kayenta to automatically assign a pressure-dependent strength ratio according to Eq. (B.19), enter "**RK** $= -1.0$".	1	Eq. (A.5) page 70
N	**PROP** (24) **(RN)**	Off-set parameter. Must be non-negative. Set $N = 0$ to suppress kinematic hardening. For problems with kinematic hardening, the backstress invariant $\sqrt{J_2^{\alpha}}$ will not be permitted to grow any larger than N. The initial yield surface is defined by $F_f^{\text{initial}}(I_1, N) = F_f(I_1) - N$, where F_f describes the shear limit surface (softening threshold). Roughly speaking, the shear strength can increase by an amount N before softening will commence.	Pa	Eq. (4.40) page 92 page 224
H	**PROP** (25) **(HC)**	Kinematic hardening parameter. Set $H = 0$ and $N = 0$ to suppress kinematic hardening. Otherwise, this parameter affects how "quickly" the yield surface evolves toward the ultimate shear failure surface.	Pa	Eq. (4.79) page 224
	PROP (26) **(CTPSF)**	For host codes that include a void-insertion option (invoked in ALEGRA, for example, by defining I1SOFTLIM), then the variable represents fracture cut-off of principal stress. Otherwise, this variable is free.	Pa	N/A
I_1^{cut}	**PROP** (27) **(CUTI1)**	Tensile cut-off in allowable value of the first stress invariant I_1. If the first invariant I_1 (which is proportional to the negative of pressure) reaches this cut-off value in tension, the isotropic part of the stress is replaced with this value. In early versions of code [33], this parameter was required as an *ad hoc* patch to avoid "false elastic domains" or pathological yield function contours disruptive to convergence (*cf.*[12]). These algorithmic issues prevented the older predecessor model from damaging all the way to zero tensile strength. Kayenta does not suffer this shortcoming. Now this input parameter is available if you really want an I_1 cutoff, but leaving it unspecified is the best choice (the code will automatically set it equal to **PEAKI1**.	Pa	cf. [12]

—	**PROP** (28) **(CUTPS)**	Principal stress tensile cut-off. If a predicted principal stress is found to exceed this value, then it is replaced with this value. See discussion regarding the state variable "**CRACK**" in the next table.	Pa	N/A
T_1	**PROP** (29) **(T1)**	Primary rate dependence parameter in the Duvaut-Lions overstress model. To specify a *constant* intrinsic material response time, set this user input equal to the characteristic response time. Use the other "T" parameters to enable dependence on strain rate and pressure.	s	Eq. (7.22)
T_2	**PROP** (30) **(T2)**	Rate dependence parameter. See main text.	s^{-1}	Eq. (7.22)
T_3	**PROP** (31) **(T3)**	Rate dependence parameter. See main text.	1	Eq. (7.22)
T_4	**PROP** (32) **(T4)**	Rate dependence parameter. See main text.	s^{-1}	Eq. (7.22)
T_5	**PROP** (33) **(T5)**	Rate dependence parameter. See main text.	Pa	Eq. (7.22)
T_6	**PROP** (34) **(T6)**	Rate dependence parameter. See main text.	s	Eq. (7.22)
T_7	**PROP** (35) **(T7)**	Rate dependence parameter. See main text.	Pa^{-1}	Eq. (7.22)

—	**PROP** (36) **(J3TYPE)**	Integer-valued control parameter for specifying the desired type of 3rd-invariant yield surface: 1. Gudehus 2. Willam-Warnke 3. Mohr-Coulomb	1	page 70
a_2^{PF}	**PROP** (37) **(A2PF)**	Potential function parameter (=**A2** for associative). Assign this parameter in the same way you would assign a value to a_2, except that this parameter is used to generate the flow potential surface (i.e., the plastic strain rate will be normal to the flow potential surface). If a_2^{PF} is unspecified or zero, it will be automatically set equal to a_2.	Pa^{-1}	page 77
a_4^{PF}	**PROP** (38) **(A4PF)**	Potential function parameter (=**A4** for associative). Assign this parameter in a manner similar to a_4 except that this parameter will be used to generate the flow potential. If a_4^{PF} is unspecified or zero, it will be automatically set equal to a_4.	1	page 77
R^{PF}	**PROP** (39) **(CRPF)**	Potential function parameter (=**CR** for associative). Flow potential analog of the yield surface parameter R. If R^{PF} is unspecified or zero, it will be automatically set equal to R.	1	page 77
Ψ^{PF}	**PROP** (40) **(RKPF)**	Potential function parameter (=**RK** for associative). Flow potential analog of the yield surface parameter Ψ. If Ψ^{PF} is unspecified or zero, it will be automatically set equal to Ψ.	1	page 77
—	**PROP** (41) **(SUBX)**	Subcycle control parameter. If zero, Kayenta will select an appropriate default subcycle step size, called `DTSUB` in the source code. If **SUBX** is nonzero, then Kayenta's default subcycle increment will be multiplied by 10^{SUBX} (ten raised to the power). If, for example, you want the code to decrease `DTSUB` by a factor of 10, then set **SUBX** $= 1$. If you want the subcycle size `DTSUB` to altered by a factor "x", then set **SUBX** to the base ten log of "x" [That is, **SUBX**=$\log_{10} x = (\ln x)/(\ln 10)$].	1	page 138 page 147 Fig. 9.3

—	**PROP** (42) **(DEJAVU)**	Not truly a user input. This is set equal to 1.0 when the input parameters have been checked (and altered for self consistency) by Kayenta's internal data check routine. To bypass data check (which is not advisable), the user may set DEJAVU=1.0. Otherwise, this parameter should be left unspecified (i.e., defaulted to zero)	1	N/A
t^{fail}	**PROP** (43) **(FAIL0)** **TFAIL**	For option **SOFTENING**=1, t^{fail} is a material-specific (and scale-dependent) characteristic failure time. Loosely speaking, it represents the amount of time required for an element to lose half of its initial strength and stiffness. A proper implementation of Kayenta requires user specification of t^{fail} to be accompanied by a reference element size so that the host code can automatically adjust the value of **TFAIL** to be larger for larger elements and smaller for smaller elements. Syntax for specifying the scale will vary with host code. Rule of thumb: if the reference element is of width w and if the crack growth speed is c_{crack} (which is typically a fraction of the Rayleigh wave speed), then t^{fail} should be on the order of w/c_{crack}.	s	Eq. (5.4) Fig. 5.3
k	**PROP** (44) **(FAIL1)** **FSPEED**	For option **SOFTENING**=1, this parameter controls the rate at which damage proceeds. Large **FSPEED** (> 30) will result in a sudden loss of strength and stiffness, whereas small **FSPEED** (< 5) will produce a more gradual softening process. A microphysically based choice for 3-D problems would use a value of 3, but fitting to actual data usually gives better results when much larger values are used. To emulate the first Johnson-Holmquist damage model (JH1), use a large value. Smaller values emulate the JH2 model.	1	Eq. (5.4) Fig. 5.3
—	**PROP** (45) **(FAIL2)**	Depending on **SOFTENING**: SOFTENING = 3, value of the constant equivalent strain to fracture. SOFTENING = 4, parameter D1 from the Johnson-Cook fracture model. SOFTENING = 5, parameter C1 from the Xue-Weirzbicki fracture model.	1	Eq. (5.7) Eq. (5.8) Eq. (5.10)

—	**PROP** (46) **(FAIL3)**	Depending on **SOFTENING**: SOFTENING = 4, parameter D2 from Johnson-Cook Fracture. SOFTENING = 5, parameter C2 from Xue-Weirzbicki Fracture	1	Eq. (5.8) Eq. (5.10)
—	**PROP** (47) **(FAIL4)**	Depending on **SOFTENING**: SOFTENING = 4, parameter D3 from Johnson-Cook Fracture. SOFTENING = 5, parameter C3 from Xue-Weirzbicki Fracture.	1	Eq. (5.8) Eq. (5.10)
—	**PROP** (48) **(FAIL5)**	Depending on **SOFTENING**: SOFTENING = 4, D4 from Johnson-Cook Fracture. SOFTENING = 5, C4 from Xue-Weirzbicki Fracture.	1	Eq. (5.8) Eq. (5.10)
—	**PROP** (49) **(FAIL6)**	Depending on **SOFTENING**: SOFTENING = 4, D5 from Johnson-Cook Fracture. SOFTENING = 5, N from Xue-Weirzbicki Fracture.	1	Eq. (5.8) Eq. (5.10)
—	**PROP** (50) **(FAIL7)**	Depending on **SOFTENING**: SOFTENING = 4, Reference strain rate $\dot{\varepsilon}_0$ from Johnson-Cook Fracture. SOFTENING = 5, Toggle cutoff from Xue-Weirzbicki Fracture. A nonzero value disables the fracture cutoff.	1	Eq. (5.8) Eq. (5.10)
—	**PROP** (51) **(FAIL8)**	Depending on **SOFTENING**: SOFTENING = 4, Melt temperature from Johnson-Cook Fracture.	1	Eq. (5.8)
—	**PROP** (52) **(FAIL9)**	Depending on **SOFTENING**: SOFTENING = 4, Room temperature from Johnson-Cook Fracture.	1	Eq. (5.8)
$(I_1^{\text{peak}})^{\text{I}}$	**PROP** (53) **(PEAKI1I)**	Theoretical initial tensile limit of I_1 for intact material.	Pa	Eq. (5.1b)
$(\tau_Y)^{\text{I}}$	**PROP** (54) **(STRENI)**	Initial high-pressure strength intercept for intact material.	Pa	Eq. (5.1c)

$(s_F)^{\mathrm{I}}$	**PROP** (55) **(FSLOPEI)**	Failed high-pressure strength intercept.	Pa	Eq. (5.1a)
$(I_1^{\mathrm{peak}})^{\mathrm{F}}$	**PROP** (56) **(PEAKI1F)**	Theoretical failed tensile limit of I_1. If unspecified, defaults to zero (i.e., failed material has no tensile strength).	Pa	Eq. (5.1b)
$(\tau_Y)^{\mathrm{F}}$	**PROP** (57) **(STRENF)**	Failed high-pressure strength intercept.	Pa	Eq. (5.1c)
—	**PROP** (58) **(SOFTENING)**	If zero, then the limit surface is treated as a non-hardening yield surface. If **SOFTENING** is a nonzero integer, then material softening (loss of strength and stiffness) is applied. The **SOFTENING** parameter specifies the approach to be used for softening. These options are: 1 = time-to-failure. 2 = {reserved for developers} 3 = constant equivalent strain to failure. 4 = Johnson-Cook failure. 5 = Xue-Wierzbicki failure.	1	page 67
$(s_F)^{\mathrm{F}}$	**PROP** (59) **(FSLOPEF)**	Initial slope of the *failed* TXC limit surface. If unspecified, defaults to a value appropriate to sand.	Pa	Eq. (5.1a)
—	**PROP** (60) **(FAILSTAT)**	FAILSTAT is a control parameter available for verification testing. Setting it equal to 1.0 will stop the code at the *onset* of material failure when softening is enabled. Noting the stress state at this stopping point allows generating failure statistics that can be compared with the failure statistics specified in user input. If it is set to -1, the code will generate a so-called barf file with the information pertaining to the material state at the first instance of material failure. (See page 143 for information on barf files.)	1	N/A

—	PROP (61) (IEOSID)	Equation of state ID. Set to 0 (default) for standard Kayenta bulk and and shear moduli functions, 1 for the bulk modulus to be updated by the Mie Gruüneisen equation of state, and 3 for the bulk modulus to be updated by an equation of state supplied by the host code. See host code developers about functionality. Other values of EOSID are used to enable the calculation of the elastic bulk and shear moduli using equations of state that are currently under development. See the Kayenta developers for the current state of these newer equations of state	1	page 116
	PROP (62) (EVLEOS)		1	N/A
	PROP (63) (DILATIM)	Limit on plastic dilatation. When set, the maximum value of plastic dilatation As this value of plastic dilatation is reached, plastic flow becomes more deviatoric to retard further accumulation of plastic dilatation.	1	N/A
ν	PROP (64) (NU) POISSON	Poisson's ratio. Only meaningful if EOSID is 1 or 3. When specified, the elastic shear modulus is computed from the equation of state response for the bulk modulus and Poisson's ratio (using the assumption of isotropy of the elastic stiffness). If instead the shear modulus is given, Poisson's ratio is computed at startup from the equation of state computed bulk modulus and shear modulus at initialization. Poisson's ratio is presumed to remain constant throughout the remainder of the simulation and is used to compute an updated shear modulus from the equation of state bulk modulus.	1	N/A
$(s_Y)^{\mathrm{I}}$	PROP (65) (YSLOPEI)	High-pressure slope of the initial limit surface.	Pa	Eq. (5.1d)
$(s_Y)^{\mathrm{F}}$	PROP (66) (YSLOPEF)	High-pressure slope of the failed limit surface. If unspecified, defaults to 0.0.	Pa	Eq. (5.1d) Fig. 5.2

—	**PROP** (67) **(SPALLI1)**	The value of I_1 beyond which the stress state will never be allowed. This differes from PEAKI1 in that Kayenta computes the amount of strain corresponding to stress increments beyond this value, and then Kayenta sends a request for the host code to insert void or to invoke any other similar control of tensile deformation control.	Pa	Eq. (5.12)
—	**PROP** (68) **(FREE08)**	Not used — control for research testing of new code.		N/A
—	**PROP** (69) **(FREE07)**	Not used — control for research testing of new code.		N/A
—	**PROP** (70) **(FREE06)**	Not used — control for research testing of new code.		
—	**PROP** (71) **(FREE05)**	Not used — control for research testing of new code.		
—	**PROP** (72) **(FREE04)**	Not used — control for research testing of new code.		
—	**PROP** (73) **(FREE03)**	Not used — control for research testing of new code.		
—	**PROP** (74) **(FREE02)**	Not used — control for research testing of new code.		
—	**PROP** (75) **(FREE01)**	Not used — control for research testing of new code.		

If Kayenta is compiled to include theory for joints, additional user inputs are required, as listed here. Documentation of joints is available only in relatively obscure conference proceeding (See Ref. [20], available upon request). Each of the following input keywords is appended with **01**, **02**, or **03** to indicate the joint normal direction. For example, SPACE02 is the spacing of joints whose normal points in the 2-direction. For orthotropic joints, the three directions are aligned with the coordinate directions used by the host code. To specify any other orientations and/or to model non-orthotropic joint sets, see the next table of this Appendix.

Symbol	ASCII Name	Name and meaning	SI Unit	Defining Equation
	PROP (--) (CKN)	Initial joint normal stiffness.	$\mathrm{Pa\,m^{-1}}$	cf. [20]
	PROP (--) (VMAX)	Maximum joint closure.	m	cf. [20]
	PROP (--) (SPACE)	Joint spacing.	m	cf. [20]
	PROP (--) (SHRSTIFF)	Initial shear stiffness.	$\mathrm{Pa\,m^{-1}}$	cf. [20]

B.1.1 Other input parameters (available only in special builds)

When Kayenta is compiled with -D KMM_ANISOTROPIC to include up to four arbitrarily oriented joint sets, the relevant user parameters are the same as those listed above for orthotropic joints plus two inputs for specifying joint orientation:

Symbol	ASCII Name	Name and meaning	SI Unit	Defining Equation
	PROP(--) **(STRIKE)**	Initial Joint strike angle.	rad	cf. [20]
	PROP(--) **(DIP)**	Initial Joint dip angle.	rad	cf. [20]

With the generally anisotropic option, all joint parameter keywords are appended with **1**, **2**, **3**, or **4** to indicate the joint ID number. For example, **SPACE2** is the spacing of joints in the second joint set.

Kayenta has the option of using a true equation of state to compute elastic moduli, requiring additional EOS input parameters as given in the table below:

Symbol	ASCII Name	Name and meaning	SI Unit	Defining Equation
	PROP(--) (TMPRXP)	Homologous temperature exponent, used to control rate of thermal softening. Thermal softening is a feature that is not available in the current public release of Kayenta.	1	Eq. (5.8)
T_{melt}	PROP(--) (TMPRM0) TMELT0	Initial melt temperature used in thermal softening model. Thermal softening is a feature that is not available in the current public release of Kayenta.	K	Eq. (5.8)
ρ_0	PROP(--) (RHO0)	Initial density. Used only if EOSID is 1 or 3	$\text{kg}\,\text{m}^{-3}$	Eq. (6.4)
	PROP(--) (TMPR0)	Initial temperature. Used only if EOSID is 1 or 3	K	
c_s	PROP(--) (SNDSP0)	Initial sound speed	$\text{m}\,\text{s}^{-1}$	Eq. (6.8)
c_v	PROP(--) (CV)	Specific heat at constant volume (required input)	$\text{J}\,\text{kg}^{-1}\,\text{K}^{-1}$	Eq. (6.7)
γ	PROP(--) (GRPAR)	Grüneisen parameter	1	page 114 Eq. (6.12) Eq. (6.13) Eq. (6.22)
s_1	PROP(--) (S1)	Linear US-UP coefficient Used only if EOSID is 1 or 3	1	page 115 Eq. (6.8)
	PROP(--) (EOS01)	Derived EOS parameter, set by the EOS at startup. Used only if EOSID is 1 or 3		
	PROP(--) (EOS02)	Derived EOS parameter, set by the EOS at startup. Used only if EOSID is 1 or 3		
	PROP(--) (EOS03)	Derived EOS parameter, set by the EOS at startup. Used only if EOSID is 1 or 3		

	PROP(--) (EOS04)	Derived EOS parameter, set by the EOS at startup. Used only if EOSID is 1 or 3		
	PROP(--) (EOS05)	Derived EOS parameter, set by the EOS at startup. Used only if EOSID is 1 or 3		
	PROP(--) (EOS06)	Derived EOS parameter, set by the EOS at startup. Used only if EOSID is 1 or 3		
s_2	PROP(--) (EOS07)	Derived EOS parameter, set by the EOS at startup. Used only if EOSID is 1 or 3		page 115 Eq. (6.8)
	PROP(--) (EOS08)	Derived EOS parameter, set by the EOS at startup. Used only if EOSID is 1 or 3		
	PROP(--) (EOS09)	Derived EOS parameter, set by the EOS at startup. Used only if EOSID is 1 or 3		
	PROP(--) (EOS10)	Derived EOS parameter, set by the EOS at startup. Used only if EOSID is 1 or 3	1	
	PROP(--) (EOS11)	Derived EOS parameter, set by the EOS at startup. Used only if EOSID is 1 or 3		
	PROP(--) (EOS12)	Derived EOS parameter, set by the EOS at startup. Used only if EOSID is 1 or 3		

B.2 Internal State Variables (Plottable Output)

Symbol	ASCII Name	Name and meaning	SI Unit	Defining Equation
κ	**SV(1)** **(KAPPA)** **ELN** **EL**	The value of I_1 at which the meridional yield profile first branches away from the crack failure surface and begins to morph into the cap function associated with porosity. Recalling that $\overline{\kappa} = \kappa$, the internal state variable κ typically will be negative. As a rule of thumb: increasing the user-input parameter R will increase κ (and therefore decrease $\overline{\kappa}$). Recalling Fig. 4.16, κ is *not* the point at which the meridional profile has a zero slope — it is the *branching* location. The zero slope point is reached at a higher pressure. Isotropic hardening is controlled by the evolution of κ. In Kayenta physics source code, κ is denoted by **ELN** or by **EL** in the subcycling. Note: future builds of Kayenta are anticipated to replace the **KAPPA** output variable with the $\overline{X}$ variable in Fig. 4.5.	Pa	Eq. (4.30) Eq. (4.73) Fig. 4.5
—	**SV(2)** **(INDEX)**	Indicator for the nature of plastic loading (this output is used primarily by code developers for debugging)	1	page 136
$\dot{\varepsilon}^{\text{equiv}}$	**SV(3)** **(EQDOT)**	L_2 (Frobenius) norm of input strain rate tensor. $\dot{\varepsilon}^{\text{equiv}} = \sqrt{\dot{\varepsilon}_{ij}\dot{\varepsilon}_{ij}}$	s^{-1}	Section 8
I_1	**SV(4)** **(I1)**	First stress invariant (positive in tension).	Pa	Eq. (3.7a)
$\sqrt{J_2}$	**SV(5)** **(ROOTJ2)**	Square root of the second stress invariant $\sqrt{J_2}$ (always positive). This the equivalent shear stress in the material.	Pa	Eq. (3.7b) Eq. (3.9) page 136

α_{11}	**SV**(6) **(ALXX)**	11 component of the backstress	Pa	page 91 page 78
α_{22}	**SV**(7) **(ALYY)**	22 component of the backstress	Pa	page 91 page 78
α_{33}	**SV**(8) **(ALZZ)**	33 component of the backstress	Pa	page 91 page 78
α_{12}	**SV**(9) **(ALXY)**	12 component of the backstress (= 21 component)	Pa	page 91 page 78
α_{23}	**SV**(10) **(ALYZ)**	23 component of the backstress (= 32 component)	Pa	page 91 page 78
α_{31}	**SV**(11) **(ALXZ)**	31 component of the backstress (= 13 component)	Pa	page 91 page 78
G^{α}	**SV**(12) **(GFUN)**	Kinematic hardening decay function, equal to 1.0 initially and then decays down to 0.0 as the max allowable kinematic hardening (determined by the shift parameter) is approached.	1	Eq. (4.82) page 91
γ^p_{equiv}	**SV**(13) **(EQPS)** **EQP**	Equivalent uniaxial plastic shear strain (conjugate to $\sqrt{J_2}$). Specifically, $\gamma^p_{\text{equiv}} = \int \sqrt{2}\|\dot{\underset{\approx}{\gamma}}^p\|\mathrm{d}t$, where $\dot{\underset{\approx}{\gamma}}^p$ is the deviatoric part of the plastic strain rate $\dot{\underset{\approx}{\varepsilon}}^p$.	1	Eq. (4.35)
ε^p_v	**SV**(14) **(EQPV)**	Equivalent plastic volume strain: $\varepsilon^p_v = \int \mathrm{tr}\,\dot{\underset{\approx}{\varepsilon}}^p \mathrm{d}t$.	1	Section 8

κ_0	**SV(15)** **(EL0)**	Legacy output, not of interest to users equal to the calculated initial value for κ (the cap branch value of I_1). This is not really an internal state variable. It was originally introduced to prevent the cap from contracting past its initial value in response to pore expansion. Such behavior is now allowed but potentially unstable. Its value will remain constant throughout the calculation. Keep in mind: $\overline{\kappa}$ is typically positive and therefore $\kappa \equiv -\overline{\kappa}$ is typically negative. This output variable will be unused in future builds of Kayenta that replace the **KAPPA** state variable with the $\overline{X}$ variable in Fig. 4.5.	Pa	Fig. 4.16
h^*_κ	**SV(16)** **(HK)**	(Isotropic hardening parameter) Proportionality factor appearing in the relationship $\dot{\kappa} = \dot{\lambda}^* h^*_\kappa$.		Eq. (4.76)
ε_v^{tot}	**SV(17)** **(EVOL)**	Total volume strain, $\int \mathrm{tr}\, \dot{\underset{\approx}{\varepsilon}}\, \mathrm{d}t$.	1	page 136
$\sqrt{J_2^\alpha}$	**SV(18)** **(BACKRN)**	Square root of the second backstress invariant. This is like the equivalent shear stress, except applied to the backstress. The value of **BACKRN** is not permitted to exceed the user specified limit value of N	Pa	Eq. (4.82)

—	SV(19) (CRACK)	Flag indicating that the material has reached a stress at which softening (loss of load-carrying capability) *should* engage. CRACK is zero in non-softening regions. It equals 1.0 if a tensile cut-off (CUTI1 or CUTPS) has been reached. It equals 2.0 if the limit surface has been reached (i.e., when no further kinematic hardening can occur). If CRACK is nonzero, Kayenta has reached the limit of its applicability and all subsequent Kayenta predictions might be nonphysical. When CRACK becomes nonzero, Kayenta continues to run by holding the stress at its limit state rather than allowing the stress to drop as it should (i.e., Kayenta runs like a classical plasticity model after CRACK becomes nonzero). Kayenta never actually softens because doing so would result in mesh-dependent solutions without host-code intervention. For these types of problems, a more advanced beta version of Kayenta should be requested.	1	page 136
—	SV(20) (SHEAR)	Flag equal to 0.0 if the material response is elastic. Otherwise, if positive, the response is plastic. The value ranges from 0.0 if the trial stress rate is tangent to the yield surface to 1.0 if the trial stress rate is normal to the yield surface (i.e., pushing directly against it).	1	Fig. 8.1 page 136
f	SV(21) (YIELD) F	Value of the yield function.	Pa^2	Eq. (4.42)
$\overline{\theta}$	SV(22) (LODE)	Lode angle in degrees ranging from -30 in triaxial extension to $+30$ in triaxial compression. The Lode angle is frequently denoted β in other publications about Kayenta.	deg	Eq. (3.34) page 136
σ_{11}^L	SV(23) (QSSIGXX)	Internal Kayenta variable (quasistatic "low" stress)	Pa	Eq. (7.10)
σ_{22}^L	SV(24) (QSSIGYY)	Internal Kayenta variable (quasistatic "low" stress)	Pa	Eq. (7.10)

σ_{33}^L	**SV**(25) **(QSSIGZZ)**	Internal Kayenta variable (quasistatic "low" stress)	Pa	Eq. (7.10)
σ_{12}^L	**SV**(26) **(QSSIGXY)**	Internal Kayenta variable (quasistatic "low" stress)	Pa	Eq. (7.10)
σ_{23}^L	**SV**(27) **(QSSIGYZ)**	Internal Kayenta variable (quasistatic "low" stress)	Pa	Eq. (7.10)
σ_{31}^L	**SV**(28) **(QSSIGZX)**	Internal Kayenta variable (quasistatic "low" stress)	Pa	Eq. (7.10)
$\dot{\lambda}^*$	**SV**(29) **(DCSP)**	Plastic consistency parameter, equal to the magnitude of the plastic strain rate. This interpretation applies because Kayenta uses a *normalized* flow direction and a *unit* normal to the yield surface.	1/s	Eq. (4.51) Eq. (4.86)
κ_L	**SV**(30) **(QSEL)**	Internal Kayenta variable (quasistatic "low" value of κ). In Eq. (7.15), q^L stands for any internal state variable. This is the particular instance for which $q^L = \kappa_L$, which is the quasistatic value of the isotropic hardening ISV.	Pa	Eq. (7.15)
α_{11}^L	**SV**(31) **(QSBSXX)**	Quasistatic backstress. In Eq. (7.15), q^L stands for α_{ij}^L.	Pa	Eq. (7.15)
α_{22}^L	**SV**(32) **(QSBSYY)**	Quasistatic backstress. In Eq. (7.15), q^L stands for α_{ij}^L.	Pa	Eq. (7.15)
α_{33}^L	**SV**(33) **(QSBSZZ)**	Quasistatic backstress. In Eq. (7.15), q^L stands for α_{ij}^L.	Pa	Eq. (7.15)

α^L_{12}	**SV** (34) **(QSBSXY)**	Quasistatic backstress. In Eq. (7.15), q^L stands for α^L_{ij}.	Pa	Eq. (7.15)
α^L_{23}	**SV** (35) **(QSBSYZ)**	Quasistatic backstress. In Eq. (7.15), q^L stands for α^L_{ij}.	Pa	Eq. (7.15)
α^L_{31}	**SV** (36) **(QSBSZX)**	Quasistatic backstress. In Eq. (7.15), q^L stands for α^L_{ij}.	Pa	Eq. (7.15)
t^{grow}	**SV** (37) **(TGROW)**	Total time during which the material has been undergoing progressive damage. This output may be regarded as an "age of damage". As such, a color plot of this variable will reveal not only damaged material, but it also suggests the failure sequence.	s	Fig. 5.3
$1-D$	**SV** (38) **(COHER)**	$Coherence = 1 - damage$ The value ranges from 1 for an intact material to 0 for fully failed material.	1	Eq. (5.1b) Fig. 5.3
	SV (39) **(TMPR)**	Temperature	K	
	SV (40) **(TMPRM)**	Temperature	K	
	SV (41) **(SNDSP)**	Speed of sound	$\mathrm{m\,s^{-1}}$	
	SV (42) **(RHO)**	Density	$\mathrm{kg/m^3}$	

	SV(43) **(ENRGY)**	Energy	J/kg	
	SV(44) **(ALPHAMG)**	Free variable for EOS ISV		
	SV(45) **(EOS1)**	Free variable for EOS ISV		
	SV(46) **(EOS2)**	Free variable for EOS ISV		
	SV(47) **(EOS3)**	Free variable for EOS ISV		
	SV(48) **(EOS4)**	Free variable for EOS ISV		
	SV(49) **(RTJ2IN)**	$\sqrt{J_2}$ invariant of the plastic stress state		
$\varepsilon^{\text{eqdot}}$	**SV**(50) **(ACCSTRAIN)**	Accumulated equivalent softening strain. Accumulated only when softening is active and the stress state is on the yield surface. $$\varepsilon^{\text{eqdot}} = \varepsilon^{\text{eqdot}} + \dot{\varepsilon}^{\text{equiv}} * dt$$.	1	

B.2.1 Other plottable parameters (available only in special builds)

The following variables are available if Kayenta is compiled with special compile options.

Symbol	ASCII Name	Name and meaning	SI Unit	Defining Equation
	(TGROWCTPS)	Just like **TGROW** but controls the contraction of the limit surface along the hydrostatic axis.		
	(COHERCTPS)	Just like **COHER** but controls the contraction of the limit surface along the hydrostatic axis.		
	(JNTOPN1)	Joint Opening for the first joint set.	m	cf. [20]
	(JNTOPN2)	Joint Opening for the second joint set.	m	cf. [20]
	(JNTOPN3)	Joint Opening for the third joint set.	meter	cf. [20]
	(JNTOPN4)		meter	cf. [20]
	(SPALL1)			
	(ELNUM)	Element number flag used for model development host code debugging. If ELNUM is negative at initialization, Kayenta writes a MatModLab input file for deformation history of an element numbered ELNUM. Use of ELNUM is currently only supported in the Alegra host code.		

B.3 Other Symbols (used only in this report)

Symbols are listed here only if they appear in multiple locations throughout this User's Guide (or if they are local variables specifically used in the source code).

Symbol	ASCII Name	Name and meaning	SI Unit	Defining Equation
C_{ijkl}		Fourth-order elastic stiffness tensor	Pa	Eq. (4.4)
δ_{ij}	**DELTA**	Kronecker delta	1	
$\Delta\gamma^p_{ij}$	**DEIJPL**	Deviatoric plastic strain increment defined as $\Delta\gamma^p_{ij} = \left(\dot{\varepsilon}^p_{ij} - \frac{1}{3}\dot{\varepsilon}_{kk}\delta_{ij}\right)\Delta t$	1	
$\Delta\varepsilon^p_v$	**VOLPLAS**	Plastic volume strain increment $= \dot{\varepsilon}^p_{kk}\Delta t$	1	
	DFDSIG	Derivative of the plastic potential with respect to stress	—	
t		time	sec	
Δt	**DT**	time increment	sec	
E		Young's modulus	Pa	Eq. (4.12)
f_f		The part of the meridional yield profile function associated with microcracks: $f_f = F_f - N$	Pa	Eq. (4.29) Fig. 4.6
F_f	**FF**	Meridional shear limiter function	Pa	Eq. (4.39)
f_c		The part of the meridional yield profile function associated with porosity: $f_c = \sqrt{F_c}$	1	Eq. (4.29) Fig. 4.5

F_c	**FC**	Meridional nominal yield function (Pelessone function)	1	Eq. (4.32) Eq. (4.30)
ϕ	**PHI**	Friction angle (for Mohr-Coulomb theory)	1	Eq. (B.3)
g	**G**	Flow potential function	Pa^2	Eq. (4.51)
Γ	**GAMMAP**	Octahedral yield shape function (depends on **J3TYPE**)	1	page 70
$H_{ij}^{\alpha}, \underset{\approx}{\mathbf{H}}_{\alpha}$		Kinematic hardening modulus tensor	Pa	Eq. (4.81)
HYD		Acronym: Hydrostatic loading. The stress is diagonal (no shears).		page 35
I_1	**RI1**	First stress invariant, $I_1 = \mathrm{tr}\,\underset{\approx}{\sigma}$. This is positive in tension.	Pa	Eq. (3.7a)
$\overline{I_1}$		Negative of $\overline{I_1}$. This is positive in compression	Pa	Eq. (3.7a)
J_2	**RJ2**	Second stress invariant, $J_2 = \frac{1}{2}\mathrm{tr}\underset{\approx}{\mathbf{S}}^2$ (never negative). Geometrically, $\sqrt{2J_2}$ equals the magnitude of the stress deviator, and it therefore equals the "length" of the projection of the pseudo stress vector in 3D Haigh-Westergaard (stress) space onto the octahedral-plane (i.e., $\sqrt{2J_2}$ is the Lode radius).	Pa^2	Eq. (3.7b)
J_2^{ξ}	**RELJ2ZP**	Second invariant of the shifted stress	Pa^2	Eq. (4.22) page 28
J_3	**RJ3**	Third stress invariant, $J_3 = \frac{1}{3}\mathrm{tr}\underset{\approx}{\mathbf{S}}^3$. This is positive when the stress deviator is closer to TXE than to TXC.	Pa^3	Eq. (3.7c)
$\overline{J_3}$		Negative of J_3. This is positive when the stress deviator is closer to TXC than to TXE.	Pa^3	Eq. (3.7c)
J_3^{ξ}	**RELJ3ZP**	Third invariant of the shifted stress	Pa^3	Eq. (4.22) page 28

k		This symbol is used in various contexts, so its intended meaning should be taken to be local to whatever chapter it appears in.	—	(various)
ν	**RNU**	Poisson's ratio	1	Eq. (4.12)
p		Mean stress, $p = \frac{1}{3}\operatorname{tr}\underset{\approx}{\sigma} = \frac{I_1}{3}$. The mean stress is positive in compression. The *pressure* $\overline{p}$, which is positive in compression is the negative of the mean stress: $\overline{p} = -\overline{p}$.	Pa	
$\overline{p}$		Pressure = negative of mean stress, $\overline{p} = -\frac{1}{3}\operatorname{tr}\underset{\approx}{\sigma} = \frac{\overline{I_1}}{3}$	Pa	Eq. (3.8) page 33
Π		Porosity (unloaded).	1	Eq. (4.67)
	PONE	Code parameter equal to 1.0	1	
	PTWO	Code parameter equal to 2.0	1	
	PFOUR	Code parameter equal to 4.0	1	
$\underset{\approx}{\mathbf{R}}$		Polar rotation tensor	1	Eq. (3.33) Eq. (4.3)
ρ		Mass density	kg/m^3	
$\underset{\approx}{\mathbf{S}}$		Stress deviator, $\underset{\approx}{\mathbf{S}} = \underset{\approx}{\sigma} - \frac{1}{3}(\operatorname{tr}\underset{\approx}{\sigma})\underset{\approx}{\mathbf{I}}$	Pa	Eq. (3.5)
$\underset{\approx}{\sigma}$		The stress tensor.	Pa	Eq. (3.1)
SHR		Acronym: Shear loading (one principal value of the stress deviator is zero and the others are therefore negatives of each other). SHR applies even when all principal stresses are compressive — all that matters is the nature of the stress deviator.	N/A	page 42

TXE		Acronym: Triaxial extension: Two "lateral" principal stresses are equal and the distinct eigenvalue is more tensile than the lateral stresses. A stress state can be in TXE even when all principal stresses are compressive — the axial stress merely needs to be *less* compressive than the lateral stresses.	N/A	page 37
TXC		Acronym: Triaxial compression (two "lateral" principal stresses are equal and the distinct eigenvalue is more compressive than the lateral stresses)	N/A	page 37
$\underset{\approx}{\mathbf{T}}$		The Hill tensor, defined to be the deviatoric part of $\underset{\approx}{\mathbf{S}}^2$ and therefore given by $\underset{\approx}{\mathbf{T}} = \underset{\approx}{\mathbf{S}}^2 - \frac{2}{3}J_2\underset{\approx}{\mathbf{I}}$	Pa	
T_{ijkl}		Plastic tangent stiffness tensor	Pa	Eq. (4.101)
τ		Signed equivalent shear stress, $\tau = \text{sgn}\left[\sqrt{J_2}, J_3\right]$. This equals $\pm\sqrt{J_2}$. It is positive when $J_3 \geq 0$, and negative when $J_3 \leq 0$.	Pa	Eq. (3.9)
$\overline{\tau}$		Negative of τ. This is positive when the stress is closer to TXC, and negative when closer to TXE	Pa	Eq. (3.4)
τ	**TAU**	Characteristic material response time	sec	Eq. (7.4)
$\overline{\theta}^{\xi}$	**RLODE**	Lode angle associated with the shifted stress tensor $\underset{\approx}{\xi} = \underset{\approx}{\sigma} - \underset{\approx}{\alpha}$ ($\overline{\theta}^{\xi} = 30^\circ$ when $\underset{\approx}{\alpha}$ is TXC and $\overline{\theta}^{\xi} = +30^\circ$ when $\underset{\approx}{\xi}$ is TXE). When this variable is requested as output, its value is given in degrees (not radians).	rad	Eq. (3.34)
$\sin 3\overline{\theta}^{\xi}$	**SIN3BTAP**	Sine of three times the Lode angle $\overline{\theta}^{\xi}$.	1	Eq. (3.34)
$\underset{\approx}{\xi}$	**ZETA**	Shifted stress tensor, $\underset{\approx}{\xi} = \underset{\approx}{\sigma} - \underset{\approx}{\alpha}$. When kinematic hardening is activated, the yield surface origin will be at $\underset{\approx}{\xi} = \underset{\approx}{\mathbf{0}}$ instead of at the zero stress origin. The backstress tensor $\underset{\approx}{\alpha}$ represents the amount by which the origin has translated.	Pa	page 91
f_K	**FK**	Bulk modulus reduction factor for ubiquitous jointing.	1	Eq. (4.33)

f_G	`FG`	Shear modulus reduction factor for ubiquitous jointing.	1	Eq. (4.34)
$\underset{\approx}{\mathbf{N}}$		Yield surface unit normal, equal to the gradient of the yield function divided by its own magnitude.	1	Eq. (4.52)
$\underset{\approx}{\mathbf{M}}$		Flow surface unit normal, equal to the gradient of the flow function divided by its own magnitude.	1	Eq. (4.53)
$\mathscr{F}$		Magnitude of the derivative of the yield function w.r.t. stress. This scalar can have ambiguous units because yield functions themselves are ambiguous [12]; the units here correspond to the yield function used in Kayenta.	Pa	Eq. (4.52)
$\mathscr{G}$		Magnitude of the derivative of the flow function w.r.t. stress.	Pa	Eq. (4.53)

B.4 Datasets

This section cites parameters for some materials that have already been fit to Kayenta. Datasets undergo continual refinement as additional material data become available, so consult the model developers to obtain the latest values. This section concludes with simplified datasets for mimicking simpler classical theories (von Mises plasticity, Mohr-Coulomb theory, etc.)

B.4.1 Dataset for Salem Limestone

```
$
$ Kayenta parameters for Sidewinder Tuff
$ Units are SI
  B0 = 4.0e9       $Pa
  B1 = 6.5e9       $Pa
  B2 = 0.1e9       $Pa
  G0 = 3.69e9      $Pa
  A1 = 496.83e6    $Pa
  A2 = 6.293e-10   $1/Pa
  A3 = 481.08e6    $Pa
  A4 = 1.e-10      $Dimensionless
  P0 = -70.e6      $Pa
  P1 = 1.8e-11     $1/Pa
  P2 = 2.15e-19    $1/Pa^2
  P3 = 0.08        $strain
  CR = 15.0        $Dimensionless
  RK = 0.7         $Dimensionless
  CUTI1 = 3.e6     $Pa
  CUTPS = 1.e6     $Pa
  J3TYPE = 3       $Dimensionless
```

This list presumes that your implementation of Kayenta sets defaults for unlisted parameters.

B.4.2 Dataset for Sidewinder Tuff

```
$
$ Kayenta parameters for Sidewinder Tuff
$ Units are SI
  B0 = 4.0e9       $Pa
  B1 = 6.5e9       $Pa
  B2 = 0.1e9       $Pa
  G0 = 3.69e9      $Pa
  A1 = 496.83e6    $Pa
  A2 = 6.293e-10   $1/Pa
  A3 = 481.08e6    $Pa
  A4 = 1.e-10      $Dimensionless
  P0 = -70.e6      $Pa
  P1 = 1.8e-11     $1/Pa
  P2 = 2.15e-19    $1/Pa^2
  P3 = 0.08        $strain
  CR = 15.0        $Dimensionless
  RK = 0.7         $Dimensionless
  CUTI1 = 3.e6     $Pa
  CUTPS = 1.e6     $Pa
  J3TYPE = 3       $Dimensionless
```

This list presumes that your implementation of Kayenta sets defaults for unlisted parameters.

B.4.3 Dataset for lab scale intact Climax Granite

```
$
$ Kayenta parameters for Lab-scale Intact Climax Granite
$
  B0 = 43.00e9   $Pa
  B1 = 750.0e9   $Pa
  B2 = 100.0e9   $Pa
  G0 = 34.73e9   $Pa
  A1 = 1355.e6   $Pa
  A2 = 3.43e-10  $1/Pa
  A3 = 1328.e6   $Pa
  A4 = 3.82e-2   $Dimensionless
  P0 = -556.e6   $Pa
  P1 = 9.e-14    $1/Pa
  P2 = 0.        $1/Pa^2
  P3 = 0.05      $strain
  CR = 227.5     $Dimensionless
  RK = 0.72      $Dimensionless
  RN = 17.0e6    $Pa
  HC = 150000.e6 $Pa
  CUTI1 = 30.e6  $Pa
  CUTPS = 10.e6  $Pa
  J3TYPE = 3     $dimensionless
```

This list presumes that your implementation of Kayenta sets defaults for unlisted parameters.

B.4.4 Dataset for field scale jointed Climax Granite

```
$
$ Kayenta parameters for field-scale JOINTED Climax Granite
$
  B0 = 43.00e9   $Pa
  B1 = 750.0e9   $Pa
  B2 = 100.0e9   $Pa
  G0 = 34.73e9   $Pa
  RJS = 0.06     $Meters (Joint spacing)
  RKS = 8.0e10   $Pa/Meter (Joint shear stiffness)
  RKN = 1.6e11   $Pa/Meter
  A1 = 1379.e6   $Pa
  A2 = 6.51e-11  $1/Pa
  A3 = 1328.e6   $Pa
  P0 = -556.e6   $Pa
  P1 = 9.e-14    $1/Pa
  P2 = 0.        $1/Pa^2
  P3 = 0.05      $strain
  CR = 227.5     $Dimensionless
  RK = 0.80      $Dimensionless
  RN = 17.0e6    $Pa
  HC = 150000.e6 $Pa
  CUTI1 = 30.e6  $Pa
  CUTPS = 10.e6  $Pa
  J3TYPE = 3     $dimensionless
```

This list presumes that your implementation of Kayenta sets defaults for unlisted parameters.

B.4.5 Dataset for 23MPa Concrete

The following values are taken primarily from [94]. In that publication, the symbols b_0, b_1, etc. are used for what we denote G_0, G_1, etc. The a parameters in that publication are denoted as B parameters in this User's Guide.

```
B0 = 5.5e9            $Pa
B1 = 28.78e9          $Pa
B2 = 0.623e9          $Pa
G0 = 1.9026e9         $Pa
G1 = 0.890513         $Dimensionless
G2 = 3.55e-9          $1/Pa
A1 = 1255.7e6         $Pa
A2 = 1.93e-10         $1/Pa
A3 = 1248.2e6         $Pa
P0 = -1.067e8         $Pa
P1 = 7.66e-10         $1/Pa
P2 = 3.88e-20         $1/Pa^2
P3 = 0.1538           $Dimensionless(strain)
CR = 10.0             $Dimensionless
RK = -1.              $Dimensionless
RN = 3.0e6            $Pa
HC = 1.0e11           $Pa
CUTI1 = 3e6           $Pa
CUTPS = 1.e6          $Pa
J3TYPE=2
```

This list presumes that your implementation of Kayenta sets defaults for unlisted parameters.

B.4.6 Dataset for Conventional Strength Portland Concrete

```
B0 = 1.0954e10        $Pa
G0 = 7.5434e9         $Pa
A1 = 4.26455e8        $Pa
A2 = 7.51e-10         $1/Pa
A3 = 4.19116e8        $Pa
A4 = 1.0e-10          $Dimensionless
P0 = -1.95520e8       $Pa
P1 = 1.2354e-9        $1/Pa
P3 = 0.065714         $Dimensionless(strain)
CR = 12.0             $Dimensionless
RK = -1.              $Dimensionless
CUTI1 = 3.0e6         $Pa
CUTPS = 1.0e6         $Pa
J3TYPE=2
```

This list presumes that your implementation of Kayenta sets defaults for unlisted parameters.

B.4.7 PARTIAL Dataset for Johnson-Cook verification tests

```
$
$ JC parameters taken from Johnson1985 for steel 4340
$ This input showcases von Mises plasticity with
$ Johnson-Cook fracture.

  B0 = 159.0e9        $Pa
  G0 = 77.0e9         $Pa
  P0 = -1.0e+99       $Pa
  CR = 0.001          $Dimensionless
  RK = 1.0            $Dimensionless
  RN = 0              $Pa
  HC = 0              $Pa
  CTI1 = 1.e99        $Pa
  CTPS = 1.e99        $Pa

  STRENI  =  792.0e6  $Pa
  YSLOPEI =  0.0      $Dimensionless
  PEAKI1I =  1.0e+99  $Pa
  FSLOPEI =  0.0      $Dimensionless

  $ Default behaves like a sand
  STRENF  = 0.0       $Pa
  YSLOPEF = 0.0       $Dimensionless
  PEAKI1F = 0.0       $Pa
  FSLOPEF = 0.0       $Dimensionless

  FAIL1 = 7.0         $Dimensionless

  FAIL2 =  0.05       $Dimensionless
  FAIL3 =  3.44       $Dimensionless
  FAIL4 = -2.12       $1/Pa
  FAIL5 =  0.002      $Dimensionless
  FAIL6 =  0.61       $1/Kelvin
  FAIL7 =  1.00       $1/Sec
  FAIL8 =  1793.0     $Kelvin
  FAIL9 =  298.0      $Kelvin

  SOFTENING = 4.0     $Dimensionless
  J3TYPE    = 1.0     $Dimensionless
```

This list presumes that your implementation of Kayenta sets defaults for unlisted parameters.

B.4.8 Datasets for mimicking classical (simplified) models

Kayenta is truly a unification of many simpler theories. By appropriately setting parameters, Kayenta can be made to exactly replicate results from simpler idealized theories, as illustrated below.

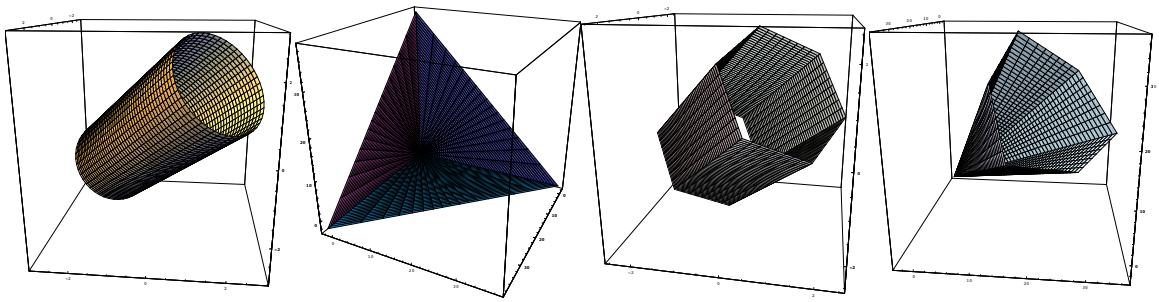

(a) Von Mises **(b)** Max stress **(c)** Max shear (Tresca) **(d)** Mohr-Coulomb

Figure B.1. Other yield surface shapes supported by Kayenta. The grid lines shown on these sketches correspond to lines of constant z and constant $\overline{\theta}$.

In most finite-element codes, you can modify an existing data set (e.g., one for a real material) by simply redefining a material parameter *in a separate input line*, leaving the original value unchanged. By deviating from a correct input set to a "toy" input set in this way (rather than over-writing preferred values), you can retain a record of what the material parameters *should be*, thereby mitigating unintentional dissemination of physically bad input sets.

The following specialized input sets use an "aprepro" syntax to show where you need to provide values. Specifically, all required or computed values appear in braces {}. Specify numerical values wherever "**VALUE**" appears, and then ensure all other values in braces are computed as shown (they can be computed by hand or piped into aprepro).

Von-Mises material

Von Mises theory can be duplicated by using the following simplified set of Kayenta input values:

```
$
$ Kayenta parameters for replicating non-hardening von Mises plasticity
$
  A1     = {yield_stress_in_shear = VALUE}
  B0     = {linear_elastic_bulk_modulus = VALUE}
  G0     = {linear_elastic_shear_modulus = VALUE}
```

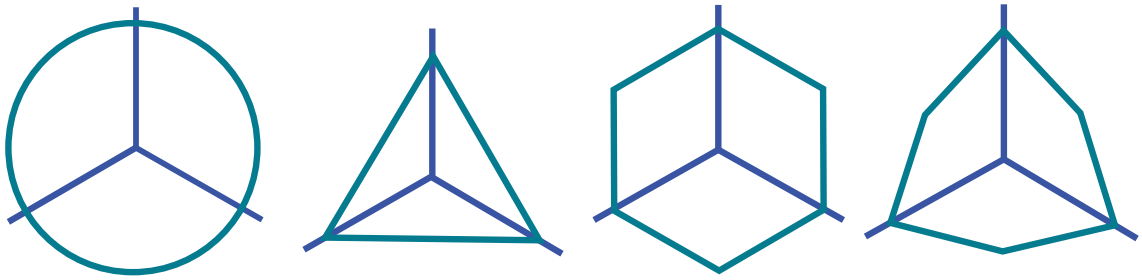

(a) Von Mises **(b)** Max stress **(c)** Max shear (Tresca) **(d)** Mohr-Coulomb

Figure B.2. Classical simplified octahedral profiles. None of these models adequately describes rock failure surfaces, but the failure surfaces for real rocks sometimes share some qualitative features with these models, depending on the level of confining pressure. In these figures, the axes represent projections of the compressive principal stress axes onto the octahedral plane, taking stress to be positive in *tension*. For the max stress and Mohr-Coulomb models, the size of the octahedral profile increases with pressure. For all of these models, the meridional profile is a straight line.

```
J3TYPE = 1      $Use Gudehaus, which is capable of a circular octhedral profile
RK     = 1      $Set TXE/TXC ratio = 1.0 to make a circlular octahedral profile
P0     = -1.e99 $make yield in hydrostatic compression impossible
CUTI1  = 1.e99  $set pressure cut-off to $infinityŤ
CUTPS  = 1.e99  $set principal stress cut-off to $infinityŤ
CR     = 0.001  $minimize the size of the curved part of the cap
```

This list presumes that your implementation of Kayenta sets defaults for unlisted parameters.

Maximum Principal Stress failure

The very simplistic fracture criterion that initiates failure when the largest principal stress reaches a critical value can be modeled in Kayenta by using the following parameter set:

```
$ Kayenta parameters for duplicating a maximum principal stress criterion
$
${max_allowed_principal_stress = VALUE}
B0 = {VALUE}    $bulk modulus
G0 = {VALUE}    $shear_modulus
P0 = -1.e99     $ turn off the cap function
J3TYPE=3
```

```
A1={SQRT(3)*max_allowed_principal_stress}
A4={1/SQRT(3.0)}
RK = 0.5
A4PF = {1/SQRT(3.0)}
RKPF = 0.5
```

This list presumes that your implementation of Kayenta sets defaults for unlisted parameters.

Tresca

The simplistic criterion that a material fails when its largest shear stress reaches a critical value can be modeled by using the following Kayenta parameters:

```
$ User must specify values in braces
$
  B0 = {bulk_modulus}
  G0 = {shear_modulus}
  P0 = -1.e99     $ turn off the cap function
  J3TYPE=3
  A1={2.0*yield_stress_in_shear/sqrt(3.0)}
  RK = 1.0
  RKPF = 1.0
```

This list presumes that your implementation of Kayenta sets defaults for unlisted parameters.

Mohr-Coulomb

Classical Mohr-Coulomb theory for brittle failure can be derived from an idealization that the material contains a large population of equal sized cracks. Being all the same size, any given crack loaded in pure shear will fail (grow) if the resolved shear stress τ on the crack face exceeds a critical threshold value S_0. If a crack face is additionally subjected to a normal compressive stress $\overline{\sigma_N}$, then the applied shear τneeded to induce crack growth must be larger than S_0 by an amount $\tau^{\text{fric}} = \mu\overline{\sigma_N}$, where $\mu$is the coefficient of friction. Stated differently, a given crack is *safe* from failure if

$$\tau - \tau^{\text{fric}} = S_0 \tag{B.2}$$

or, recalling that $\tau^{\text{fric}} = \mu\overline{\sigma_N}$,

$$\tau - \tan\Phi\overline{\sigma_N} \quad \text{, where} \quad \tan\Phi \equiv \mu \tag{B.3}$$

This criterion must be satisfied by all cracks in the material. Since Mohr-Coulomb theory arises from an idealization that the material contains a large population of cracks (uniformly random in orientation), a

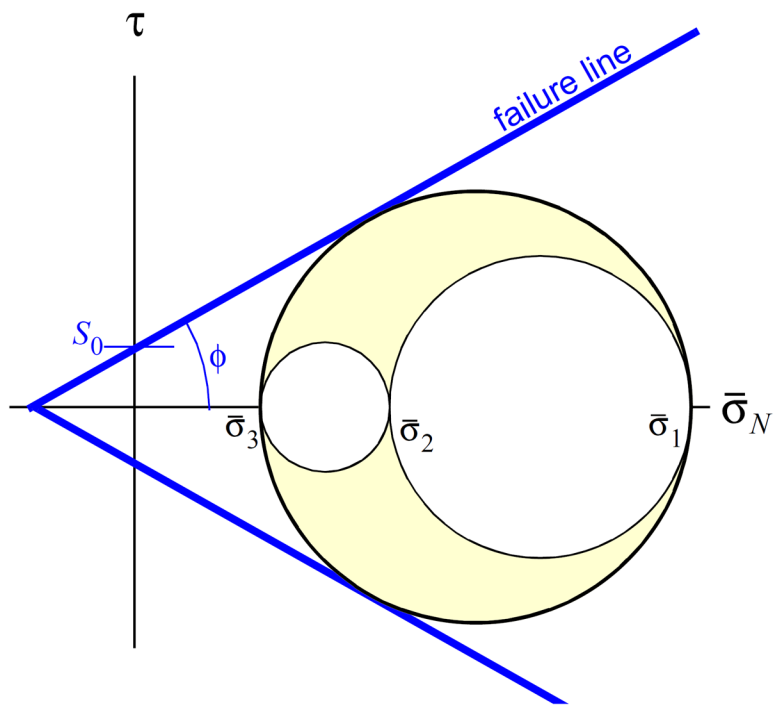

Figure B.3. A stress at the limit state under Mohr-Coulomb theory.

material is safe from failure under general stress states only if all points on the Mohr's diagram for the stress fall below the "failure line" defined by $\tau = S_0 + \tan\Phi\overline{\sigma_N}$. Failure is therefore deemed to occur when the outer Mohr's circle first "kisses" the failure line. Working out the geometry of Fig. B.3, a circle of radius R, centered at $\overline{\sigma_N} = C$, will be tangent to the failure line if and only if

$$R = S_0 \cos\Phi + C \sin\Phi \tag{B.4}$$

For the outer Mohr's circle,

$$R = \frac{\overline{\sigma_1 - \sigma_3}}{2} \qquad \text{and} \qquad C = \frac{\sigma_1 + \sigma_3}{2} \tag{B.5}$$

or, removing the overbars (defined such that $\overline{\sigma}_k = -\sigma_k$),

$$R = \frac{\sigma_3 - \sigma_1}{2} \qquad \text{and} \qquad C = \frac{-(\sigma_3 + \sigma_1)}{2} \tag{B.6}$$

Substituting these into Eq. (B.4) gives

$$\boxed{\frac{\sigma_3 - \sigma_1}{2} = S_0 \cos\Phi - \frac{\sigma_3 + \sigma_1}{2} \sin\Phi} \tag{B.7}$$

This is the Mohr-Coulomb failure criterion cast in terms of principal stresses. Eq. (3.7a) and Eq. (3.7b) on page 33 of the main report imply

$$\frac{\sigma_3 - \sigma_1}{2} = \sqrt{J_2} \cos\overline{\theta} \tag{B.8a}$$

$$\frac{\sigma_3 + \sigma_1}{2} = \frac{I_1}{3} - \frac{\sqrt{J_2}}{\sqrt{3}} \sin\overline{\theta} \tag{B.8b}$$

Therefore, the stress invariant version of Eq. (B.7) is

$$\sqrt{J_2} \cos\overline{\theta} = S_0 \cos\Phi - \frac{I_1}{3} \sin\Phi - \frac{\sqrt{J_2}}{\sqrt{3}} \sin\overline{\theta} \sin\Phi \tag{B.9}$$

or, solving for $\sqrt{J_2}$,

$$\sqrt{J_2} = \frac{S_0 \cos\Phi - \frac{I_1}{3} \sin\Phi}{\cos\overline{\theta} - \frac{1}{\sqrt{3}} \sin\overline{\theta} \sin\Phi} \tag{B.10}$$

Recall from Eq. (4.39) that Kayenta's limit function F_f fits the *triaxial compression (TXC)* meridional profile to the following functional form

$$\sqrt{J_2} = a_1 - a_3 e^{-a_2 \overline{I}_1} + a_4 \overline{I}_1 \text{ in TXC}(\overline{\theta} = 30^\circ) \tag{B.11}$$

In triaxial compression (TXC), the Lode angle is $\overline{\theta} = 30^\circ$ so that

$$\cos\overline{\theta} = \cos 30^\circ = \frac{\sqrt{3}}{2} \qquad \text{and} \qquad \sin\overline{\theta} = \sin 30^\circ = \frac{1}{2} \tag{B.12}$$

Therefore, Eq. (B.10) specializes to TXC loading as

$$\sqrt{J_2} = \frac{2\sqrt{3}}{3 - \sin\Phi}\left(S_0 \cos\Phi - \frac{I_1}{3}\sin\Phi\right) \qquad \textbf{(Mohr-Coulomb in TXC)} \tag{B.13}$$

Being careful to note that , comparing this result with Eq. (B.11) implies that Kayenta's limit surface parameters for Mohr-Coulomb theory should be set as

$$a_1 = \left(\frac{2\sqrt{3}}{3 - \sin\Phi}\right) S_0 \cos\Phi \tag{B.14a}$$

$$a_2 = 0 \tag{B.14b}$$

$$a_3 = 0 \tag{B.14c}$$

$$a_4 = \left(\frac{2\sqrt{3}}{3 - \sin\Phi}\right) \frac{\sin\Phi}{3} \tag{B.14d}$$

Therefore, the general Mohr-Coulomb criterion in Eq. (B.10) may be written in the form required for Kayenta as

$$\begin{aligned} &\sqrt{J_2}\Gamma(\overline{\theta}) = f_f(\overline{I}_1) f_c(\overline{I}_1), \\ &\text{where } f_f(\overline{I}_1) = a_1 + a_4 \overline{I}_1, \quad f_c(\overline{I}_1) = 1 \\ &\text{and } \Gamma(\overline{\theta}) = \frac{2\sqrt{3}}{3 - \sin\Phi}\left(\cos\overline{\theta} - \frac{\sin\Phi \sin\overline{\theta}}{\sqrt{3}}\right) \end{aligned} \tag{B.15}$$

Naturally, **J3TYPE** $= 3$ is appropriate (see page 70). A classic Mohr-Coulomb material has no cap; to make the cap function f_c always equal 1, the cap and crush curve features should be disabled as described on page page 275. Classical Mohr-Coulomb theory is meant to apply to brittle rupture, so kinematic hardening should be disabled as described on page page 275. An appropriate value for the TXE/TXC strength ratio Ψ must be determined by evaluating Eq. (B.10) in TXE where $\overline{\theta} = -30^\circ$:

$$\sqrt{J_2} = \frac{2\sqrt{3}}{3 + \sin\Phi}\left(S_0 \cos\Phi - \frac{I_1}{3}\sin\Phi\right) \qquad \textbf{(Mohr-Coulomb in TXE)} \tag{B.16}$$

The TXE/TXC strength ratio is then given by the ratio of the right-hand sides of Eq. (B.16) and Eq. (B.13):

$$\Psi = \frac{3-\sin\Phi}{3+\sin\Phi} \qquad \text{Note: The Inverse relationship is } \sin\Phi = 3\left(\frac{1-\Psi}{1+\Psi}\right) \tag{B.17}$$

For this classical Mohr-Coulomb theory, the slope of the TXC meridional profile, $\frac{\mathrm{d}J_2}{\mathrm{d}\overline{I}_1}$, equals $\sin\Phi$. Therefore, may be eliminated from Eq. (B.14d) and Eq. (B.17) to reveal that the TXE/TXC strength ratio is coupled to the slope of the TXC meridional profile according to

$$\Psi = \frac{1}{1+\sqrt{3}A}, \text{ where } A \equiv \left(\frac{\partial J_2}{\partial \overline{I}_1}\right)_{\overline{\theta}=30^\circ} = \frac{1}{\sqrt{6}}\left(\frac{\mathrm{d}r}{\mathrm{d}\overline{z}}\right)_{\overline{\theta}=30^\circ} \tag{B.18}$$

In other words, in Mohr-Coulomb theory, the strength ratio cannot be specified independently from the slope of the meridional profile. On page 273, this relationship is applied to non-Mohr-Coulomb models to support a pressure varying strength ratio.

Incidentally, the Mohr-Coulomb G function in Eq. (B.15) may be written

$$\Gamma(\overline{\theta}) = \frac{\cos(\overline{\theta}-\overline{\theta}_0)}{\cos\left(\frac{\pi}{6}-\overline{\theta}_0\right)} \tag{B.19}$$

where

$$\overline{\theta}_0 = -\arctan\left[\frac{\sin\Phi}{\sqrt{3}}\right] = -\left[\sqrt{3}\left(\frac{1-\Psi}{1+\Psi}\right)\right] \tag{B.20}$$

Here, $\overline{\theta}_0$ is the Lode angle at which the material has the lowest shear strength (i.e., the angle where the yield surface is closest to the origin).

Below, we show the skeleton required for setting Kayenta inputs to run classical Mohr-Coulomb theory. This input set also shows how to set parameters if you wish to run with non-associativity (where the flow potential function differs from the yield function only by having a different value for Φ). Values for (a_1, a_2, a_3, a_4) and for (a_2^{PF}, a_4^{PF}) are set by using Eq. (B.14). Values for Ψ and Ψ^{PF} are set by using Eq. (B.17).

```
$ Kayenta parameters for duplicating a classical Mohr-Coulomb material
$ in BOTH the octahedral and meridional profiles.
$
$ Replace the four occurances of "VALUE" in this file with the appropriate
$ Mohr-Coulomb parameter. You may generate Kayenta input parameters
$ by using the command "aprepro this_file output_file". Preferably, if
$ your finite element code supports embedded aprepro directives, then
$ drop this file DIRECTLY into your finite element Kayenta input block.
```

```
$
$ {friction_angle = VALUE}     $angle "phi" in Kayenta Appendix B
$ {dilation_angle = VALUE}     $for associativity, this equals "phi"
$
$ {cohesion = VALUE}           $parameter "S_sub0" in Kayenta Appendix B
$                              $This equals yield stress in simple shear.


$ Let Aprepro compute some helper quantities
$          {scalef = 2.0*sqrt(3)/(3.0-sin(friction_angle))}
$          {scaleg = 2.0*sqrt(3)/(3.0-sin(dilation_angle))}
$
B0 = {VALUE}     $bulk modulus
G0 = {VALUE}     $shear modulus
J3TYPE=3         $Mohr-Coulomb octahedral option
A1 = {scalef*cohesion*cos(friction_angle)}
A2 = 0.0
A3 = 0.0
A4 = {scalef*sin(friction_angle)/3.0}
RK = {(3.0-sin(friction_angle))/(3.0+sin(friction_angle))}
A4PF = {scaleg*sin(dilation_angle)/3.0}
RKPF = {(3.0-sin(dilation_angle))/(3.0+sin(dilation_angle))}
P0 = -1.e99     $ turn off the cap and crush-curve features
CR = 0.001      $ prevent cap influence on shear response
```

This list presumes that your implementation of Kayenta sets defaults for unlisted parameters.

Pressure-varying strength ratio

If (unlike Mohr-Coulomb theory) the meridional profile is curved, then the user can set $RK = 1$ to instruct Kayenta to use Fig. B.4, this feature allows a smooth transition from a Mohr-Coulomb distorted hexagon (or triangle) at low pressures to a von Mises circle at high pressures.

To conclude this appendix, sub-input sets are summarized for controlling various features of Kayenta.

Sub-input set for *linear* elasticity

```
B1 = 0.0
B2 = 0.0
B3 = 0.0
B4 = 0.0
G1 = 0.0
G2 = 0.0
G3 = 0.0
G4 = 0.0
```

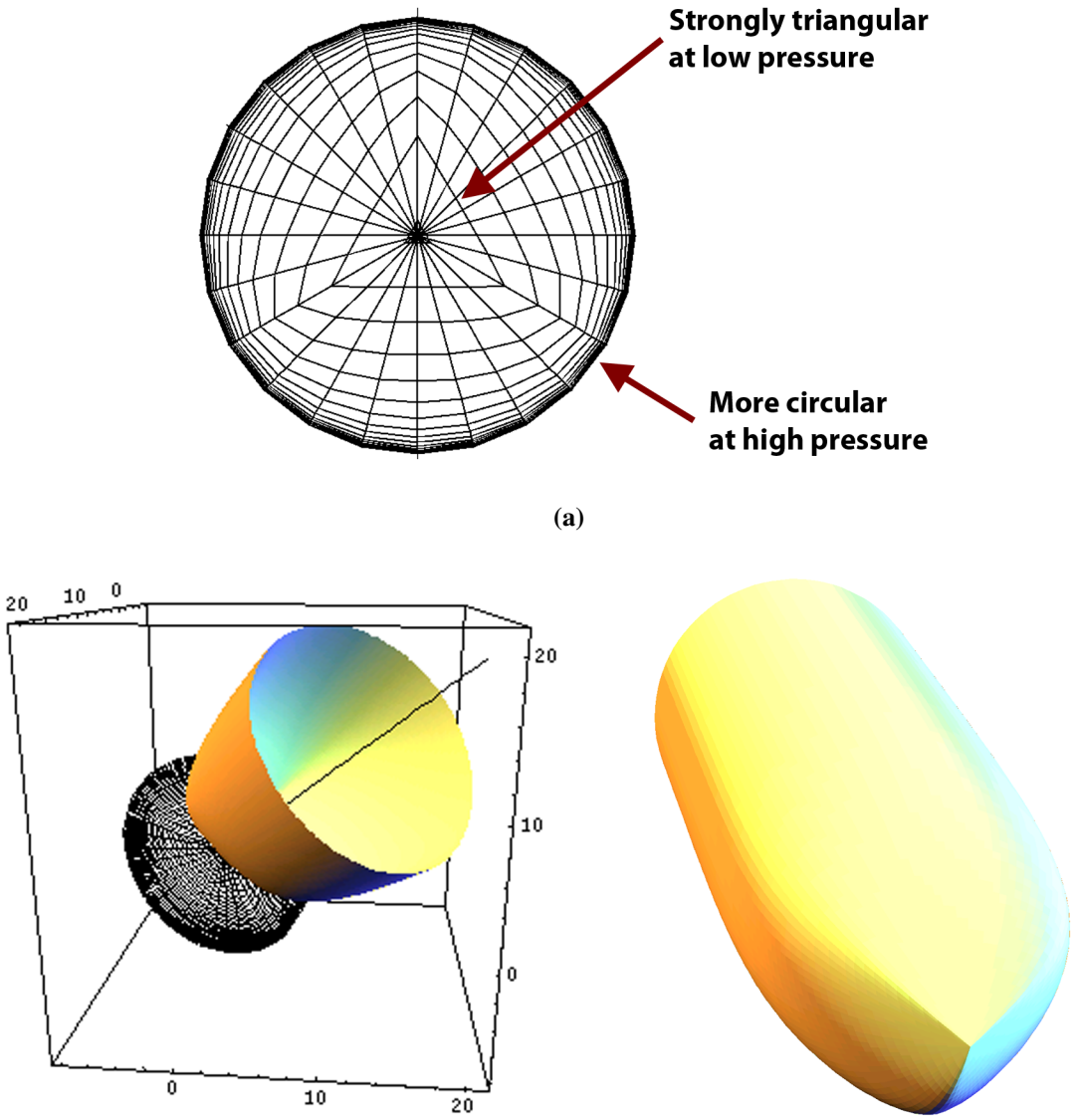

Figure B.4. Pressure varying strength ratio (enabled by setting $RK = -1.0$). At low pressure, this material (SiC-N) has a meridional slope nearly equal to $A = 1/\sqrt{3}$, for which Eq. (B.18) gives a strength ratio of 1/2, which is appropriate for a maximum principal stress failure criterion. At high pressures, the meridional slope approaches zero, for which Eq. (B.18) gives a strength ratio of 1, which (with **J3TYPE** $= 2$) corresponds to a circular (von Mises) octahedral profile.

*Set **B0** to the constant bulk modulus and set **G0** to the constant shear modulus. To additionally disable any form of plasticity, set **A1** to a very large number and disable cut-offs as well as the cap and crush curve as described below.*

Sub-input set for "turning off" all rate dependence

```
T1 = 0.0
T2 = 0.0
T3 = 0.0
T4 = 0.0
T5 = 0.0
T6 = 0.0
T7 = 0.0
```

*For LINEAR rate dependence, set **T1** to the material's characteristic response time and all other **T** parameters to zero.*

Sub-input set for disabling kinematic hardening

```
HC=0.0
RN=0.0
```

Sub-input set for associativity

```
CRPF=0.0
RKPF=0.0
A2PF=0.0
A4PF=0.0
```

This list presumes that your implementation of Kayenta sets defaults for unlisted parameters. If not, associativity requires that all parameters that end in "PF" be set equal to their yield parameter counterparts.

Sub-input set for disabling cap and crush curve

```
P0 = -1.e99       $put the cap at infinity
P1 = 0.0
P2 = 0.0
P3 = 0.0          $set porosity to zero
CR = 0.001        $minimize the size of the curved part of the cap
```

This list presumes that your implementation of Kayenta sets defaults for unlisted parameters. Kayenta's internal user-input processor and initializer will recognize these inputs as "cap disablers" and adjust the model appropriately.

Sub-input set for disabling tensile cut-off limits

```
CUTI1   = 1.e99   $ set pressure (I1) cut-off to "infinity"
CUTPS   = 1.e99   $ set principal stress cut-off to "infinity"
```

This list presumes that your implementation of Kayenta sets defaults for unlisted parameters.

References

[1] Brian M. Adams, Mohamed S. Elbeida, Michael S. Eldred, John Jakeman, Laura P. Swiler, William J. Bohnhoff, Keith R. Dalbey, John P. Eddy, Kenneth T. Hu, and Dena M. Vigil. *Dakota, A Multilevel Parallel Object-Oriented Framework for Design Optimization, Parameter Estimation, Uncertainty Quantification, and Sensitivity Analysis*. Sandia National Laboratories Report SAND2010-2183, Albuquerque, NM, 2014.

[2] D.F. Aldridge. *Elastic wave radiation from a pressurized spherical cavity*. Sandia National Laboratories Report SAND2002-1882, Albuquerque, NM, 2002.

[3] J.G. Arguello, A.F. Fossum, D.H. Zeuch, and K.G. Ewsuk. Continuum-based FEM modeling of alumina powder compaction. *KONA*, 19:166–177, 2001.

[4] J.H. Argyris, G. Faust, J. Szimmat, E.P. Warnke, and K.J. Willam. Recent developments in the finite element analysis of prestressed concrete reactor vessel. *Nuclear Eng. Des*, 28:42–75, 1974.

[5] B. Banerjee. An evaluation of plastic flow stress models for the simulation of high-temperature and high-strain-rate deformation of metals., 2005.

[6] Z.P. Bazant and J. Planas. *Fracture and Size Effect in Concrete and Other Quasibrittle Materials*. CRC Press LLC, Boca Raton, FL, 1998.

[7] R. Becker, 2003. unpublished presentation materials.

[8] M.L. Blanford. Jas3d: A multi-strategy iterative code for solid mechanics analysis. Unpublished, 1998.

[9] R.I. Borja, K.M. Sama, and P.F. Sanz. On the numerical integration of three invariant elastoplasticity constitutive models. *Comput. Methods Appl. Mech. Engr.*, 192:1227–1258, 2003.

[10] L.F. Boswell and Z. Chen. A general failure criterion for plain concrete. *Int. J. Solids Struct.*, 23:621–630, 1987.

[11] E.A. Boucheron, K.H. Brown, K.G. Budge, S.P. Burns, D.E. Carroll, S.K. Carroll, M.A. Christon, R.R. Drake, C.G. Garasi, T.A. Haill, J.S. Peery, S.V. Petney, J. Robbins, A.C. Robinson, R.M. Summers, T.E. Voth, and M.K. Wong. *ALEGRA: User Input and Physics Descriptions Version 4.2*. Sandia National Laboratories Report SAND2002-2775, Albuquerque, NM, 2002.

[12] R. Brannon and S. Leelavanichkul. A multi-stage return algorithm for solving the classical damage component of constitutive models for rocks, ceramics, and other rock-like media [uintah-related publication]. *International Journal of Fracture*, 163:133–149, 2010.

[13] R. M. Brannon. Elements of phenomenological plasticity: geometrical insight, computational algorithms, and applications in shock physics. *Shock Wave Science and Technology Reference Library: Solids I*, 2:189–274, 2007.

[14] Rebecca M. Brannon. Elements of phenomenological plasticity: Geometrical insight, computational algorithms, and topics in shock physics. In Yasuyuki Horie, editor, *ShockWave Science and Technology Reference Library*, volume 2, pages 189–274. Springer Berlin Heidelberg, 2007.

[15] R.M. Brannon. Rotation and reflection: a review of useful theorems associated with orthogonal tensors, 2004. http://www.mech.utah.edu/˜brannon/public/rotation.pdf.

[16] R.M. Brannon. Tutorial: Large-deformation kinematics, 2006.

[17] R.M. Brannon. Animatioin: Stretch, rotation, and intuition about strain-rate approximations, 2012.

[18] R.M. Brannon, J.A. Burghardt, S.J. Bauer, and D.R. Bronowski. Experimental assessment of unvalidated assumptions in classical plasticity theory. Technical Report SAND2009-0351, Sandia National Laboratories, Jan 2009.

[19] R.M. Brannon and W.J. Drugan. Influence of non-classical elastic-plastic constitutive features on shock wave existence and spectral solutions. *J. Mech. Phys. Solids*, 41(2):297–330, 1993.

[20] R.M. Brannon, A.F. Fossum, and O.E. Strack. A computational model for three-dimensional materials containing arbitrary joint sets. In *Final Report and Proceedings of the GSFM 2010 Workshop: 11 - 15 January 2010. Defense Threat Reduction Agency, DTRA-TR-10-27, April 2011. Washington, DC.*, 2010.

[21] R.M. Brannon and T.J. Gowen. Aleatory quantile surfaces in damage mechanics. *J. Eur. Ceram. Soc.*, 34:2643–2653, 2014.

[22] R.M. Brannon and S. Leelavanichkul. Survey of four damage models for concrete. Technical report, Sandia National Laboratories Report SAND2009-5544, Albuquerque, NM, 2009.

[23] R.M. Brannon, J.M. Wells, and O.E. Strack. Validating theories for brittle damage. *Metallurgical and Materials Transactions*, 38A:2861–2868, 2007.

[24] R.M. Brannon and M. K. Wong. *MIG Version 0.0 Model Interface Guidelines: Rules to Accelerate Installation of Numerical Models Into Any Compliant Parent Code*. Sandia National Laboratories Report SAND96-2000, Albuquerque, NM, 1996.

[25] A.A. Brown, J. Casey, and D.J. Nikkel. Experiments conducted in the context of the strain-space formulation of plasticity. *Int. J. Plasticity*, 19:1965–2005, 2003.

[26] J.A. Burghardt. Nonlocal plasticity, instability, and well-posedness of the elastic-plastic initial-boundary value problem. *University of Utah PhD dissertation*, 2011.

[27] M.M. Carroll and Holt A.C. Static and dynamic pore-collapse relations for ductile porous materials. *J. Appl. Phys.*, 43:1626–1636, 1972.

[28] J.K. Dienes, Q.H. Zuo, and J.D. Kershner. Impact initiation of explosives and propellants via statistical crack mechanics. *Journal of Mechanics and Physics of Solids*, 54(10):2235–2240, 2006.

[29] A.A. DiGiovanni and J.T. Fredrich, 2003. private communication.

[30] D. Drumheller. *Introduction to Wave Propogation in Nonlinear Fluids and Solids*. Cambridge Univ. Press, 1998.

[31] G. Duvaut and J.L. Lions. *Les Inequations en Mecaniquie et en Physique*. Dunod, Paris, 1972.

[32] G.V. Farnsworth and A.C. Robinson. Improved kinematic options in ALEGRA. Technical report, Sandia National Laboratories Report SAND2003-4510, Albuquerque, NM, 2003.

[33] A.F. Fossum and R.M. Brannon. *The Sandia GeoModel: Theory and User's Guide*. Sandia National Laboratories Report SAND2004-3226, Albuquerque, NM., 2004.

[34] A.F. Fossum and R.M. Brannon. Unified compaction/dilation, strain-rate sensitive, constitutive model for rock mechanics structural analysis applications. In *ARMA/NARMS*, pages 04–546, 2004.

[35] A.F. Fossum and R.M. Brannon. On a viscoplastic model for rocks with mechanism-dependent characteristic times. 2006.

[36] C.D. Foster, R.A. Regueiro, A.F. Fossum, and R.I. Borja. Implicit numerical integration of a three-invariant, isotropic/kinematic hardening cap plasticity model for geomaterials, 2004. submitted to Elsevier Science.

[37] D.J. Frew, M.J. Forrestal, and W. Chen. A split hopkinson pressure bar technique to determine compressive stress-strain data for rock materials. *Experimental Mechanics*, 41:40–46, 2001.

[38] T. Fuller and M.S. Swan. Payette: an object-oriented material model driver (model developer and user's guide). This software is research code developed at the University of Utah in collaboration with Sandia National Laboratories., December 2011.

[39] T. Fuller and M.S. Swan. matmodlab: an object-oriented material model driver (model developer and user's guide). This software is research code that extends early work on the "Payette" driver developed at the University of Utah in collaboration with Sandia National Laboratories., July 2014.

[40] T.J. Fuller, R.M. Brannon, O.E. Strack, and J.E. Bishop. Initial inclusion of thermodynamic considerations in kayenta. Technical report, Sandia National Laboratories Report SAND2010-4687, Albuquerque, NM, 2010.

[41] Y.C. Fung. *Foundations of Solid Mechanics*. Prentice-Hall, Englewood Cliffs, NJ, 1965.

[42] M.D. Greenberg. *Foundations of Applied Mathematics*. Prentice-Hall, Englewood Cliffs, NJ, 1978.

[43] A.L. Gurson. Continuum theory of ductile rupture by void nucleation and growth. part i: Yield criteria and flow rules for porous ductile media. *J. Engng Mater. Technol.*, 99:2–15, 1977.

[44] E.L. Hoffman and C.A. Lavin. *WISDM: Weapons Information System and Data Management, Version 2.2.0.* Sandia National Laboratories. Electronic. Sandia Network., April 2002.

[45] M.A. Homel, R.M. Brannon, and J.E. Guilkey. Simulation of shaped-charge jet penetration into drained and undrained sandstone using the material point method with new approaches for constitutive modeling. In J. Oliver E. OÃśate and A. Huerta, editors, *11th World Congress on Computational Mechanics (WCCM XI) , 5th European Conference on Computational Mechanics (ECCM V), 6th European Conference on Computational Fluid Dynamics (ECFD VI)*, 2014.

[46] F. Huq, R.M. Brannon, and L. Graham-Brady. Initialization of discrete statistical crack properties in continuum-scale domains. In *Continuum Models Discrete Systems –13, July 21-25, 2014, Salt Lake City, UT*, 2014.

[47] F. Jay. *IEEE Standard Dictionary of Electrical and Electronic Terms*. Institute of Electrical and Electronic Engineers, 1984. ANSI/IEEE Std. 100-1984.

[48] J. Jiang and S. Pietruszczak. Convexity of yield loci for pressure sensitive materials. *Comput. Geotech.*, 5:51–63, 1988.

[49] G. R. Johnson and W. H. Cook. A constitutive model and data for metal subjected to large strains, high strain rates, and high temperatures. *Proceedings of the 7th International Symposium on Ballistics*, 547(11):541–547, 1983.

[50] G. R. Johnson and W. H. Cook. Fracture characteristics of three metals subjected to various strains, strain rates, temperatures and pressures. *Int. J. of Engineering Fracture Mechanics*, 21(1):31 – 48, 1985.

[51] G.R. Johnson and et al. User instructions for the 1995 version of the epic code. Technical report, Alliant Techsystems, Inc., Hopkins, Minnesota, 1994.

[52] G.R. Johnson and T.J. Holmquist. An improved computational constitutive model for brittle materials. *AIP Conf. Proc.*, 309:981–84, 1994.

[53] M Kachanov. Continuum model of medium with cracks. *J. of the Engineering Mechanics Division*, 106:1039–1051, 1980.

[54] K. Kamojjala, R. Brannon, A. Sadeghirad, and J. Guilkey. Verification tests in solid mechanics. *Engr. with Computers*, in press:online doi: 10.1007/s00366–013–0342–x, 2013.

[55] K. Kamojjala and R.M. Brannon. Data relocalization to mitigate slow convergence caused by under-resolved stress fields in computational damage mechanics. *J. Eur. Ceram. Soc.*, 34:2723–2730, 2014.

[56] K.C. Kamojjala. Systematic code verification and validation of damage in high-strength armor materials. *University of Utah PhD dissertation*, 2014.

[57] P. Knupp and K. Salari. *Code verification by the method of manufactured solutions*. Sandia National Laboratories Report SAND2000-1444, Albuquerque, NM, 2000.

[58] J.R. Koteras and A.S. Gullerud. *Verification of Computer Codes in Computational Science and Engineering*. Chapman & Hall/CRC, 2002.

[59] P.V. Lade. Elasto-plastic stress-strain theory for cohesionless soil with curved yield surfaces. *Int. J. Solids Struct.*, 13:1019–1035, 1977.

[60] P.V. Lade and J.M. Duncan. Elastoplastic stress-strain theory for cohesionless soil. *J. Geotech. Engrg. Div., ASCE*, 101:1037–1053, 1975.

[61] R. B Leavy, R. M. Brannon, and O.E. Strack. The use of sphere indentation experiments to characterize ceramic damage models. *Int. J. Appl. Ceram. Technol.*, 7:DOI:10.1111/j.1744–7402.2010.02487.x 1–10, 2010.

[62] J. Lubliner. *Plasticity Theory*. Macmillan, New York, NY, 1990.

[63] J. Lubliner. *Plasticity Theory*. Dover Publications, 2008.

[64] D.J. Macon, R.M. Brannon, and O.E. Strak. *Plastic cap evolution law derived from induced transverse isotropy in dilatational triaxial compression*. Sandia National Laboratories Report SAND2014-1217, Albuquerque, NM, 2014.

[65] G. Maier and T. Hueckel. *Int. J. Rock. Mech. Min. Sci. Geomech. Abstr.*, 16:399, 1979.

[66] L.E. Malvern. *Introduction to the Mechanics of a Continuous Medium*. Prentice-Hall, Englewood Cliffs, NJ, 1969.

[67] H. Matsuoka and T. Nakai. Stress-deformation and strength characteristics of soil under three different principal stresses. *Proc. JSCE*, 232:59–70, 1974.

[68] A. Needleman and J.R. Rice, 1978.

[69] M. Ortiz and A. Pandolfi. Finite-deformation irreversible cohesive elements for three-dimensional crack-propagation analysis. *International Journal for Numerical Methods in Engineering*, 44(9):1267–1282, 1999.

[70] B. Paliwal and K.T. Ramesh. An interacting micro-crack damage model for failure of brittle materials under compression. *Journal of Mechanics and Physics of Solids*, 56(3):896–923, 2008.

[71] K. Park and G. H. Paulino. Cohesive zone models: A critical review of traction-separation relationships across fracture surfaces. *Appl. Mech. Rev.*, 64:060802–1 – 20; doi:10.1115/1.4023110, 2011.

[72] D. Pelessone. A modified formulation of the cap model gulf atomics report ga-c19579. Technical report, Defense Nuclear Agency under Contract, January 1989. prepared under Contract DNA-001086-C-0277.

[73] W.H. Press, B.P. Flannery, S.A. Teukolsky, and W.T. Vetterling. *Numerical Recipes in FORTRAN*. Cambridge University Press, Melbourne, Australia, 1992.

[74] T.A. Pucik. A case study of instability and nonuniqueness induced by nonassociated plastic flow. Unpublished Manuscript, 1993.

[75] T.A. Pucik. Material model driver, April 2004. Memorandum of Record.

[76] M. Rashid. Incremental kinematics for finite-element applications. *Int. J. Numerical Meth. in Engr.*, 36(23):3937–3956, 1993.

[77] P.J. Roache. *Verification and Validation in Computational Science and Engineering*. Hermosa publishers, Albuquerque, NM, 1998.

[78] I.S. Sandler and T.A. Pucik. *Mechanics of Materials and Structures*. Elsevier Science B.V., New York, 1994.

[79] I.S. Sandler and D. Rubin. An algorithm and a modular subroutine for the cap model. *Int. J. Numer. & Anal. Meth. Geomech.*, 3:173, 1979.

[80] L.E. Schwer and et al. *Guide for verification and validation in computational solid mechanics*. ASME, October 2006.

[81] L.E. Schwer and Y.D. Murry. A three-invariant smooth cap model with mixed hardening. *Int. J. for Num. And Anal. Mech. In Geomech.*, 18:657–688, 1994.

[82] P.E. Sensey, A.F. Fossum, and T.W. Pfeifle. Non-associative constitutive laws for low porosity rocks. *Int. J. for Num. and Analytical Meth. in Geomech.*, 7:101–115, 1983.

[83] J. Simo and T. Hughes. *Computational Inelasticity*. Springer, 2000.

[84] D. Simons. Single-element load paths to complement actd v&v problems 1&2, 2003. Northrop Grumman Information Technology unpublished presentation slides for ACTD V&V Working Group Meeting.

[85] O.E. Strack, R.B. Leavy, and R.M. Brannon. Aleatory uncertainty and scale effects in computational damage models for failure and fragmentation. *Int. J. Numer. Meth. Engng*, in press:online doi: 10.1002/nme.4699, 2014.

[86] D. Sulsky, A. Chen, and H. L. Schreyer. A particle method for history-dependent materials. *Comput. Meths. Appl. Mech. Engrg.*, 118:179–196, 1994.

[87] M.S. Swan. Incorporation of a general strain-to-failure fracture criterion into a stress-based plasticity model through a time-to-failure softening mechanism. Master's thesis, University of Utah, 2012. Retrieved from ProQuest Dissertation and Theses, UMI No. 1506806.

[88] L.M. Taylor and D.P. Flannagan. Pronto 3d a three-dimensional transient solid dynamics program. Technical report, Sandia National Laboratories Report SAND87-1912, Albuquerque, NM, 1989.

[89] P.A. Taylor. Cth reference manual: The geo-effective stress (geffs) model. Technical report, Sandia National Laboratories Report SAND2004-5313, Albuquerque, NM, 2004.

[90] T. Telford. *CEB-FIB Model Code 1990*. European Design Code, Lausanne, Switzerland, 1993.

[91] A. Tonge. A unified framework which uses multi-scale microstructure information for modeling dynamic failure in brittle materials. *The Johns Hopkins Department of Mechanical Engineering, PhD dissertation*, 2014.

[92] V. Tvergaard. *J. Mech. Phys. Solids*, 30:399, 1982.

[93] V. Tvergaard. *Advances in Applied Mechanics*, 27:83, 1990.

[94] T.L. Warren, A.F. Fossum, and D.J. Frew. Penetration into low strength (23 mpa) concrete: target characterization and simulations. *Int J. Impact Engr.*, 30(5):477–503, 2004.

[95] T. Wierzbicki, Y. Bao, Y.W. Lee, and Y. Bai. Calibration and evaluation of seven fracture models. *International Journal of Mechanical Sciences*, 47(4-5):719 – 743, 2005.

[96] M. Wilkins and M. Guinan. Impact of cylinders on a rigid body. *J of Appl. Phys.*, 44(3):1200–1206, 1973.

[97] M.L. Wilkins, R.D. Streit, and J.E. Reaugh. Cumulative-strain-damage model of ductile fracture: simulation and prediction of engineering fracture tests. Technical report, Lawrence Livermore National Laboratory, 1980.

[98] K.J. Willam and E.P. Warnke. Constitutive model for the triaxial behavior of concrete, 1975. ISMES Seminar on Concrete Structures Subjected to Triaxial Stresses.

[99] S. Wolfram. *The Mathematica Book, 4th Ed*. Cambridge Univ. Press, 1999.

[100] M.K. Wong, J.R. Weatherby, C.D. Turner, A.C. Robinson, T.A. Haill, and D.E. Carroll. Physics applications in the ALEGRA framework, June 2001. First MIT Conference on Computational Fluid and Solid Mechanics.

[101] T. Wright. *The Physics and Mathematics of Adiabatic Shear Bands*. Cambridge University Press, 2002.

Sandia National Laboratories